UNIVERSITA' DEGLI STUDI DI VERONA

DEPARTMENT OF BIOTECHNOLOGY

PhD School in Natural Science and Engineering

PhD Course in Biotechnology

Cycle XXXII

Investigation on Bacterial Selenite Reduction to Elemental Selenium by *Bacillus mycoides* SeITE01 and *Stenotrophomonas maltophilia* SeITE02 through Spectroscopic and Metabolomics Analyses, with Characterization of Biogenic Selenium Nanoparticles (Bio-SeNPs)

PhD Thesis

Author:

Baggio Greta

Advisor:

Prof. Giovanni Vallini

Co-Advisor:

Prof. Raymond J. Turner

Prof. Silvia Lampis

ABBREVIATIONS

2', 3'-cAMP	2', 3'-cyclic adenosine monophosphate
4-HB	4-hydroxybenzoate
A	Absorbance
Ade	Adenine
AMP	Adenosine 5''-monophosphate
Arg	Arginine
Asp	L-aspartate
Bio-SeNPs	Biogenic Selenium NanoParticles
Bio-SeNRs	Biogenic Selenium NanoRods
BSH	Bacillithiol
ChNPs, ChSeNPs	Chemical Nanoparticles, Chemical Selenium NanoParticles
CFU	Colony Forming Unit
Cys	L-cysteine
dA	2''-deoxyadenosine
dCTMP	2''-deoxycitydine 5''-monophosphate
Dh	Hydrodynamic Diameter
DLS	Dynamic Light Scattering
EDX	Energy Dispersive X-ray Analysis
EPS	Extracellular Polymeric Substances
FT, FTIR	Fourier Transform, Fourier transform infrared
G	Guanine
GC-MS	Gas Chromatography-Mass Spectrometry
Gln	Glutamine
Glu	Glutamate
GPx	Glutathione Peroxidase
GS-Se$^-$	Selenopersulfide of glutathione
GS-Se-SG	Selenodiglutathione
GSH	Glutathione

His	L-histidine
Hyp	Trans-4-hydroxyproline
IAA	Indole-3-acetic acid
IPyA	Indole-3-pyruvic acid
IR, MIR, FIR, NIR	Infrared, Mid-Infrared, Far-Infrared, Near-Infrared
KEGG	Kyoto Encyclopedia of Genes and Genomes
LC-MS	Liquid Chromatography-Mass Spectrometry
Lys	Lysine
LMW	Low-molecular-weight
Met	Methionine
MS	Mass Spectrometry
NAC	N-acetyl-L-cysteine
NB	Nutrient Broth
NMR	Nuclear Magnetic Resonance
NMs	Nanomaterials
PAA	Phenylacetic acid
PCs, PCA	Principal Components, Principal Component Analysis
PdI	Polydispersity Index
Phe	Phenylalanine
PHFs	Poly-β-hydroxy Fatty acids
Pro	Proline
Q or coenzyme Q	Ubiquinone
ROS	Reactive Oxygen species
RS-Se-SR	Selenotrisulfides
RT	Retention Time
SDS-PAGE	Sodium Dodecyl Sulphate-PolyAcrylamide Gel Electrophoresis
Sec	Selenocysteine
SEM	Scanning Electron Microscopy
SeMet	Selenomethionine

SH	Thiols
T or %T	Transmittance
TCA cycle	Tricarboxylic acid cycle
TEM	Transmission Electron Microscopy
Thr	L-Threonine
TMP	Thymidine 5''-monophosphate
Trp	Tryptophan
Trx, TrxR	Thioredoxin, Thioredoxin Reductase
Tyr	L-tyrosine
U	Uracil
UPLC	Ultra performance liquid chromatography

ABSTRACT

Bacillus mycoides SeITE01 and *Stenotrophomonas maltophilia* SeITE02 are environmental bacterial isolates that rely on detoxification processes to transform selenite (SeO_3^{2-}), a highly toxic and bioavailable chemical species of selenium, into insoluble and virtually nontoxic elemental selenium (Se^0) with the formation of biogenic selenium nanoparticles (Bio-SeNPs).

In the last decade, Bio-SeNPs have attracted attention for their interesting applications in the nanotechnology, industrial and medical fields not only due to their special physico-chemical features, but also for their attractive antimicrobial activities and anticancer properties. These worthwhile biotechnological traits are related to the presence on Bio-SeNPs of an external organic coating, whose composition and role are mostly unknown and currently under investigation.

In the first part of this thesis, FTIR (Fourier Transform Infrared) spectroscopy was applied to study the SeO_3^{2-} bio-reduction process analysing the bio-molecular composition of both SeITE01 and SeITE02 cells. The analysis was conducted during the diverse cellular growth phases and in different conditions, namely untreated (growth without the presence in the medium of sodium selenite Na_2SeO_3) and Se-treated (exposure to the stress factor SeO_3^{2-}). Moreover, along with FTIR spectroscopic analyses, the biogenic intracellular and extracellular SeNPs bio-produced by the bacterial strains and collected with two extraction methods (vacuum filtration and pelleting processing) were examined also using DLS (Dynamic Light Scattering) measurements and TEM (Transmission Electron Microscopy) imaging.

In the second part of this research, metabolomics was used to investigate the biological reduction and effect of Na_2SeO_3 on SeITE01 and SeITE02 cells by a LC-MS (Liquid Chromatography Mass-Spectrometry) approach. Both intracellular and extracellular metabolites and their concentration fluxes during a defined time course and in response to the exposure of bacterial cells to SeO_3^{2-} were studied.

From the results obtained with all the investigation techniques it was possible to observe and underline two distinct behaviors and trends assumed by the bacterial strains.

SeITE01 cells showed substantial changes when exposed to SeO_3^{2-}, activating a series of macromolecular responses and biochemical pathways to defend the cells against the toxic action of both the oxyanion and the Se nanostructures. Moreover, different FTIR spectral trends were acquired with regard to the organic coatings present on the surfaces of the biogenic SeNPs synthesized by this bacterium, and the most marked differences were recorded according to their different localization (intracellular or extracellular). The Bio-SeNPs production in this Gram-positive microorganism was also described by the data collected with the DLS and the zeta-potential measurements. The analyzed Bio-SeNPs showed an average dimension between 637 and 393 nm for the intracellular Bio-SeNPs, and 147 nm for the extracellular ones. Low value of negative potentials suggest a lower stability of these nanostructures in solution. On the contrary, the Gram-negative bacterium SeITE02 did not present drastic changes in the macromolecular composition after SeO_3^{2-} exposure, and the variations recorded were mainly due to the maintenance of vital cellular functions. DLS data revealed an average size of 315 nm for the intracellular Bio-SeNPs and 160 nm for the extracellular ones, whilst negative potential values at or below -30 mV were recorded, indicating a remarkable stability of these biogenic Se nanostructures and a lower tendency to form aggregates and thus to precipitate.

Thus, the results obtained in the course of this investigation revealed two distinct attitudes and responses on the part of the two microorganisms SeITE01 and SeITE02 to the SeO_3^{2-} exposure and Bio-SeNPs production.

CHAPTER I:

SELENIUM AND BIOGENIC SELENIUM NANOPARTICLES

1.1 SELENIUM

1.1.1 Characteristics, toxicity and environmental occurrence

Selenium (Se) is a naturally occurring, semi-metallic trace element that was discovered 200 years ago by the Swedish chemists Jöns Jakob Berzelius (1779-1848) and Johan Gottlieb Gahn (1745-1818) [1, 2].

This chemical element that has an atomic number of 34, an atomic weight equal to 78.96, and six different naturally occurring stable isotopic masses from 74 to 82 [3] belongs to the chalcogen group of the periodic table (Group VIA). Thus, it exhibits and shares common chemical properties with sulfur (S) and tellurium (Te), generating compounds structurally related to those of sulfur, but more toxic due to different reactivity properties [4]. Moreover, being classified as a metalloid, it shows properties of both metals and non-metals, finding numerous and diversified applications in different sectors. In the technological and industrial areas, it is used extensively in both electronic and glass field for the production of microelectronic circuits and photovoltaic cells [4, 5], it is also added to animal feed and food supplements [6], and it is employed in the production of plastics, pigments and ceramics [4, 7]. In the medical fields, instead, the applications of this particular element are mainly due to its antioxidant and cancer prevention activities [8-10].

In most all living organisms including humans, selenium is an essential micronutrient as it is a key component of a variety of amino acids and functional selenoproteins, such as selenocysteine (Sec) and selenomethionine (SeMet), and of enzymes such as glutathione peroxidase (GPx) and thioredoxin reductase (TrxR) [3, 4, 11].

Depending on its dosage, this element can be toxic and dangerous for health. In adults, the correct daily intake of Se should range from 50 to 200 μg/day, but,

at the same time, an intake less than 40 μg/day may be considered dietary deficiency and an intake major than 400 μg/day can lead to toxic effects [11, 12].

In the environment, Se is found in geological raw material (e.g. native rocks), in water bodies, in sediments and soils, but it can also be naturally released into the surrounding environment by the erosion of rocks and volcanic activities. In addition, also the anthropogenic activities, such as metal mining and smelting, accumulation in municipal landfills, oil refining, and irrigation of Se-rich soils contribute to influence and intensify the presence of this element not only in the soil, but also in waters and the atmosphere, as represented in Scheme 1.1 [13-15]. Thus, the constant increase of this metalloid in the environment has converted it into a contaminant, and in some area of the world starting to represent an important public health concern.

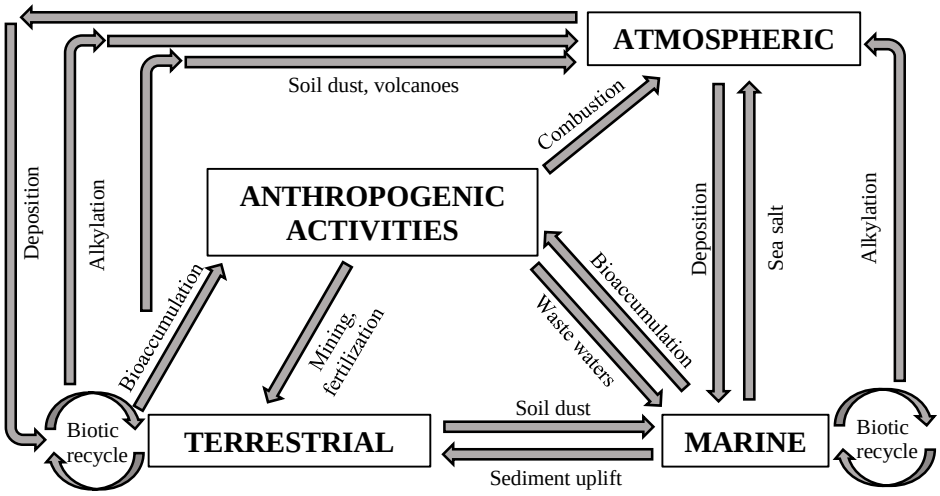

Scheme 1.1. Global selenium cycle considering the anthropogenic influence and activities. Figure modified from Lenz et al. [15].

In nature, Se exists in four oxidation states, depending on both the pH and the redox potential of the soil [14]: selenide (Se^{2-}), elemental selenium (Se^{0}), selenite (Se^{4+}), and selenate (Se^{6+}). However, Se toxicity is not only related to its quantity in contaminated areas, but also to its form. In fact, the most toxic forms for biota are represented by selenate (SeO_4^{2-}) and selenite (SeO_3^{2-}), as these two oxyanions (SeO_x^{2-}) have the ability to replace sulfur in proteins or other sulfur-containing biomolecules and their high reactivity with sulfhydryl

groups leads to the formation of reactive oxygen species (ROS) and cause oxidative damages [3]. Moreover, they are soluble and non-volatile species, and tend to bio-accumulate into biological systems.

For these reasons, in the last decades many studies have tried to identify different bio-reduction processes that could transform the chemically active and toxic forms of Se into the insoluble, volatile and thus not biologically available form of Se^0. Numerous responses have been found in the study and application of different species present in all domains of life, including *Bacteria*, *Archaea*, *Eukarya*, as well as viruses, given their direct involvement and important role not only in the Se cycle but also in the carbon, nitrogen and phosphorous cycles in nature [16, 17].

Interestingly, the conversion of the toxic and pollutant forms of Se into the elemental form performed by these macro and microorganisms takes place through the production of Se nanomaterials.

1.1.2 Bacterial metabolism of selenium

In soil, sediments, and water, the microbial reduction of SeO_4^{2-} and SeO_3^{2-} is known to be an important process for removing the toxic and soluble Se oxyanions (SeO_x^{2-}) from the environment.

Se-utilizing microorganisms can metabolize these forms of Se in a dissimilatory or assimilatory manner. The first occurs under anaerobic conditions and SeO_x^{2-} are used as electron acceptors. The second, instead, provides the bacterial employment of these ions as substrates for producing biologically active Se compounds such as seleno-amino acids, and Se-containing cofactors [16, 18-20].

1.1.2.1 Selenium respiration

Under anoxic conditions, several electron acceptors (e.g. NO_3^-, SO_4^{2-}, S^0, Fe^{3+} or Mn^{4+}) can be utilized by different bacteria for anaerobic respiration as the terminal step of their electron transport chain. In 1989, Macy and co-workers showed that SeO_4^{2-} could be used by bacteria, in particular by

microorganisms belonging to the *Pseudomonas* species, for cellular respiration [21]. Almost at the same time, Oremland et al. reported evidence for SeO_4^{2-} respiration during experiments performed with sediments slurries [22]. The bacterial strategy described by these research groups was thus termed dissimilatory reduction. From a thermodynamic point of view, the reduction of SeO_4^{2-} to SeO_3^{2-} coupled with the oxidation of an electron donor, such as formate, acetate, lactate or glucose, provides energy to support bacterial growth [16, 18, 21-23]. Subsequent studies showed also that phylogenetically diverse groups of microorganisms are able to couple dissimilatory SeO_4^{2-} reduction with anaerobic growth [21, 24-27]. Interestingly, SeO_4^{2-} reducing bacteria not only are phylogenetically diverse (Scheme 1.2), but also are able to couple growth to reduction of a wide range of electron acceptors [16].

The best-characterized microorganisms that exploit this strategy are *Thauera selenatis* [28], *Bacillus selenitireducens* [26], *Enterobacter cloacae* SLD1a-1 [29], and *Sulfurospirillum barnesii* [30, 31], whose characteristics are listed in Table 1.1.

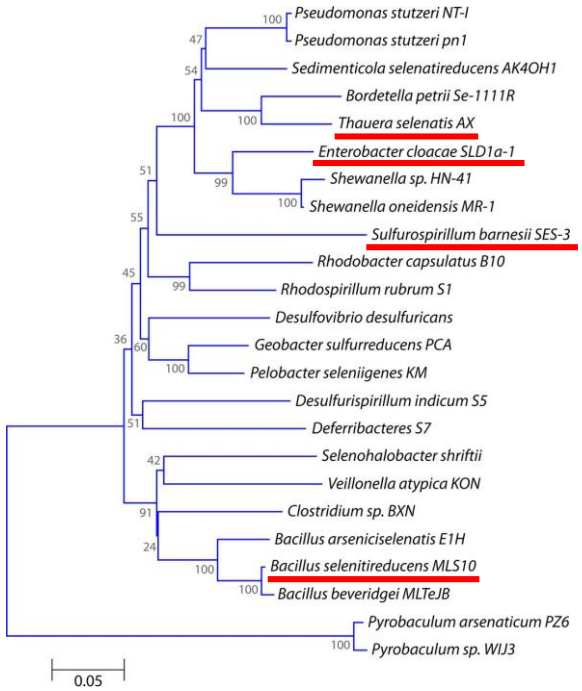

Scheme 1.2. Phylogenetic tree of Se oxyanion-respiring bacteria based on 16s rRNA gene sequences [16]. Red lines show the best studied microorganisms.

Table 1.1. Best-characterized respiring bacteria and their description [26, 28, 29-31].

ORGANISM	ENVIRONMENT	TAXONOMY	ELECTRON DONOR(S)	ELECTRON ACCEPTOR(S)
Thauera selenatis AX	Selenate-contaminated drainage water of San Joaquin Valley	*Betaproteobacteria*	H_2	SeO_4^{2-}, SeO_3^{2-}, NO_3^-
Bacillus selenitireducens strain MLS10	Mono Lake sediments, eastern California	Gram-positive; *Firmicutes*	Lactate, glucose	SeO_3^{2-}
Enterobacter cloacae SLD1a-1	Frashwater samples from San Luis Drain	Gram-negative; *Gammaproteobacteria*	Glucose	SeO_4^{2-}, SeO_3^{2-}, NO_3^-
Sulfurospirillum barnesii SES-3	Selenate-contaminated freshwater marsh, Nevada	Gram-negative; *Deltaproteobacteria*	Lactate, H_2	SeO_4^{2-}, SeO_3^{2-}, NO_3^-, AsO_4^{3-}, Fe(III)

Finally, provided the bacteria involved are capable of metabolizing both the oxyanions SeO_4^{2-} and SeO_3^{2-}, usually sequentially, then elemental Se, which appears in the form of biogenic Se nanoparticles (Bio-SeNPs), is the end product of SeO_4^{2-} reduction.

1.1.2.2 Selenium assimilation

In contrast to the dissimilatory reduction of SeO_x^{2-} used to energize the bacterial cell, the assimilatory reduction of Se oxyanions is employed by both aerobes and anaerobes for the synthesis of Se amino acids, namely Sec and SeMet [3, 4]. These amino acids are incorporated into selenoproteins having essential roles in the proper functioning of bacterial metabolism. In selenoproteins, Se has structural and enzymatic roles, serving oxido-reductase functions against ROS. Additionally, various other functions have been documented including protein folding, micronutrient delivery, and protein repair [18, 32].

1.2 SELENIUM NANOPARTICLES (SeNPs)

1.2.1 Definition, synthesis methods and applications

The term nanotechnology refers to the science of developing and utilizing materials, systems or devices at roughly 1-100 nm scale. At these dimensions, material constituents, devices, and structures exhibit novel optical, electrical, photo-electrical, magnetic, mechanical, chemical, and biological properties that are different from their bulk properties. For these reasons, the nanotechnology field with the design and manipulation of materials at the atomic scale has the potential to deliver considerable benefits to society [33].

Selenium nanoparticles (SeNPs) can be defined as a zero-valent elemental Se aggregates, whose dimensions may vary depending on the process used for their synthesis and extraction.

These particular structures can be produced using different approaches, from physical methods, such as laser ablation [34, 35], ultraviolet radiation [34, 36] and hydrothermal techniques, to chemical processes, such as acid decomposition, catalytic reduction, and precipitation [34, 37]. During the production, however, both chemical and physical approaches have drawbacks, such as the requirement for high temperatures and pressures, acidic pH of the medium and expensive chemicals, and the generation of toxic by-products. Furthermore, nanoparticles made by physicochemical approaches require functionalization with hydrophilic, hydrophobic, conductive, or anticorrosive chemical groups for their possible industrial and biomedical applications [33, 34, 38].

Considering the above issues, the development of new production methods is on rise with the goals for clean, cost-effective, environmentally friendly, and efficient synthesis techniques [33, 39-41]. As a result, the production of biogenic SeNPs by live organisms is promising, primarily because these materials are safe, inexpensive, and utilize ecofriendly and nontoxic materials. Moreover, biological approaches for nanoparticles production are relatively easy and can be performed at ambient conditions [33].

Thus, the novel and important properties that distinguish these materials after reaching into the nanoscale have opened the doors to innovations in energy, manufacturing, and medical treatment.

Nanowires formed by Bio-SeNPs have demonstrated novel photoconductivity [42], while amorphous Bio-SeNPs have shown unique photoelectric, semiconducting, and X-ray-sensing properties [43]. In addition, Se in the nanoforms have gained importance as a possible supplement in the treatment of several diseases due to the change in the properties and efficacy of the material in the nanosize [44], providing better biocompatibility, efficacy, and lower toxicity as compared to various organic and inorganic forms of Se. In fact, biologically synthesized SeNPs have been exploited for medical purposes such as antioxidants [45], anti-cancer and antimicrobial agents [46-51].

1.2.2 Bacterial mechanisms of Se oxyanion reduction and hypothesized Bio-SeNPs formation

Historically, the biosynthesis of the first bacteriogenic SeNPs using the microbe *Escherichia coli* dates back to 1974 by Gerrard and colleagues [52]. After that, many living macro and microorganisms have been reported to use the inherent detoxification processes to transform the highly toxic oxyanions SeO_4^{2-} and SeO_3^{2-} into the elementary form of selenium (Se^0) and into biogenic SeNPs.

Although the bacterial mechanisms to reduce selenites and selenates are numerous and different and may include one or several metabolic pathways and enzymes, the microbial synthesis of Bio-SeNPs can be arbitrarily divided into four stages: (i) transport of SeO_x^{2-} into the cells; (ii) redox reactions; (iii) export of Se^0 nuclei out of the cell; (iv) assembly of Se^0 into Bio-SeNPs.

From this list, however, it is important to point out that steps (ii) and (iv) always occur, while (i) and (iii) depend on the characteristics of the single microorganisms and where the reductive detoxification mechanisms take place [16, 53].

1.2.2.1 Transport of SeO_x^{2-} into the cells

The first step in Se metabolism and reduction, which corresponds to the transport of selenates and selenites into the intracellular compartments of bacterial cells, had few studies. The analysis reported by Aguilar-Barajas and co-workers [54] has hypothesized that SeO_4^{2-} uptake could occur through a sulfate permease, given the structural similarity of this oxyanion with sulfate SO_4^{2-}, as well as molybdate MoO_4^{2-} and chromate CrO_4^{2-}. Besides that, these researchers have shown that an additional non-specific low-efficiency anion transport system, which requires high MoO_4^{2-} concentrations to function optimally, could act as a SO_4^{2-}, SeO_4^{2-} and SeO_3^{2-} carrier. Unfortunately, this transporter has not been further characterized. In *E. coli* cells, instead, it was observed that the sulfate transport complex ABC, which is encoded by the *cysAWTP* operon and is composed of two CysA ATP-binding proteins and two transmembrane proteins (CysT and CysP), represents one of the mechanisms used for SeO_3^{2-} uptake. In this microorganism, SeO_3^{2-} is also transported by sulfate permease, although a significant uptake has been observed after the repression of this transporter as well, highlighting the presence of one and/or more SeO_3^{2-} uptake systems [55]. Another different system has been identified for the bacterium *Ralstonia metallidurans*. In this case, the transition from a much slower SeO_3^{2-} uptake to a faster one may be explained by a slow activation of an unknown SeO_3^{2-} transport system. This transporter allows the accumulation of the oxyanions within the cells through the activation of two competitive and distinct (but with similar kinetics) ways, namely assimilation (a faster pathway) and detoxification (a slower route) [56].

Although these studies have brought significant knowledge and the research groups have advanced more hypotheses, no specific transporters of SeO_3^{2-} have yet been found in microorganisms. Moreover, as the reduction of SeO_x^{2-} does not always occur intracellularly, this step is not obligatory.

1.2.2.2 Bacterial mechanisms of SeO_x^{2-} reduction: selenate SO_4^{2-}

As briefly described in the previous paragraph, a number of different microorganisms have evolved the biochemical machinery to use SeO_4^{2-} as a terminal electron acceptor in the anaerobic respiration. Generally, this dissimilatory strategy can be divided into a two-step process, involving first the reduction of SeO_4^{2-} into SeO_3^{2-} and, then, to insoluble Se^0. This second step is often associated with the appearance of brick red-colored solution indicating the formation of Bio-SeNPs, which can be located both inside the cell and in the extracellular medium.

In the SeO_4^{2-} reductive process, the enzymes and electron transport pathways involved have been investigated relatively well compared to the assembly and secretion of Bio-SeNPs. This in-depth knowledge of the SeO_4^{2-} respiration system is due to the investigation and characterization of different microbial strains, such as the Gram-negative bacteria *T. selenatis* and *E. cloacae* SLD1a-1 and the Gram-positive microbe *Bacillus selenatarsenatis* SF-1, some of which have already been presented and listed in Table 1.1.

In the case of *T. selenatis*, biochemical analysis conducted by Schröder et al. in 1997 [57] allowed the authors of [57] to purify for the first time the selenate reductase (Ser) enzyme, lately named as SerABC selenate reductase, and demonstrate that it was a complex consisting of three heterologous subunits (α, β and γ) located in the periplasmic space. In particular, the enzyme consisted of a catalytic unit (SerA; 96 kDa), an iron-sulfur protein (SerB; 40kDa), a heme b protein (SerC; 23 kDa), and a molybdenum cofactor. Moreover, SerA and SerB were found to contain a cysteine-rich motif and two types of iron-sulfur (i.e., [3Fe-4S] and [4Fe-4S]) clusters [16, 58, 59].

In the schematic model describing the SeO_4^{2-} respiration pathway in *T. selenatis* presented by Debieux and co-workers [60] and reported also by Nancharaiah and Lens [16], the membrane-bound quinol cytochrome c oxidoreductase (QCR) can supply electrons for SeO_4^{2-} reduction that are firstly shunted to periplasmic cytochrome c4 (cytc4) and then to SerABC,

where SeO_4^{2-} is reduced to SeO_3^{2-} in the periplasmic compartment. Subsequently, it was proposed that SeO_3^{2-} is transported from the periplasmic place to the cytoplasm via a sulfate transporter and it is reduced to elemental selenium in the cytoplasm via thiol-mediated detoxification. Recently, a new 95-kDa protein called SefA (selenium factor A) was isolated from the Se nanostructures bio-synthesized by *T. selenatis* cells into the extracellular medium. Evidence demonstrated that SefA protein is involved in stabilization of Bio-SeNPs by preventing their aggregation and may possibly aid in the secretion process [60]. Thus, through *T. selenatis* SeO_4^{2-}-respiring bacterium it is possible to observe the accumulation of red Bio-SeNPs both in the cytoplasm and in the extracellular medium [16, 58, 60].

E. cloacae SLD1a-1, instead, experienced a different situation. In SLD1a-1, intracellular accumulation of Bio-SeNPs is not detected during the SeO_4^{2-} respiration. Biochemical studies suggested that the SeO_4^{2-} reductase used by this bacterium is a membrane-bound trimeric complex with a catalytic subunit of 100 kDa, whose active site is positioned in the inner cell membrane and faces the periplasmic compartment [16, 61, 62]. In this way, the SeO_4^{2-}-to-SeO_3^{2-} reduction into Bio-SeNPs occurs in the periplasmic compartment, with their release into the extracellular environment [61].

Finally, the last strain presented in this section is *B. selenatarsenatis* SF-1, a Gram-positive bacterium that was isolated from the effluent sediments of a glass manufacturing plant, that uses lactate and SeO_4^{2-} as the electron donor and acceptor, respectively [16, 63, 64]. The SeO_4^{2-} reductase of *B. selenatarsenatis* SF-1 is a membrane-bound and a trimeric molybdoenzyme positioned on the cell membrane. In the proposed scheme for the SeO_4^{2-} respiration in this microorganism [16], the electrons from the quinol pool (QH_2) are channeled to the catalytic subunit (SrdA) via SrdC and an iron-sulfur protein, named SrdB. Here, the active site that faces outside the cell allows the SeO_4^{2-} reduction by the molybdenum-containing subunit SrdA, permitting the production of the biogenic end products SeNPs that are finally released into the extracellular medium.

1.2.2.3 Bacterial mechanisms of SeO_x^{2-} reduction: selenite SO_3^{2-}

The microbial reduction process that allows the transformation and detoxification of SeO_3^{2-} into Se^0 has been extensively studied and discussed by numerous research groups over the years, and it was widely recognized to be mediated by the organic biomolecules thiols (SH) [4, 65-69].

In the cytoplasm, SeO_3^{2-} can react with glutathione (GSH) and forms selenodiglutathione (GS-Se-SG), which is further reduced to selenopersulfide of glutathione ($GS\text{-}Se^-$) by NADPH-glutathione reductase. This molecule, being an unstable intermediate, undergoes a hydrolysis reaction with protons to finally form Se^0 and reduced GSH. In this way, a new and further reduction cycle can restart.

Thus, the different mechanisms that have been proposed for the reduction of SeO_3^{2-} to Se^0 in microorganisms may occur via: a) Painter reactions with the SH groups of GSH and proteins [65, 66, 68, 70]; b) the thioredoxin (Trx) and the TrxR system [68, 72]; c) siderophore-mediated reduction [72, 73]; d) abiotic reduction coupled with sulfide-mediated reduction [72, 73]; e) dissimilatory reduction [30], as represented in Scheme 1.3.

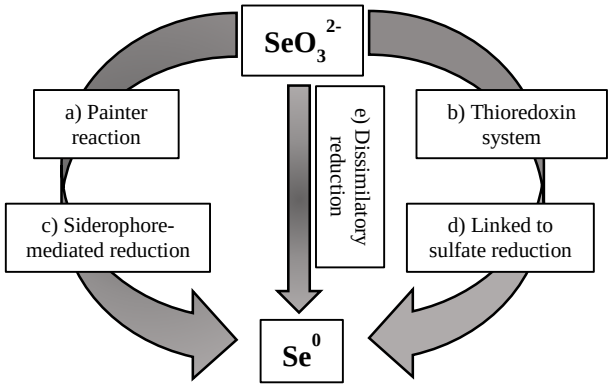

Scheme 1.3. Mechanisms proposed for SeO_3^{2-} reduction in microorganisms. Scheme modified from Nancharaiah and Lens [16].

The so-called Painter-type reaction takes the name from Painter, who first observed in 1941 the high reactivity between SeO_3^{2-} and SH groups and demonstrated the formation of the molecule selenotrisulfides (RS-Se-SR) according to Reaction (1) [65].

$$4RSH + H_2SeO_3 \rightarrow RS\text{-}Se\text{-}SR + RSSR + 3H_2O \quad (1)$$

In 1988, Rabenstein and Tan confirmed the generation of RS-Se-SR through in vivo experiments on *E. coli* cells exposed to SeO_3^{2-} by using ^{77}Se nuclear magnetic resonance (^{77}Se-NMR) [59]. Earlier, in 1971, Ganther proposed an analogous Painter-type reaction between the reduced GSH and SeO_3^{2-} showing the formation of selenotrisulfide of glutathione (GS-Se-SG) [66]. During the reduction process, this compound, which was later renamed selenodiglutathione, is converted to the selenopersulfide anion ($GS\text{-}Se^-$) by glutathione reductase, as described in Reaction (2).

$$GS\text{-}Se\text{-}SG + NADPH \rightarrow GSH + GS\text{-}Se^- + NADP^+ \quad (2)$$

Ganther also proposed that the $GS\text{-}Se^-$ anion, which is an unstable compound, is converted into the reduced GSH and Se^0 according to the following Reaction (3).

$$GS\text{-}Se^- + H^+ \rightarrow GSH + Se^0 \quad (3)$$

In 2004, Kessi and Hanselmann [69] carried out a modification of the reaction steps proposed by Painter [65] and Ganther [68]. They suggested that Reaction (4) must modify Reaction (1) to take into account the formation of superoxide anions during the first step of the abiotic reduction of SeO_3^{2-} with GSH, which are then removed by superoxide dismutases and catalase enzymes to protect the cells from the oxidative stress.

$$6GSH + 3SeO_3^{2-} + 4H^+ \rightarrow 3GS\text{-}Se\text{-}SG + 2O_2^- + 5H_2O \quad (4)$$

Moreover, Björnstedt and co-workers showed in 1992 that in *E. coli* cells SeO_3^{2-} can be a substrate for the thioredoxin system, causing nonstoichiometric oxidation of NADPH [71]. A few years later, Yamada et al. reported that the levels of reduced thioredoxin [$Trx(SH)_2$] and TrxR can increase in *E. coli* cells grown in presence of SeO_3^{2-} in the cultivation medium [67]. Following these observations, it was proposed that the reduced Trx can react with GS-Se-SG and form the oxidized thioredoxin ($Trx\text{-}S_2$), reduced GSH, and $GS\text{-}Se^-$. Subsequently, reduced GSH and Se^0

are released from the reactive anion, as described in (3). Thus, in this detoxification system [$Trx(SH)_2$] and the enzyme TrxR were hypothesized to be involved in the reduction of SeO_3^{2-} and GS-Se-SG, respectively [71], as follows in Reactions (5) and (6):

$$Trx(SH)_2 + GS\text{-}Se\text{-}SG \rightarrow Trx\text{-}S_2 + GSH + GS\text{-}Se^- + H^+ \quad (5)$$

$$Trx\text{-}S_2 + NADPH + H^+ \rightarrow Trx(SH)_2 + NADP^+ \quad (6)$$

In addition to the mechanisms described so far, the oxyanion SeO_3^{2-} can react abiotically with the reactive biogenic sulfide, yielding both the Se^0 and S^0 [72, 73] (Reaction 7):

$$SeO_3^{2-} + 2HS^- + 4\ H^+ \rightarrow Se^0 + 2S^0 + 3H_2O \quad (7)$$

Even an iron siderophore called pyridine-2,6-bis(thiocarboxylic acid) (PDTC; $[C_7H_3O_2S_2]^{2-}$) produced by *Pseudomonas stutzeri* KC was proposed for the detoxification of SeO_3^{2-} through reduction and formation of insoluble Se^0 precipitates [74].

Although it is thought that the glutathione-mediated reactions are the main mechanisms involved in the microbial reduction of SeO_3^{2-}, respiratory reductases (i.e., nitrite reductase, sulfite reductase, and hydrogenase 1) [75-78] and dissimilatory strategies [78] can be considered as additional and significant options.

1.2.2.4 Export and assembly of bacterial Bio-SeNPs

The formation of an amorphous red elemental nanoprecipitate has been found as the stable and final product of SeO_4^{2-} and SeO_3^{2-} reduction by several microorganisms. Although significant progress has been made in understanding the possible mechanisms and strategies involved in the microbial reduction of these oxyanions, nowadays there are unresolved questions on the microbial genesis of intracellular and/or extracellular Se^0 nanospheres. Particularly, still there is insufficient information regarding the secretion of biogenic intracellularly synthesized SeNPs.

Diverse hypotheses have been formulated to explain the emergence of Bio-SeNPs both inside the cell and in the extracellular medium.

For *T. selenatis*, as presented above, it has been supposed that, once in the cytoplasm, the resultant Se^0 seeds are covered by the protein SefA, forming Bio-SeNPs prior to its export from the cell [60]. However, the process by which SefA-Se^0 is exported from the cell remains unknown.

Large amounts of Se-containing particles were registered in the extracellular growth medium of the photosynthetic bacterium *Rhodospirillum rubrum* after SeO_3^{2-} reduction [79]. For this strain, the researchers proposed a vesicular secretion system as a transport mechanism of the biogenic SeNPs out of the cells.

A similar strategy was also suggested by Lampis et al. for *Stenotrophomonas maltophilia* SeITE02 [80]. In this Gram-negative bacterium, the reduced Bio-SeNPs seeds formed intracellularly may be released outside the cells through the process of outer membrane vesiculation, where in response to stress, a section of the outer membrane may form a distinct spherical vesicle composed of a lipid bilayer that encloses material exclusively from the periplasm. However, Lampis and co-workers did not exclude the possibility that the release of Bio-SeNPs may be due to cell lysis, or as they wrote, "a result of some cells bursting" [80].

The latter hypothetical mechanism was, instead, observed by Tomei et al. in the case of the Gram-negative sulfate-reducing microorganism *Desulfovibrio desulfuricans*, whose release of Bio-SeNPs into the medium is considered to be due to cell lysis [81].

Unfortunately, there is not enough experimental evidence in support of either vesicular secretion or cell lysis for the release of intracellularly formed Bio-SeNPs. Furthermore, the mechanisms behind the location of reduction sites and the transportation mechanisms require further and better investigations and clarifications.

Another stage that is still understudied and not entirely clear is the assembly of the Bio-SeNPs. Some authors suggested that the formation of Bio-NPs might involve an Ostwald ripening mechanism, a thermodynamically spontaneous process where small and unstable Se^0 clusters aggregate to form bigger and more stable particles. Such particles, in fact, work as

nucleation seeds for the forming Bio-SeNPs, so that other small Se particles can dissolve and redeposit on forming Bio-SeNPs until their stability is reached [82]. Based on this principle, Kessi and Hanselmann suggested that in *R. rubrum* culture grown in the presence of SeO_3^{2-} larger-sized SeNPs could form by aggregation of small ones, whose original size could be around 35-45 nm. The presence of larger particles of about 250-300 nm, which sedimented during centrifugation of the cells, can be the result of aggregation phenomena of the 35-45 nm particles [69].

1.2.3 Bio-SeNPs and the presence of an external capping layer

A specific and interesting characteristic of the biogenic SeNPs is the presence of associated molecules on their surface.

Currently, the information obtained from various studies reported that these molecules could influence the properties of the nanostructures, such as surface charge and stability over time [4, 53, 80, 83-89]. It was also observed that some of them could be strongly attached to the surface, while others can be removed by mild or stringent processes, as detergent and organic solvent treatments and washing steps [85, 88, 89].

Nowadays, there is no common definition in literature for this associated material and many questions, as their origin, role, composition, strain-specificity and strength of the bound interaction are still open and under investigation.

Nevertheless, the hypothesis that emerged from the study of these particular structures is that the external organic coating present on their surface could originate from the cells themselves or from substances produced by the cells, such as EPS, acronym for extracellular polymeric substances [53, 83-89].

In order to understand which classes of molecules are associated to Bio-SeNPs surface, their capping layers have been analyzed mainly by both spectroscopic techniques (such as Fourier transform infrared (FTIR) spectroscopy and Energy Dispersive X-ray Analysis (EDX)) and classical biochemical approaches (such

as sodium dodecyl sulfate-polyacrylamide gel electrophoresis (SDS-PAGE) and proteomics methods). The obtained results showed that the surface-associated bio(macro)molecules belong mainly to functional groups of proteins, lipids, carbohydrates and nucleic acids [80, 83-90], reinforcing, thus, the hypothesis of a microbial origin.

Furthermore, to provide a more in-depth knowledge and additional information on the potential of this coating layer, over the years various research groups have tried to functionalize inorganic nanostructures with organic and/or biological molecules investigating and comparing their effect with that deriving from nanostructures of biological origin [85, 91-93]. What they observed was that the chemical nanostructures once covered with a biological capping showed behaviors and properties similar to the biological ones. For example, during the study of inorganic metal-based nanoparticles (ChNPs) Stark et al. highlighted how associated molecules could change the properties such as mobility, stability, reactivity and catalytic activity of these ChNPs [91]. They also observed that the capping layer determined the efficiency of NPs in applications such as antimicrobial or anticancer treatments, since the superficial presence of these molecules seemed to mediate the uptake of ChNPs by other cells (microorganisms or cancer cells), even if the details and the steps of this operation are still under debate. Moreover, the authors stressed the role that these associated molecules may have in ChNPs stability, as they tended to aggregate when the single ChNP stability is compromized, for example, by a change in pH from extracellular environment to the cytosol [91].

In 2011, Dobias et al. synthesized ChSeNPs in the presence of an alcohol dehydrogenase that was identified to be strongly associating with *E. coli* biogenic SeNPs. In this work, the authors noticed a three-fold decrease in the average size of ChSeNPs when the protein was present during the synthesis. Moreover, ChSeNPs synthesized with this process resulted perfectly spherical compared to standard ChSeNPs and were reported to bind bacterial proteins [85].

In addition, to shed light on the possible role of associated EPS, in 2016 Jain and co-workers compared biogenic SeNPs to ChSeNPs exposed or not to the

EPS or the protein bovine serum albumin (BSA). They noted that ChSeNPs without any capping agent tend to form wires due to ChSeNPs destabilization, whilst those exposed to EPS or BSA, on the contrary, were spherical and more stable. The authors hypothesized that the EPS stabilizing effect was due to electrostatic repulsion and, partially, to steric hindrance [92].

Addition of an artificial capping layer has also been used to analyze ChSeNPs properties such as antimicrobial and antioxidant activities. In 2017, Prateeksha et al. synthesized SeNPs using polyphenols extracted from honey in order to obtain honey polyphenol-conjugated SeNPs (SeNPs@HP) as a drug delivery vector against *Pseudomonas aeruginosa* biofilms. SeNPs@HP proved to be more effective to inhibit biofilm formation than ChSeNPs and HP alone [93].

In conclusion, given the importance of the capping layer, many studies so far attempted to determine its composition, origin and role with different analytic approaches. Proteins, EPS-like molecules, carbohydrates, humic acids and lipids have been found associating to the SeNPs bio-produced by different microorganisms. Moreover, different kinds of association may exist between the extracted Bio-SeNPs and the organic material. Part of this material could just co-purify with the nanostructure biologically synthetised, whereas some of these bio-molecules could be strongly bound and others more weakly associated. Additionally, the capping layer may be complex with some bio-molecules bound specifically to the Se atoms on the surface, and other material interacting with this primary layer through traditional bio-molecular interactions.

Thus, understanding what kinds of molecules may constitute the capping layer and how they are bound to the metal/metalloid core is an important goal for a more in-depth knowledge of both the biosynthetic mechanism(s), transport and maturation of the Bio-SeNPs of microbial origin.

1.2.4 Bacterial strains used in this thesis

In this study, two different microorganisms have been used and investigated: the Gram-positive bacterium *Bacillus mycoides* SeITE01 and the Gram-negative bacterium *Stenotrophomonas maltophilia* SeITE02.

Both SeITE01 and SeITE02 have been isolated from the same environment, the rhizosphere of Se hyperaccumulator plant *Astragalus bisulcatus*, and are capable of resisting to high concentrations of SeO_3^{2-} [Se(IV)], reducing it under aerobic conditions to nontoxic elemental selenium Se^0 with the formation of biogenic SeNPs [70, 80, 89, 94].

1.2.4.1 *Bacillus mycoides* SeITE01

Bacillus mycoides SeITE01 is an aerobic, rod shaped bacterium that belongs to the *Firmicutes* phylum. Sequencing of the 16S rRNA gene confirmed that strain SeITE01 could be associated to the *Bacillus cereus* group, which includes *B. thuringensis*, *B. anthracis*, *B. mycoides*, *B. pseudomycoides*, *B. cytotoxicus* and *B. wheihenstephanensis* [70, 94]. Phenotypic analysis of the bacterial growth showed that SeITE01 spreads on Nutrient agarized plates with thin, branching projections (rhizoid growth). This elaborated chiral colony pattern was first described as a typical trait of *Bacillus mycoides* species by Flügge in 1886, who called them “mycoides” due to their fungal-like growth [95].

B. mycoides is a common soil bacterium, occurring in the rhizosphere of different plant species. Several studies also reported on the contribution of these bacteria to the Induced Systemic Resistance (ISR) in plants even by PGP (plant growth promoting) traits [70, 96]. In addition, these species have been recognized not only for their biotechnological applications at an industrial scale for the generation of biofuels (e.g. hydrogen), biopolymers (e.g. polyhydroxyalkanoates), and bioactive molecules (e.g. acyl-homoserine lactonases) [97], but they have been considered also for bioremediation strategies due to their degradative efficiency toward toxic organic compounds [63, 64, 98-100].

Strain SeITE01 is in fact able to grow in the presence of up to 25 mM SeO_3^{2-} and to produce nearly spherical Bio-SeNPs with dimensions between 50 and 600 nm depending on the incubation time. Moreover, Lampis et al. observed that the oxyanion SeO_3^{2-} negatively affected SeITE01 growth rate, as the cultures reached stationary phase more rapidly when exposed to selenite than when not exposed [70]. According to the models presented in Section 2.2.3, a Painter-type reaction was hypothesized also for this bacterium, although this detoxification process is still under investigation and numerous questions are open. In fact, to further clarify this reaction mechanism, an activity assay was performed on native proteins extracted from both the EPS fraction, cytosolic, periplasmic compartments, and the supernatant of SeITE01 cultures treated with 2 mM of the salt sodium selenite Na_2SeO_3, in order to localize SeO_3^{2-} reduction activity [70]. From the results of this experiment, it was possible to observe the appearance of a red color (mostly typical of amorphous Se^0) in the membrane and supernatant fractions after the addition of NADH as electron donor, while no activity was evidenced in EPS fraction. On the other hand, only little activity was detected in the cytosolic fraction. Thus, the authors proposed that the main pathway for SeO_3^{2-} reduction could involve proteins secreted by the cell or at the membrane/cell wall level, while at the cytoplasmic level, a Painter-type reaction as ancillary reduction could occur. In addition, another hypothesis could consider the initial SeO_3^{2-} reduction at the cytoplasmic level with the subsequent Bio-SeNPs release after the cell lysis. In the same work, SEM (Scanning Electron Microscopy) and TEM (Transmission Electron Microscopy) images of SeITE01 cells grown with 2 mM Na_2SeO_3 were also collected [70]. SEM observation showed the presence of Bio-SeNPs after 6 h as spherical or oblong particles from 50 to 100 nm in size, but overall inhomogeneous, whilst an average dimension was observed to increase to 50-400 nm after 48 h of growth, leading to the hypothesis of an Ostwald ripening-like growth mechanism. The TEM, instead, showed clearly the presence of electron-dense particles mainly extracellularly (and rarely intracellularly), where Bio-SeNPs seemed to be

embedded in EPS-like material (greyish material that surrounds the Bio-SeNPs).

Beside microscopy observations, presence of EPS-like material and the proposed model for SeNPs bio-synthesis, the origin and composition of the capping layer is still under investigation. Further analyses are necessary to find out which specific molecules are associated to the SeNPs bio-produced by this strain in order to clarify both the synthesis model and eventually the role of such molecules in possible Bio-SeNPs applications.

1.2.4.2 *Stenotrophomonas maltophilia* SeITE02

S. maltophilia is a ubiquitous Gram-negative, rod-shaped, aerobic and non-fermentative Gamma-proteobacterium widespread in different environmental niches [101, 102]. It occurs in the rhizosphere of a variety of plants such as wheat, oat, cucumber, maize, oilseed rape, and potato [103, 104], and it has been isolated either from soils or aquatic environments [105]. The genus *Stenotrophomonas* is nowadays considered even for its potential application in bioremediation [106].

The strain SeITE02 is able to grow in the presence of up to 50 mM SeO_3^{2-} and synthesize Bio-SeNPs with an average dimension between 100 and 250 nm [94, 80]. Also in the case of this bacterium, the Bio-SeNPs synthesis mechanism is still unclear, even if synthesis localization [101], interaction with nitrite reduction pathway, and role of GSH [99] have been investigated. Finally, a Painter-type reaction was hypothesized to occur, even if a concomitant reduction pathway involving an alcohol dehydrogenase (AdH) was also investigated [80]. Moreover, since it has been observed that SeO_3^{2-} was not completely reduced to Se^0, other pathways such as volatilization and assimilation could be present in this microorganism.

Formation of Bio-SeNPs from Se^0 was characterized as well: TEM and SEM investigation led to the hypothesis of a release mechanism from the cells followed by a nucleation mechanism, resembling Ostwald ripening mechanism once the Bio-SeNPs are secreted in the extracellular matrix [80].

Presence of EPS-like material associated to the biogenic SeNPs was also evidenced, with FTIR analysis indicating the presence of N-H, C-H, C-O, C-N, C=O and S-H bonds mainly related to the Amide bands in proteins, lipids, carbohydrates and nuclei acids [80].

To date, the bio-produced SeNPs from SeITE01 and SeITE02 strains have been investigated mainly for their antimicrobial activity, especially against biofilms [49-51]. It has been observed that the biogenic SeNPs are more efficient as an antimicrobial agent compared to both the ChSeNPs and the oxyanion SeO_3^{2-}. Presently, it is unknown if the presence of the organic molecules on the surface of the SeNPs bio-synthesized by the bacteria could play a role in this activity. The high effectiveness of SeITE01 and SeITE02 Bio-SeNPs as antibacterial agents and the long-time dependent stability of Bio-SeNPs in aqueous solution are, however, evidence that leads to thinking of a possible and direct involvement of the capping in the regulation of these properties.

1.2.5 General objectives of this thesis

This PhD thesis focuses on the investigation of the microbial biotransformation process of SeO_3^{2-} and on the biological effect of this oxyanion on both *Bacillus mycoides* SeITE01 and *Stenotrophomonas maltophilia* SeITE02 cells.
This analysis was conducted to study the cellular behavior of the two strains over the duration of growth phases and in different conditions, namely untreated (growth without the presence in the medium of sodium selenite Na_2SeO_3) and Se-treated (exposure to the stress factor SeO_3^{2-}).
The chosen approaches were FTIR spectroscopy (Chapter II) and metabolomics (Chapter III).
Beyond monitoring the physiological response of these two strains to SeO_3^{2-} and the exploration into Bio-SeNPs production, an additional objective was the characterization of the organic capping layer present on the surface of these biogenic SeNPs. The spectroscopic acquisition of the intracellular and

extracellular bio-synthetised SeNPs by the two strains and collected with two extraction methods (pelleting processing and vacuum filtration, respectively) is presented in Chapter II.

CHAPTER II:

SPECTROSCOPIC INVESTIGATION ON SeO_3^{2-} BIO-REDUCTION BY SeITE01 AND SeITE02 STRAINS

2.1. INTRODUCTION

2.1.1 General concepts

Infrared (IR) spectroscopy is a technique based on the absorption of light by the quantized vibrational energy levels of the molecular groups present in a sample [107, 108].

The proper term used to designate light is electromagnetic radiation, which is the result of the composition of electric and magnetic waves presented, respectively, as electric and magnetic vectors. These two waves and their fields undulate in planes perpendicular to each other, and move through space in a third direction perpendicular to the planes of the undulation, as shown in Figure 2.1. The absorbance of the light derives precisely from the interaction of the electric vector with the matter. The amplitude of this vector changes over the time and has the form of a sine wave. Since the wave's motion is repetitive, they go through cycles, and the term that describes the distance forward traveled by a wave during a single cycle is called wavelength (Figure 2.1) [107].

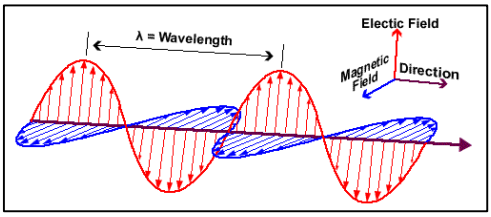

Figure 2.1. Description of a light wave. The arrow show the wavelength (λ) of the wave.

The units of the wavelength are distance per cycle, and it is indicated with the Greek letter lambda (λ). Together with λ, another significant property of the light wave is its wavenumber, denoted by the letter W. This unit determines the

number of cycles a wave undergoes per unit length, and it is measured in units of cycles per centimeter (abbreviated as cm^{-1}). Since the wavelength has units of distance/cycle and wavenumbers have, instead, units of cycles/distance, the two quantities are reciprocals of each other. Moreover, W has an important property, as it is directly proportional to the energy of a light wave. Thus, high wavenumber light has more energy than low wavenumber light [107]. This particular behavior is described in the electromagnetic spectrum illustrated in Figure 2.2, where higher energies are reported to the left and lower energies to the right.

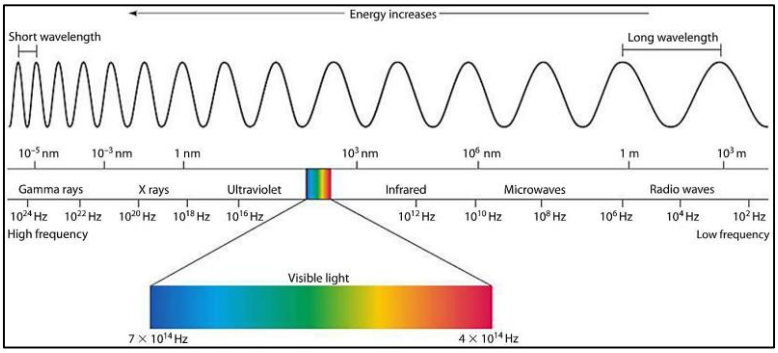

Figure 2.2. The electromagnetic spectrum.

Another important property of light waves is their frequency, which is a measure of the number of cycles a wave undergoes per unit time. Frequency is typically measured in cycles/second or Hertz (Hz) and the units are frequently written as sec^{-1} and represent with the Greek letter nu (ν).

Taken together, the most important features of the light waves (ν, λ and W) are linked and related to each other thanks to different proportionality ratios. Considering again Figure 2.2, it proves that moving from right to left across the spectrum there is an increase in energy, wavenumber, and frequency, but a decrease in wavelength. Similarly, moving in the opposite direction from left to right, is it possible to observe an increase in wavelength but a decrease in energy wavenumber, and frequency.

In the IR region of the electromagnetic spectrum (Figure 2.2), three spectral ranges can be identified as related to the experimental set-up to generate and detect this radiation: near, mid and far-IR, as described in Scheme 2.1.

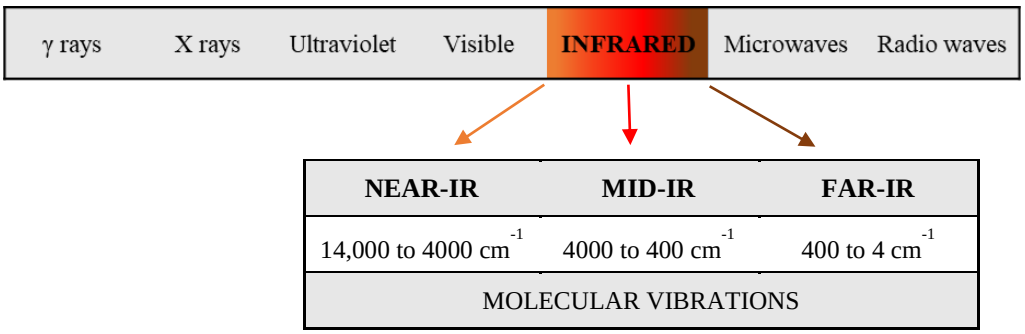

Scheme 2.1. Subdivision of the IR spectrum.

The mid-infrared (MIR) region conventionally covers the range between 4000-400 cm^{-1}, the far-infrared (FIR) the range 400-4 cm^{-1}, and the near-infrared (NIR) the 14,000 to 4000 cm^{-1} range. Typical absorptions from molecular vibrations of organic compounds are found in the MIR range [107-108].

An absorption spectrum is obtained by measuring the ratio T (that corresponds to transmittance) between the intensity of light transmitted through a sample I_S and the incident one I_B: $T = I_S/I_B$ as a function of the frequency or of the wavenumber (cm^{-1}). T can be expressed as a percentage (%T = 100xT) and represented by the abbreviation %T.

Given the Beer's law for the absorption of light by a sample: Is = Ib exp (- μx), where x is the thickness and μ is the absorption coefficient containing information on the sample composition, the physically most meaningful quantity is the absorbance A = -log T = μx. The resulting spectrum can be used for qualitative and sometimes quantitative analyses [107-110].

Figure 2.3 shows a representative IR spectrum of an organic sample acquired in the wavenumber region between 4000 and 800 cm^{-1} and plotted with the Y-axis units as transmittance (%T) on the left and as absorbance (A) on the right.

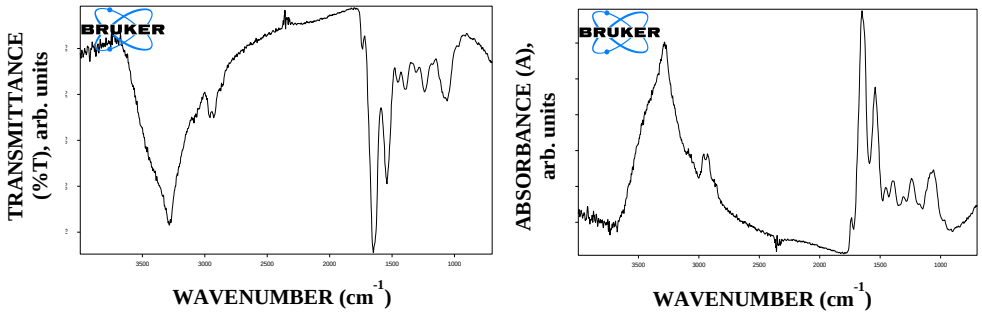

Figure 2.3. A representative IR spectrum (4000-800 cm^{-1}) plotted in percent transmittance (%T) on the left and in absorbance (A) on the right.

The main vibrations that are responsible for the absorption of light in the MID range can be classified into stretching modes, where the vibrations interact and modify the bond length, and the bending modes, in which case the bond angles are involved. Moreover, some bonds can vibrate in-phase (originating symmetric vibration), or out-of-phase (promoting asymmetric vibration), as illustrated in Figure 2.4.

Not all the vibrations are able to absorb light due to some physical selection rules related to the requirement of a change in the electric dipole [108, 111].

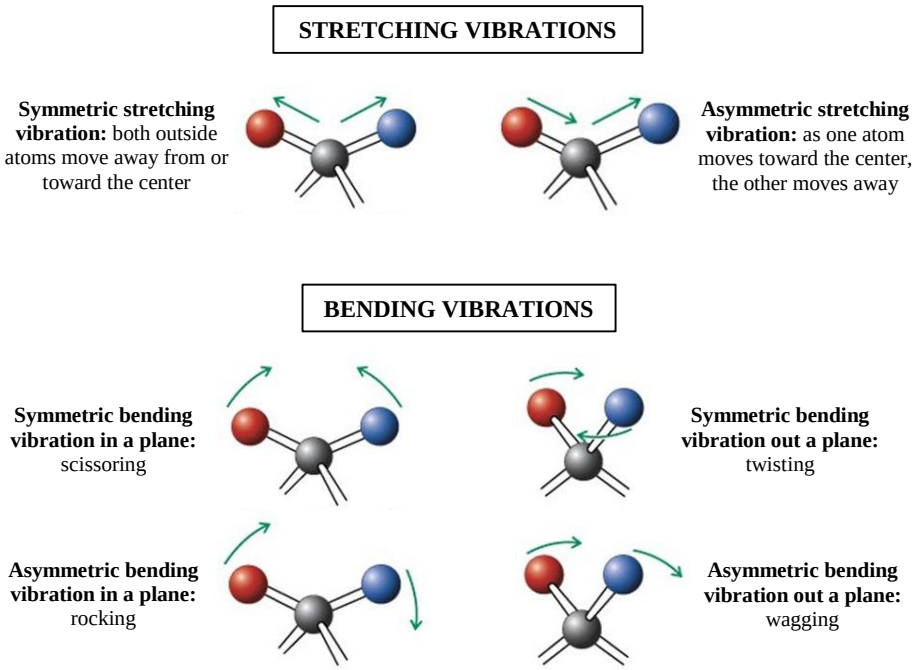

Figure 2.4. Vibrational modes in the IR active molecule.

2.1.2 Fourier Transform Infrared (FTIR) Spectroscopy Technology: the FTIR Spectrometer

IR spectroscopy has become one of the most important and useful analytical techniques today available in the scientific and industrial fields. In this paragraph, the different components constituting an IR spectrometer, or more precisely spectrophotometer, will be presented, in order to understand how this instrument works to collect and elaborate the final spectrum of a studied sample. Two types of IR spectrometers have been developed over the years: dispersive and Fourier transform (FT) instruments [108]. Although both tools allow acquiring the spectra in the range 4000-400 cm^{-1} and providing nearly identical results for a given compound, the FT has better performance than the dispersive one, and for this reason, nowadays, it is mainly used for spectroscopic analyses.

2.1.2.1 Dispersive Infrared Spectrometers

Historically, the first generation of IR spectrometers emerged in 1940s, based on dispersive spectrometers. These instruments employed prisms made of materials such as sodium chloride, but their popularity declined in the 1960s with the technological development of cheaper but excellent quality grating, which quickly replaced them as part of this technology.

To acquire the spectrum, first both the sample and the reference must be positioned in the respective chambers (reference and sample cell). Then, a beam of IR radiation from a hot wire is produced and it is divided by means of mirrors into two parallel beams of equal-intensity radiation. Each of them hits the sample and the reference and moves into the monochromator, which disperses them into a continuous spectrum of frequencies of IR light. The monochromator is composed of a rapidly rotating sector (beam chopper) that passes the two beams alternately to a diffraction grating (or prism in older instruments). The slowly rotating diffraction grating varies the frequency or wavelength of radiation reaching the thermocouple detector, which senses the ratio between the intensities of both the reference and sample beams. In this way, the detector establishes which frequencies have been absorbed by the sample and which, instead, are unaffected by the light

passing through the sample. After that, the signal from the detector is amplified, and the recorder draws the resulting spectrum on a chart, plotting it as the frequency of IR radiation changes by rotation of the diffraction grating. For this reason, it is said that these tools record the spectra in the frequency domain [108]. The components described above and their position within a simple dispersive spectrometer are schematically illustrated in Figure 2.5.

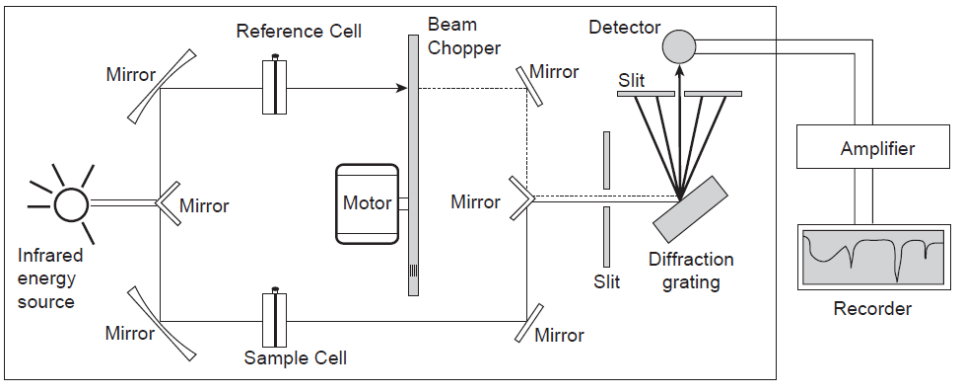

Figure 2.5. Schematic representation of a dispersive IR spectrometer.

2.1.2.2 Fourier Transform (FT) Spectrometers

Fourier transform infrared (FT-IR) spectrometers were developed for commercial use in the 1960s, although their use was initially intended only for advanced research due to the instrument costs and the large computers required to run them. The most modern IR spectrometers operate on a different principle as compared to the dispersive ones. This is based on the pattern called interferogram and the mathematical operation known as FT (Fourier Transform).

The interferogram is a complex signal, a superposition of cosine waves (wave-like pattern) that contains all the frequencies that make up the IR spectrum. The FT, which is named in honor of the French mathematician Joseph Fourier (1768-1830), is the mathematical function that allows the transformation of the interferogram into the final spectrum, separating the individual absorption frequencies from the pattern. As shown in Figure 2.6, when the FT is applied, it converts the x-axis unit of the interferogram,

plotted in IR intensity versus optical path difference (cm), in IR intensity versus cm^{-1}, and vice versa.

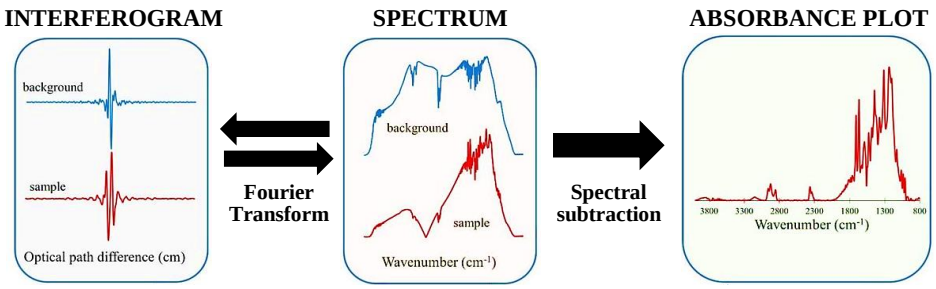

Figure 2.6. Correlation between the interferogram and the FT elaboration.

This is allowed because the Fourier transform of a line is a cosine wave, and the Fourier transform of a cosine wave is a line.

The work principle of FT-IR spectroscopy is based on the Michelson interferometer: the light beam enters a beam splitter, a semi-reflecting film placed at a 45° angle to the incoming radiation, which allows the incoming radiation to pass through, separating itself into two perpendicular beams. The first, that is oriented at a 90° angle, goes to a stationary or "fixed" mirror and, then, it returns to the beam splitter. The second one, which is not deflected, moves to a moving mirror and then returns to the beam splitter. In this particular case, it is the motion of the mirror that causes the variation of the pathlength of the second beam. In fact, when the two beams meet again together at the beam splitter, they recombine, but the differences present in their pathlength (differing wavelength content) give rise to both constructive and destructive interferences.

Therefore, it is the combination of the interference pattern derived from the combined beam that originates the new wave-like pattern, the interferogram. Afterwards, the interference pattern is oriented toward the sample by the beam splitter, and as it passes through the chamber containing the sample, the sample simultaneously absorbs all of the wavelengths (frequencies) normally found in its IR spectrum.

The modified interferogram signal that reaches the detector contains all the information about the amount of energy that was absorbed by that

compound at every wavelength. Finally, the signal is digitalized by the computer that mathematically processes the interferogram through the FT operation and extracts the individual frequencies that were absorbed from the sample. In this way, the plot of a typical IR spectrum is reconstructed and acquired [108, 109, 112, 113].

The transmittance/absorbance spectrum is obtained by collecting the interferogram of light with and without the sample (background) and by calculating the ration of the corresponding Fourier transformed signals, as illustrated in Figure 2.6. The schematic diagram of an FT-IR spectrometer describing the different movements of the beams and the individual components necessary for the elaboration of the final spectrum is thus reported in Figure 2.7.

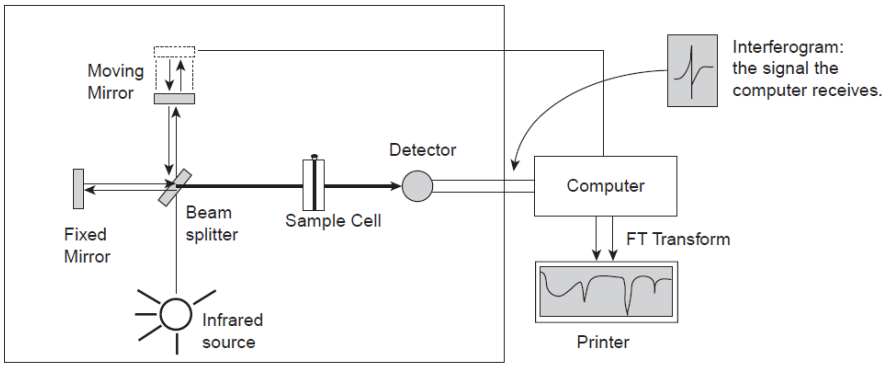

Figure 2.7. Schematic representation of a FT-IR spectrometer.

2.1.3 FTIR spectroscopic applications

Thanks to its widespread use since the mid-1980s, FTIR spectroscopy has been exploited as an important analytical technique for spectroscopic investigations in many different research areas and disciplines, from the industrial to the biological field. Nowadays, the use of this powerful tool is constantly expanding, particularly with the advent of increasingly sophisticated sampling techniques and technological improvements [111].

2.1.3.1 Industrial and Environmental applications

- Pharmaceutical industry. FTIR spectroscopy has been extensively used in both qualitative and quantitative pharmaceutical analysis. This technique is important for the evaluation of the raw materials used in the production, and for the selection of molecules that may be active or non-active ingredients. Moreover, this instrument can be used for the characterization of several crystalline forms (polymorphs) of pharmaceutical solids, whose different structures can exhibit significantly different physical and chemical properties [114, 115].
- Food science. Qualitative and quantitative information about food samples can be obtained with the FTIR approach. In particular, the study and the determination of the different fats and oil isomers (cis- and trans-) represents an important aspect for public health. Although both of them show the predominant natural cis-configuration, during industrial processing substantial isomerization from a cis- to a trans-configuration (which is mainly composed of triglycerides) occurs. Thus, to allow and guarantee a correct labeling of commercially available foods, it is fundamental to determine and report the correct trans-content of fats and oils. With this technology, this step can be carried out quickly, easily and reproducibly [116-118].
- Agriculture. FTIR spectroscopy has a significant implication in agriculture for the analysis, control and evaluation of commercial grains [119].

- Pulp, Paper and paint industry. The employment of FTIR spectroscopy in these industries allows quality control, product improvement and failure analysis [120, 121].
- Environment. FTIR spectroscopy has been applied to a broad range of environmental sampling problems, including air, water and soil analysis. Moreover, determining the composition of the atmospheric gases is important for understanding global climate changes and for an estimation of pollutants quantities [122, 123].

2.1.3.2 Biological applications

- Clinical chemistry and disease diagnosis. FTIR spectroscopy is well known for its extensive studies on proteins, peptides, lipids and nucleic acids, and important information has been gathered in describing these classes of macromolecules. However, the last decade has seen a rapid rise in the number of studies of more complex systems. This technology has emerged as a powerful investigation tool not only for clinical studies that include glucose, blood and urine analysis, but also for the characterization of tissue and for disease diagnosis, providing further information about the structural changes associated with malignancy [124-126].
- Plants. The use of FTIR spectroscopy for the study of the plant world has brought significant benefits in understanding these living systems. The analysis and description of plant material (cell walls, leafs, trunk) allowed the identification of new bioactive compounds in medicinal plants, and a better understanding of the interaction with possible pathogens and colonizers [127]. Moreover, it is possible to apply this technique to examine the quality of animal food necessary for their forage.
- Microbiology. FTIR spectroscopy has proved to be a valuable tool for characterizing and differentiating the complex nature of the microbial cells. This instrumentation, in fact, is a rapid method for the taxonomic classification of different bacterial strains, and it provides the elucidation of their functional groups, and the identification of

microorganisms responsible for infections. Moreover, particular cell compounds and structures, such as cell storage materials or spores and endospores, can be characterized. Then, different types of samples can be studied without the need for elaborate preparation: microbial biomass, biofilm and liquid culture can all give information on the uniqueness of the analyzed bacterial fingerprint [109, 110, 128-130].

- Nanotechnology. In the last few decades with the advent of the nanotechnologies in the scientific landscape developed, numerous research groups have turned their attention to the spectroscopic characterization and analysis of the peculiar characteristics of these nanostructures. Both chemical and biological syntheses have been investigated, as well as numerous applications in both the industrial and bio-medical fields [131-136]. In particular, numerous studies have examined the microbial biosynthetic production of selenium nanoparticles (Bio-SeNPs) by numerous bacterial species, belonging to both Gram-positive (such as *Bacillus* [137, 138], *Lactobacillus* [139]) and Gram-negative (as *Stenotrophomonas* [80], *Ochrobactrum* [140], *Azospirillum* [141-143], *Pseudomonas* [144, 145], *Acinetobacter* [146], *Escherichia* [147]) microorganisms.

2.2 RESEARCH INNOVATIONS AND OPEN QUESTIONS

In the present thesis, the employment of the FTIR spectroscopic technique for the investigation of the microbial behavior of *Bacillus mycoides* SeITE01 and *Stenotrophomonas maltophilia* SeITE02 is described.

Moreover, the spectra of the biogenic selenium nanostructures (Bio-SeNPs) deriving from the reduction process of selenite SeO_3^{2-} (Se(IV)) to elemental selenium (Se(0)) produced by the two environmental strains are acquired.

The main purposes of this research are collection of the bio-molecular composition of each bacterial strain during their growth cycle, investigation of the influence of Na_2SeO_3 exposure on the microbial cultures, and examination of the possible modification of the cellular components and structures caused by the effect of the oxyanion SeO_3^{2-}.

Furthermore, this analysis aims to characterize the organic coating present on the surface of the SeNPs bio-produced by SeITE01 and SeITE02 extracted with two different methods, which allow us to investigate separately both the nanostructures released into the growth medium (extracellular Bio-SeNPs) and those still present in the microbial cells (intracellular Bio-SeNPs).

The novelty of these experiments are the collection of both the bacterial cells of SeITE01 and SeITE02 during a time course and in two different growth conditions (untreated and Se-treated), and the comparison of the spectroscopic cellular trend within each strain between the untreated and Se-treated cultures. In addition, the acquisition of the FTIR spectra of both the extracellular and the intracellular SeNPs bio-synthesized by the strain *Bacillus mycoides* SeITE01 and those extracellularly bio-produced by *Stenotrophomonas maltophilia* SeITE02 represent also a major contribution of the study.

Thus, the main questions which this PhD thesis aims to answer through the use of FTIR spectroscopy are the following:

- What are the main FTIR spectroscopic features that can be identified in the two strains? What classes of macromolecules do they belong to?
- What is the spectroscopic evolution of the time course in response to cells exposure or not exposure to Na_2SeO_3?

- What are the spectroscopic features of the Bio-SeNPs synthesized by SeITE01 and SeITE02? Does the associated external capping has the same organic composition?
- Do nanostructures have different spectroscopic trends depending on the extraction methods?

2.3 MATERIALS AND METHODS

2.3.1 Bacterial strains and growth conditions

Bacillus mycoides SeITE01 and *Stenotrophomonas maltophilia* SeITE02 were grown aerobically in enriched medium Nutrient Broth (NB, Thermo SCIENTIFIC, Oxoid).

The salt Na_2SeO_3 (Sigma Aldrich) from a filter-sterilized stock solution (50 mM) was added to the exposed culture medium at the final concentration of 2 mM for SeITE01 and 0.5 mM for SeITE02.

All the microbiological experiments were conducted in biological triplicates.

The strains were pre-culture for 24 h at 27°C on an orbital shaker (150 rpm) in 13 ml sterile culture tubes with ventilation caps (Sarstedt s.r.l.) prepared with 5 ml of sterile NB. The analyses were then carried out in 250-ml Erlenmeyer flasks containing 100 ml of NB inoculated with aliquots from previous stationary-phase cultures with a final optical density equal to A_{600} = 0.01 (Eppendorf® Biophotometer), and the corresponding concentration of SeO_3^{2-}. The flasks remained agitated on the orbital shaker until the end of the experiments. Each sample of the three biological replicates, then, was always collected by the same flask previously numbered, using a sterile serological pipette (Sarstedt s.r.l.) to avoid environmental contaminations.

2.3.2 Bio-SeNPs synthesis and extraction methods

The bacterial cultures of SeITE01 and SeITE02 exposed to Na_2SeO_3 were left in agitation (150 rpm, IKA® KS 260 basic) for 24 h and 48 h (27°C, AHSI s.p.a). Between these times, the total SeO_3^{2-} depletion occurred visually accompanied by a clear increase in the color of the flasks (from light orange to deep-bright red), a change indicating that the SeNPs have been biologically synthetised.

Then, the bacterial suspensions corresponding to each exposure time were collected in a 50 ml Falcon tubes (Sarstedt s.r.l) and pelleted by centrifugation at 4°C for 20 min at 8300 xg (Eppendorf® Centrifuge 5810R, F-45-30-11 rotor). At this point, the resulting supernatant and pellet were processed with two distinct methods, in order to extract separately the Bio-SeNPs released into the

medium, called extracellular Bio-SeNPs, from those still present in the cells, named intracellular Bio-SeNPs.

The supernatant was collected through vacuum filtration (Merck Millipore Filter, 0.22 μm, Steritop Threaded Bottle Top Filter Sterile, 500-mL, polyethersulfone membrane, radio-sterilized) to separate the extracellular nanostructures from cellular residues and debris still present in the growth medium. Then, it was centrifuged at 4°C for 1 h at 31000 xg (Beckman Coulter Centrifuge, JA-20 rotor) and the Bio-SeNPs pellet was recovered, washed twice with sterile ddH_2O and stored at 4°C.

The pellet deriving from the initial centrifuge, which instead contained both the cells and the intracellular Bio-SeNPs, was washed twice with sterile physiological solution (0.9% NaCl), resuspended in 50 ml of ice cold 1.5 M Tris-HCl pH 7.4 (Sigma Aldrich), and divided into five 15-ml Falcon tubes (Sarstedt s.r.l) each containing 10 ml of solution. Cells were then sonicated in ultrasonic processor UP50H (Dr. Hielscher GmbH) (7 cycles of 1 min sonication + 1 min rest in ice), and precipitated through centrifugation at 8300 xg, 4°C for 20 min. In order to separate Bio-SeNPs from the lysate, the supernatant was fractionated by mixing with 1-octanol (1:2, v/v) (Sigma Aldrich). The mixture was stirred 10 sec on a vortex and kept undisturbed overnight at 4°C, in order to favor the migration of SeNPs in the aqueous phase. The next day, the upper phase and interface containing the insoluble cell fraction were discarded, and the bottom aqueous phase was transferred into clean 2 mL eppendorf tubes (Sarstedt s.r.l) and centrifuged at 4°C for 45 min at 20000 xg. The supernatant was discarded, the pellet washed three times and, finally, resuspended in sterile ddH_2O and stored at 4°C.

2.3.3 FTIR spectroscopic analysis

2.3.3.1 Bacterial cells preparation

Cells of SeITE01 and SeITE02 were collected for FTIR measurements at different time points during the bacterial growth, namely after 3, 12, 24, 48, and 72 h of incubation (27°C, 150 rpm). Both the exposed (Se-treated) and unexposed (untreated) to Na_2SeO_3 samples were prepared following the same steps (Scheme 2.2). For each time point, 2 ml of bacterial culture were taken, pelleted by centrifugation at 4°C for 10 min at 4500 xg (Eppendorf® Centrifuge 5810R, F-45-30-11 rotor), and washed twice with sterile physiological solution (0.9% NaCl), in order to eliminate traces of NB that could interfere and mask the identification of the peaks. The resulting pellet was, then, resuspended in 100 µl of ddH_2O previously sterilized, and 7 µl where finally settled down onto BaF_2 support (Crystaltechno Ltd) and dried for 24 h at 40°C before measurement.

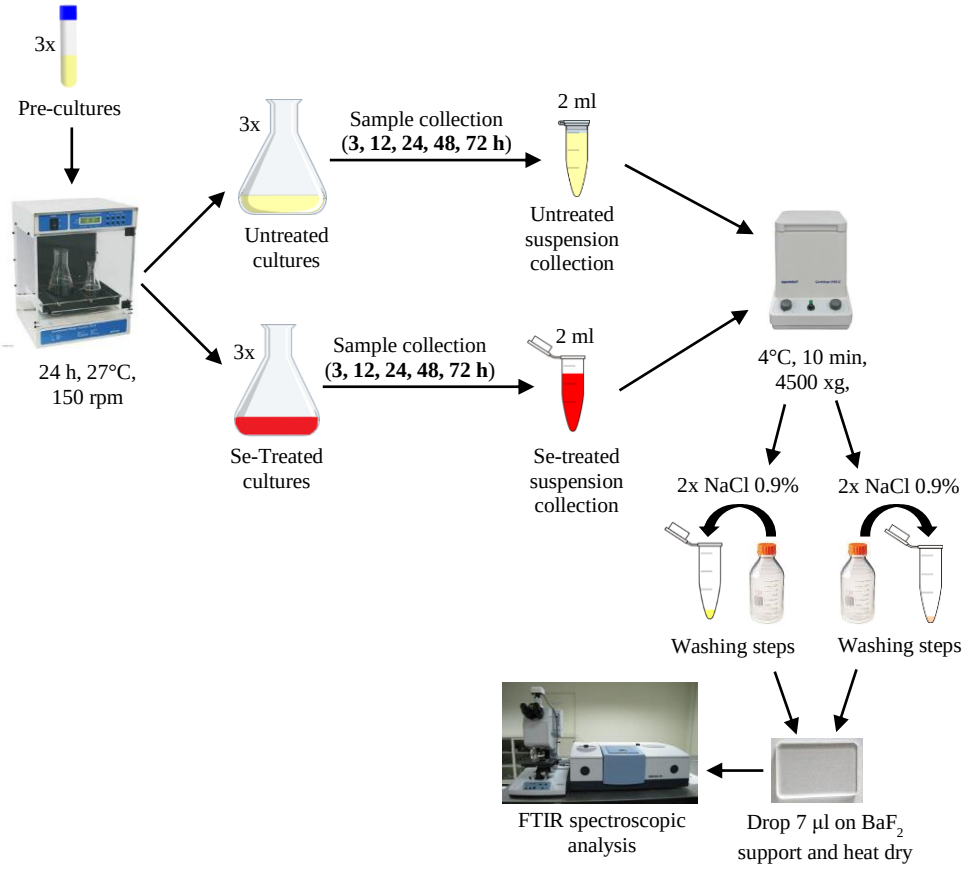

Scheme 2.2. SeITE01 and SeITE02 cells preparation for FTIR spectra acquisition.

2.3.3.2 Bio-SeNPs preparation

The intracellular and the extracellular biogenic nanostructures previously extracted from both SeITE01 and SeITE02 cultures (paragraph 3.2) were washed twice with ddH_2O and centrifuged at 4°C for 45 min at 20000 xg. Then, the resulting pellet was resuspended in a minimum amount of ddH_2O and a drop of 7 µl was deposited on a slide of BaF_2 support (Crystaltechno Ltd) and dried for 24 h at 40°C before measurement. All the steps describing both the extraction methods for the collection of the extracellular (supernatant) and intracellular (pellet) Bio-SeNPs and those necessary for the preparation of samples for FTIR analyses are illustrated in Scheme 2.3.

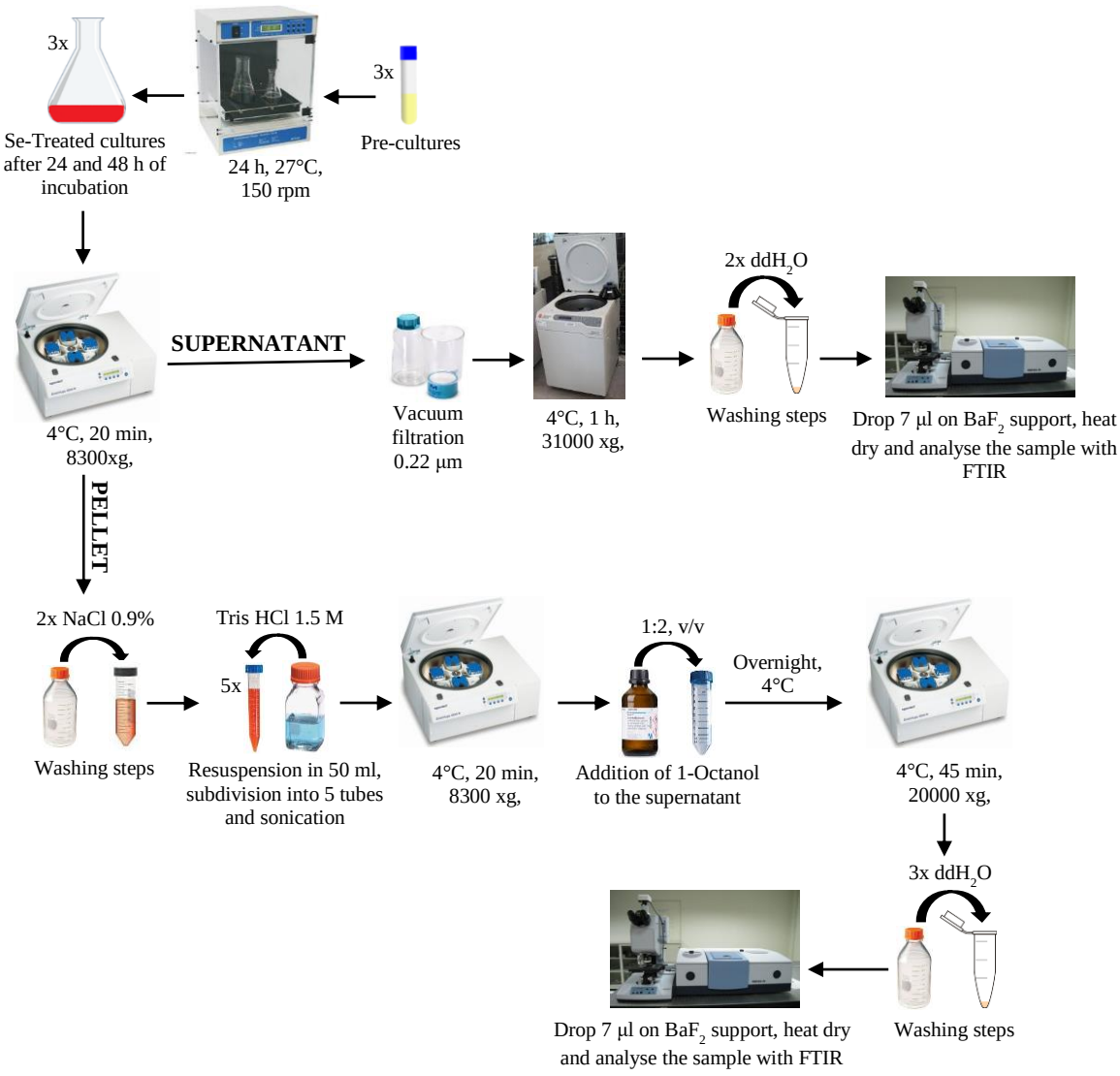

Scheme 2.3. SeITE01 and SeITE02 Bio-SeNPs preparation for FTIR spectra acquisition.

2.3.3.3 Spectra acquisition and data processing

Mid-infrared spectra were collected in transmission mode in the wavenumber range 4000-950 cm^{-1} with a Vertex 70 Bruker spectrometer coupled to a Hyperion 3000 Vis/IR microscope equipped with a photoconductive MCT detector and a 15x objective.

For all the samples, at least 10 point by point spectra with a reasonable S/N ratio were acquired at 4 cm^{-1} resolution on a 50 µm x 50 µm area by co-adding 64 scans (about 30 s acquisition time).

Spectra elaboration was performed using OPUS 7.5 Build (Bruker Optik GmbH 2014), an easy-to-use, powerful, all-in-one spectroscopy software.

The single point spectra were converted from transmittance into absorbance and baseline corrected with the Rubber band method (which determines support points by finding the convex hull of each spectrum) in two separate regions: 4000-2500 cm^{-1} and 1800-950 cm^{-1}.

Since the most meaningful behavior was observed in the 1800-950 cm^{-1} IR range for both bacterial cells and Bio-SeNPs, the subsequent analysis and discussion will concentrate on this particular region.

For each sample the single point absorbance spectra were averaged and the average spectra were all area normalized to allow their comparison. In this way, the relative intensity of an absorption band depends on the relative amount of the corresponding molecular component with respect to the total amount of the sampled material.

OriginPro® 8.5 was, finally, used for the graphical elaboration and spectra comparison (Scheme 2.4).

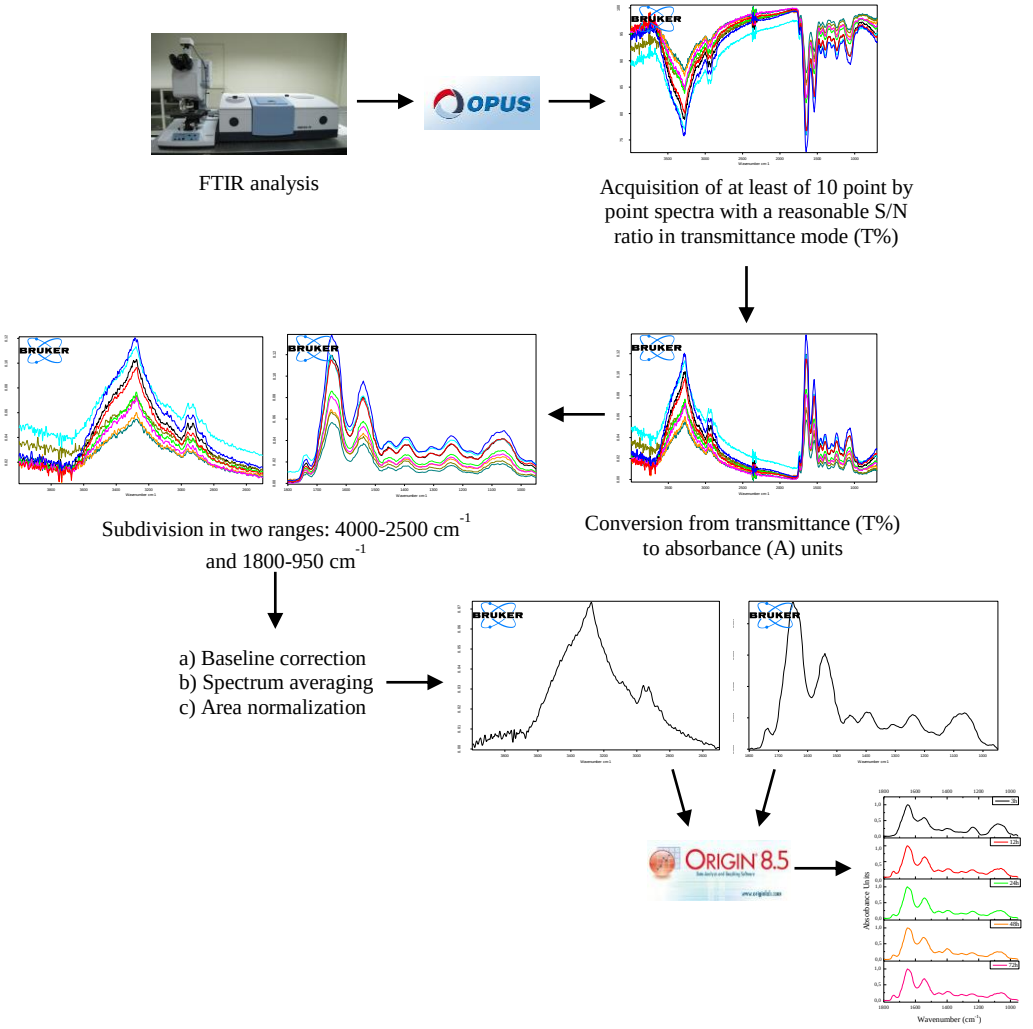

Scheme 2.4. Graphical representation of FTIR spectrum elaboration.

2.3.4 Dynamic Light Scattering (DLS) analysis and Zeta-potential measurement

DLS and zeta-potential analyses on the biogenic Se nanostructures bio-synthesized by SeITE01 and SeITE02 were executed at the Technological Platform Center (CPT) at the University of Verona.

The measurements were performed by using a Zen 3600 Zetasizer Nano ZS Malvern Instruments (Worcestershire, UK) equipped with a 633 nm Helium-Neon laser light source (4.0 mW), in order to acquire scattering information at a fixed angle of 173°. For each sample, an aliquot of 300 µl was taken and transferred into a quartz cuvette (10 mm path length) and data were collected at

25°C. Both the mean size distribution and zeta-potential of the Bio-SeNPs were measured in biological triplicates.

Finally, all the values registered were obtained using the software provided with the instrument.

2.3.5 Transmission Electron Microscopy (TEM) analysis

The TEM characterization of SeNPs bio-produced by SeITE01 and SeITE02 strains was performed at the Microscopy and Imaging Facility (MIF) at the University of Calgary (Calgary, AB, Canada) using the Hitachi H-7650 (120 kV) transmission electron microscopes (TEM).

The Bio-SeNPs collected by both the extraction methods were observed after 24 and 48 h of growth time. This allowed comparing the morphology and the temporal evolution of the Bio-SeNPs still present in the bacterial cell and not yet secreted (intracellular Bio-SeNPs) with those already present in the growth medium (extracellular Bio-SeNPs).

After being extracted and stored at 4°C, the samples were diluted 1:1000 in sterile ddH_2O, in order to collect images of the individual Bio-SeNP, and then, spotted on CF300-Cu-Carbon Film Copper grids (Electron Microscopy Sciences) and air-dried for 24 h.

Then, the free-license ImageJ software, a Java-based image-processing program, was used to determine the average size of the Bio-SeNPs.

2.4 RESULTS AND DISCUSSION

PART I: *Bacillus mycoides* SeITE01

2.4.1 FTIR spectroscopic investigation of bacterial cells

FTIR spectroscopy is an analytical technique frequently used in microbiology to obtain important information on the cellular and structural composition of numerous bacterial species.

In the present thesis, this informative tool was used to study the microbial behavior of *Bacillus mycoides* SeITE01 and monitor the changes of its molecular and macromolecular composition under optimal (untreated cells) and stressful (Se-treated cells) growth conditions.

The time points for this spectroscopic analysis were chosen based on the growth curves previously collected by our research group in Verona laboratory [70] in order to analyze the different growth phases experienced by the strain. For the untreated cells, 3 h and 12 h represent the beginning and 24 h the end of the exponential phase, while 48 h and 72 h indicate, respectively, the start and the maintenance of the stationary phase. In the case of the cultures spiked with 2.0 mM of Na_2SeO_3, instead, a decrease in cell growth is recorded at around 12 h of incubation, the stationary phase is already reached at 24 h and maintained until 48 h, while the beginning of the cellular decline is observable at 72 h.

For a better description and discussion of the data, the first spectra to be analysed will be those acquired from the bacterial cells not exposed to SeO_3^{2-}. Subsequently, those treated with Na_2SeO_3 will be described.

All the spectra shown and analyzed in the following paragraphs are the average area normalized FTIR spectra obtained as described in section 3.3.3.

FTIR spectroscopic investigation of untreated cells

In Figure 2.8A and 2.8B, the FTIR spectra of SeITE01 cells grown in enriched NB medium and incubated in absence of stress factors are represented. Figure 2.8A lists the spectra at each time point individually, while they are shown overlapped in Figure 2.8B. A different color was assigned to each spectrum to favor their recognition and distinguish the bands. The same colors will also be

used in the discussion of the spectra acquired for the untreated bacterial cells of the strain SeITE02.

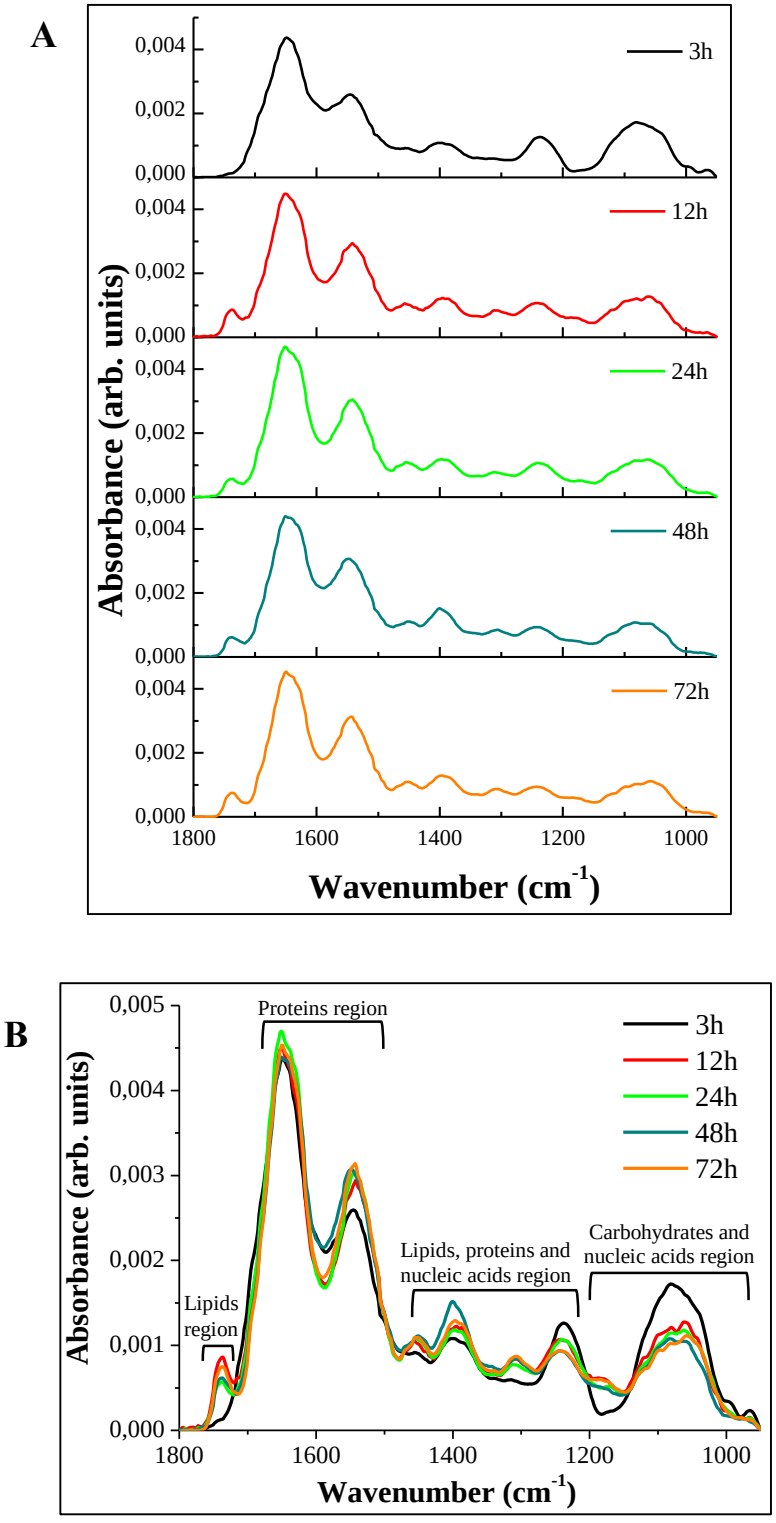

Figure 2.8. Average area normalized FTIR spectra of SeITE01 untreated cells in the 1800-950 cm^{-1} IR region during the time course. Spectra are represented individually (A) and overlapped (B).

From a first general inspection of the FTIR spectra shown in Figure 2.8, some observations can be done.

The 3 h spectrum shows broad and less resolved bands than those at more advanced stages of growth and development. This is particularly evident in the range between 1150 and 1000 cm^{-1}, an IR domain characterized by the presence of bands mainly related to carbohydrates and nucleic acids. In this range, several bands, whose intensities seem more pronounced starting from the 12 h of growth, are instead absent in the 3 h spectrum. Similar trends can be observed in the case of the biomasses analyzed after 12 h of incubation time. Even their intensities seem very similar and follow the same spectroscopic pattern.

For a better understanding of the spectroscopic trends of the samples during the time course, the spectra were grouped together (two by two) as follow: 3 h with 12 h (black and red spectra, A), 12 h with 24 h (red and green spectra, B), 24 h with 48 h (green and dark cyan spectra, C), and 48 h with 72 h (dark cyan and orange spectra, D). The four different juxtapositions are listed in Figures 2.9 A, B, C and D.

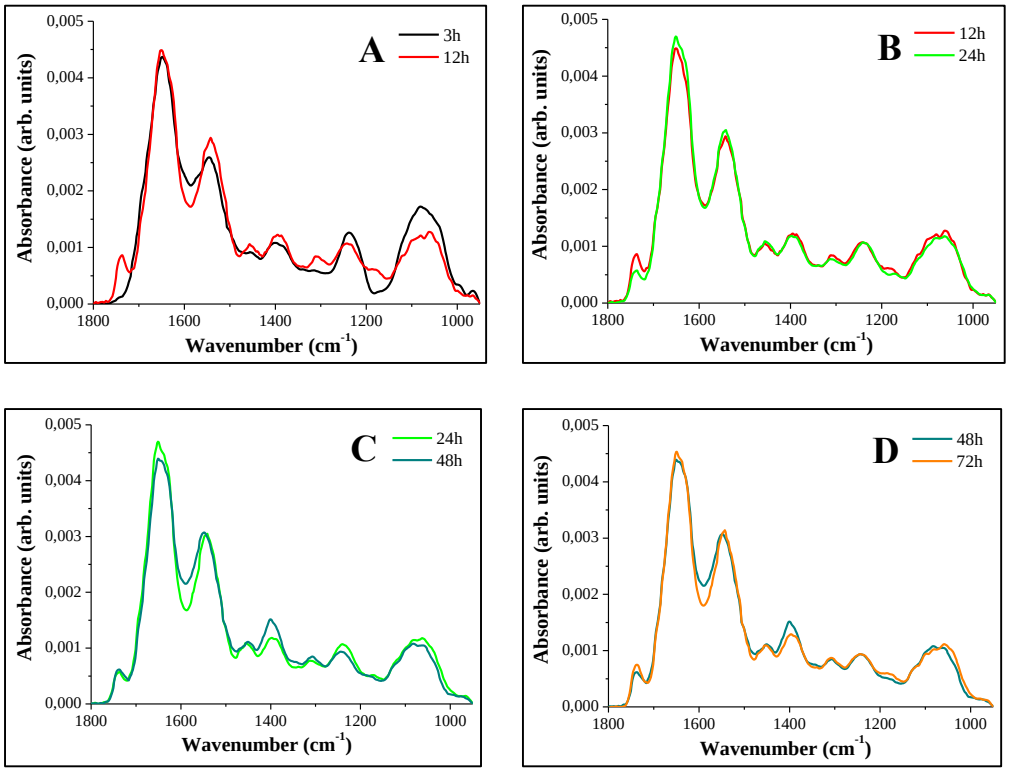

Figure 2.9. Comparison between the untreated SeITE01 average area normalized spectra collected at the different time points: 3 h with 12 h (A), 12 h with 24 h (B), 24 h with 48 h (C), and 48 h with 72 h (D).

The previous statement can be confirmed by the comparisons shown in Figures 2.9 B, C and D, which have delineated a quite similar spectroscopic trends and intensities among the bands of the spectra acquired at 12, 24, 48 and 72 h.
For this reason, the 24 h was chosen as representative for the identification of the most important bands and corresponding assignments, as well as for the comparison with the spectrum recorded at 3 h. Figures 2.10 and 2.11 report the spectra acquired at 3 h (black spectrum) and 24 h (green spectrum) with indication of the main bands, while the corresponding assignments for both untreated and Se-treated samples are summarized in Table 2.1 [80, 110, 141, 142, 148, 149]. After that, the comparison between the two spectra are shown in Figure 2.12, where the light blue asterisks represent the shared bands, while the red arrows underline the major differences between the two IR spectra.

Table 2.1. Wavenumbers of the main bands and their assignments for the FTIR spectra of SeITE01 untreated (indicated in Fig. 2.10, 2.11 and 2.12) and Se-treated cells (indicated in Fig. 2.15, 2.16, 2.17 and 2.18) [80, 110, 141, 142, 148, 149].

WAVENUMBER (cm^{-1})	**ASSIGNMENTS OF FUNCTIONAL GROUPS AND THE BIOMOLECULE CONTRIBUTOR**
~ 1740-1725 cm^{-1}	• C=O stretching vibration of ester functional groups in lipids
~ 1650 cm^{-1}	• α-helical structure of amide I (predominantly the C=O stretching vibration in proteins)
~ 1640 cm^{-1}	• β-sheet structure of amide I (predominantly the C=O stretching vibration in proteins)
~ 1545 cm^{-1}	• Amide II absorption and N-H bending coupled to a C-N stretching vibrational mode in proteins
~ 1455 cm^{-1}	• Asymmetric bending modes of CH_3 in proteins • Vibrational modes of CH_2/CH_3 groups in proteins and lipids
~ 1410 cm^{-1} (**only Se-treated**)	• Stretching C-N • Deformation C-H and N-H
~ 1400-1380 cm^{-1}	• Symmetric bending modes of CH_3 groups in skeletal proteins • Symmetric stretching of COO^- group in amino acids and fatty acids
~ 1315-1310 cm^{-1}	• Amide III band components in proteins
~ 1280 cm^{-1} (**only Se-treated**)	• Amide III band components in proteins • Stretching vibration of C-O-C in polyesters
~ 1240-1230 cm^{-1}	• PO_2^- asymmetric stretching of phosphodiesters in phospholipids
~ 1200-1050 cm^{-1}	• Stretching vibration of C-O, C-C and C-O-C bending vibration in polysaccharides and polyesters
~ 1100-1080 cm^{-1}	• P=O symmetric stretching in DNA, RNA and phospholipids
~ 1055 cm^{-1} (**only Se-treated**)	• P-O or C-O stretching of DNA
~ 980-965 cm^{-1}	• Symmetric stretching vibration of phosphoryl groups

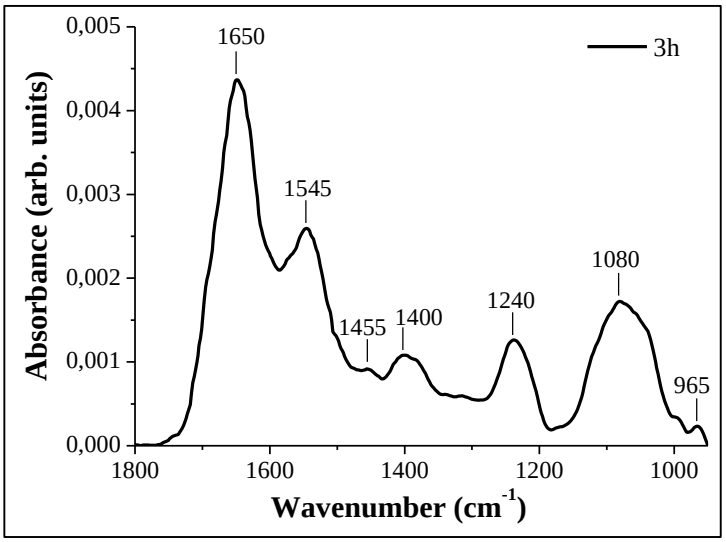

Figure 2.10. Average area normalized FTIR spectrum of SeITE01 untreated cells in the 1800-950 cm^{-1} IR region after 3 h of growth.

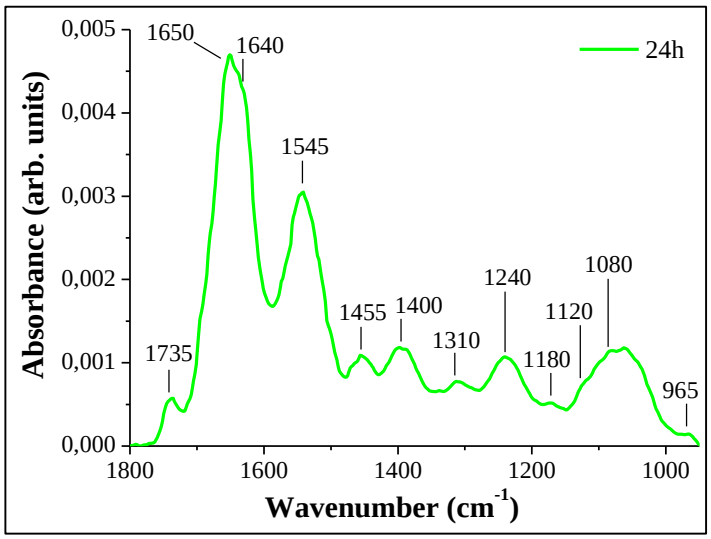

Figure 2.11. Average area normalized FTIR spectrum of SeITE01 untreated cells in the 1800-950 cm^{-1} IR region after 24 h of growth.

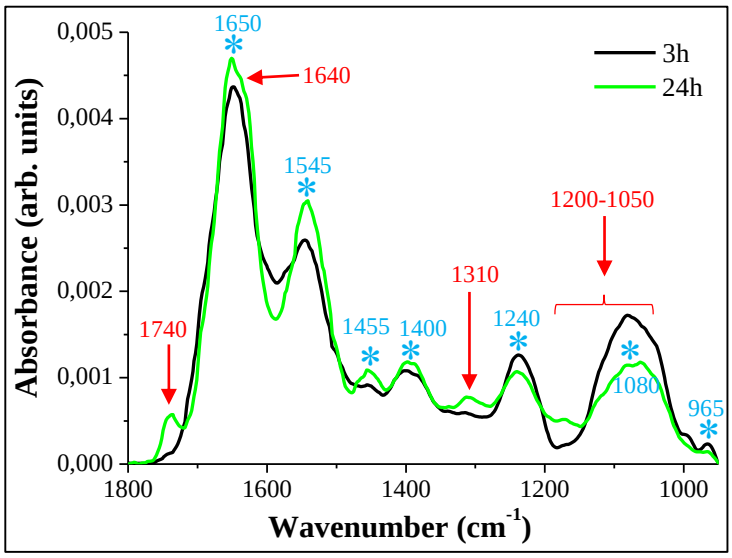

Figure 2.12. Average area normalized FTIR spectra of SeITE01 untreated cells in the 1800-950 cm^{-1} IR region after 3 h and 24 h of growth. Light blue asterisks indicate shared peaks, while red arrows and bracket indicate the bands and the spectral region showing the significant variations between the two spectra.

As regards the shared bands, those at around 1650 and 1545 cm^{-1} are assigned to vibrations of different proteins structures corresponding to the Amide I and Amide II. The band recorded at around 1455 cm^{-1} corresponds to the asymmetric bending modes of CH_3 in proteins and the CH_2/CH_3 vibration modes in lipids and proteins, while those at 1400 cm^{-1} can be mainly attributed either to the symmetric bending of the CH_3 groups in proteins and the symmetric stretching of COO^- group in proteins and lipids. The bands located at around 1240 and 1080 cm^{-1} are related to the PO_2^- asymmetric stretching of phosphodiesters in phospholipids and the P=O symmetric stretching in DNA, RNA and phospholipids, respectively. Finally, a weak band corresponding to the symmetric stretching vibration of phosphoryl groups and the C-C, C-O stretching in deoxyribose of DNA can be observed at around 965 cm^{-1}.

The IR bands located at 1740, 1640, 1310, and between 1200-1050 cm^{-1} represent, instead, the major differences between the two spectra. The bands present in the 1200-1050 cm^{-1} wavenumber range, which correspond to the stretching vibration of C-O, C-C and C-O-C bending vibration in polysaccharides and polyesters, are not entirely absent in the 3 h trend. Their identification is masked by the broad and overlapped band positioned at around

1080 cm^{-1} (P=O symmetric stretching in DNA, RNA and phospholipids). Even the small weak shoulder recorded at around 1640 cm^{-1}, corresponding to the C=O stretching vibration in the β-sheet structure of Amide I, is not resolved in the 3 h spectrum due to its overlap with the most intense band at 1650 cm^{-1} (α-helical structure of Amide I).

In fact, it is important to remember that after 3 h of growth the cells have just started the exponential phase, so the signal obtained from the pelleting and the processing of these biomasses will certainly be less intense and defined than those collected after 24 h. Moreover, the signal deriving from the main cellular structures, including the walls, the membranes and the genetic material itself, will be more complicated to acquire in this first stage of growth. This explanation can also be adopted in the case of the bands observed at 1180 cm^{-1} corresponding to the stretching and bending vibrations in carbohydrates, at 1310 cm^{-1} referred to Amide III in proteins, and 1740 cm^{-1} that represents the C=O stretching vibration of ester functional groups in lipids. In particular, the presence of this weak band in SeITE01 cells, even if it is a low intensity band, is very interesting. Returning to the macromolecular class of lipids and fatty acids, it can generally be referred to the lipid composition of membranes and cell walls [128]. However, this band can also be associated with the presence of cell storage materials, such as poly-β-hydroxy fatty acids (PHFs) to give an example, which are frequently found in many prokaryotes as energy and carbon reserve compounds [109, 142].

In conclusion, the IR spectra measured for the untreated biomasses of SeITE01 are very similar to the typical IR trend of an intact microbial cell [109, 110, 128-130, 142, 149]. Although some bands in the early stage of growth are still broad and unresolved, general similar trends and molecular behaviors were exhibited by these bacterial cultures.

FTIR spectroscopic investigation of Se-treated cells

A diverse and more "dynamic" situation is, instead, experienced by the cells grown in the presence of the stress factor Na_2SeO_3.

The spectroscopic trends of the Se-treated cultures acquired at different time points (3, 12, 24, 48, and 72 h) and the comparison resulting from the overlapped sketch of their spectra are presented in Figure 2.13A and 2.13B, respectively.

Further different colors were assigned to the spectra deriving from the cultures exposed to SeO_3^{2-}.

Also in this case, the different coloring helps to highlight the possible variations in the spectroscopic trend, and allows us to distinguish these sets of samples from the previous ones just analyzed. SeITE02 cultures grown in the presence of the oxyanion will be represented in the same manner.

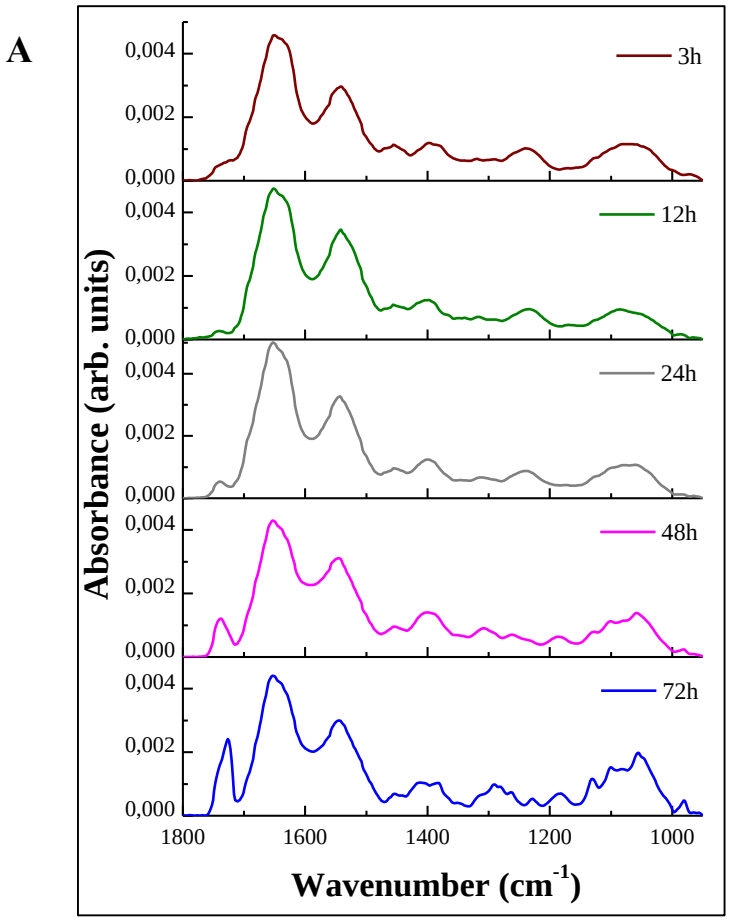

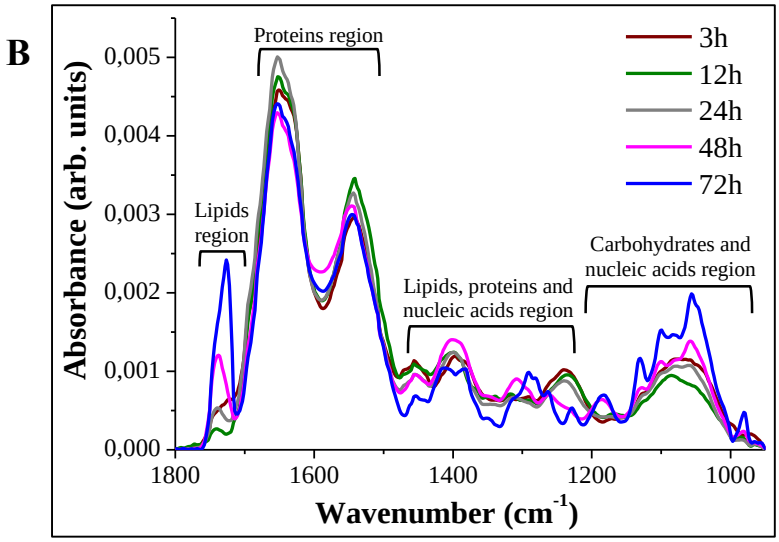

Figure 2.13. Average area normalized FTIR spectra of SeITE01 Se-treated cells in the 1800-950 cm^{-1} IR region during the time course. Spectra are represented individually (A) and overlapped (B).

As in the previous case, the spectra were grouped and depicted two by two (Figure 2.14 A, B, C, and D) to better highlight their behavior and evolution with the passage of the incubation time.

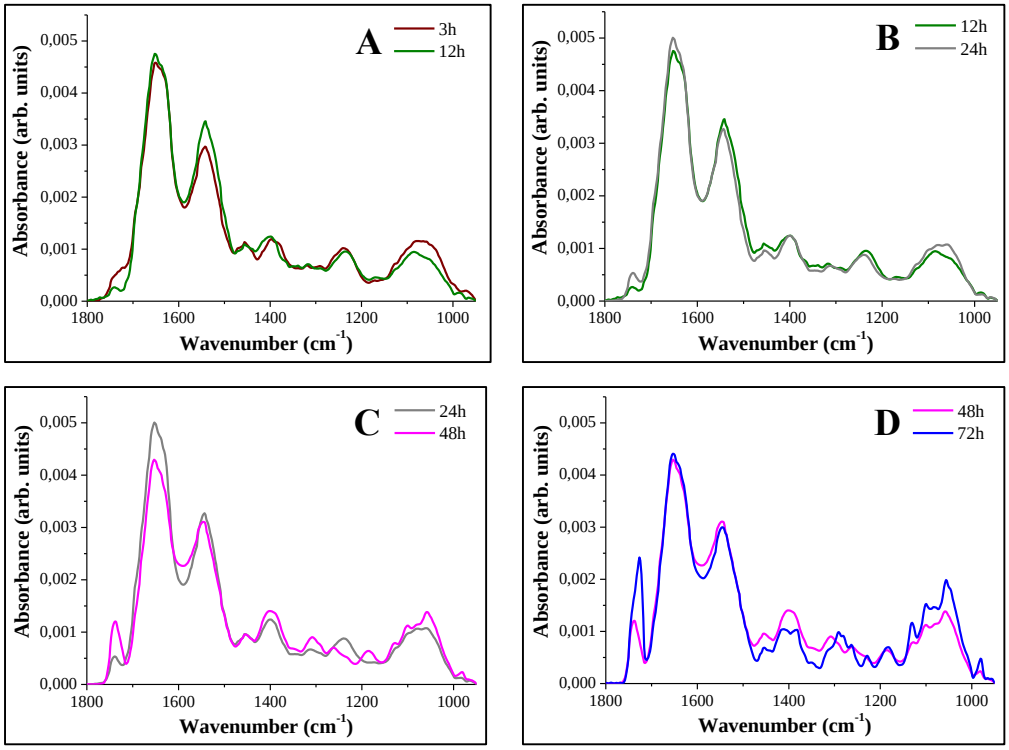

Figure 2.14. Comparison between Se-treated SeITE01 average area normalized spectra collected at the different time points: 3 h with 12 h (A), 12 h with 24 h (B), 24 h with 48 h (C), and 48 h with 72 h (D).

From a general view of Figures 2.13 and 2.14, it is possible to observe how the trend of the spectra acquired after 3, 12 and 24 h is comparable with that of the untreated cells previously illustrated in Figures 2.8 and 2.9.

Starting from 48 h, however, a substantial change in the bands is recognizable. Even if the IR range between 1500-1300 cm^{-1} is characterized by a very low signal and the bands present in it are difficult to assign, a notable increase in intensity in correspondence to both the spectroscopic regions between 1800 and 1700 cm^{-1} and 1300 and 950 cm^{-1} is observed.

Although at 48 h and 72 h of exposure time a cellular decline is registered and a greater quantity of cellular debris in the biomasses could be detected by the FTIR instrument, it must be remembered that in the presence of SeO_3^{2-} the cells synthesize biogenic Se nanostructures.

The formation and release of the Bio-SeNPs into the media and their interaction with the cellular structures could cause a possible alteration of the cellular walls and membranes. In this way, several mechanisms and modifications can be triggered by the cells, which can lead to the acquisition of different FTIR spectra. This hypothesis is also reinforced by the fact that the major spectral changes are principally observed starting from the liberation of the Bio-SeNPs in the NB medium (event that mainly takes place around 24 h) and not with the uptake or during the cellular reduction of the oxyanion SeO_3^{2-}.

Figures 2.15, 2.16, and 2.17 describe the individual spectra collected after 24 h (grey spectrum), 48 h (magenta spectrum), and 72 h (blue spectrum), whose behaviors can be taken as representatives of the evolution of the spectroscopic trends during the time course. In these figures, the positions of the main bands are reported, while the corresponding assignments are described in Table 2.1 [80, 110, 141, 142, 148, 149].

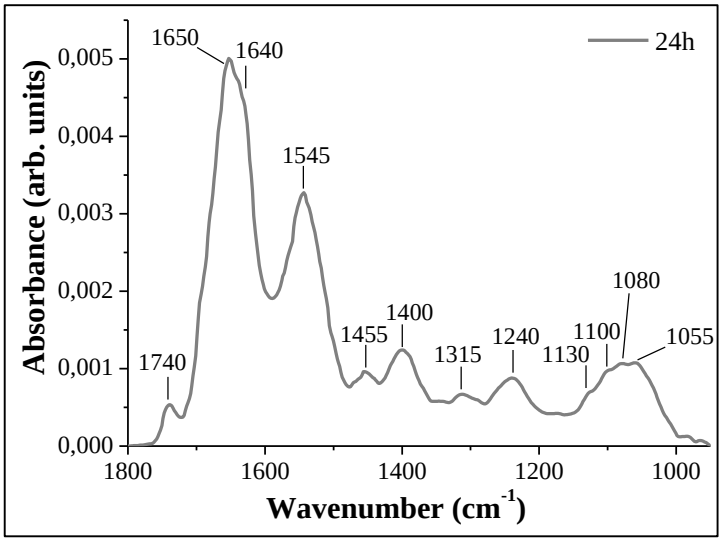

Figure 2.15. Average area normalized FTIR spectrum of SeITE01 Se-treated cells in the 1800-950 cm^{-1} IR region after 24 h of growth.

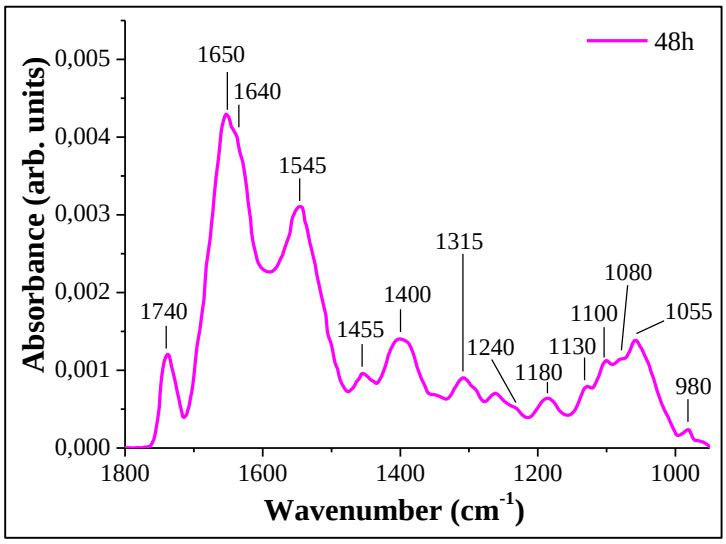

Figure 2.16. Average area normalized FTIR spectrum of SeITE01 Se-treated cells in the 1800-950 cm^{-1} IR region after 48 h of growth.

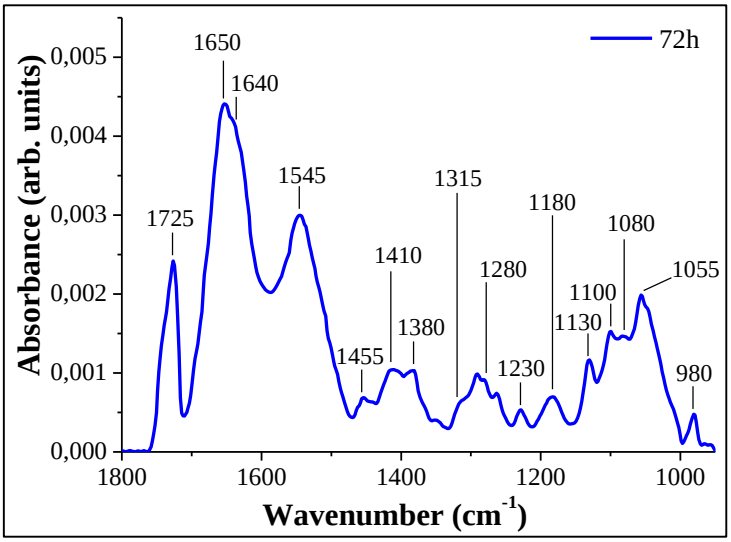

Figure 2.17. Average area normalized FTIR spectrum of SeITE01 Se-treated cells in the 1800-950 cm^{-1} IR region after 72 h of growth.

In order to deepen and confirm the assumptions previously advanced, the spectrum collected at 24 h is compared with those of 48 h and 72 h, as shown in Figure 2.18A. Here, the bands and the regions that undergo greater variations are grouped together and indicated by red brackets and arrows.

To better highlight the differences, enlargements of the regions with the major changes are shown in Figure 2.18B (1765-1700 cm^{-1}), C (1450-1150 cm^{-1}) and D (1150-960 cm^{-1}).

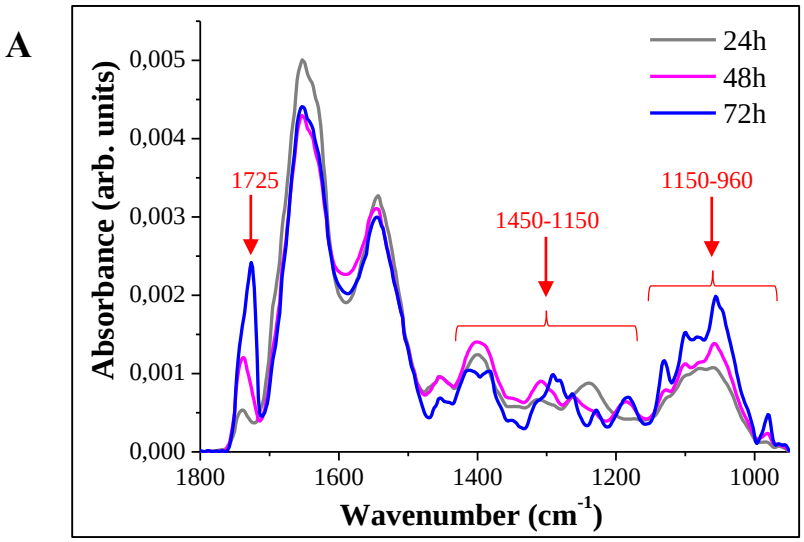

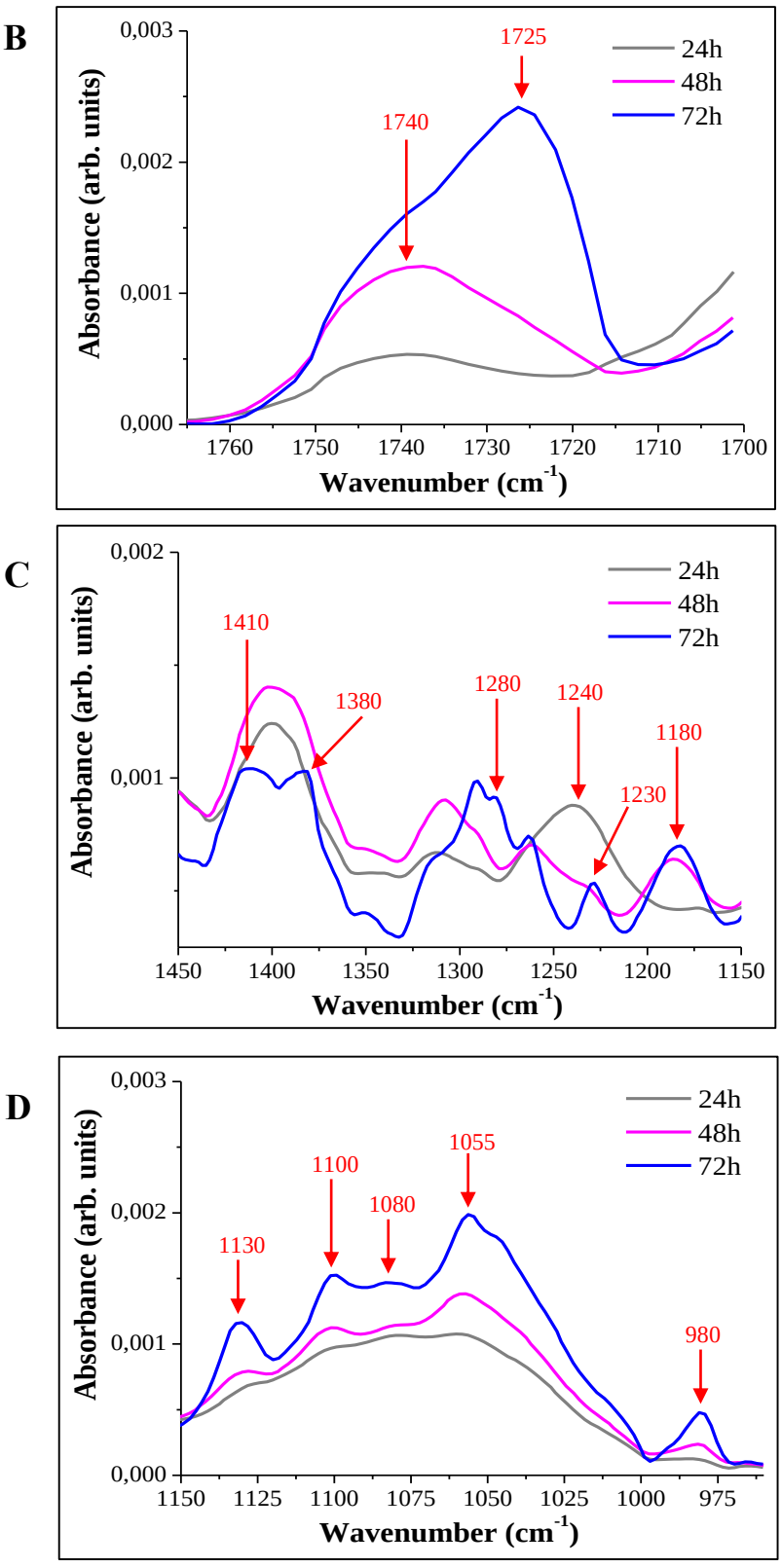

Figure 2.18. Average area normalized FTIR spectra of SeITE01 Se-treated cells in the 1800-950 cm^{-1} (A), 1765-1700 cm^{-1} (B), 1450-1150 cm^{-1} (C), and 1150-960 cm^{-1} (D) after 24 h, 48 h and 72 h. Red arrows and brackets indicate the peaks and the spectral regions showing the significant variations between the spectra.

From the analysis of the spectral ranges reported in Figure 2.18B, C and D, the major diversities can be observed in the spectrum describing the cells after 72 h of incubation with Na_2SeO_3.

In the wavenumber domain between 1765 and 1700 cm^{-1} (Figure 2.18B), a new resolved band positioned at 1725 cm^{-1}, which corresponds to the C=O stretching vibration of ester functional groups in lipids, seems to overlap the one previously identified in both the spectra of the 24 h and the 48 h located at around 1740 cm^{-1}. Its assignment is additionally confirmed by the presence of a new polyester-related band located at 1280 cm^{-1} (stretching vibration of C-O-C, Figure 2.18C) and other well-resolved bands connected to the stretching and bending vibration of the C-O, C-C, and C-O-C groups in lipids within the range 1200-1050 cm^{-1} (Figure 2.18D) [142], as reported in Table 2.1.

To respond to the possible stress exerted by the bio-synthesized nanostructures present in both the intracellular and extracellular compartments, the cells could enhance the production and the storage of the reserve bio-polyesters PHFs, with the clear increase in intensity of the relative bands. However, the appearance of new lipid-related bands could suggest further cellular responses, mainly directed to the activation of protective or defence mechanisms aimed at the fortification of the cell walls and membranes.

Several articles in literature have, in fact, described the toxic action of different nanomaterials (NMs) and the antibacterial activities that they exert on numerous microorganisms [130, 150-155]. It has been shown that these structures can exert toxicity at the cellular level through different methodologies, including (but not limited to) the generation of ROS, direct oxidation of cells upon contact, toxicity of residual catalysts and physical contact with the cell membrane, and interruption of energy transduction [151, 153]. Thus, the spectral changes started already at 48h but mostly expressed and detected at the late time point of the 72 h could describe the cellular mobilization of new biochemical pathways and mechanisms necessary to increase the production of the phosphoric groups in phospholipids to strengthen the structure of the cell walls and membranes. These responses could therefore avoid damages and changes in membrane permeability and fluidity due to a process known as lipid

peroxidation, where the double bonds on fatty acid tails of membrane phospholipids are oxidized due to the presence of ROS. This process is extremely harmful to the cells, as the peroxidized fatty acids can trigger reactions that generate other free radicals, leading to more cell membrane and DNA damage, while the enhancement of the permeability makes cells more susceptible to osmotic stress [154, 155]. Therefore, the protection and the repair of the external cellular structures, the first line of defense, is an essential step for the active and balanced maintenance of numerous and fundamental processes for the cells, including the electron transport phosphorylation and the energy transduction processes. These regulatory systems may be disrupted if membrane integrity is compromized or if a redox-sensitive NMs contact the membrane-bound electron carriers and withdraws electrons from the transport chain [154].

In addition, the detection of further bands belonging not only to lipids, but also to the macromolecular classes of carbohydrates and nucleic acids can support the previously advanced hypothesis.

In the 1450-1150 cm^{-1} IR range (Figure 2.18C), numerous are the spectral changes observed in the samples. The appearance of the new and sharp band at around 1180 cm^{-1} and related to the vibrational modes in carbohydrates could once again be explained by the cellular effort to increase the resistance of cell walls against the presence of and/or the contact with the Bio-SeNPs. It is, in fact, important to remember that *B. mycoides* SeITE01, a Gram-positive microorganism, has a thick ring of peptidoglycan and teichoic acid which increase the cellular structural integrity. The peptidoglycan, in turn, presents a carbohydrate backbone, so the presence and the increase in intensity of this band together with other numerous bands positioned in the 1150-1050 cm^{-1} wavenumber region and belong to the class of carbohydrates and polysaccharides (Figure 2.18D), may represent an additional proof of the reinforcement of cellular barriers mobilized by SeITE01 in presence of the Bio-SeNPs.

Moreover, the well-defined band located at 1230 cm^{-1}, mainly related to the PO_2^- asymmetric stretching of phosphodiesters in phospholipids, describes the

cellular effort to counteract the cellular decline and to provide the genetic material necessary not only to keep cells active in their biological processes, but also to respond to the alteration and changes caused by oxidative processes.

The significant activation of all these biological responses including lipids, carbohydrates and nucleic acids, could be referred to the stimulatory hormetic effect described by Lead and co-workers [155]. Although it is a poorly understood phenomenon, it appears to be related to the activation of global cell repair mechanisms that overcompensate for the exposure to the toxicant. The result is a beneficial effect, where improvements in the cell fitness, stress tolerance, growth, or longevity may be observed.

However, despite numerous bands have been presented and their significant actions in favor of the viable maintenance of the cell have been described, some evidences of structural damages and loss of the cellular integrity are present in the IR behavior of the cultures exposed to SeO_3^{2-} after 72 h.

This is firstly represented by the new bands near 1410 cm^{-1} (C-N stretching, C-H and N-H deformation) and 1380 cm^{-1} (symmetric CH_3 bending in proteins and symmetric stretching of COO^- groups in amino acids and fatty acids) that may indicate the unsaturated aldehydes due to the deformation of the hydroperoxides or lipid endoperoxides [130]. Secondly, the disappearance of the band registered at 1240 cm^{-1} (PO_2^- asymmetric stretching of phosphodiesters in phospholipids) and present only in the spectral trend of the 24 h may be related to DNA alteration and/or damage caused by ROS [130, 152].

Untreated vs. Se-treated cells: a comparison of FTIR spectroscopic data

The FTIR spectroscopic investigation of the bacterial cells of *Bacillus mycoides* SeITE01 ends with the direct comparison of the spectra deriving from both the untreated and Se-treated cultures. To summarize graphically the previous observations and deductions, the comparison between the two different sets of spectra collected at the single time points are proposed in Figure 2.19A (3 h, black and wine spectra), B (12 h, red and olive spectra), C (24 h, green and grey spectra), D (48 h, dark cyan and magenta spectra) and E (72 h, orange and blue spectra).

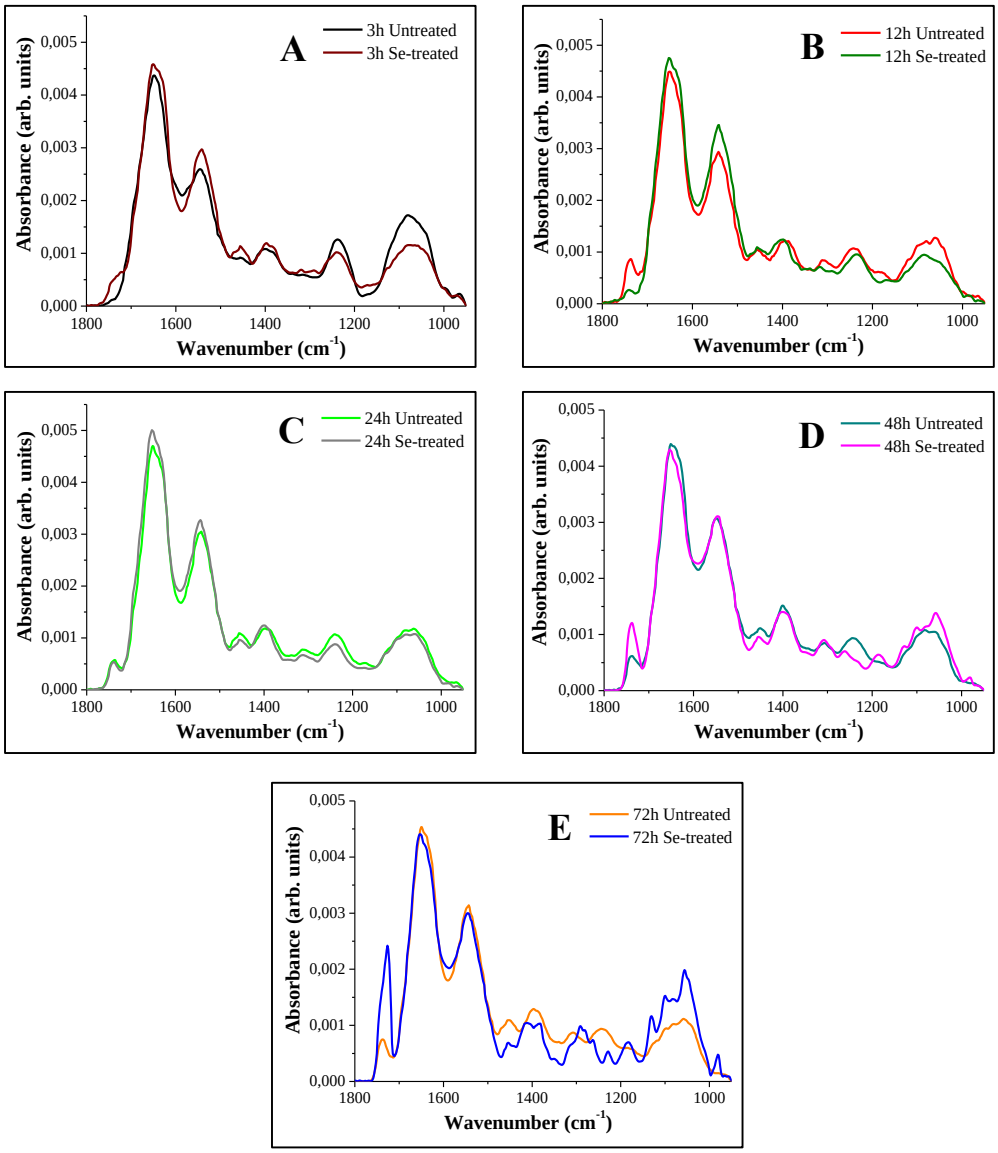

Figure 2.19. Comparison between the untreated and Se-treated SeITE01 average area normalized spectra collected at the different time points: 3 h (A), 12 h (B), 24 h (C), 48 h (D), and 72 h (E).

The bands of both spectra collected at 3 h of growth show a greater tendency to be broader and to overlap weaker peaks that can be located in the neighboring spectral regions. As previously stated, this could be explained by the fact that the cells are starting their fast growth phase and, therefore, it is expected that there is a larger diversity in the physiological state of the bacterial cells at this time (i.e., those rapidly growing and dividing and those still in the lag phase). Thus, the acquired FTIR signals and bands are not as well resolved and sharp as those recorded in more advanced times of growth due also to the heterogeneity of the samples. However, at these early hours, a general

molecular trend similar to that observed in the late time points is already observable, and peaks related to proteins, lipids and carbohydrates can be detected.

In the 12 h spectra, instead, it is possible to observe how the toxic action of the oxyanion negatively affects the Se-treated bacterial growth compared with the untreated one. The cell proliferation and the molecular development are slowed down by the presence of SeO_3^{2-}, whose action seems to affect more the improvement of the carbohydrate and nucleic acid region (1150-960 cm^{-1} wavenumber domain). However, it is significant to observe and emphasize how the protein region is not affected by this toxicity. On the contrary, the Amide I (1650 and 1640 cm^{-1}) and the Amide II (1545 cm^{-1}) bands increase their intensity (albeit slightly), and the weak band of the Amide III appears at around 1315 cm^{-1}. In the case of the untreated cells, the bands of the main classes of macromolecules start to be sharper, and storage material begins to be produced by the microbial cultures, as indicated by the peak located at 1740 cm^{-1}.

The spectroscopic trend of the two cultures appears to be almost identical at 24 h, when both the untreated and the Se-treated cells begin to experience the stationary phase. Starting from the 48 h, however, a greater difference becomes visible in the case of the Se-treated cells. As described above, the spectroscopic trend begins to change, and both an increase in intensity and a greater definition of the peaks are observed, especially in the spectrum collected at 72 h of incubation time. The major variations are noticed in the spectral domains of lipids (1765-1700 cm^{-1}), in the mixed region composed of lipids, proteins and carbohydrates (1450-1150 cm^{-1}), and in the carbohydrates and nucleic acids range (1150-960 cm^{-1}). As in the previous case, the protein region (1700-1500 cm^{-1} range) does not appear to undergo marked modifications.

The substantial variations of the spectroscopic behavior of the cells can be traced to the fact that the total reduction of Se(IV) to Se(0) happens at around 48 h [71], thus leading to the release of the Bio-SeNPs in the growth medium. Here, the contact of these nanostructures with the bacterial walls and membranes occurs, triggering a series of cellular mechanisms designed to protect and maintain the stability of these first line of defence.

In conclusion, the spectroscopic information obtained with the FTIR spectroscopic technique allowed investigating and monitoring the cellular and temporal evolution of SeITE01 bacterial cells under favorable and unfavorable conditions of growth. The spectroscopic analysis has highlighted important differences between the untreated and the Se-treated cultures during the growth cycle. This is observed especially in the late hours of exposure to SeO_3^{2-} in which most of the Se nanostructures bio-produced by the cells are present in the growth medium. The working hypothesis is that the contact of the Bio-SeNPs with SeITE01 cellular walls and membranes causes a change in the molecular composition, which is observed in the spectroscopic trend.

2.4.2 FTIR spectroscopic investigation of Bio-SeNPs

The qualitative characterization and analysis of the bioorganic components of the capping layer present on the surface of the bio-synthesized selenium nanostructures from SeITE01 and their relative contents featured by vibration modes of their typical functional groups have been obtained by the FTIR spectroscopic technique. The average area normalized spectra of the Bio-SeNPs collected after 24 h and 48 h of incubation time in presence of Na_2SeO_3 gathering from both the extraction methods have been acquired. These two different procedures allow separating and collecting the Bio-SeNPs expelled from the cells and thus present in the growth medium through a vacuum filtration (0.22 μm pore size) from those still inside them and extracted with the sonication and phase separation. The term extracellular will refer to the Bio-SeNPs deriving from the first extraction method, i.e. those filtered by the supernatant, while intracellular will indicate the Bio-SeNPs obtained with the second technique and deriving from the processing of the pellets of the bacterial cultures. Also in this case, the use of different colors for the distinction of the peaks recorded in the diverse spectra allows an easier comparison and a faster identification of possible differences. Orange and purple correspond to the intracellular spectra at 24 h and 48 h, while dark cyan and red were used to distinguish the extracellular samples after 24 h and 48 h, respectively. The

presentation of the spectra of all samples is shown in Figure 2.20, where the individual spectra are illustrated in Figure 2.20A and their overlapped sketch in Figure 2.20B.

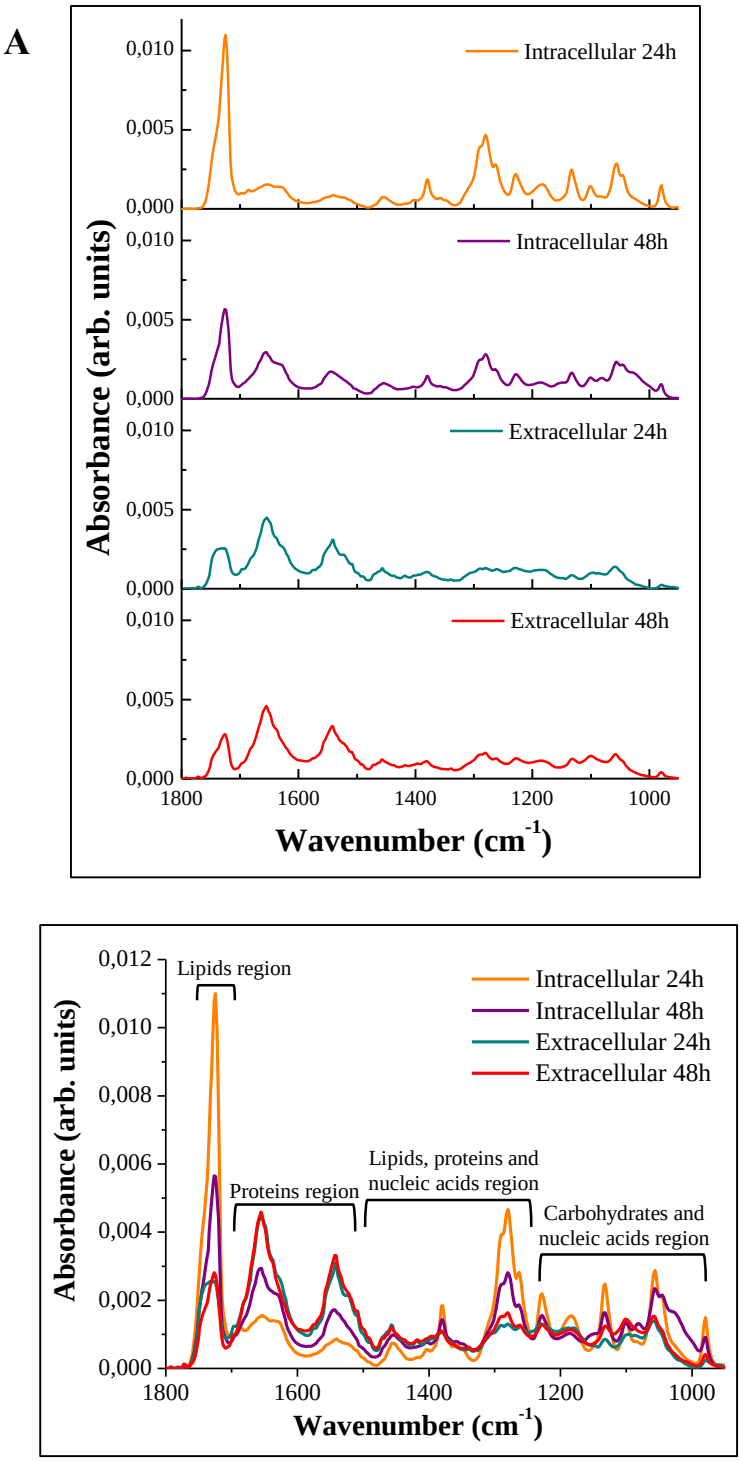

Figure 2.20. Average area normalized FTIR spectra of both intracellular and extracellular SeNPs bio-synthesized by SeITE01 in the 1800-950 cm^{-1} IR region after 24 h and 48 h of incubation with Na_2SeO_3. Spectra are represented individually (A) and overlapped (B).

A first observation of Figure 2.20 would indicate the presence of two distinct spectroscopic trends, each characteristic of the different method employed for the extraction but more particularly of the different localization of the biogenic Se nanostructures. Moreover, a significant divergence in intensity and definition of the bands characterizes the two classes of Bio-SeNPs.

The spectra of the intracellular Bio-SeNPs deriving from the processing of bacterial pellets will be firstly presented and compared. Then, the extracellular Bio-SeNPs collected by vacuum filtration will be described.

As in the case of SeITE01 cells, the assignments of the main bands for both the intracellular and the extracellular SeNPs bio-synthesized by this strain will be presented together in Table 2.2.

FTIR spectroscopic investigation of intracellular Bio-SeNPs

Figures 2.21 and 2.22 show the spectra of Bio-SeNPs extracted from the biomasses after 24h and 48h with the indications of the positions of the bands, while Table 2.2 reports the corresponding assignments [142, 143, 148].

Table 2.2. Wavenumbers of the main bands and their assignments for the FTIR spectra of intracellular (indicated in Figures 2.21, 2.22 and 2.23) and extracellular (indicated in Figures 2.24, 2.25 and 2.26) SeNPs bio-synthesized by SeITE01 [142, 143, 148].

WAVENUMBER (cm^{-1})	**ASSIGNMENTS OF FUNCTIONAL GROUPS AND THE BIOMOLECULE CONTRIBUTOR**
~ 1740-1725 cm^{-1}	• C=O stretching vibration of ester functional groups in lipids
~ 1685 cm^{-1} (**only intracellular 24h**)	• Amide I band components resulting from antiparallel pleated sheets and β-turns of proteins
~ 1650 cm^{-1}	• α-helical structure of amide I (predominantly the C=O stretching vibration in proteins)
~ 1630 cm^{-1} (**only intracellular**)	• β-sheet structure of amide I (predominantly the C=O stretching vibration in proteins)
~ 1545 cm^{-1}	• Amide II absorption and N-H bending coupled to a C-N stretching vibrational mode in proteins
~ 1455 cm^{-1}	• Asymmetric bending modes of CH_3 in proteins • Vibrational modes of CH_2/CH_3 groups in proteins and lipids
~ 1380 cm^{-1}	• Symmetric bending modes of CH_3 groups in skeletal proteins • Symmetric stretching of COO^- group in amino acids and fatty acids
~ 1290 cm^{-1}	• Amide III band components in proteins • N-H thymine
~ 1280 cm^{-1}	• Amide III band components in proteins • Stretching vibration of C-O-C in polyesters
~ 1230 cm^{-1}	• PO_2^- asymmetric stretching of phosphodiesters in phospholipids

~ 1200-1050 cm^{-1}	•	Stretching vibration of C-O, C-C and C-O-C bending vibration in polysaccharides and polyesters
~ 1155 cm^{-1} (**only intracellular 48h**)	•	Stretching vibration of hydrogen-bonding C-OH groups
~ 1100-1080 cm^{-1}	•	P=O symmetric stretching in DNA, RNA and phospholipids
~ 1055 cm^{-1}	•	P-O or C-O stretching of DNA
~ 1045-1025 cm^{-1} (**only intracellular**)	•	-CH_2OH groups and C-O stretching and bending frequencies of the C-OH groups of carbohydrates
~ 980 cm^{-1}	•	Symmetric stretching vibration of phosphoryl groups

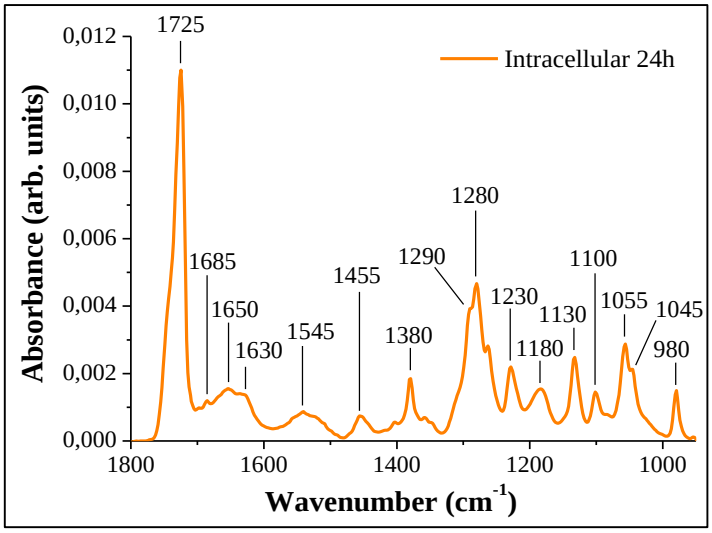

Figure 2.21. Average area normalized FTIR spectrum of intracellular SeNPs bio-synthesized by SeITE01 in the 1800-950 cm^{-1} IR region extracted after 24 h of incubation time.

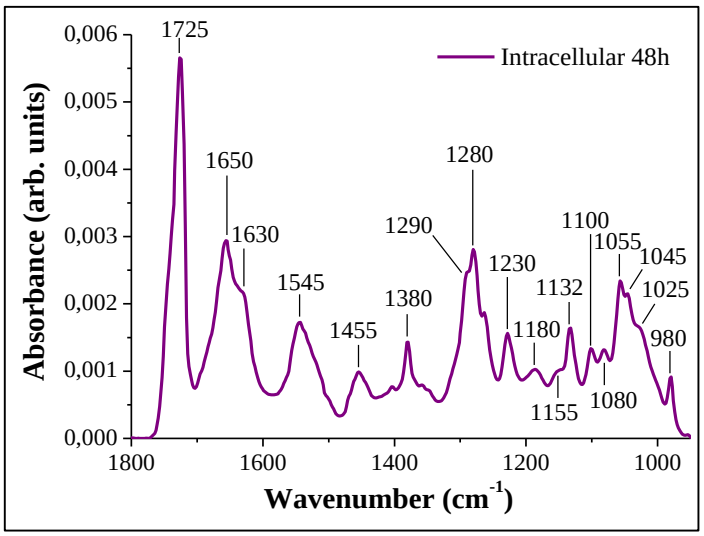

Figure 2.22. Average area normalized FTIR spectrum of intracellular SeNPs bio-synthesized by SeITE01 in the 1800-950 cm^{-1} IR region extracted after 48 h of incubation time.

The comparison of the intracellular Bio-SeNPs extracted after 24 h and 48 h of incubation with SeO_3^{2-} is shown in Figure 2.23. Here, only the bands and the spectral regions that exhibit significant discrepancies are indicated through red arrows and a bracket. Given the complexity of the spectra, the shared bands are not represented.

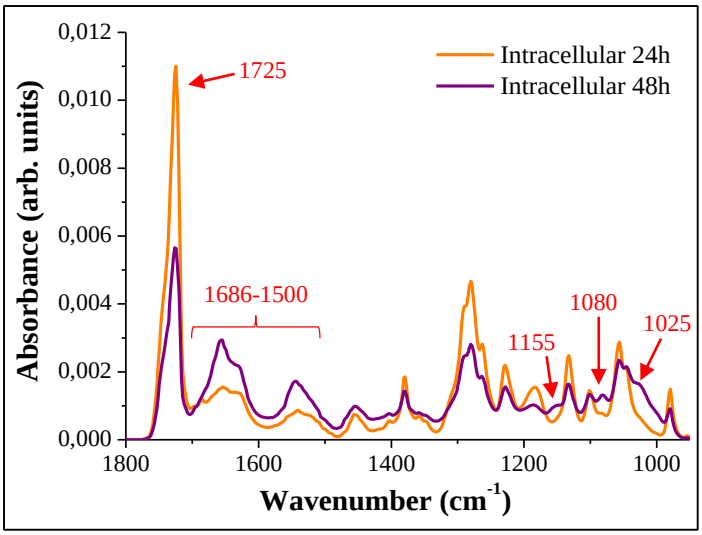

Figure 2.23. Average area normalized FTIR spectra of intracellular SeNPs bio-synthesized by SeITE01 in the 1800-950 cm^{-1} IR region after 24 h and 48 h. The red arrows and the bracket indicate the bands and the spectral region showing the significant variations between the two spectra.

Numerous sharp and intense bands related to lipids, carbohydrates and nucleic acids can be identified in both the intracellular spectra of the purified Bio-SeNPs. However, what appears to be decidedly significant between the two types of samples is represented by the behavior of some bands in the IR domain between 1800-1500 cm^{-1} and 1155-1025 cm^{-1}, as indicated with red arrows and bracket in Figure 2.23.

In the first mentioned range and in the case of the spectrum referred to the 24 h, both the remarkable intensity assumed by the typical band of the ester moieties positioned at 1725 cm^{-1} and the almost total disappearance of the bands relative to the Amide I and II can be observed.

The band at 1725 cm^{-1} is not entirely a novel, as its appearance accompanied by the presence of other bands at 1280 cm^{-1} and in the range 1200-1050 cm^{-1} had already been treated in the description of the cultures incubated with SeO_3^{2-} up to 72 h. The presence of this well resolved band (and those associated with it)

combined with its considerable intensity in both the samples could suggest its important involvement in the lipid composition of the organic capping of the Bio-SeNPs. These can be associated as being of membrane origin, since it is well known that lipids are main components of membranes, but specific lipid analysis is required for detailed identification.

Nevertheless, the protein portion attracts the most attention. The weak and poorly defined Amide I bands positioned at 1650 and 1630 cm^{-1}, the broad band of the Amide II at around 1545 cm^{-1} and the interesting appearance of a new band at 1685 cm^{-1} corresponds to the Amide I band components resulting from antiparallel pleated sheets and β-turns of proteins describe a rather different spectroscopic behavior of the nanospheres collected at 24 h with respect to those of 48 h. In the latter, a remarkable definition of the peaks is featured by a strong absorption of these bands. This different behavior could be related to the different development phase and to the "age" of nanostructures inside the cells. At 24 h, the registered protein portion is significantly lower than that detected at 48 h in the form of Amide I and II indicating that only a small amount of protein structures is adhered to the capping surface. Moreover, the band recorded at 1685 cm^{-1} allows to advance the hypothesis that the protein structures present on the Bio-SeNPs layer after 24 h of incubation time may present a different β-structured composition and arrangement on the organic surface. Therefore, at 48 h the disappearance of this band, the detection of the sharp and intense bands of the Amide I and II could indicate the achievement of a differently ordered protein structure.

However, it is also important to remember that the secondary structure of proteins identified spectroscopically in the Bio-SeNPs capping layer can differ from that of natural cellular proteins. The FTIR spectroscopic tool, although sensitive, cannot provide their individual characteristics, which requires additional investigation techniques, such as proteomic methods [53]. Numerous research groups have in fact analyzed, purified and studied the proteins associated with the Se nanostructures bio-produced by different microorganisms to not only classify and identify them, but also to understand what role they may have in controlling the stability, shape and size of these

important bio-structures [53, 60, 84, 85, 87, 88, 156]. From the results of these investigations, it was possible to identify a varied number of proteins with different functions. Selenium-binding protein (SeBP; 42 kDa) [156], high-affinity proteins [84], protein called Se-factor A (SeA; 95 kDa) [60], propanol-preferring alcohol dehydrogenase (AdhP), isocitrate dehydrogenase (IdH), outer membrane protein C precursor (Porin ompC, ompC), isocitrate lyase (AceA) [85], outer membrane porins and elongation factor Tu (EF-Tu) [87] are some examples.

In the particular case of SeNPs bio-produced by SeITE01 after 24 h, the analysis conducted by Bulgarini et al. highlighted the presence of most of the proteins previously indicated [88]. However, additional proteins such as the protein translocase SecDF, PBP, lysozyme, peptidoglycan endopeptidase, peptidase P60, ribosomal proteins S5, S7 and L5, glutamate dehydrogenase, and thiol:disulfide interchange protein have also been identified [88].

Finally, in the range between 1155 and 1025 cm^{-1}, three weak bands attributed to the vibration modes of carbohydrates and characteristic of the only 48h spectrum of the intracellular Bio-SeNPs are recorded.

A longer incubation and growth period inside the bacterial cells could better balance the partition and the distribution of the four classes of macromolecules (lipids, proteins, carbohydrates and nucleic acids) on the external organic layer, corresponding also to a balance of the intensity of the bands relative to each category.

FTIR spectroscopic investigation of extracellular Bio-SeNPs

The discussion of the data for the Bio-SeNPs obtained through the vacuum filtration (extracellular) will be presented in the same pattern as the intracellular Bio-SeNPs described above.

Figures 2.24 and 2.25 show the single spectra collected after 24 h and 48 h with the indications of the main bands, while Table 2.2 lists the corresponding assignments [142, 143, 148].

The comparison and the indication of the possible differences recognized between the two spectra is, instead, illustrated in Figure 2.26.

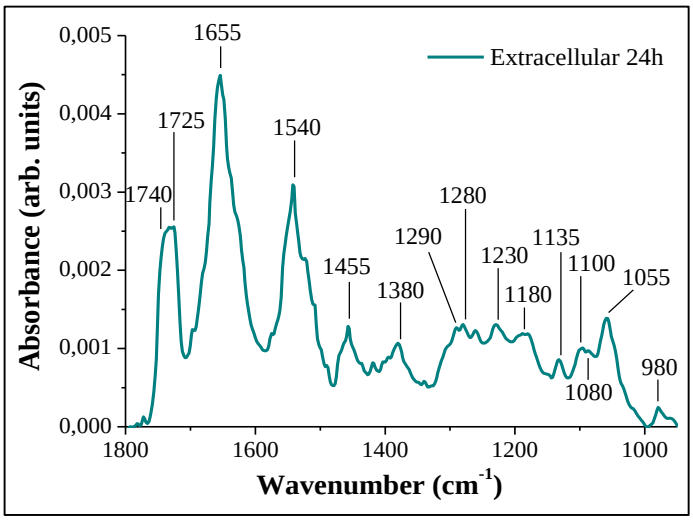

Figure 2.24. Average area normalized FTIR spectrum of extracellular SeNPs bio-synthesized by SeITE01 in the 1800-950 cm^{-1} IR region extracted after 24 h of incubation time.

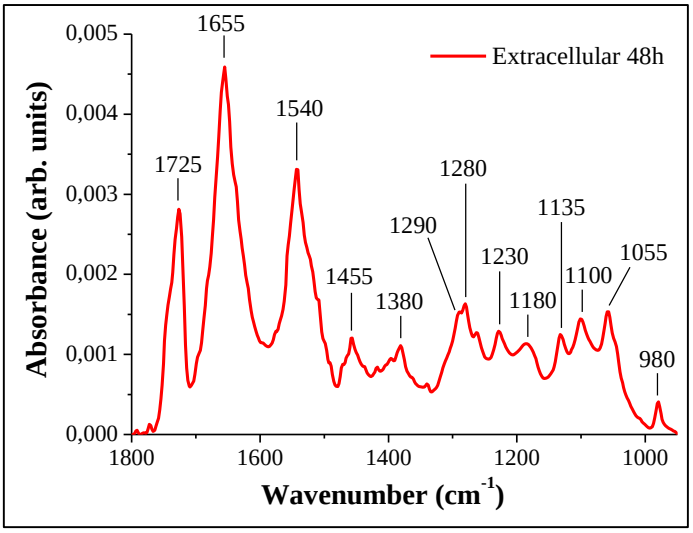

Figure 2.25. Average area normalized FTIR spectrum of extracellular SeNPs bio-synthesized by SeITE01 in the 1800-950 cm^{-1} IR region extracted after 48 h of incubation time.

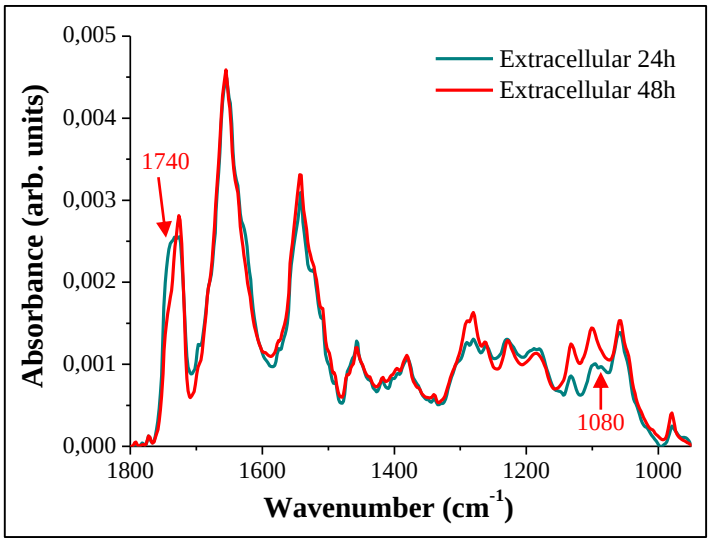

Figure 2.26. Average area normalized FTIR spectra of extracellular SeNPs bio-synthesized by SeITE01 in the 1800-950 cm^{-1} IR region after 24 h and 48 h. Red arrows indicate the peaks showing the significant variations between the two spectra.

From the overlap of the spectra, a remarkable similarity of both the position and intensity of most the registered bands is observed. Only two weak bands indicated in the spectrum of the 24 h and absent in that of 48h differentiate their trends. The first is represented by the weak shoulder positioned at 1740 cm^{-1} (C=O stretching vibration of ester functional groups in lipids), whilst the second is recorded around 1080 cm^{-1} and is assigned to the P=O symmetric stretching in DNA, RNA and phospholipids.

The spectroscopic characterization of the Bio-SeNPs released by the stressed and dying cells underlines the stable state of the particles once outside the cells compared to those still present in the intracellular compartment. The extracellular Bio-SeNPs have intense and well-resolved protein bands (Amide I and II), whose absorbance exceeds that of the peaks relative to lipids. Probably, during the release phase, some protein components present on the bacterial membranes may have adhered to the surface of the Bio-SeNPs, stabilizing and allowing a differently ordered conformation of the proteins' secondary structures.

2.4.3 DLS analysis and TEM imaging of Bio-SeNPs

DLS analyses were carried out on both the intracellular and extracellular SeNPs bio-produced by SeITE01 and retrieved after 24 h and 48 h.

This instrument allows determining three significant parameters for the study and characterization of the nanostructures: hydrodynamic diameter (Dh), polydispersity index (PdI), and surface charge (Zeta-potential).

The Dh is defined as "the size of a hypothetical hard sphere that diffuses in the same fashion as that of the particle being measured". In most cases, however, the particles or macromolecules that populate a solution are non-spherical, dynamic (tumbling), and differently solvated. Because of this, the diameter calculated from the diffusional properties of the particle is usually indicative of the apparent size of the dynamic hydrated/solvated particle.

The PdI is an indication of the particle's quality with respect to their size distribution. Its numerical value ranges from 0.0 (for a perfectly uniform sample with respect to the particle size) to 1.0 (for a highly polydisperse sample with multiple particle size populations).

Zeta-potential is instead correlated to the stability of the particles [157]. In the case of Bio-SeNPs characterization, values higher than 30 mV or lower than -30mV indicate that these structure have the ability to remain dispersed in aqueous solution and not to aggregate [88, 158].

In Figure 2.27, the results are reported concerning the average dimension of the nanostructures, where the relative spectra are represented with the same colors as the FTIR spectra.

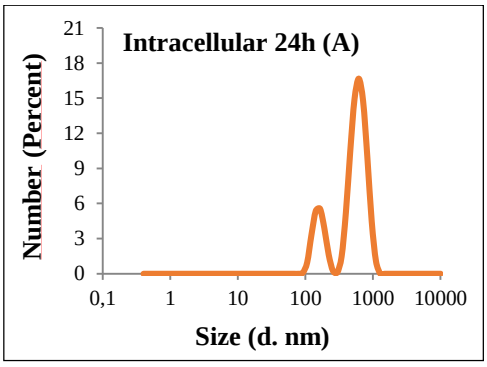

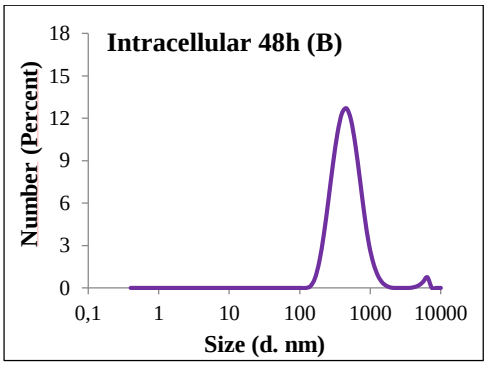

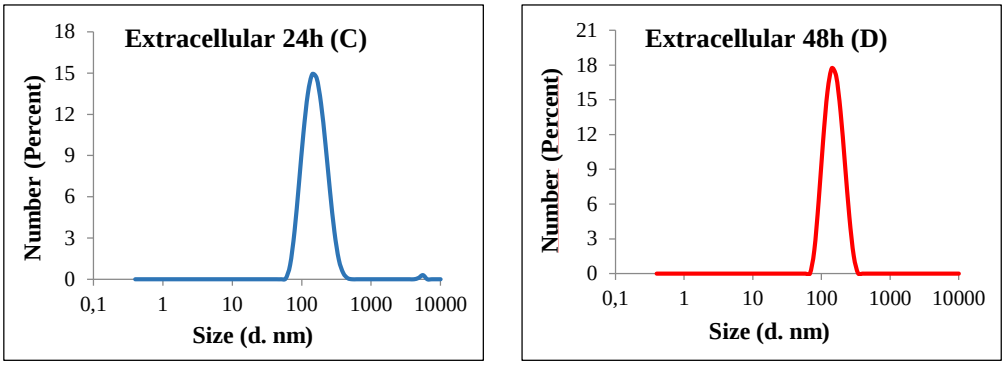

Figure 2.27. DLS spectra of both the intracellular (A, B) and extracellular (C, D) SeNPs bio-synthesized by SeITE01 after 24 h and 48 h.

The intracellular Bio-SeNPs collected after 24 h show an average size of 637 ± 34 nm with a high value of polydistribution (PdI = 0.6). In this sample, in fact, it is possible to distinguish two distinct peaks belonging to two different populations, the first positioned at around 150 nm and the second at 700 nm. After 48 h, otherwise, an average size of 393 ± 9.8 nm is observed, and a PdI equal to 0.27 is registered. From the vacuum filtration, instead, populations with similar average size are analyzed: 148 ± 0.9 nm and 147 ± 0.4 nm for the 24 h and 48 h, respectively. This result is principally due to the use of filters with pores not larger than 220 nm. In fact, this filter size was used to avoid the contamination of the filtrate by bacterial cells or cellular debris, but they also involve a selection of the nanostructures present in the supernatant since those with dimensions greater than the pores will remain trapped in the filter. Thus, with this approach only a biased view of the size of the Bio-SeNPs can be obtained, but at the same time the collection of uncontaminated samples is guaranteed. In addition, the PdI values for these samples are very low, equal to 0.18 for the Bio-SeNPs at 24 h and 0.13 for those at 48 h.

Figure 2.28 reports the zeta-potential observed for the diverse Bio-SeNPs.

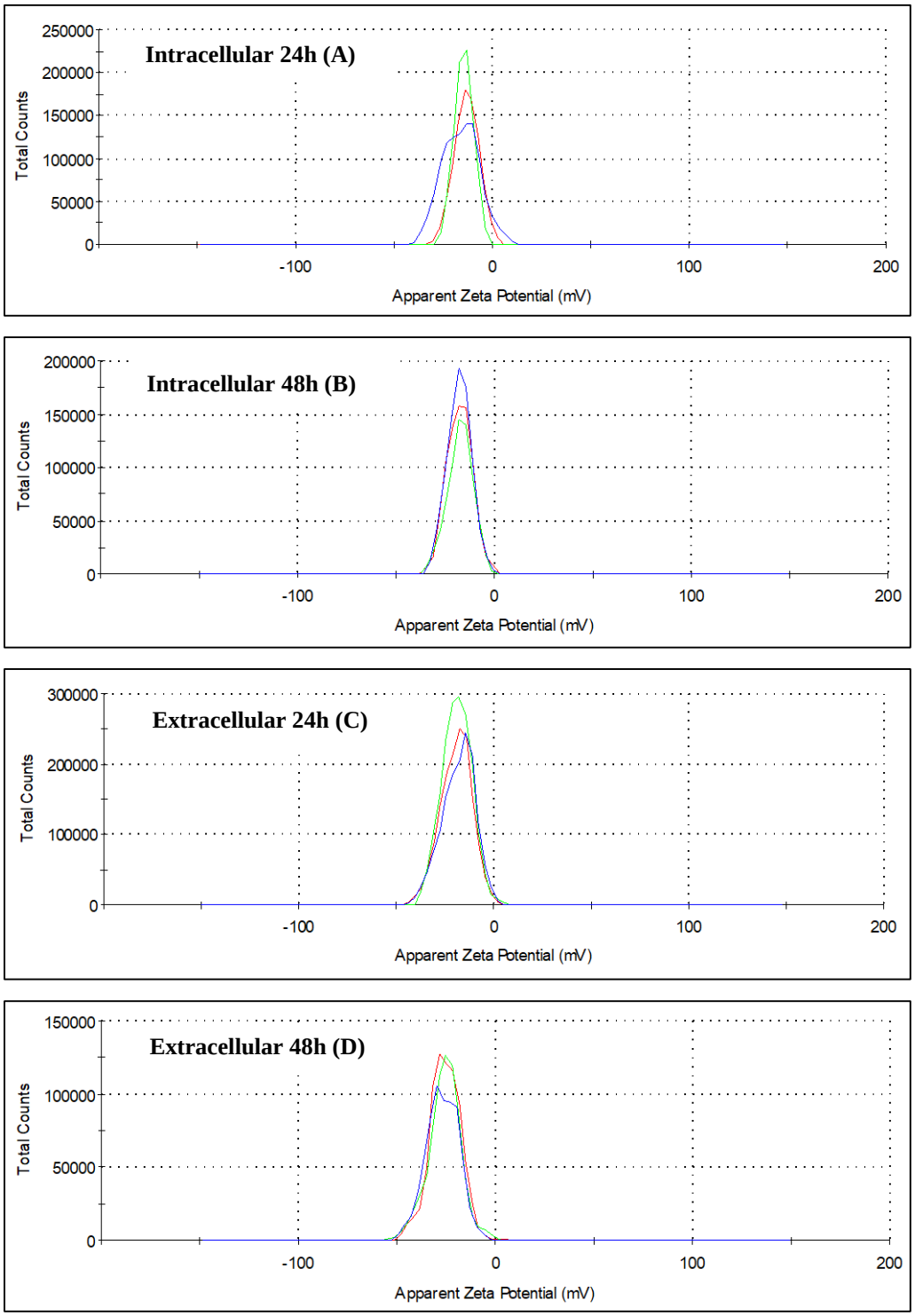

Figure 2.28. Zeta-potential analyses of both the intracellular (A, B) and extracellular (C, D) SeNPs bio-synthesized by SeITE01 after 24 h and 48 h. The three different lines (blue, green and red) represent the technical triplicates collected for each sample.

For all samples, negative values were recorded. However, they were more negative in the case of the extracellular SeNPs biologically produced (-18.8 mV for 24 h and -26 mV for 48 h) than in the intracellular one (-14.5 mV for 24 h and -17.7 mV for 48 h), indicating a lower stability in the case of the latter samples.

This could be due to a lower abundance of negatively charged functional groups on the organic capping of the Bio-SeNPs that have been extracted from the bacterial pellets. These surface-associated biomolecules must be responsible for not only the negative values of zeta-potential, but also they evidently serve as additional factor(s) stabilizing these Se nanospheres in aqueous suspensions and their morphology in the course of their biogenesis [53, 80, 86, 88, 143].

The TEM images describing the intracellular and the extracellular Bio-SeNPs are illustrated in Figures 2.29 and 2.30, respectively.

In these samples, it is possible to observe a heterogeneity in the dimension of the analyzed Bio-SeNPs. In fact, the size of the intracellular Bio-SeNPs measured with the software ImageJ reported an average dimension close to 124 ± 33 nm for the those extracted after 24 h and to 161 ± 36 nm after 48 h. For the extracellular ones, at 24 h the Bio-SeNPs show an average size of approximately 69 ± 28 nm. At 48 h, instead, the average dimension increases to 109 ± 54 nm. These data differ from those collected with the DLS as the latter technique does not discriminate the single Bio-SeNP from the aggregate, considerably increasing the possible real size of the nanostructures.

In the images here presented, as in the following ones, the Se nanostructures are distinguishable from other organic material present in solution by the darkness they acquired. At the TEM, these electron-dense structures assume a dark gray-black color, while the gray-whitish coloration is correlated with the presence of other biological materials.

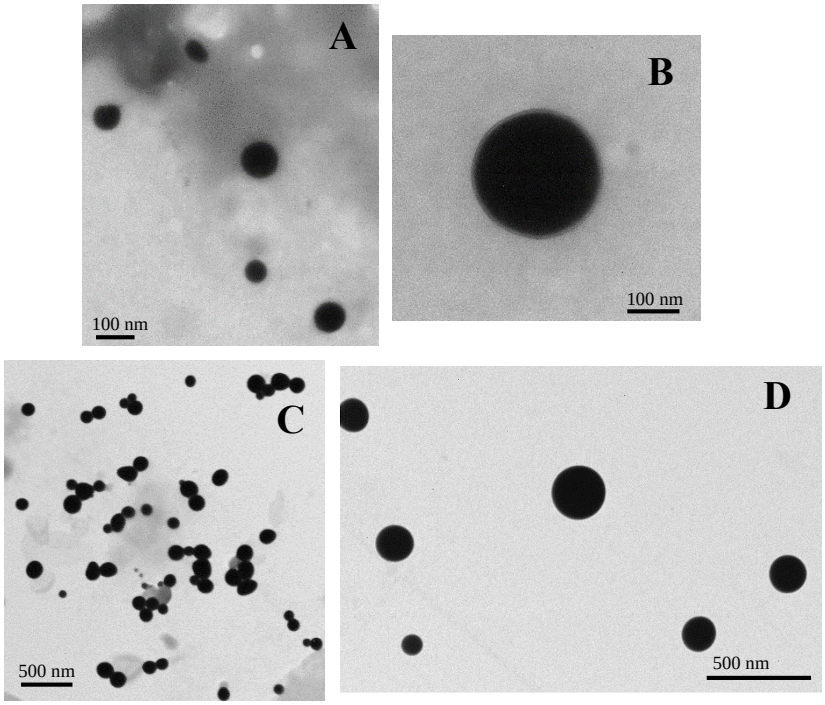

Figure 2.29. TEM images of intracellular SeNPs bio-synthesized by SeITE01 after 24 h (A and B) and 48 h (C and D).

The collected images of Figure 2.29 allows observing the presence of possible organic material surrounding the nanostructures (less dense-greyish color) mainly in the samples related to the intracellular Bio-SeNPs extracted after the 24 h of exposure time (Figure 2.29A). It could probably derive from "contamination" of cellular material originated from the various passages of sonication or purification that was not eliminated during the washing steps. Although much less intense, organic material can also be observed in the case of the Bio-SeNPs collected after 48 h (Figure 2.29C). Probably, a longer incubation time allows a simpler and cleaner extraction of these particular microbial SeNPs. Furthermore, for both the extraction times the Bio-SeNPs assume and maintain a spherical shape.

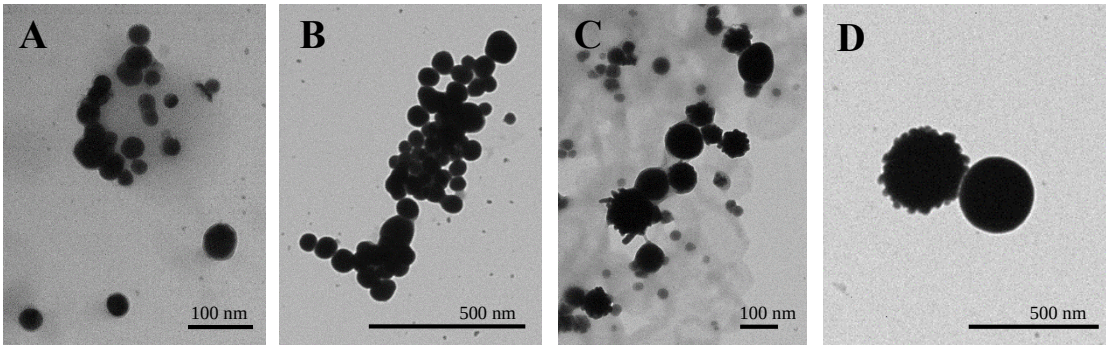

Figure 2.30. TEM images of extracellular SeNPs bio-synthesized by SeITE01 after 24 h (A and B) and 48 h (C and D).

In the case of Bio-SeNPs extracted from the supernatant with the vacuum filtration process, the most significant observation concerns the considerable change in morphology that the Bio-SeNPs undergo with the passage of the incubation time, and in particular starting from the 48 h of exposure with Na_2SeO_3. In Figure 2.30C and D, a new capping conformation is observable, where the surface no longer seems to be covered and surrounded in the Bio-SeNPs regularly, and the attached bio-structures seem to go towards the external environment. Furthermore, greater aggregation of the nanostructures is observed, and a linear crystal-like secondary morphology appears, as reported in Figure 2.31.

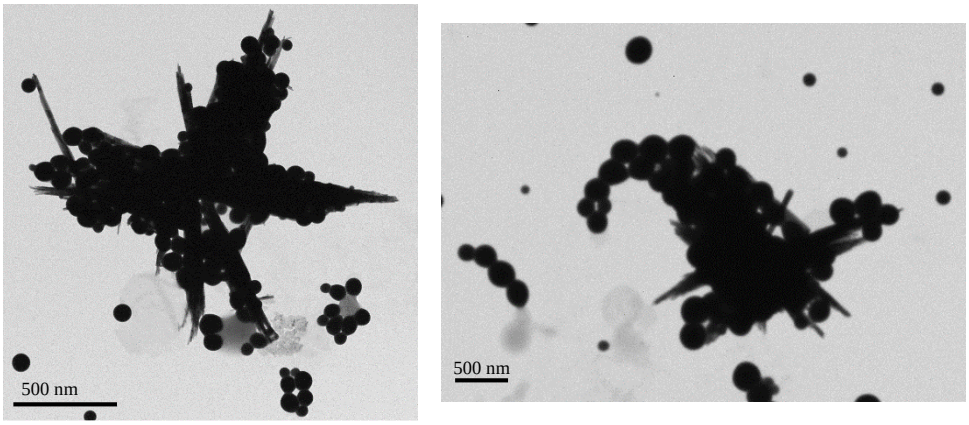

Figure 2.31. TEM images of extracellular SeNPs bio-synthesized by SeITE01 after 48 h of incubation. SeNPs aggregation and appearance of linear crystal-like structures.

PART II: *Stenotrophomonas maltophilia* SeITE02

2.4.4 FTIR spectroscopic investigation of bacterial cells

The spectroscopic investigation of the Gram-negative strain *Stenotrophomonas maltophilia* SeITE02 was conducted in the same manner as for the microorganism SeITE01.

Even in this case, the choice of the different time points for the construction of the time course referred to the growth curves previously conducted by our research group [101]. For the cells cultured in NB medium under optimal conditions and in absence of stress factor, 3, 12 and 24 h depict the beginning and the end of the exponential phase, while 48 h and 72 h denote the maintenance of the stationary phase. When the cells are treated with 0.5 mM of Na_2SeO_3, a lag phase and a decrease in bacterial cell replication is registered at 12 h and 24 h. Afterwards, a partial recovery took place at around 48 h, and the stationary phase begins to be observed at 72 h.

The first part of this section will consider the spectroscopic analysis and discussion performed on SeITE02 untreated cells, which will be followed by those conducted on Se-treated cultures.

All the spectra that will be illustrated and described are represented with the same colors adopted for those of SeITE01, in order to distinguish the presence of different peaks during the temporal evolution of the analyzed cultures.

FTIR spectroscopic investigation of untreated cells

In Figure 2.32A and 2.32B, the untreated spectra acquired in the mid-IR domain between 1800 and 950 cm^{-1} are presented. The first (Figure 2.32A) illustrates the single spectra listed one above the other, while the second (Figure 2.32B) reports their relative overlapping.

Subsequently, the comparison of the spectra grouped two by two will be presented, as shown in Figure 2.33A (3 h with 12 h), B (12 h with 24 h), C (24 h with 48 h) and D (48 h with 72 h).

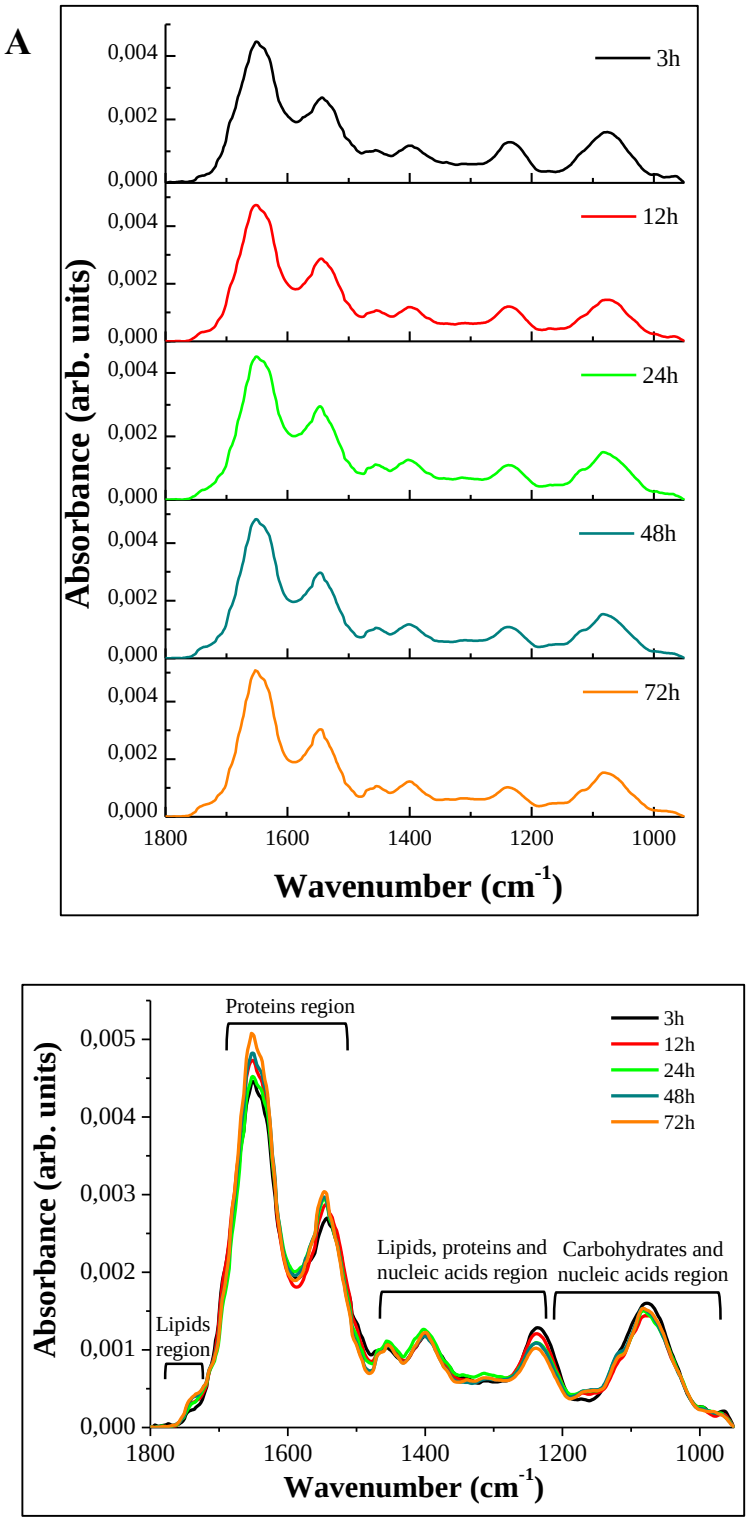

Figure 2.32. Average area normalized FTIR spectra of SeITE02 untreated cells in the 1800-950 cm^{-1} IR region during the time course. Spectra are represented individually (A) and overlapped (B).

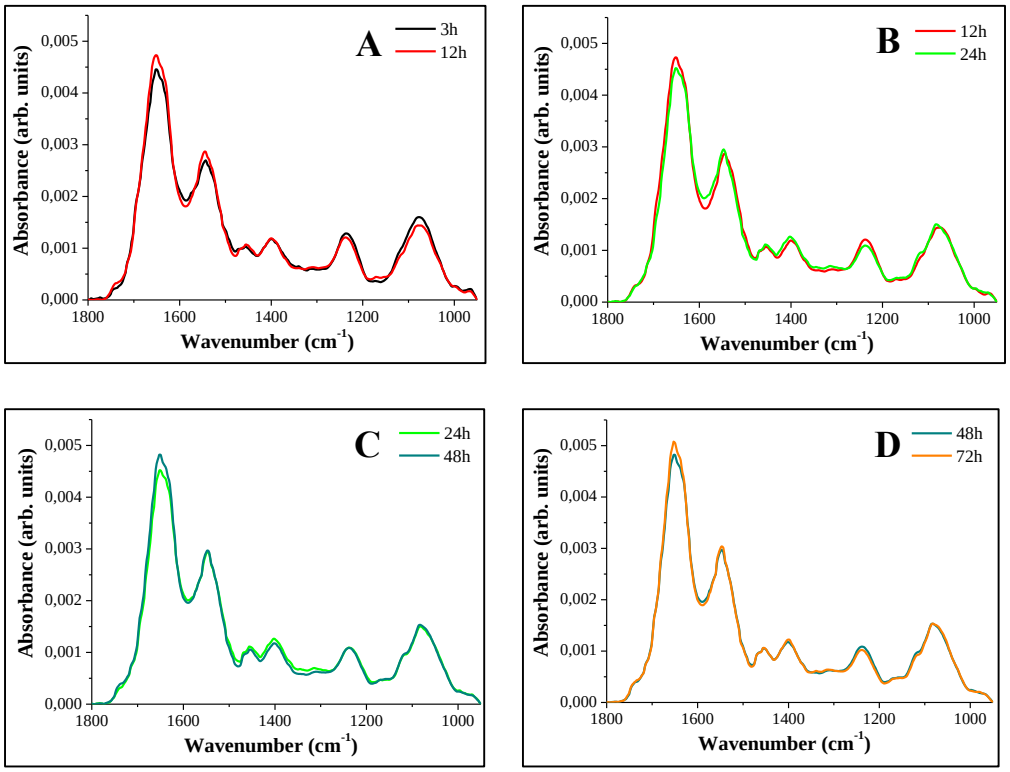

Figure 2.33. Comparison between untreated SeITE02 average area normalized spectra collected at the different time points: 3 h with 12 h (A), 12 h with 24 h (B), 24 h with 48 h (C), and 48 h with 72 h (D).

The comparison of the untreated samples deriving from the observation of the previous figures does not seem to highlight substantial differences or evolutions of the bands between the different spectra collected during the time course. Even the intensity does not seem to change over the time, although a slight hint of increase seems to be visible with regard to the Amide I bands (1650-1635 cm^{-1} wavenumber region).

For this set of samples, since all the spectra manifest the same trend, it was decided to consider the spectrum recorded at 24 h (green spectrum) as representative and to use it to describe the positions of the most significant bands, as shown in Figure 2.34.

The assignments of the main bands for both the untreated and the Se-treated spectra are, instead, indicated in Table 2.3 [80, 110, 141, 142, 148].

Table 2.3. Wavenumbers of the main bands and their assignments for the FTIR spectra of SeITE02 untreated (indicated in Fig. 2.34) and Se-treated cells (indicated in Fig. 2.37, 2.38, 2.39) [80, 110, 141, 142, 148].

WAVENUMBER (cm^{-1})	ASSIGNMENTS OF FUNCTIONAL GROUPS AND THE BIOMOLECULE CONTRIBUTOR
~ 1740 cm^{-1} (**only Se-treated**)	• C=O stretching vibration of ester functional groups in lipids
~ 1650 cm^{-1}	• α-helical structure of amide I (predominantly the C=O stretching vibration in proteins)
~ 1640 cm^{-1}	• β-sheet structure of amide I (predominantly the C=O stretching vibration in proteins)
~ 1545 cm^{-1}	• Amide II absorption and N-H bending coupled to a C-N stretching vibrational mode in proteins
~ 1470 cm^{-1}	• CH_2 bending mode of the acyl chains of lipids
~ 1455 cm^{-1}	• Asymmetric bending modes of CH_3 in proteins • Vibrational modes of CH_2/CH_3 groups in proteins and lipids
~ 1400 cm^{-1}	• Symmetric CH_3 bending mode in proteins • Symmetric stretching of COO^- group in amino acids and fatty acids
~ 1315 cm^{-1} (**only untreated**)	• Amide III band in proteins
~ 1240 cm^{-1}	• PO_2^- asymmetric stretching of phosphodiesters in phospholipids
~ 1200-1050 cm^{-1}	• Stretching vibration of C-O, C-C and C-O-C bending vibration in polysaccharides and polyesters
~ 1165 cm^{-1} (**only Se-treated**)	• Stretching vibration of C-O, C-C and C-O-H bending vibration
~ 965 cm^{-1} (**only Se-treated**)	• Symmetric stretching vibration of phosphoryl groups

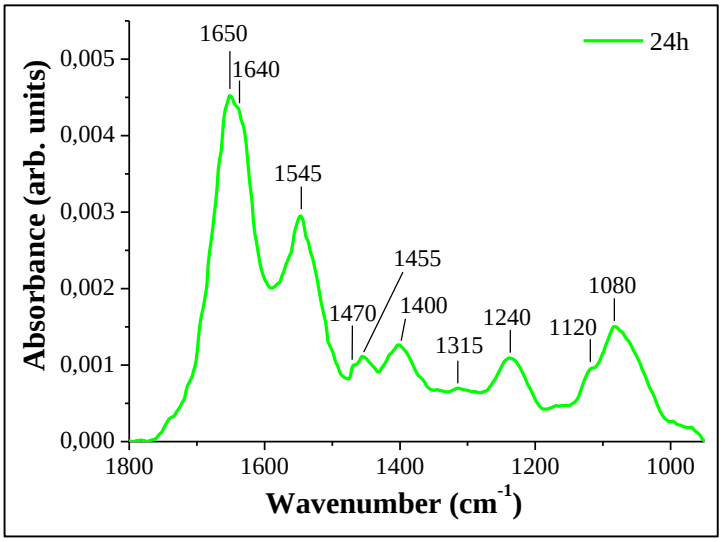

Figure 2.34. Average area normalized FTIR spectra of SeITE02 untreated cells in the 1800-950 cm^{-1} IR region after 24 h of growth.

As described previously in the case of SeITE01, the absorption bands at around 1650 and 1640 cm^{-1} are responsible for the rise in Amide I principally due to the stretching vibrations of C=O groups at α-helical and β-sheet structures of proteins, respectively. Amide II band in proteins, instead, shows up at around 1545 cm^{-1} due to N-H bending coupled to a C-N stretching vibrational mode of the peptide groups. The bands registered at 1470 and 1455 cm^{-1} correspond to the CH_2 bending mode of the acyl chains of lipids, and to the asymmetric bending mode of CH_3 in proteins and the vibrational modes of CH_2/CH_3 groups in lipids and proteins, respectively, while that at 1400 cm^{-1} could mainly be attributed to the symmetric bending of the CH_3 groups in lipids or the symmetric stretching of COO^- group in proteins. Around 1315 cm^{-1} it is possible to observe the weak band associated to the Amide III in proteins, and at around 1240 cm^{-1} that related to the PO_2^- asymmetric stretching of phosphodiesters in phospholipids. Lastly, the stretching vibration of C-O, C-C and C-O-C bending vibration in polysaccharides and polyesters can be referred to the bands detected at 1200-1050 cm^{-1}.

Thus, the cultures of SeITE02 grown under optimal conditions exhibit bands attributable to all the four classes of macromolecules: proteins, lipids, carbohydrates and nucleic acids.

The present analysis has shown that the molecular composition of SeITE02 remains completely unchanged during the different growth phases experienced by this microorganism, information that in any case enriches the knowledge of this strain so far acquired.

FTIR spectroscopic investigation of Se-treated cells

A situation very similar to that just described for the SeITE02 untreated samples is presented for the cells exposed to the toxic oxyanion SeO_3^{2-}.

The spectroscopic trend of the samples at the different time points (3, 12, 24, 48 and 72h) and their comparisons and overlapping are illustrated in Figures 2.35 and 2.36, respectively.

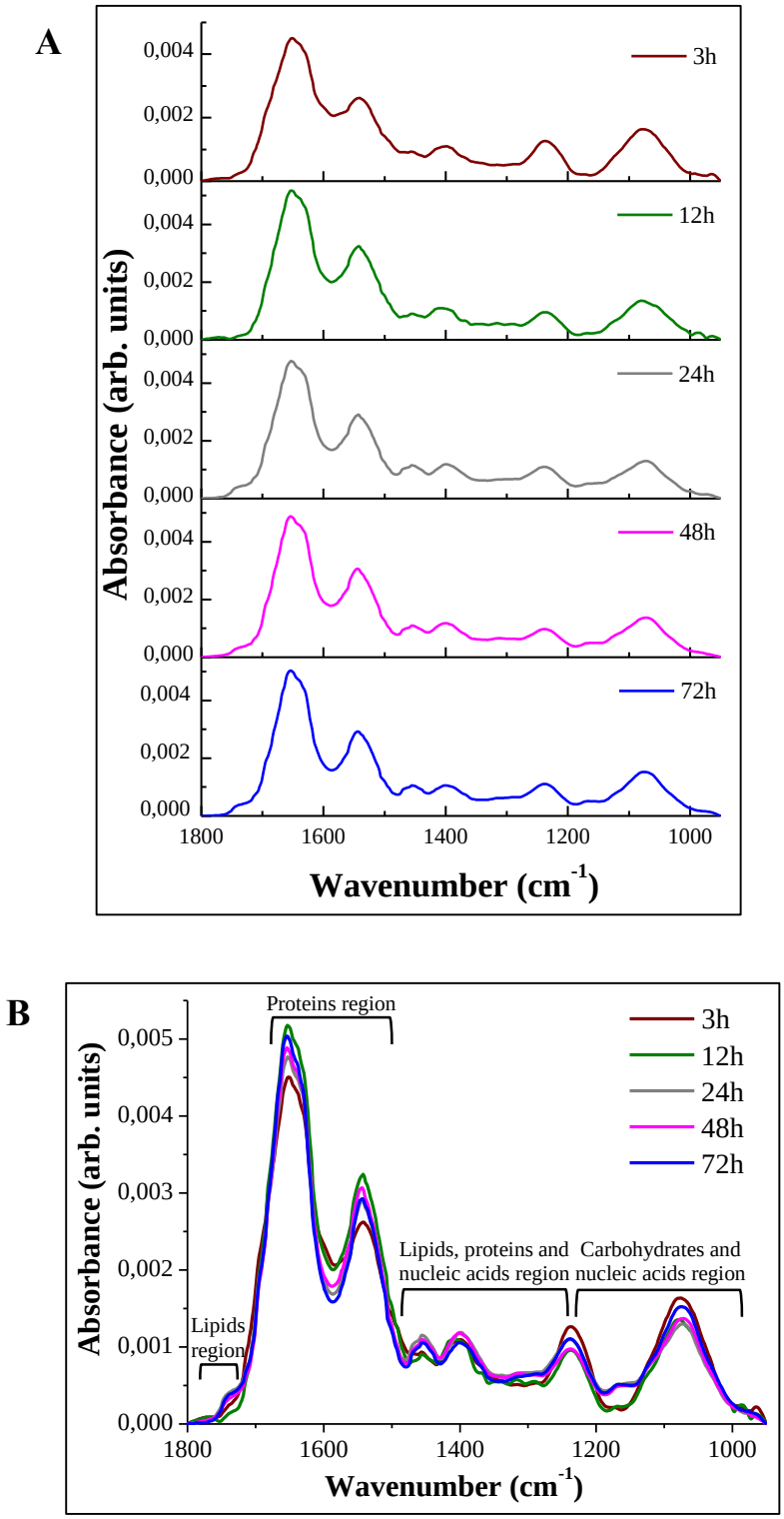

Figure 2.35. Average area normalized FTIR spectra of SeITE02 Se-treated cells in the 1800-950 cm^{-1} IR region during the time course. Spectra are represented individually (A) and overlapped (B).

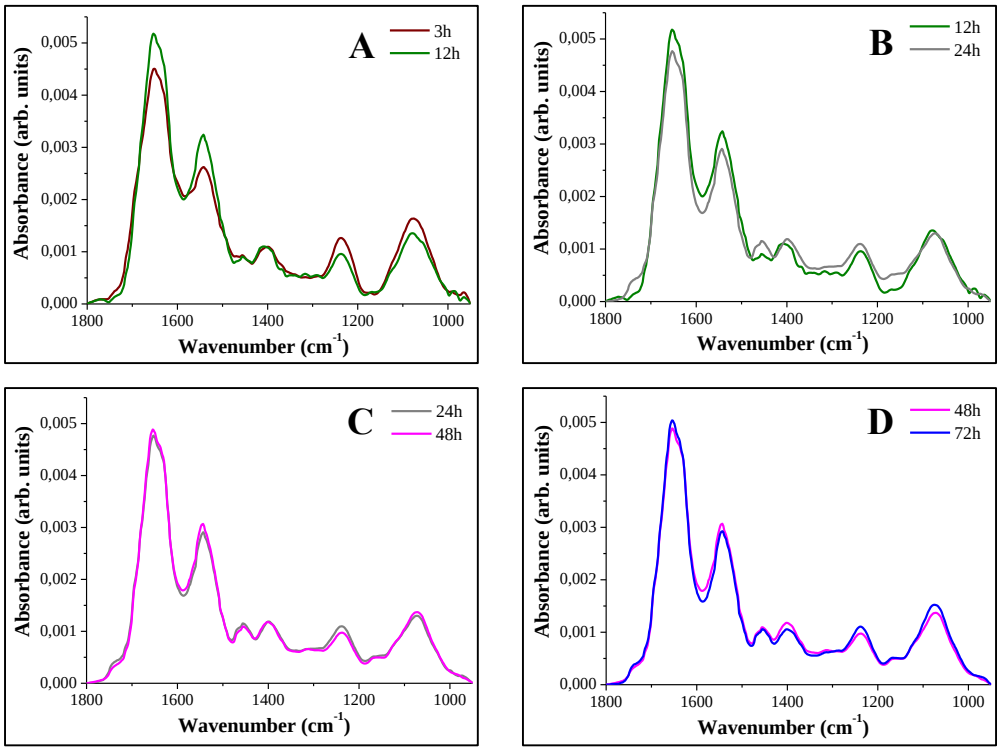

Figure 2.36. Comparison between Se-treated SeITE02 average area normalized spectra collected at the different time points: 3 h with 12 h (A), 12 h with 24 h (B), 24 h with 48 h (C), and 48 h with 72 h (D).

The growth in presence of the oxyanion and the concomitant synthesis and release of Se nanostructures into the NB media does not seem to alter the biochemical and molecular composition of the cultures, contrary to what was observed for the SeITE01 strain. In this case, both the position of almost all bands and their intensities seem to remain quite constant at all the time points selected. Moreover, the appearance and the detection of new peaks is decidedly complex due to the low intensity that they assumed.

Nevertheless, the study of the spectroscopic behavior of these samples makes it possible to identify two different groups with two distinct trends, although their divergences are mainly due to a slight difference in intensity.

The first group is composed by the spectra acquired after 3 h and 12 h, while the second comprises those recorded after 24, 48 and 72 h. Based on this classification, the spectrum of 3 h (Figure 2.37, wine spectrum) and that of 24 h (Figure 2.38, grey spectrum) were considered to represent this different spectral behavior, although barely accented. The corresponding assignments are reported in Table 2.3 [80, 110, 141, 142, 148].

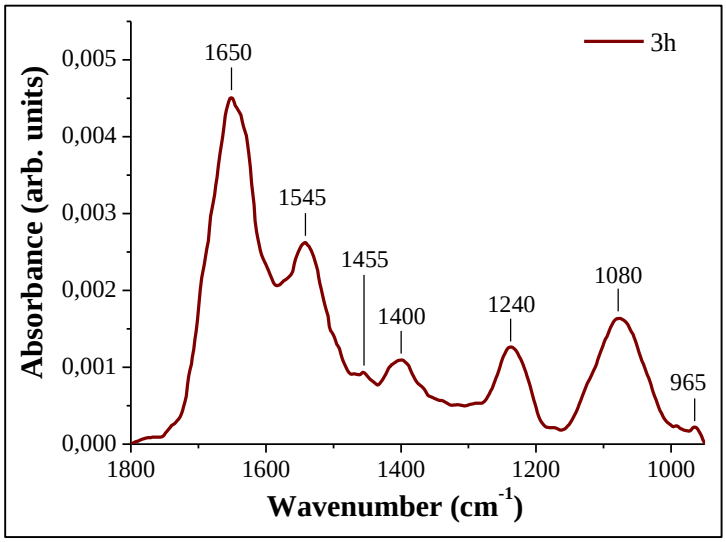

Figure 2.37. Average area normalized FTIR spectrum of SeITE02 Se-treated cells in the 1800-950 cm^{-1} IR region after 3 h of growth.

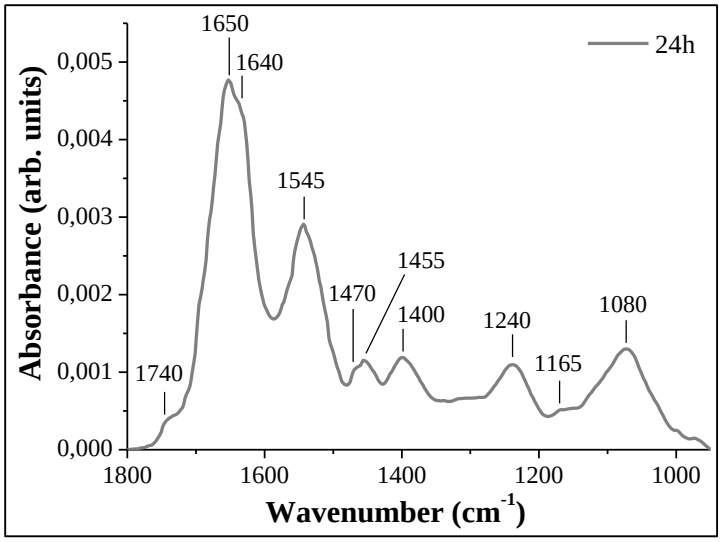

Figure 2.38. Average area normalized FTIR spectrum of SeITE02 Se-treated cells in the 1800-950 cm^{-1} IR region after 24 h of growth.

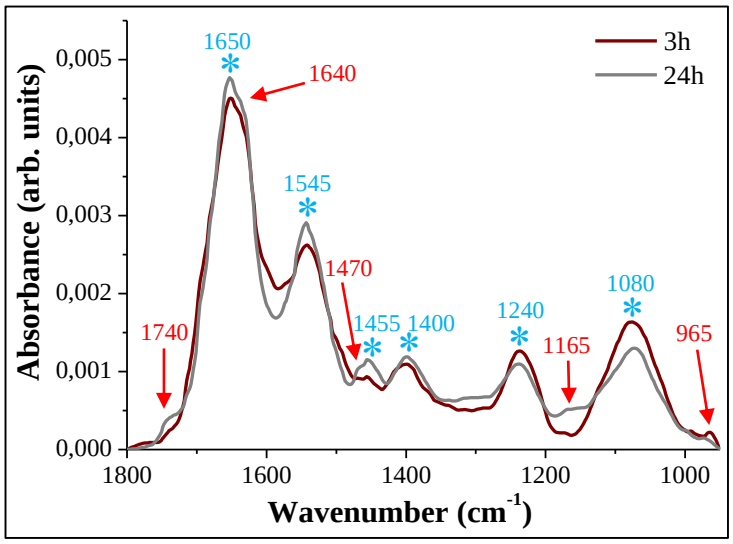

Figure 2.39. Average area normalized FTIR spectra of SeITE02 Se-treated cells in the 1800-950 cm^{-1} IR region after 3 h and 24 h of growth. Light blue asterisks represent shared bands, while red arrows indicate the bands showing the significant variations between the two spectra.

Figure 2.39 shows the overlap of the two representative spectra for the Se-treated cells of SeITE02. The common bands to the two samples (light blue asterisks) are attributable to those widely described in the previous discussions. They are positioned at 1650 and 1540 cm^{-1}, typical of the Amide I and II in proteins, at around 1455 and 1400 cm^{-1}, characteristics of the protein and lipid region, and near 1240 and 1080 cm^{-1}, representing mainly the carbohydrates and nucleic acids domain. The red arrows, on the other hand, represent the new bands that, although very low in intensity, seem to characterize the molecular composition of the cells at the late hours of growth and the behavior they can adopt in the presence of and following the contact with the bio-synthesized SeNPs. The appearance of the band at 1740 cm^{-1} could suggest the ability of SeITE02 to produce PHFs due to the stress suffered by the addition of Na_2SeO_3 in the growth medium. However, the detection of this weak and hardly visible absorption band after 24 h of exposure suggests, instead, a possible mobilization of lipids in favor of the stability and the maintenance of the robustness of the membranes. The further detection of the bands at 1470 cm^{-1} (CH_2 bending of the acyl chains of lipids) and 1165 cm^{-1} (stretching vibration of C-O, C-C and C-O-H bending vibration mainly in the carbohydrates region) can confirm the present assumption. The disappearance from 24 h of the peak at 965 cm^{-1},

present in the 3 h spectrum and related to the symmetric stretching vibration of phosphoryl groups in nucleic acids and the stretching vibrations of C-C, C-O in deoxyribose of DNA, could be mainly traced to a decrease in the production of genetic material by the microorganism.

Untreated vs. Se-treated cells: a comparison of FTIR spectroscopic data

Finally, a direct comparison of the untreated and Se-treated cultures over time is illustrated in Figure 2.40.

The 3 h is represented by the letter A (black and wine spectra), the 12 h with B (red and olive spectra), the 24 h with C (green and grey spectra), the 48 h with D (dark cyan and magenta spectra), and the 72 h with the letter E (orange and blue spectra).

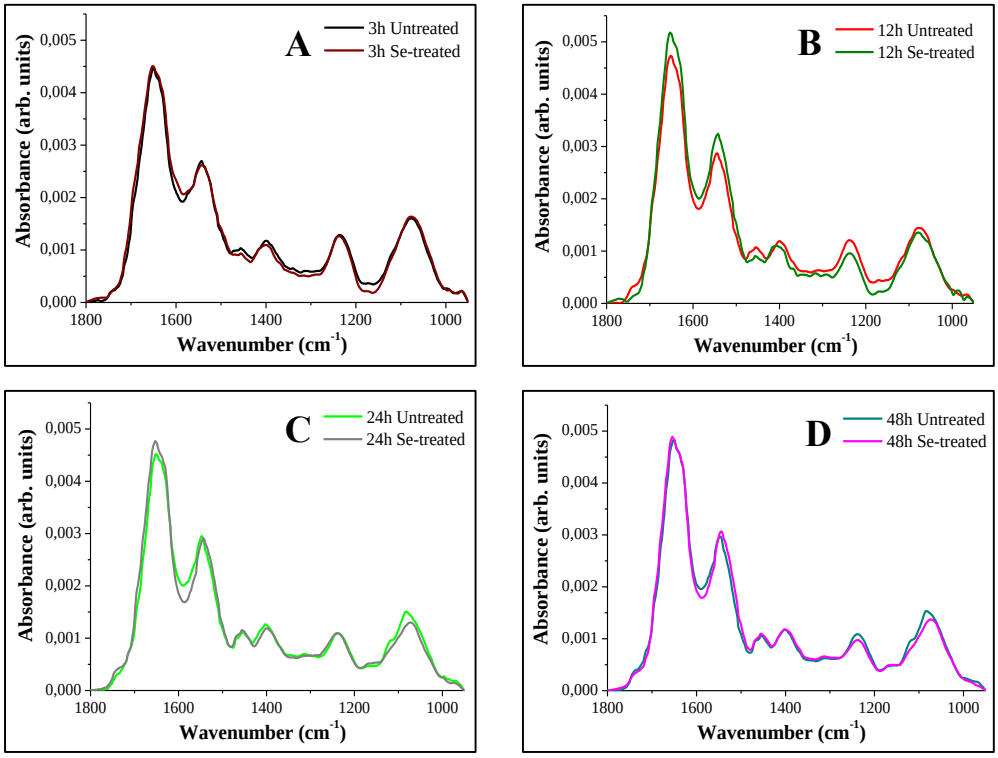

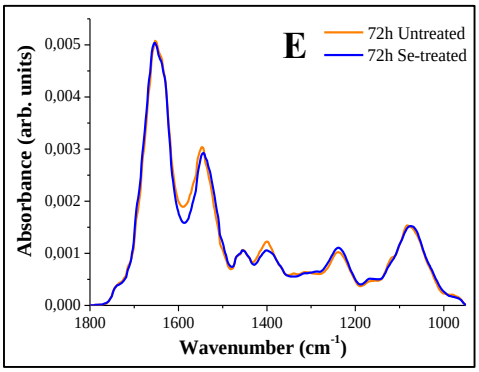

Figure 2.40. Comparison between the untreated and Se-treated SeITE02 average area normalized spectra collected at the different time points: 3 h (A), 12 h (B), 24 h (C), 48 h (D), and 72 h (E).

This direct comparison further reinforces the observations made so far for the *Stenotrophomonas maltophilia* SeITE02 strain. From a spectroscopic point of view, it is possible to conclude that SeITE02 cells do not undergo a toxic impact by SeO_3^{2-} or the Bio-SeNPs, since the analysis of the trends of both the untreated and the Se-treated cells seems to be very similar to each other.

Na_2SeO_3 exposure, in fact, does not involve substantial mutations of the bands in the characteristic domains of the main macromolecules present in the mid-IR wavenumber region and, consequently, the spectra themselves do not present changes in their spectroscopic behavior during the entire time course.

2.4.5 FTIR spectroscopic investigation of Bio-SeNPs

The spectroscopic study of the biologically synthesized selenium nanostructures from SeITE02 bacterial cells was carried out using the FTIR spectroscopic tool.

The results of both the extraction techniques (vacuum filtration and bacterial pellet processing) were obtained and analyzed, as shown in Figure 2.41.

The same colors adopted for the distinction of SeITE01 SeNPs' spectra were employed also for SeITE02. The intracellular spectra acquired after 24 h and 48 h are represented as orange and purple, while the extracellular ones collected after 24 h and 48 h as dark cyan and red.

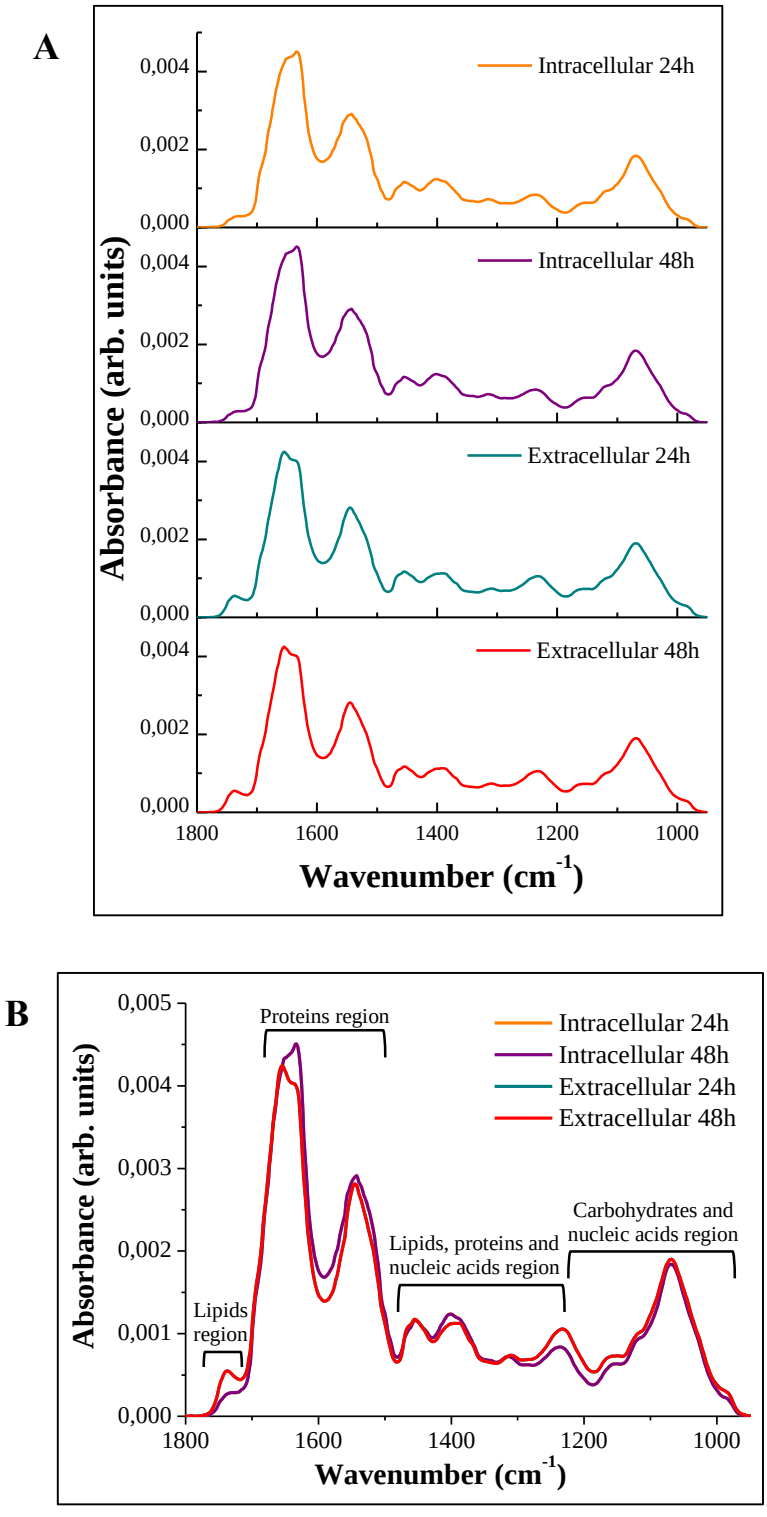

Figure 2.41. Average area normalized FTIR spectra of both intracellular and extracellular SeNPs bio-synthesized by SeITE02 in the 1800-950 cm^{-1} IR region after 24h and 48h of incubation with Na_2SeO_3. Spectra are represented individually (A) and overlapped (B). In the latter, the spectra of both the intracellular and extracellular samples extracted after 24 h are completely hidden from those collected after 48 h of incubation time.

The almost perfect match of the spectroscopic trends observed in Figure 2.41B completely hides the spectra of both the intracellular and extracellular samples acquired after 24 h of exposure, allowing only the observation of those collected after 48 h. Thus, given the absence of new bands or significant differences between the Bio-SeNPs collected at the different incubation times and with the two distinct extraction techniques, the treatment of their FTIR spectra will not be divided into two distinct sections but will be discussed together.

Moreover, the description of their bands will be addressed only to the spectra collected at 48 h, as presented in Figure 2.42 and Table 2.4 [80, 143, 148].

Table 2.4. Wavenumbers of the main bands and their assignments for the FTIR spectra of both intracellular and extracellular SeNPs bio-synthesized by SeITE01 (indicated in Fig. 2.42) [80, 143, 148].

WAVENUMBER (cm^{-1})	ASSIGNMENTS OF FUNCTIONAL GROUPS AND THE BIOMOLECULE CONTRIBUTOR
~ 1740-1725 cm^{-1}	• C=O stretching vibration of ester functional groups in lipids
~ 1650 cm^{-1}	• α-helical structure of amide I (predominantly the C=O stretching vibration in proteins)
~ 1640 cm^{-1}	• β-sheet structure of amide I (predominantly the C=O stretching vibration in proteins)
~ 1545 cm^{-1}	• Amide II absorption and N-H bending coupled to a C-N stretching vibrational mode in proteins
~ 1455 cm^{-1}	• Asymmetric bending modes of CH_3 in proteins • Vibrational modes of CH_2/CH_3 groups in proteins and lipids
~ 1400 cm^{-1}	• Symmetric CH_3 bending mode in proteins • Symmetric stretching of COO^- group in amino acids and fatty acids
~ 1315 cm^{-1}	• Amide III band components in proteins
~ 1230 cm^{-1}	• PO_2^- asymmetric stretching of phosphodiesters in phospholipids
~ 1200-1050 cm^{-1}	• Stretching vibration of C-O, C-C and C-O-C bending vibration in polysaccharides and polyesters
~ 1160 cm^{-1}	• Stretching vibration of C-O, C-C and C-O-H bending vibration
~ 980 cm^{-1}	• Symmetric stretching vibration of phosphoryl groups

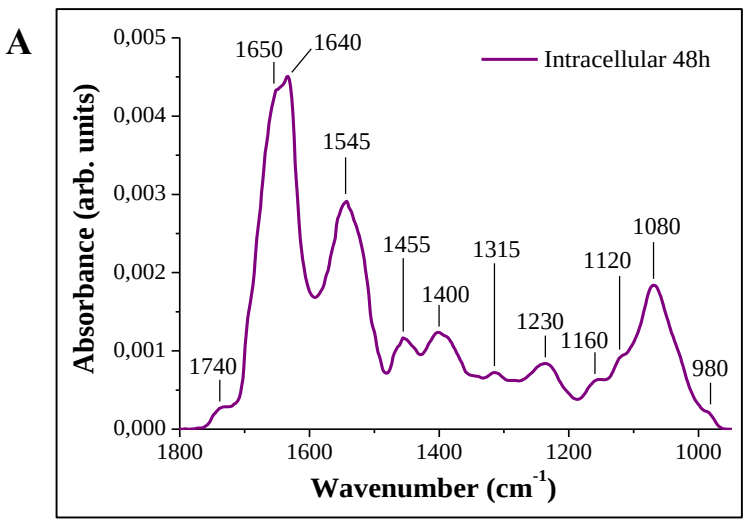

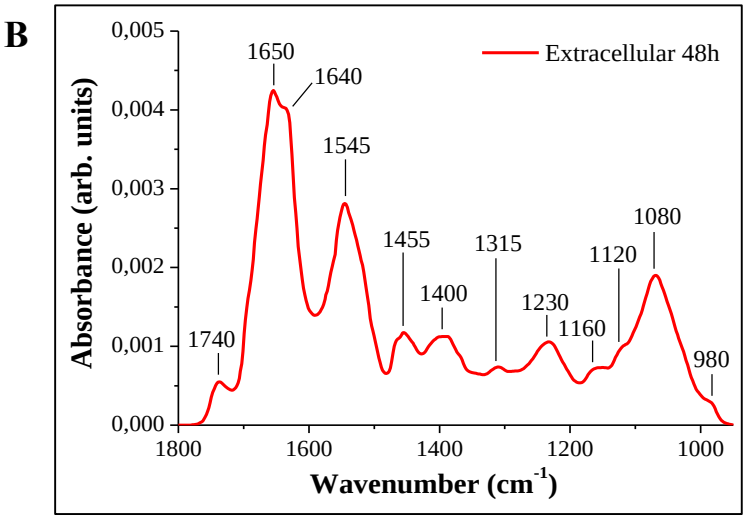

Figure 2.42. Average area normalized FTIR spectra of intracellular (A) and extracellular (B) SeNPs bio-synthesized by SeITE02 in the 1800-950 cm^{-1} IR region extracted after 48 h of incubation time.

In the organic capping of these biogenic Se nanostructures, numerous bands are connected to the macroclass of proteins. In all the samples analyzed, it is possible to identify the sharp and well-resolved bands relative to the Amide I (1650 and 1640 cm^{-1}) and Amide II (1545 cm^{-1}), and the weak but well-recognizable band of the Amide III (1315 cm^{-1}). Moreover, even the bands recorded at 1455 and 1400 cm^{-1} fall within this category. In addition to proteins, however, also lipids (1740 and 1400 cm^{-1}), carbohydrates (range between 1200-1050 cm^{-1}) and several nucleic acids (1230 and 980 cm^{-1}) bands are recorded.

Despite the remarkable similarity in both intensity and bands location, there is a small difference observed from the comparison of the spectra belonging to the two different categories (intracellular and extracellular) (Figure 2.42); it is a slight modification of the relative intensities of the two bands related to the Amide I. In the organic capping of the intracellular SeNPs the β-sheet organization in proteins seems to be slightly more accentuated than the α-helical one, while in the extracellular ones the opposite behavior is observed, with a predisposition to assume the α-helical structure than the β-sheet.

Besides this, the trend of nanospheres extracted with the two different procedures and in the two different incubation times are absolutely identical, as shown in Figure 2.43.

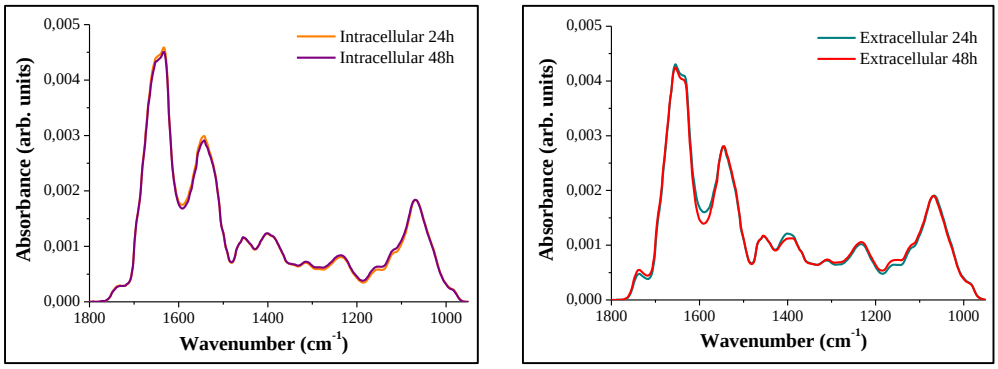

Figure 2.43. Comparison between the average area normalized FTIR spectra of both intracellular and extracellular SeNPs bio-synthesized by SeITE02 in the 1800-950 cm^{-1} IR region after 24 h and 48 h.

2.4.6 DLS analysis and TEM imaging of Bio-SeNPs

The last paragraph of the chapter focuses on the characterization of SeNPs bio-synthesized by SeITE02 performed with the DLS and TEM. Figure 2.44 shows the spectra of the average dimension of the nanostructures retrieved after 24 h (A and C) and 48 h (B and D) of incubation for both the extraction methods, whose color is the same as in the FTIR spectra.

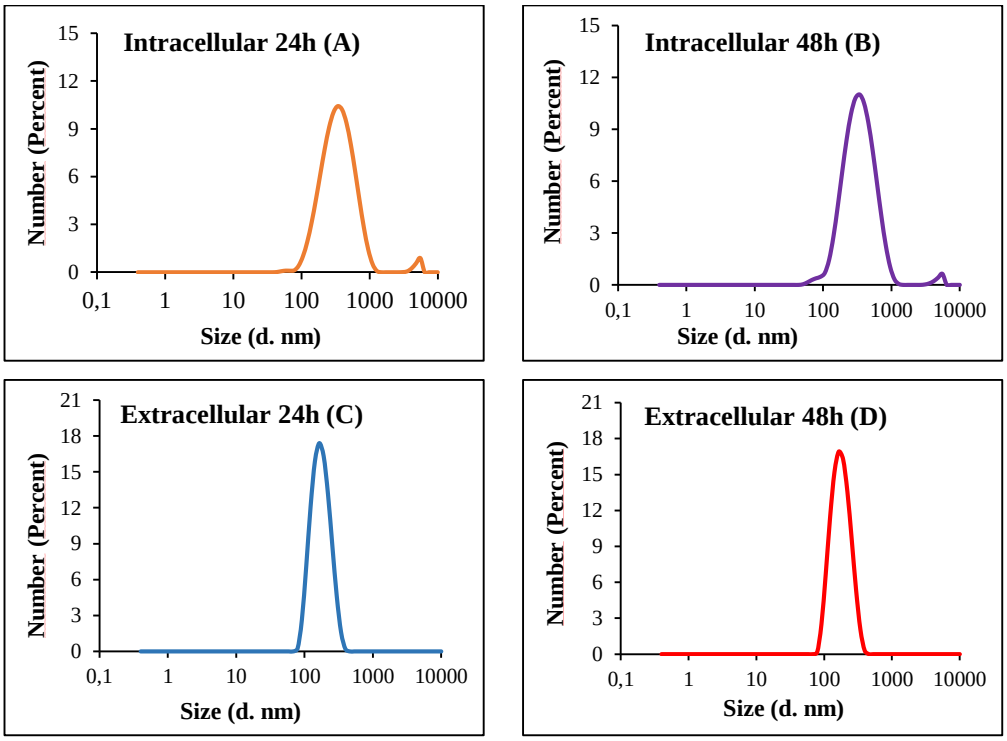

Figure 2.44. DLS spectra of both the intracellular (A, B) and extracellular (C, D) SeNPs bio-synthesized by SeITE02 after 24 h and 48 h.

The intracellular Bio-SeNPs analyzed after 24 h and 48 h show an average size of 314 ± 2.2 nm and 306 ± 4.2 nm, respectively. In both cases, the PdIs were equivalent to 0.2, a value that indicates a quite good level of particle monodispersity within the aqueous suspensions. A similar behavior is also observed in the case of Bio-SeNPs populations deriving from the extracellular samples. In fact, 163 ± 1.8 nm and 165 ± 2 nm are the average dimensions measured for these samples with very low values of PdIs equal to 0.1 and 0.09, respectively. The registration of these low values of PdIs indicates the presence of a single family of particles having all constant and very similar dimensions. Moreover, the presence in Figure 2.44 of single and sharp peak for each sample is a further proof of this statement.

In addition, Figure 2.45 reports the zeta-potential observed for the diverse Bio-SeNPs.

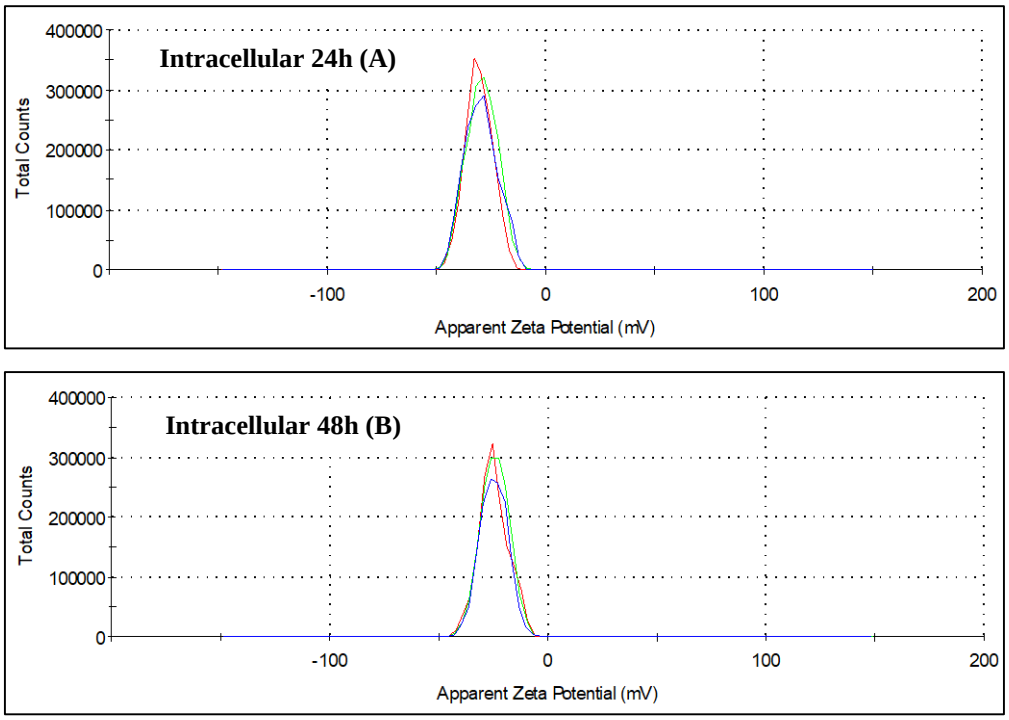

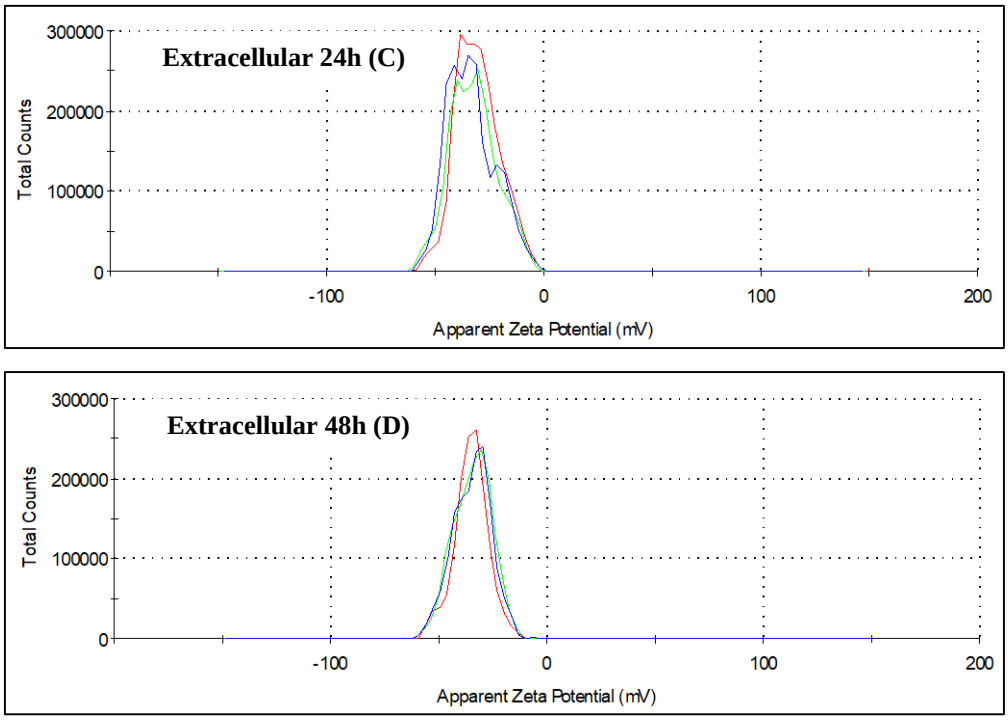

Figure 2.45. Zeta-potential analyses of both the intracellular (A, B) and extracellular (C, D) SeNPs bio-synthesized by SeITE02 after 24 h and 48 h. The three different lines (blue, green and red) represent the technical triplicates collected for each sample.

For all the analyzed samples, negative values lower or near to -30 mV were recorded: -29.6 mV and -24.6 mV for the intracellular Bio-SeNPs after 24 h and 48 h, whilst -32.1 mV and -34.7 mV for the extracellular ones at 24 h and 48 h.

Such negative zeta-potential values indicate a remarkable stability of the Bio-SeNPs and a lower tendency to form aggregates and thus to precipitate.

Finally, in Figures 2.46 and 2.47 are exhibited the TEM images acquired for both the intracellular and the extracellular Bio-SeNPs, respectively.

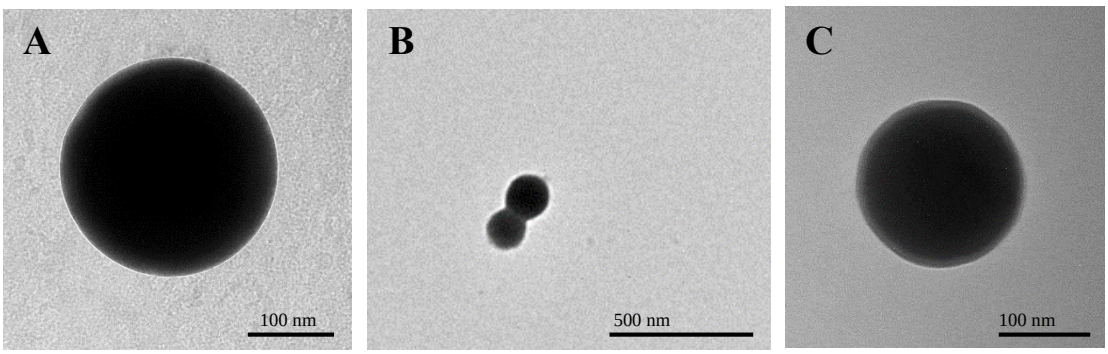

Figure 2.46. TEM images of intracellular SeNPs bio-synthesized by SeITE02 after 24 h (A) and 48 h (B and C).

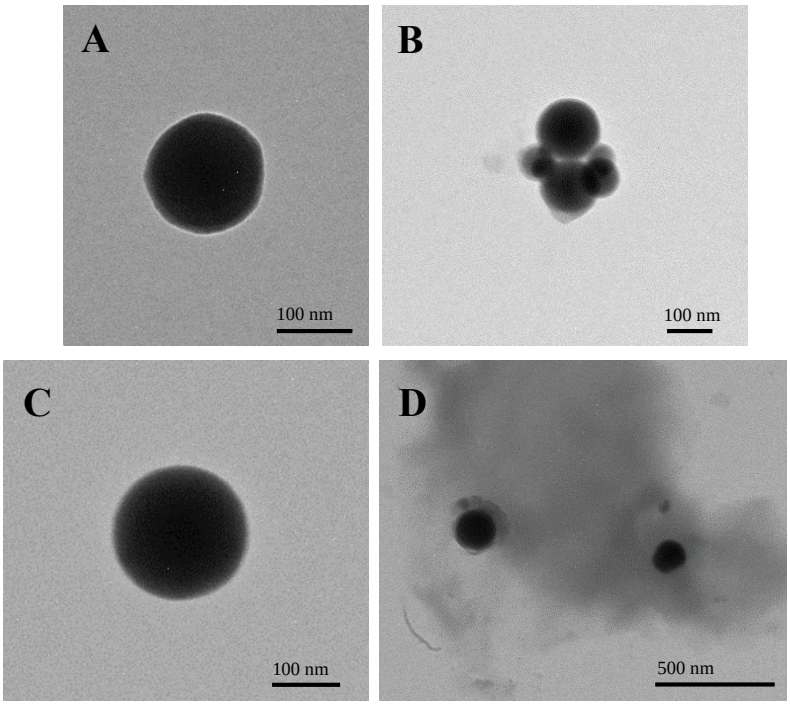

Figure 2.47. TEM images of extracellular SeNPs bio-synthesized by SeITE02 after 24 h (A and B) and 48 h (C and D).

The sizes of the Bio-SeNPs collected with both the extraction procedures and measured with the software ImageJ present also in this case average dimensions that deviate from those registered with the DLS technique. In the case of Bio-SeNPs intracellularly produced, the average size calculated is 141 ± 59 nm after 24 h and 118 ± 63 nm after 48 h. For the extracellular ones, average sizes of approximately 115 ± 32 nm and 107 ± 34 nm are registered for the 24 h and 48 h exposure time, respectively.

Moreover, the analyzed Bio-SeNPs show a spherical shape that does not change with the passing of the incubation time, and the presence of large aggregates does not seem to be present. In almost all the images, it is possible to observe how the samples do not present possible "contaminations" or materials deriving from the different extraction steps. The only exception seems to be the extracellular Bio-SeNPs collected after 48 h of incubation (Figure 2.47D), where a considerable quantity of organic material seems to surround the nanostructures.

2.5 CONCLUSIONS

The spectroscopic analysis carried out with the FTIR tool allowed us the collection of the microbial cells spectra of the Gram-positive bacterium *Bacillus mycoides* SeITE01 and the Gram-negative bacterium *Stenotrophomonas maltophilia* SeITE02. The study of the microbial bio-transformation of SeO_3^{2-} and the effect of this oxyanion on the bacterial cells was investigated analyzing the spectral evolution of the behavior of these two strains in different growth phases and in two distinct growth conditions (untreated and Se-treated).

The elaboration and interpretation of the FTIR spectra of both the untreated bacterial cultures highlighted a significant presence of all four major classes of biological macromolecules. Bands related to lipids, carbohydrates, proteins and nucleic acids have in fact been identified. Furthermore, it was possible to see that for both the bacteria the biochemical trend concerning both the intensity and the position of the bands remains almost completely constant during the entire time course.

A different situation was, instead, observed in the case of Se-treated cells. Although the presence of the oxyanion SeO_3^{2-} negatively affects the cell growth of SeITE02, the spectra recorded on the cells from the exposed cultures showed a behavior very similar to those of the untreated ones. On the contrary, a substantial modification has been recognized in the case of SeITE01 Se-treated cells, where a spectroscopic change has been observed starting from 48 h of incubation time. The most significant alterations were mainly recorded and linked to the lipid and carbohydrate bands, and the hypothesis that a modification and reinforcement of the cell walls and membranes may protect the cells from a possible toxicity exerted by the Bio-SeNPs that the bacterium itself synthesizes was therefore proposed.

In addition to the cells, the bio-synthesized selenium nanostructures from SeITE01 and SeITE02 strains were also analyzed with the FTIR spectroscopic technique, with the aim of analyzing and studying the external organic layer that covers the surface of these interesting biological structures of bacterial origin.

Two different extraction methods were applied after an incubation of 24 h and 48 h, in order to analyze separately the Bio-SeNPs released by the cells into the

medium (extracellular Bio-SeNPs) from those still contained within them (intracellular Bio-SeNPs).

The results, once again, highlighted two distinct spectroscopic behaviors depending on the strain. The analysis of the organic composition of the capping layer of SeNPs bio-produced by SeITE02 showed a trend that was very similar to that of the bacterial cultures for both the extraction technique and in both the exposure times, where the main absorption bands are related to lipids, carbohydrates but above all to proteins and nucleic acids.

On the contrary, SeITE01 Bio-SeNPs showed different trends especially dependent on their localization and the extraction method. The FTIR spectra of the intracellular Bio-SeNPs acquired at 24 h showed a high presence of lipids and carbohydrates and a tendency of the secondary protein structures to assume a differently ordered conformation. However, at 48 h an increase in proteins and a decrease in lipids intensity was recorded, indicating a better stabilization and balance between the protein and the lipid component. In the case of the extracellular Bio-SeNPs, instead, a very similar trend was registered for both the 24 h and 48 h samples, and well-defined and sharp protein bands were acquired. Probably, during the release phase, some protein components present on the bacterial membranes may have adhered to the surface of these Bio-SeNPs.

Certainly, the study of the IR wavenumber range between 4000 and 2500 cm^{-1} and the analysis of the second derivative of the spectra can add further information to those so far collected, reinforcing the hypotheses proposed or paving the way to new theories.

The FTIR spectroscopic characterization of the biogenically produced SeNPs was additionally performed by the DLS measurement and the TEM images.

The DLS provided important data on the size and stability of these nanostructures, emphasizing that the SeNPs bio-produced by SeITE02 exhibit greater stability and uniformity in size in comparison to those synthesized by SeITE01. With the second tool, it was possible to collect the images of the Bio-SeNPs of both strains during different exposure times and determine their average dimensions. Moreover, from the images a change in the morphology of

the biogenic nanostructures produced by SeITE01 starting approximately from 48h of incubation has been observed, whereas no changes were seen over the duration of the experiment in SeITE02 nanostructures.

CHAPTER III:

METABOLOMICS INVESTIGATION ON SeO_3^{2-} BIO-REDUCTION BY SeITE01 AND SeITE02 STRAINS

3.1 INTRODUCTION

3.1.1 General concepts and historical development

Metabolomics is a recent and growing discipline in the field of biological systems. This term refers to the study of biochemical processes involving metabolites and their functional activities, concentrations and dynamic interactions within living cells [159, 160].

Metabolites are low-molecular-weight organic molecules (<1000 Da) and they can be described as the starting and end products of cellular chemical reactions. They play an active role in connecting the numerous biochemical pathways needed for the normal growth and maintenance of vital functions, and for this reason, all the information acquired from metabolite data is representative of cellular phenotype in response to environmental or genetic changes. These compounds, including lipids, amino acids, carbohydrates, and vitamins, can be synthesized both endogenously, as the product of catabolism and biosynthesis, and exogenously, deriving from the degradation of nutrients or pharmaceutical compounds [161].

The global collection of all known metabolites synthetized and/or modified by an organism is called a metabolome, while the sum of biochemical reactions necessary for energy production (catabolism) and biochemical function (anabolism) takes the name of metabolism.

Briefly, metabolism is generally categorized as follows:

- Primary, it describes the activities involved in the catabolism and anabolism and it plays a key role in cellular survival. Primary metabolites are typically present and widely distributed in all living organisms (mammals, plants and microorganisms) and some common examples include lactic acid and certain amino acids.

- Secondary, instead, does not actively participate to the general physiological mechanisms (growth, development or reproduction). It has usually important functions in protection, competition and interaction between different species, and secondary compounds are often the product of primary metabolic pathways activities. As a result, they are chemically very diverse and numerous, even if many of their functions are unfortunately still unknown [160].

Together, primary and secondary metabolites keep the cells in a state of dynamic equilibrium, favoring the correct development and functioning in all biological systems.

Since metabolites are subjected to continuous turnover, their levels and distributions are exposed to enormous spatial and temporal variability. Because of these dynamic changes, some metabolites can accumulate within cells and be highly abundant (mM), while others may be quickly transformed and/or consumed and be present only in small traces (pM) [160, 162]. Consequently, their concentration and flux through various biochemical networks can afford integrative information on the physiological, maturity or pathological state of a living organism. It is so important to have an exhaustive understanding of this continuous flow, which could also derive from the relation and intercommunication of metabolomics with the other "-omics".

Genomics (genes mapping and editing), proteomics (proteins expression), and transcriptomics (genes transcriptions) are the founding bases of the emerging fields of structural and functional genomics. However, the study and application of all these sciences may not be enough to understand or characterize completely the entire biochemical pathways. Firstly, an approach built exclusively on transcriptomics may be insufficient, since there are many genes that are not under transcriptional control [163]. The proteome, also, cannot be totally predicted from the transcriptome due to some differences in regulatory mechanisms at the protein turnover rates and levels [164-166]. Secondly, changes underlined in the proteome or in the transcriptome do not always coincide with phenotypic alterations. Finally, the languages of the genome, transcriptome and proteome are based on 4 different nucleotides and 22 amino

acids, respectively. Instead, from a chemical point of view, the metabolome presents a much greater heterogeneity and variability. Its composition ranges from hydrophilic and hydrophobic elements to ionic inorganic species, volatile alcohols and ketones, organic acids, and complex natural products. Thence, this complexity virtually prevents a simultaneous collection and analysis of the complete metabolome [160, 167-169].

Although metabolomics is certainly complementary to the previous ones, it presents a unique advantage. Genomics, transcriptomics and proteomics show the probability that a process may occur, but metabolomics, as at the end of the "-omics" cascade (Figure 3.1), provides information about what is actually happening [170]. This science can be considered not only the meaningful element for the comprehension and description of the phenotype at a given instant, but the bridge between genotype and phenotype.

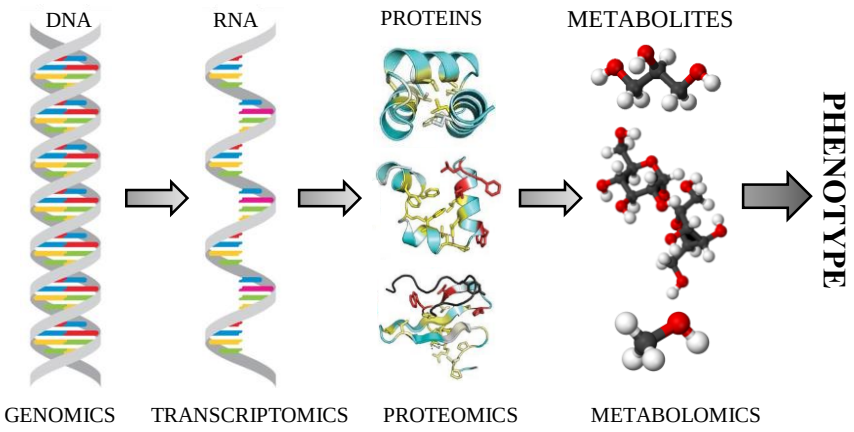

Figure 3.1. Schematic representation of the "-omics" downstream. This image captures the central dogma of biology: genes are transcribed into mRNA, which is further translated into proteins, which finally act as enzymes that catalyze the interconversion of metabolites.

From a historical perspective, the beginning of metabolomics traces back to ancient ages, around 1500-2000 BC. At that time, Traditional Chinese and Hindus Medicine practiced the first body fluids screening to detect the presence of diseases in patience's urine, maturing also the concept of herbal medicine for the treatment of illnesses. All these concepts, foundations of the ancient medicines, were practiced until the 17th century [171].

A significant increase in the understanding of today's metabolomics occurred with the presentation of broader screening approaches combined with biostatistical tools, and, in particular, with the introduction of the separation method of paper chromatography followed by gas chromatography (GC). The concept that every single person can own a "*metabolic profile*" that could be reflected in the composition of the biological fluids (urine and saliva) was introduced during the late 1940s and early 1950s by Roger Williams and co-workers. They used paper chromatography to examine and compare the normal and pathological conditions correlated with alcoholism, schizophrenia and mental illness, underlining the possibility to recognize characteristic metabolic patterns associated with each of these diseases [172]. The work of Williams, however, was apparently not reproducible, and his idea about the utility of metabolic profiling analysis remained essentially quiescent until the late 1960s. With the technological advancements and availability of GC, liquid chromatography (LC) and Nuclear Magnetic Resonance (NMR) Spectroscopy, the progress in the metabolomics field became extremely rapid. For example, in 1970 at least three different research groups published papers describing multicomponent analyses of biological fluids in patients affected by different pathologies [173-175]. In 1971, Horning and Horning introduced the terminology "*metabolic profile*" [176, 177]. They demonstrated that the employment of gas chromatography-mass spectrometry (GC-MS) can successfully characterize metabolic profilings and can be a useful tool for studies of drug metabolism and biomarkers discover. At the end of the 1990s, new acronyms and terms related to this -omics technology were suggested. The word metabolome and the concept of metabolic foot printing (or exometabolome) were first coined by Oliver et al. [167, 170, 178] and by the researchers Kell et al. [179], respectively. Finally, created in 2005, METLIN was the first metabolomics web database [180] for characterizing human metabolites. It was developed in the Siuzdak laboratory at The Scripps Research Institute (TSRI, La Jolla, California, USA) and now it contains over a million molecules ranging from lipids, steroids, plant and bacterial metabolites, small peptides, carbohydrates, drugs metabolites and toxicants. On 23 January 2007,

the Human Metabolome Project, led by Dr. David Wishart of the University of Alberta (Edmonton, Alberta, Canada) in collaboration with the University of Calgary (Calgary, Alberta, Canada) completed the first draft of the human metabolome [181]. This consists of a freely available electronic database, named Human Metabolome Database (HMDB), that today stores 113996 different metabolites entries additionally linked to 5702 protein sequences and hyperlinked to other databases (KEGG, PubChem, MetaCyc, ChEBI, PDB, UniProt and GeneBank). In Figure 3.2 are reported all the icons representing these projects.

Figure 3.2. Icons for METLIN database (on the left), Human Metabolome Project (in the middle) and Human Metabolome Database (on the right), respectively.

Starting from these ideas, other platforms have been underway (Figure 3.3). The ECMDB (*E. coli* Metabolome DataBase [182]) is an expertly curated database containing extensive metabolomic data and metabolic pathway diagrams about *Escherichia coli* (strain K12, MG1655). PMDB (Plant Metabolome DataBase [183]), instead, is a web portal created in 2008 for exploring, visualizing, and downloading plant metabolomics data.

Figure 3.3. Icons for the ECMDB and PMDB.

3.1.2 Strategies for metabolome investigation

Over the past decade, the young interdisciplinary field of metabolomics has gained increasing interest and made considerable progress. However, due to lack of detailed guidelines, various debates among investigators have arisen, extending from how samples are collected and prepared to statistical analysis. As a result, different analytical approaches have been proposed.

In 2002, Fiehn described his vision of the metabolome investigation composed by four different approaches [167], as shown in Scheme 3.1.

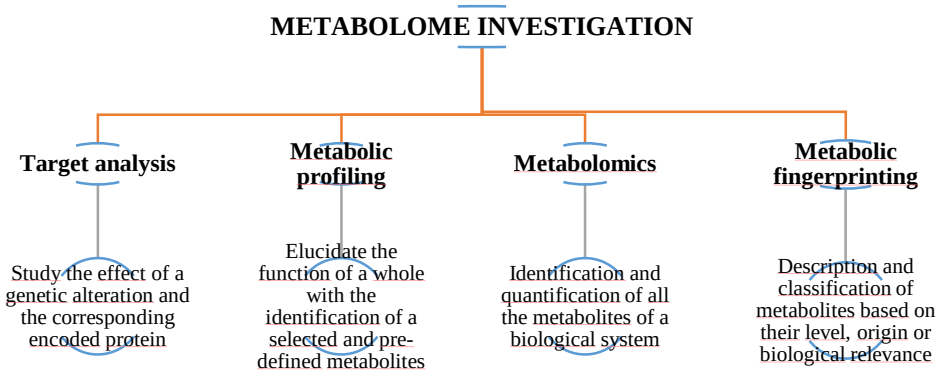

Scheme 3.1. Metabolomics investigation diagram described by Fiehn in 2002 [167].

His point of view was later questioned by Villas-Bôas and co-workers in 2004 [168] and the same approach was considered by Farhana and Villas-Bôas in 2017 [184] and by Tanveer et al. in 2018 [169]. These researchers asserted that there are only two specific strategies for the study of the metabolome, based mainly on target analysis and metabolic profiling, as shown in Scheme 3.2.

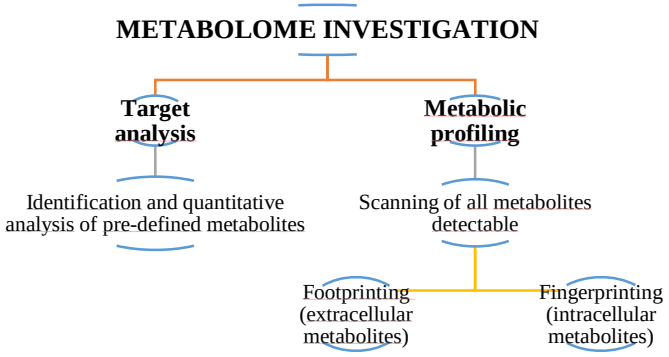

Scheme 3.2. Metabolomics investigation diagram exposed by Villas-Bôas and co-workers in 2004 [168].

Another version is brought forward by the contribution of Dettmer and Hammock (Scheme 3.3), who further elaborated in 2004 [185] and in 2006 [186] an additional investigation diagram. This scheme is similar to the previous one but the main classes and concepts are differently rearranged.

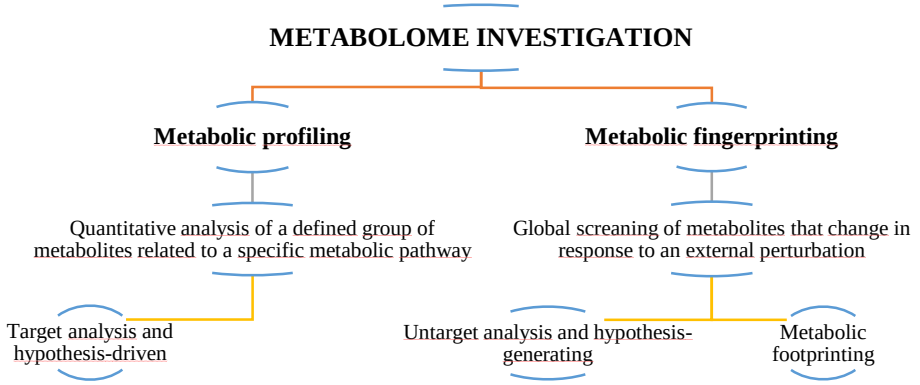

Scheme 3.3. Metabolomics investigation diagram proposed by Dettmer et al. in 2004 [185].

Although the field of metabolomics is rapidly growing and new applications and analytical tools are expected in the near future, many technical and methodological problems need to be addressed. These different visions of the metabolome investigation landscape underline the complexity, the youth and the pitfalls within this science. None of these approaches would seem to be totally wrong, but from their observation it is possible to understand that there is a strong need to establish a common language between the researchers and create experimental designs and protocols that respond promptly and efficiently to the many and varied biological samples and questions.

3.1.3 Analytical platforms

Metabolite detection and identification are the first key steps in metabolomics analysis. Collection, separation and detection of these small compounds is made possible by advanced analytical technologies that allow the understanding of their signatures in the regulation of cellular homeostasis.

Currently, however, there does not exist a single tool or method with the ability to identify all metabolites, since no distinct technique is comprehensive,

selective, and sensitive enough to analyze them simultaneously. As explained above, the main reasons are due to the chemical diversity that exists within the metabolome, along with considerable differences in concentration as well as chemical stabilities of metabolites. Moreover, it is extremely difficult to establish an efficient and universal preparation procedure for all the various types of samples [160]. Nowadays, the two major platforms used in metabolomics are NMR spectroscopy and mass spectrometry [187-195].

3.1.3.1 Nuclear Magnetic Resonance (NMR) Spectroscopy

NMR can uniquely recognize and concurrently quantify a wide range of organic compounds in the micro-molar range. It has been broadly used for metabolite fingerprinting, profiling and metabolic flux analysis especially of bio-fluid samples. This technique offers many advantages: it is robust, reproducible and non-destructive, can be utilized *in vivo*, and does not require sample elaboration or derivatization. NMR also allows the discrimination of metabolites with identical masses, the identification of unknown metabolites structure, and the elucidation of pathways transformation and compartmentalization [190]. The principal limitations of this tool are mainly connected to its low sensitivity (only the most abundant metabolites can be detected), the high initial instrument acquisition cost, and the low number of spectroscopists trained to acquire, handle and analyze the complexity of metabolome datasets [188, 190].

3.1.3.2 Mass Spectrometry (MS)

MS technology has become in the recent years the central analytical instrument in metabolomics research. This dominant role derives from its high sensitivity, widespread availability, reproducible quantitative analysis, and the ability to analyze samples with extreme molecular complexity. MS tool can profile simultaneously the effect of time, stress, nutritional status, and environmental changes of hundreds of metabolites, facilitating the reconstruction of biochemical networks. The appearance in MS field of predetection separation approaches based on chromatography (e.g., GC, LC) led to outstanding advancements and innovations, entailing an

extension of metabolome coverage. Some of the most used and new MS-based devices are reported in Table 3.1, while their respectively strengths (✓) and weakness (x) are described in Table 3.2 [189-195].

Table 3.1. List of some MS-based techniques [189-195].

PLATFORM	TOOL	FEATURES AND APPLICATIONS
Gas-Chromatography	GC-MS	• Very popular since 1970s • Analysis of only volatile compounds • Its applications are mainly focused on plants, fossil fuel/oil analysis, and illegal doping and drug control
	2D-GC (GC x GC)	• Rapid development and popularity of this approach in the last decades • Application in various fields (water treatment, food and fiber metabolites identification)
Liquid-Chromatography	LC-MS	• Quite recent introduction in MS field (from 2000) • Currently the most widely used MS technology • It is ideal for non-volatile, polar, and thermally labile compounds • Important contribution to the development of life science and bio-analytical sector
	2D-LC (LC x LC)	• Analysis of samples that are not compatible with mass spectrometry (e.g. high-molecular-weight polymers), providing important information on the distribution of the sample components along chemical dimensions (molecular weight, charge, lipophilicity, stereochemistry, etc.)
	UPLC-MS	• First appeared in 2004 • High-throughput molecular phenotyping technique • Analysis of pharmaceutical and biological compounds
Capillary-Electrophoresis	CE-MS	• It is a low flow nanoscale separation tool • Promising separation technique for charged metabolites (polar or ionic compounds) • Powerful tool for target and non-target analysis

Table 3.2. Description of strengths (✓) and weaknesses (x) of some MS-based techniques [189-195].

TOOL	ADVANTAGES AND ISSUE
GC-MS	✓ High sensibility and resolution power ✓ Excellent reproducibility and highly reproducible fragmentation ✓ Easy use of the instrument and low cost x Only volatile molecules can be analyzed (<600 Da) x Complicated sample preparation, time consuming and error prone x Derivatization of involatile compounds can produce different forms of the same metabolites x Incomplete derivatization can cause inaccurate compound quantification
2D-GC (GC x GC)	✓ Increased selectivity and peak capacity and enhanced sensitivity ✓ Elevated identification power due to the formation of ordered 2D-chromatogram patterns relative to homologous compounds x Commercially available MS spectral databases lead often to low matching values x Expensive equipment and specialist training required x More complexity as compared with 1D system
LC-MS	✓ Ability to separate and detect a wide range of metabolites ✓ Availability of a wide range of stationary phases (>800) ✓ Avoides chemical derivatization x High cost of columns manufacturing
2D-LC (LC x LC)	✓ Possibility to combine two completely different LC separation columns with independent parameters ✓ Provides high performance and greater separation power (peak capacity) in the shortest possible time x Expensive equipment and specialist training required x Lack of systematic optimization procedures and user-friendly software x More complexity as compared with 1D system
UPLC-MS	✓ Highly sensitive profiling and peak capacity in the identification of trace components in complex mixtures ✓ Rapid analysis without loss of resolution x Complex operation, time consumption, and high maintenance cost.
CE-MS	✓ Short analysis time and small injection volume (1-20 nL) ✓ High separation efficiencies ✓ Low reagent cost due to low flow rate (nL/min) x Lack of sensitivity and relatively poor reproducibility x Inability to separate neutral compounds

The maturation of metabolomics technologies and the resolution of various problems and limitations has stimulated a world-wide boom in their application. This technique can now be used to study new fields of the natural world, such as the engineering of microorganisms for the production of biofuels or the relation between metabolism and circadian rhythms. Metabolomics can also

help to identify new human disease-relevant targets or develop small-molecule inhibitors for chemical therapies [189].

Finally, Scheme 3.4 describes a general and basic workflow for the experimental design and setup of a metabolomics investigation. However, it is important to remember that in designing a metabolomics experiment different approaches and steps must be used depending on the system and the type of sample analyzed.

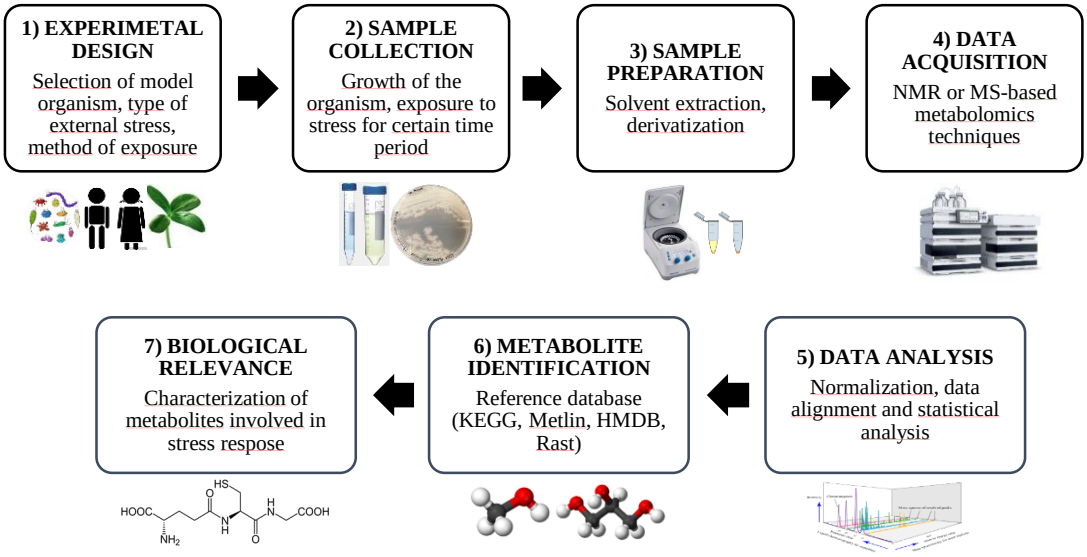

Scheme 3.4. General metabolomics experimental workflow.

3.1.4 Metabolomics and the study of metal toxicity

While technological progress has allowed a better knowledge of metals metabolism and an elucidation of their interaction with different systems, an absolute understanding of all the biochemical mechanisms and responses from various metal ion exposures is far from being completed. The use of metabolomics to elucidate such exposure responses is a novel and young undertaking [196].

Despite the premise, different studies provide a sampling of how this field can be applied to examine metal toxicity in plants, microbes and animals. The aim

is to elucidate the changes and alterations in metabolic profiling and the strategies employed by macro- and microorganisms in surviving under adverse and stressful conditions. In this sense, the importance of monitoring the effects of toxic metals on the biodiversity is strictly related to the search for new bioremediation procedures to counteract natural changes and anthropogenic activities [197].

Below some examples are given of metabolomics studies in various organisms.

3.1.4.1 Plants

The decline in plant growth as well as leaf necrosis, decrease in the rate of seed germination, turgor loss, and crippled photosynthetic apparatus are most common visual and harmful evidences of metal exposure. Furthermore, metal stress interferes negatively with the water uptake, transport, transpiration, and nutrient metabolism, and alters the uptake of essential metals [198].

In plants cadmium (Cd) and lead (Pb) are examples of the most popular metal stressors analyzed in metabolomics style experiments to date. Cd is a frequent contaminant of farmland due to industrial agriculture activities, while Pd is a pollutant from lead-based paint, leaded gasoline and pipes for water distribution [196-201]. Several plants were analyzed using metabolomics approaches, such as the model system *Arabidopsis thaliana* [199, 200] and the vetiver grass (a Pb hyperaccumulator plant) and maize (a Pb susceptible plant) [201].

In these studies, it was shown that the exposure of *A. thaliana* to Cd caused an increase in carbohydrates, organic acids, amino acids, and other stress-responsive metabolites levels, underlining an important role of antioxidant defences in the mechanisms of plant resistance to cadmium stress.

Similar behavior was observed in the case of the vetiver grass, where a massive increase in levels of key metabolites in response to Pb, including amino acids, organic acids and coenzymes was detected. On the contrary, maize showed very modest increase in some of the same metabolites, and no change in others.

These example studies provide important information on the different responses of plants induced by different metals and may highlight significant characteristics that can be used for soil bioremediation.

3.1.4.2 Humans

The application of metabolomics in human studies extends in many different areas, from medicine and pharmacology to nutritional sciences. Unfortunately, in literature nowadays there are only a few investigations involved in the identification of bioindicators in metal pollution assessment and in the understanding of the toxic effect of metals on the human metabolome [197, 202, 203]. For example, the analysis conducted by Dudka et al. [203] underlines changes in the metabolic profiles of smelter workers exposed to Pb, Ca and arsenic (As), suggesting modifications in lipids and amino acids metabolism. In light of this, the integration of metabolomics with public health can improve current clinical and research practices. It can also provide a deeper insight into the relationships between various metabolites and health status as well as to help discover new response to a given drug treatment, or the reaction to a nutritional intervention or environmental challenge [204].

3.1.4.3 Bacteria

Research on metal-microorganism interaction dates back to 1970's. However, more attention has always been given to the quantitative study of the resistance and tolerance of different strains, but little investigation has been made into how these metals generate their toxic effect.

It is known that microbes compose around 50% of the carbon biomass of the planet and they have a key role in global food chains. Thus, metal bioaccumulation and bioconversion as well as the level of resistance and tolerance in these organisms are important considerations that must be treated and understood for biosphere health and toxic metal biogeochemical cycling [196].

Several studies have been conducted to examine the relative responses of different strains exposed to the metals Cd, copper (Cu), aluminium (Al), gallium (Ga) [205-208] and the metalloid oxyanion tellurite (TeO_3^{2-}) [209].

These investigations have studied the relationship between the metal effect and the bacterial behavior from different approaches by comparing free swimming planktonic populations with surface-attached biofilms [206], or wild-type cells with mutants [209].

All the data delineate multiple effects of metals exposure and biochemical changes in cellular physiology, such as oxidative stress response, membranes perturbations, and reconfiguration of cellular metabolism [205-209].

Although the results obtained have demonstrated the ability of the metabolomics techniques to distinguish and describe the diverse strain phenotypes in response to the exposure of different metals, these tools have always been used as an end-point approaches. Thus, the study of the physiological evolution of bacterial cells in the presence of a metal could enrich the knowledge so far acquired.

3.2. RESEARCH INNOVATIONS AND OPEN QUESTIONS

In this study, the metabolomics methodology is used to investigate the microbial SeO_3^{2-} bio-reduction process and the effect of the salt Na_2SeO_3 on *Bacillus mycoides* SeITE01 and *Stenotrophomonas maltophilia* SeITE02 by employing a LC-MS approach.

The main aims are to investigate the complex biological interactions of metabolites and the possible activation/deactivation or alteration of physiological mechanisms and biochemical pathways in response to the exposure of cells to the oxyanion SeO_3^{2-}.

The use of a time course developed on the different bacterial growth phases of the two strains analyzed, and with LC-MS, possible metabolic pathways involved in SeNPs bio-synthesis are explored.

This combination represents the major novelty of these experiments.

The main questions to which this PhD thesis aims to answer are the following:

- What are the metabolites that change most when the strains are exposed to selenite SeO_3^{2-}?
- Which are the biochemical pathways involved in the detoxification of this oxyanion and in the formation of Bio-SeNPs?
- What are the time temporal changes in response to cells exposure to Na_2SeO_3?
- Does the metabolism under Na_2SeO_3 exposure change depending on the strain?
- Is it possible to identify key compound/s and use it /them for future target analysis as internal physiological marker/s?

3.3 MATERIALS AND METHODS

3.3.1 Bacterial strains and growth conditions

The environmental strains *Bacillus mycoides* SeITE01 and *Stenotrophomonas maltophilia* SeITE02 were grown aerobically in enriched medium Nutrient Broth (NB, Thermo SCIENTIFIC, Oxoid)). The salt Na_2SeO_3 (Sigma Aldrich) from a filter-sterilized stock solution (50 mM) was added to the exposed culture medium to the final concentration of 2.0 mM for SeITE01 and 0.5 mM for SeITE02.

All microbiological experiments were conducted in biological triplicates.

The strains were pre-culture for 24 h at 27°C on an orbital shaker (150 rpm, G10 Gyrotory Shaker, New Brunswick Scientific Co., Inc.) in 50-ml Erlenmeyer PYREX® flasks prepared with 20 ml of NB.

The analyses were then carried out in 250-ml Erlenmeyer PYREX® flasks containing 100 ml of NB inoculated with aliquots from previous stationary-phase cultures with a final optical density equal to A_{600} = 0.01 (Hitachi U-2000 Spectrophotometer), and the corresponding concentration of SeO_3^{2-}.

3.3.2 Evaluation of bacterial growth and SeO_3^{2-} depletion

Cellular profiles of SeITE01 and SeITE02 grown in presence or absence of Na_2SeO_3 were evaluated at different time points (0, 3, 6, 9, 12, 18, 24, 48, 72, 96 h and 0, 6, 12, 18, 24, 48, 72, 96 h, respectively) and inspected for both microbial growth curves. These were monitored by Colony Forming Units (CFU) count on agar NB and data were reported as the logarithm of the CFU per milliliter (CFU/ml (log_{10})) for each biological triplicates.

The residual SeO_3^{2-} in the medium was, instead, calculated only in the case of the exposure to Na_2SeO_3. It was determined spectrophotometrically (Varian Cary® 50 Bio UV-Vis) according to the procedures of Kessi et al. [79]. SeO_3^{2-} concentrations were evaluated by measuring the absorbance at 377 nm of the Se-2,3-diaminonaphthalene complex in cyclohexane, using a 1-cm path length quartz cuvette (Hellma® Analytics).

A standard curve (R^2 = 0.9876) was calculated as average value (n = 2) and constructed by using 0, 50, 100, 150, and 200 nmol of SeO_3^{2-} dissolved in liquid NB medium.

3.3.3 Metabolomics analysis

3.3.3.1 Metabolites extraction

Bacterial samples collection and metabolites extraction were performed in SeITE01 and SeITE02 at specific time points. In the case of SeITE01 were chosen 3, 12, 18, 24 and 48 h, while for SeITE02 6, 12, 24, and 48 h were selected.

For each microbe, all the intracellular (pellet) metabolites were collected starting always from the same number of cells: ~$2x10^6$ (SeITE01) and ~10^9 (SeITE02). The pellets from the untreated and Se-treated cultures were centrifuged at 4°C for 10 min at 16000 xg (Eppendorf® Microcentrifuge 5415C, F-45-18-11 rotor), and washed once with cold phosphate buffer saline (PBS, Sigma Aldrich, 4°C). They were then immediately stored at -80°C in order to facilitate samples quenching and block instantaneously the rapid turnover of compounds and possible biochemical reaction intermediates. Afterwards, the frozen pellets were re-suspended in 100 µl of a pre-cooled mixture of methanol and double distilled water (MetOH-ddH_2O 1:1, v/v, -20°C), followed by 1min of vortexing and then centrifugation (10min, 4°C, 16000 xg). Finally, 80 µl of the suspensions were transferred into clean glass vials (Sample Vials in Lab File®, WHEATON®, DWK Life Sciences) and used for LC-MS analysis.

The choice of MetOH as solvent and reagent for metabolite extraction and quenching has various reasons. It is not as toxic as other solvents (e.g., chloroform) and it provides the recovery of polar to mid-polar metabolites. In addition, its use at low temperatures (< -20°C) prevents the degradation of thermally labile compounds [210].

In the case of extracellular (spent medium) metabolites, 500 µl of each media were collected, centrifuged (10 min, 4°C, 16000 xg), transferred in new and clean 1.5-ml eppendorf tubes (Eppendorf®) and stored at -80°C.

50 µl of the chilled supernatants were then added with 950 µl of a pre-cooled mixture of MetOH-ddH_2O (1:1, v/v, -20°C) in order to reach a dilution equal to 1:20. The suspensions were vortexed for 1 min, centrifuged (10 min, 4°C, 16000 xg), and ultimately, 800 µl were moved into new glass vials and ran for LC-MS analysis.

The experimental design applied for this study is graphically summarized in Scheme 3.5.

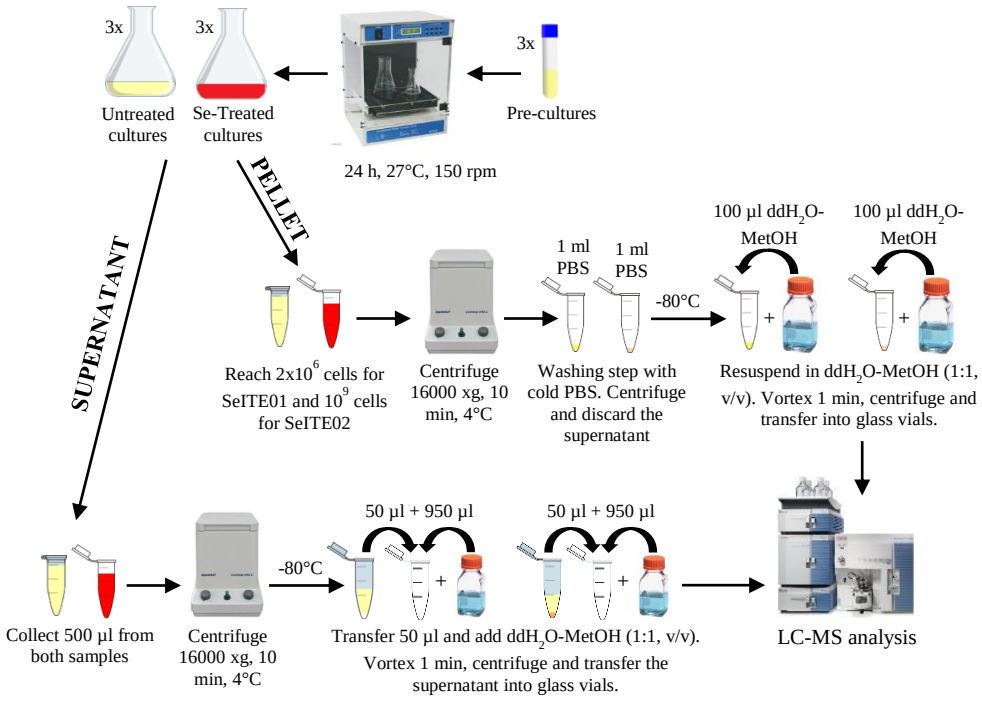

Scheme 3.5. Intracellular (pellet) and extracellular (supernatant) metabolites extraction.

The same preparation of the extracellular samples was followed also for the extraction of metabolites present in the growth media (NB, NB + Na_2SeO_3) with no bacterial cells added as abiotic controls.

The collection of these samples were carried out following the time course and the SeO_3^{2-} concentration defined for each bacterium. This operation allows the analysis of "clean" datasets from the metabolites already present in the media, and to consider only those processed and secreted by the cells. For the experiment presented here, these samples were prepared in biological duplicates.

Finally, the different categories of sample run during the LC-MS experiment are shown and summarized in Scheme 3.6.

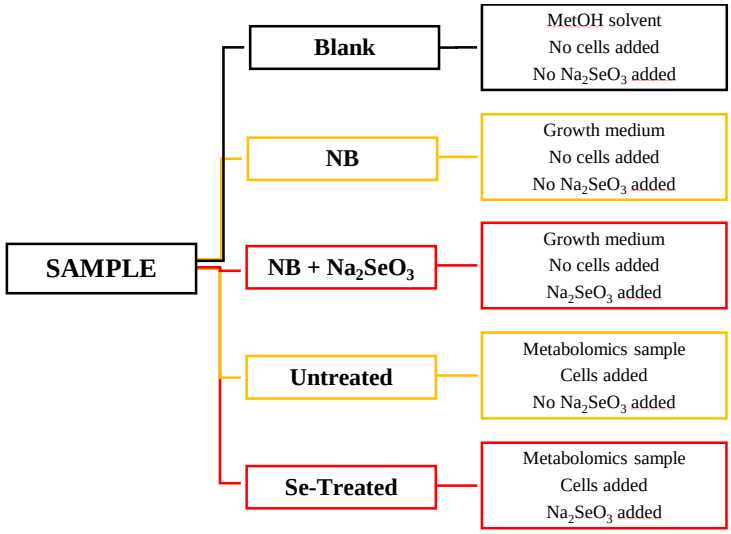

Scheme 3.6. List of all the samples prepared for LC-MS metabolomics experiment.

The terminology indicated above will be adopted throughout the discussion of all the samples presented in this thesis.

3.3.3.2 LC-MS acquisition

Metabolites present in the extracts were separated using ultra high-performance liquid chromatography (UHPLC) performed using a gradient of 20mM ammonium formate at pH 3.0 in water (solvent A) and 0.1% formic acid (% v/v) in acetonitrile (solvent B) in conjunction with a Syncronis™ HILIC LC column (100 mm × 2.1mm × 2.1 µm; Thermo Scientific).

High-resolution mass spectral data were acquired on a Thermo Scientific Q-Exactive™ HF Hybrid Quadrupole-Orbitrap mass spectrometer coupled to an electrospray ionization source.

Data were acquired in negative ion full-scan mode from 50-750 mass to charge ratio (m/z) at 240000 resolution with an automatic gain control (AGC) target of 3e6 and a maximum injection time of 200 ms.

A general representation of an LC-MS instrument is shown in Figure 3.4.

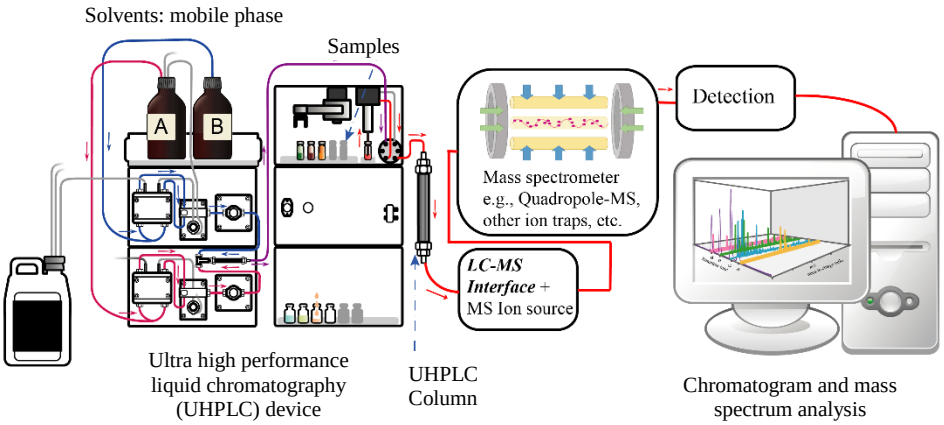

Figure 3.4. General diagram of an LC-MS instrument.

During the acquisition of all the samples from both the pellets and the spent media, different blanks (MetOH solvent) were inserted and analyzed. The run of this solvent between different sets of samples allows establishing the background signal levels present in each sample and it is also used to clean the column.

Then, the identification and relative quantification of both intracellular and extracellular metabolites were carried out with the open source software Metabolomic Analysis and Visualization ENgine (MAVEN) [211], using a pre-defined list of about 400 metabolites.

Peak assignments were determined by matching the previously established m/z and retention times (RT) of authentic standards to observe metabolite signal.

For this metabolomics experiment, the use of internal standards was not possible, as untargeted analyses were performed.

3.3.3.3. Data pre-processing

Removal of blank values from both intracellular and extracellular datasets was the first step for data processing. This operation allowed to remove the background noise collected during the LC-MS run.

Only in the case of extracellular datasets further data manipulations were performed. Both growth media values (NB, NB + Na_2SeO_3) with no

bacterial cells added were removed from the respective untreated and Se-treated data. In this way, only the metabolites extruded from the cells and not those present in the media would be considered.

In addition, after the LC-MS run, these datasets were normalized by the CFU/ml value previously determined by the growth curves. This additional step was not necessary in the case of the intracellular data, since the normalization was carried out during the preparation of the samples themselves.

3.3.3.4. Statistical analysis and elaboration

Basic statistical analyses were carried out using the software Excel 2013 (Microsoft, USA), whereas the advanced statistical approaches described below were performed with RStudio, a free and open source integrated development environment for R, a programming language for statistical computing and graphics.

The experimental design allowed collecting 125 compounds deriving from the bacterial pellets and 124 from the growth spent media as a function of different treatment conditions and time. The statistical challenge was to identify metabolites whose concentration varied significantly between treatment conditions from the analysis of their temporal changes. The challenge arose from the fact that there were very few time points and just three replicates per metabolite. Moreover, the short time series did not allow the use of the standard methods for time series analysis such as Fourier analysis, autoregressive-moving-average (ARMA) methods or wavelets.

The problem identified in the treatment of these data is very similar to that encountered for longitudinal microarray experiments. The most widely used method for identifying temporally changing genes in replicated microarray experiments is to carry out multiple pairwise comparisons across times, using statistics developed for comparing two independent samples [212]. These methods are not entirely appropriate, because they do not incorporate the fact that longitudinal microarray time course samples may be somehow correlated, as in the case of the data of this experiment. This would be a serious concern also within the context of general linear data modeling, such

as classical or mixed analysis of variance (ANOVA). In fact, time-series studies are very complex and contain multiple types of variation [213]: the variation originating from differences between bacterial cultures that are constant in time, the time-dynamic variation of each individual sample, or combinations thereof. Thus, it is necessary to incorporate this structure into the data analysis for a deep understanding the biological information in these datasets.

The analysis of the multivariate data collected in this thesis followed two different approaches. The first one was developed within the context of microarray gene expression experiments [214] and then applied to longitudinal metabolomics assays [212]. The method exploited multivariate empirical Bayes statistics to test the null hypothesis that two expected profiles are the same. A T^2 statistics equivalent to the two-sample Hottelling T^2 statistics have been derived by considering a degree of moderation of the variance-covariance matrices toward a common matrix which retain the temporal correlation structure of the data [212]. A ranking of metabolites' profiles that varied at most in time between control and treated samples was then computed. The top 10% metabolites in this ranking were considered for further analyses. The full algorithms are available in the timecourse R package. The second approach, instead, was developed in-house. Each metabolite was considered a multidimensional vector of time-course data samples, and a Principal Component Analysis (PCA) was exploited to identify the temporal dimensions where the samples varied at most. If the metabolites concentration for the untreated and Se-treated cultures showed similar temporal patterns, then the vector representations in the reduced PCA space of orthogonal coordinates should be almost overlapped, except for variations due to random noise. Then, the Euclidean distances between these vectors were expected to follow a Rayleigh distribution, which therefore defined the null hypothesis for statistical comparisons. The shape parameter of the Rayleigh distribution was estimated by nonlinear regression using the mathematical routines implemented in the R fitdistrplus package. The fit was reiterated by leaving out one extreme value of the

distribution at each time. The log-likelihood function, the Aikake information criterion and the Bayesian information criterion were then used to estimate the quality of the fits and terminate the procedure. A conservative significance threshold was then set at p-value < 10^{-4} for the rejection of the null hypothesis.

The last consideration regards the normalization of the raw data. Since they showed narrow peaked distributions with very long tails, some of the metabolites present in the dataset would dominate the statistical comparisons because of high leverage. Thus, the R package bestNormalize was used to search for their best normalization procedure. Concentration data of intracellular metabolites were normalized using the BoxCox parametric transform implemented in the geoR package [215], whereas for extracellular metabolites the Ordered Quantile (ORQ) normalization transformation was used provided by the orderNorm function implemented in the bestNormalize package [216]

Finally, the KEGG database (Kyoto Encyclopedia of Genes and Genomes, www.genome.jp), an integrated database resource generated by genome sequencing and other high-throughput experimental technologies, was used to represent graphically together the metabolites identified by the statistical tools and to recognize possible metabolite families and biochemical pathways activated after the SeO_3^{2-} exposition. For this purpose, two closest phylogenetic neighbours were chosen: *B. mycoides* ATCC® 6462™ for SeITE01, and *S. maltophilia* R551-3 for SeITE02.

The percentages reported on the bar plots were calculated based on the number of metabolites present in a given pathway related to the total number of metabolites merged on all the identified pathways.

All the individual elaborations, from blank and media removal to statistical analyses, are summarized in Scheme 3.7.

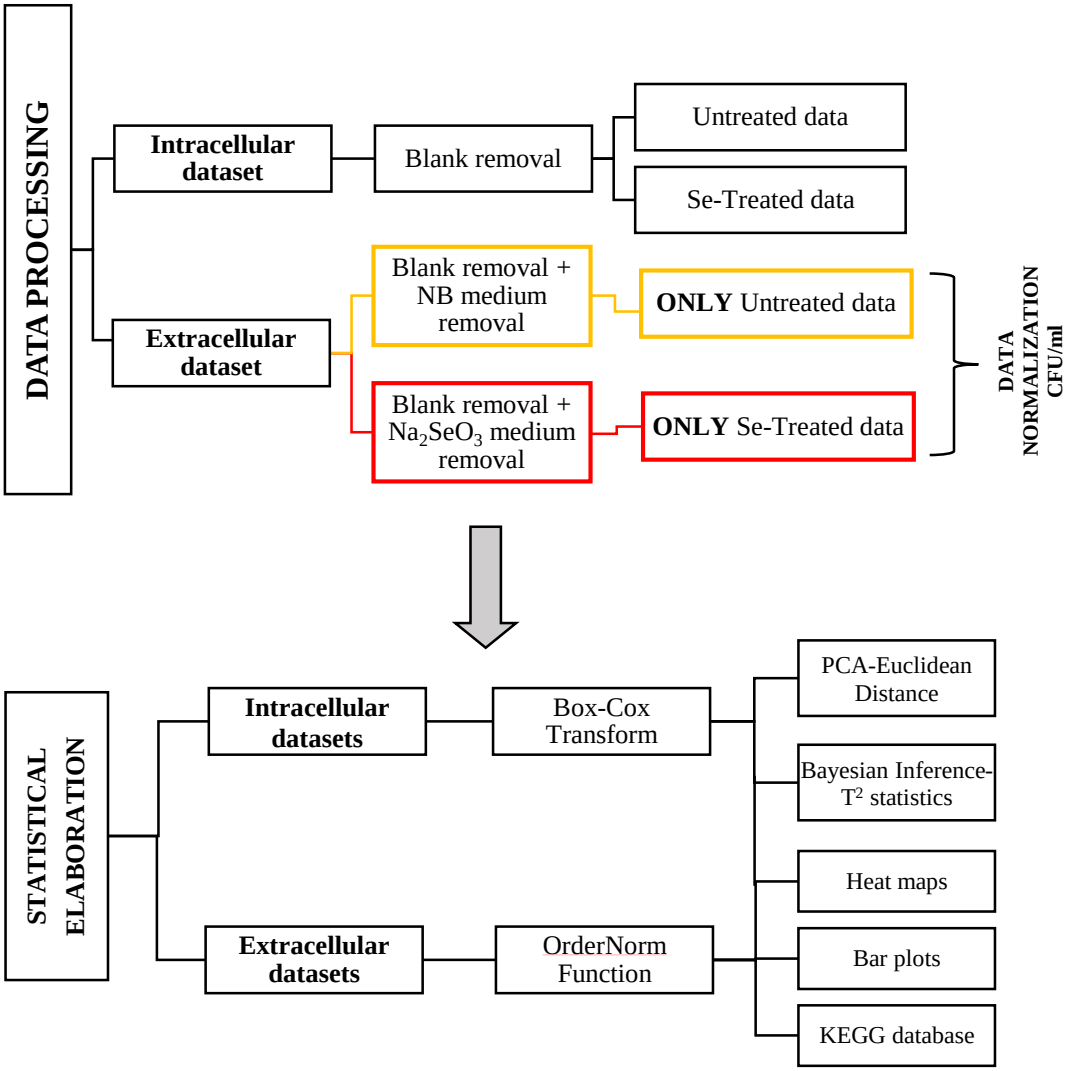

Scheme 3.7. Summary of all the steps necessary for datasets processing.

3.3.4. Transmission Electron Microscopy (TEM) analysis

SeITE01 and SeITE02 physiology investigation was performed at the Microscopy and Imaging Facility (MIF) at the University of Calgary (Calgary, AB, Canada) using the Hitachi H-7650 120 kV transmission electron microscope (TEM).

Samples were analyzed with or without the presence of Na_2SeO_3, and observed after 3, 12, 18, 24 and 48 h of growth and exposition time for SeITE01 and after 6, 12, 24, 48 h for SeITE02.

The preparation involved the centrifugation of 500 µl of each culture at 16000 xg for 10 min (Eppendorf® Microcentrifuge 5415C, F-45-18-11 rotor) and the transfer of 400 µl of supernatant in a clean eppendorf tube (Eppendorf®). Samples were then prepared in order to reach $4x10^4$ cells in 10 µl, spotted on CF300-Cu-Carbon Film Copper grids (Electron Microscopy Sciences) and air dried for 24 h.

3.4 RESULTS AND DISCUSSION

PART I: *Bacillus mycoides* SeITE01

3.4.1 Bacterial growth and biotic SeO_3^{2-} removal efficiency

The capability of *Bacillus mycoides* SeITE01 to bio-convert and reduce the toxic oxyanion SeO_3^{2-} to elemental selenium Se^0 was tested in liquid NB at 2.0 mM concentration of Na_2SeO_3.

Bacterial growth in the Se-treated and untreated flasks at different time points, the relative growth curves and the depletion of SeO_3^{2-} concentration are shown in Figure 3.5 A, B, C, respectively.

A

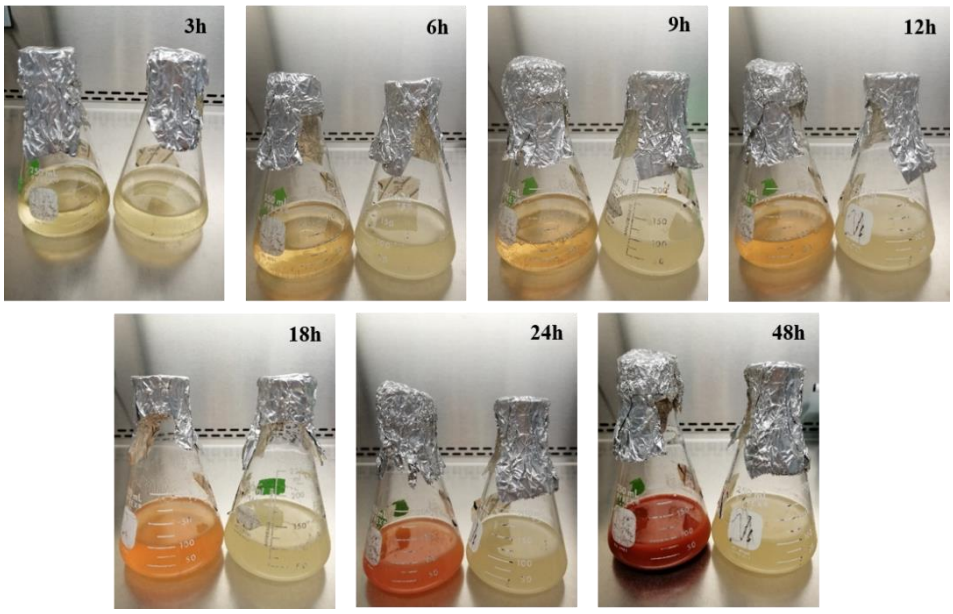

B

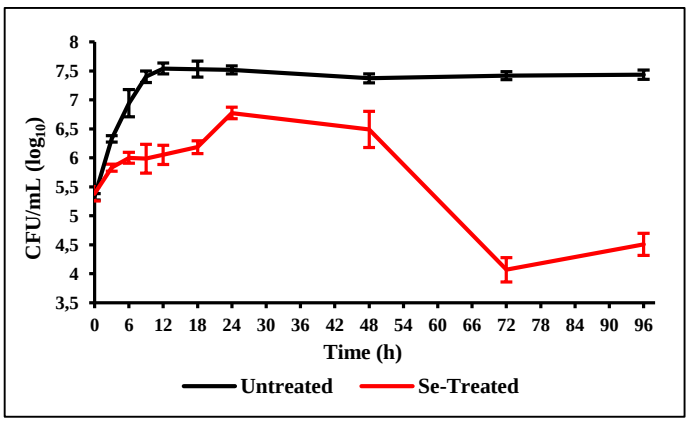

C

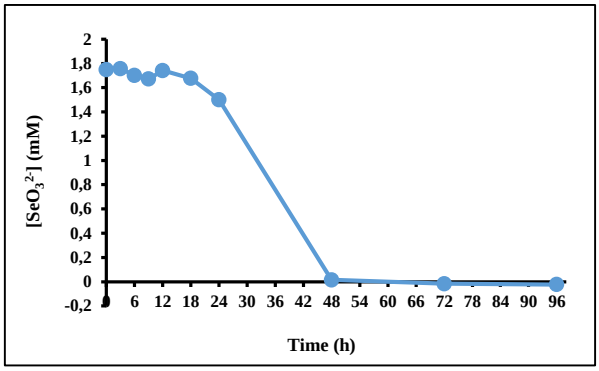

Figure 3.5. (A) Time course of SeITE01 grown in the untreated and Se-treated flasks, (B) the relative growth curves, and (C) SeO_3^{2-} depletion.

From the comparison of the growth curves in presence and absence of the metalloid-oxyanions SeO_3^{2-} it is possible to extrapolate some important deductions. In the case of the untreated culture, the exponential phase started immediately after about 3 h, while the stationary phase is reached after 18 h.

On the contrary, in the case of Na_2SeO_3 exposure the growth dynamics and final cells yield are strictly and negatively affected due to the toxic effect exerted by Se(IV) on cells growth. A lag phase between 6 h and 12 h is observed, and both the exponential and stationary phases are attained lately, around 18 h and 24 h, respectively. Moreover, a death phase arrived after 48 h compared the untreated samples, where there seems to be an extension of the stationary phase up to 96 h. The images of the flasks describe this particular behavior of the cultures. In particular, it is interesting to observe a growth arrest and a slow rate of color change in the Se-treated solutions during the lag phase (6-9-12 h).

SeO_3^{2-} depletion completed between 24 h and 48 h visually accompanied by a clear increase in the color of the flasks (from light orange to deep-bright red). The biotic reduction of this oxyanion is accompanied by the appearance of a bright red color in the medium at later time points, and it is known that this coloring is due to the excitation of the surface exciton vibrations in monoclinic selenium (m-Se) particles [70, 217].

3.4.2 Metabolomics investigation

Metabolomics experiments were designed considering the results obtained from both the growth curves and the SeO_3^{2-} depletion analysis (Figure 3.5).

The time course was constructed in order to study the evolution of cell physiologies corresponding to the different growth phases of bacterial cells: beginning (3 h) and end (12 h) of the lag phase, early (18 h) and late stage (24 h) of the exponential phase and, finally, the stationary phase (48 h).

Although intracellular and extracellular samples were collected and run all together with the LC-MS technique, the discussion of their results will be presented separately. Exception will be made for the heat maps describing all the detected metabolites (raw data), which will be presented together (Figure 3.6). However, it is fundamental to underline that only from the interweaving of the results it will be possible to obtain a global view of the metabolic turnover and a clear description of the bacterial cellular behavior.

Figure 3.6 displays the heat maps generated from the raw data of the intracellular (A) and extracellular (B) compounds identified after the LC-MS run and clustered by metabolite.

Starting from the two different preparations and sample categories it was possible to find and recognize 125 compounds deriving from the bacterial pellets and 124 from the growth spent media.

For a better reading of the maps, the different treatments were grouped separately to have all the untreated samples on the left and those Se-treated on the right, respectively. Furthermore, the different color of the squares represent the concentration level of metabolites, where red indicates the most concentrated and blue, instead, the least concentrated.

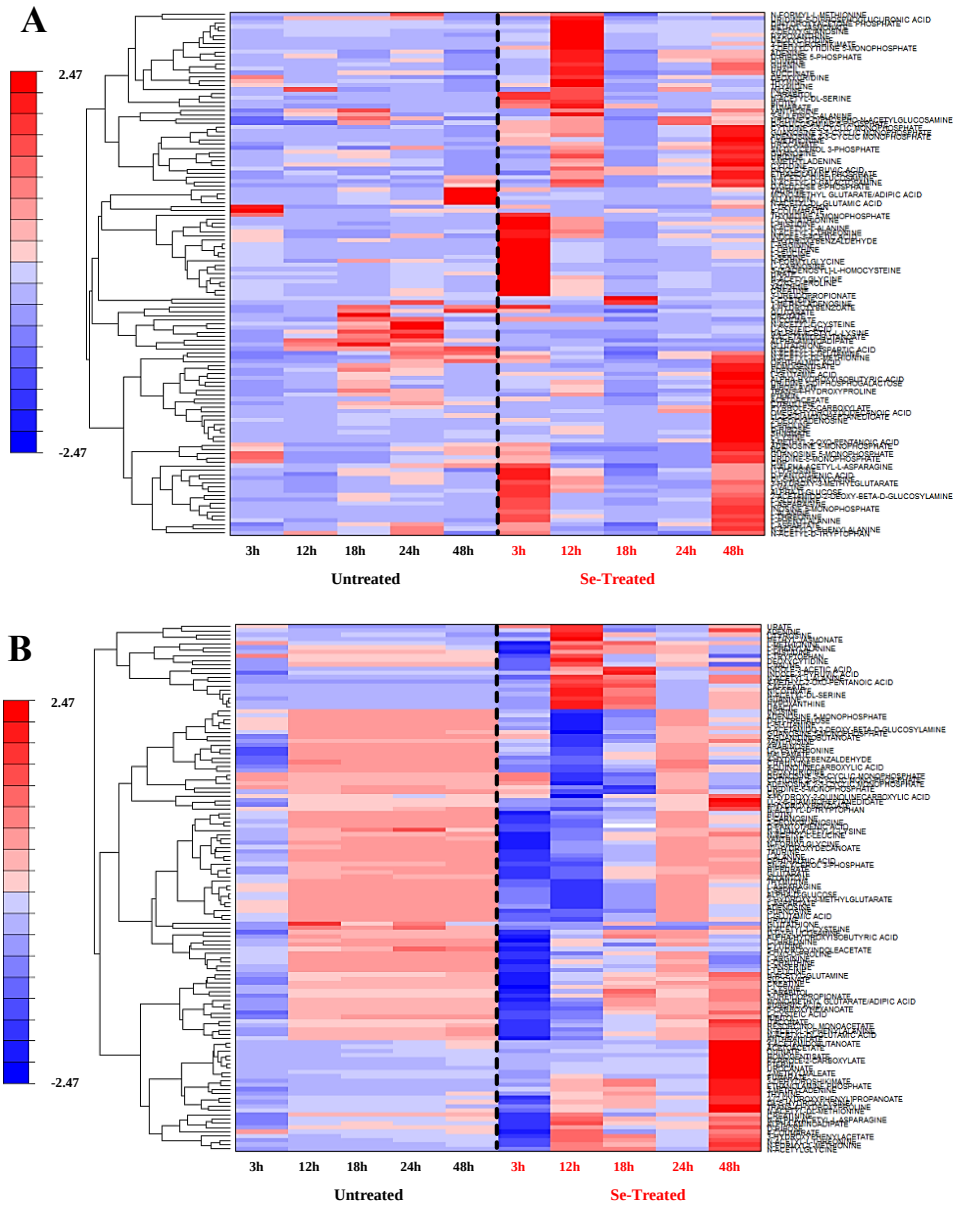

Figure 3.6. SeITE01 clustered heat maps of intracellular (A) and extracellular (B) compounds recognized after the metabolomics run. Rows represent the metabolites, columns the specific time points.

These graphical representations underline the complexity of the data but at the same time may help to understand a possible behavior of the compounds or identify the presence of similar trends or metabolite families. Although a general interpretation should not be attempted at this point due to presence of a large number of metabolites, some hypotheses can be advanced by their observations.

In the case of the untreated samples, only few compounds seem to undergo significant changes during the time course. This trend appears markedly clear in the case of extracellular metabolites, where the majority of them manifest the same response and behavior. Transitions in growth phase are visible in the heat map temporal changes. Instead, metabolites that derive from the intracellular and extracellular bacterial suspensions enriched with SeO_3^{2-} present a remarkable variation during the temporal exposure. This is highlighted the most comparing the extracellular metabolites.

Even if metabolomics is a very powerful tool for understanding and describing a given phenotype, it is known that it presents significant challenges that extend from sample preparation to statistical data analysis and interpretation.

In the case of these datasets, the statistical evaluations were very complex, due to two main reasons. First, all the experiments were performed in rich NB media in which many metabolic pathways are activated. Secondly, the two different variables, representing by the untreated and the Se-treated samples, are accompanied by an important third variable, time. As reported previously, this is a major novelty of this thesis, but its introduction excludes the possibility of using the classic statistical approaches so far applied for metabolomics studies. To recognize significant metabolic variations and changes in SeITE01 metabolism associated with SeO_3^{2-} stress during the time course, the data were analyzed by two robust statistical approaches: the combination of PCA with the Squared Euclidean Distance, and the association of Bayesian Inference with the T^2 statistics.

Intracellular data elaboration

The data processing started with the application of the PCA, a technique used in the context of multivariate statistics that allows simplifying and summarizing the data guaranteeing the minimum loss of information. The new variables obtained with this statistical tool are called principal components (PCs), whose number corresponds with the number of the variables present in the experiment. Besides being unrelated, PCs are ordered with respect to the percentage of variability present in the original data through a linear transformation of the PCs

that project the original variables in a new Cartesian system in which they are ordered in decreasing order of variance. In this way, a PC with a greater variance (PC1) is projected on the first axis, the second one (PC2) on the second axis and so on.

The first attempt at PCA analyses was conducted by preparing a new database deriving from the difference between the Se-treated and untreated datasets. However, in order to reach about 90% of the variance four PCs were needed. Thus, it was decided to analyze the original individual datasets separately, obtaining considerable improvements in the variances of the single PCs, as reported in Tables 3.3 and 3.4.

Table 3.3. SeITE01 intracellular PCs percentage of variances of the untreated metabolites.

PRINCIPAL COMPONENT (PC)	UNTREATED SAMPLES % OF VARIANCE	UNTREATED CUMULATIVE % OF VARIANCE
PC1	83.47	83.47
PC2	7.32	90.79
PC3	4.87	95.66
PC4	2.35	98.01
PC5	1.99	100.00

Table 3.4. SeITE01 intracellular PCs percentage of variances of the Se-treated metabolites.

PRINCIPAL COMPONENT (PC)	Se-TREATED SAMPLES % OF VARIANCE	Se-TREATED CUMULATIVE % OF VARIANCE
PC1	79.99	79.99
PC2	8.45	88.44
PC3	5.31	93.75
PC4	4.15	97.9
PC5	2.1	100.00

The percentage of variances in the case of the untreated compounds were equal to 83.47% for the PC1 and 7.32% for the PC2. Similar values were also obtained in the case of samples treated with Na_2SeO_3, with the PC1 equivalent to 79.99%

and the PC2 to 8.46%. Reaching about 90% and 88% of variance within the PC1 and PC2 of the different treatments, this allowed the compression of all the temporal information on the first two dimensions. The resulting biplots are illustrated in the Figure 3.7, where the untreated metabolites are plotted in the biplot on the left, and the treated in the biplot on the right.

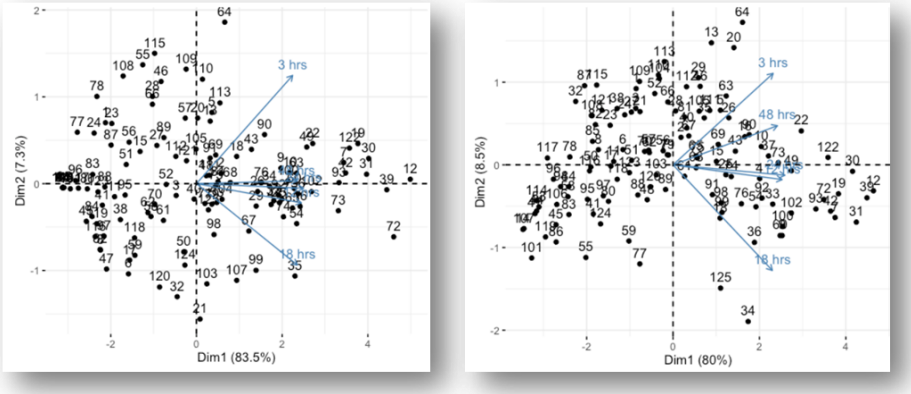

Figure 3.7. SeITE01 intracellular PCA biplots of the untreated (left) and Se-treated (right) metabolites.

Starting from the temporal information of the PCA, the Euclidean distances between the same metabolites of the Se-treated and untreated samples were determined to evaluate a possible modification of the metabolites themselves following the exposure with the toxic oxyanion. If the treatment did not involve any modification of the compounds, they must be in the same position occupied by the corresponding untreated metabolites (or at least in the close proximity considering the presence of the experimental measurement error). Repeating this comparison several times, a normal bivariate distribution of the points with covariance = zero and an average centered on the position of the untreated metabolite should be obtained. Then, calculating the Euclidean distances of all these points from the position occupied by the untreated solutes, it was possible to obtain a new random variable that follows the Rayleigh distribution (Figure 3.8). For this study, it was decided to consider a p-value < 10^{-4} to discriminate the statistically significant metabolites (Table 3.5).

This choice allows maintaining a conservative attitude and avoids the introduction of false positives in the lists of the most relevant metabolites.

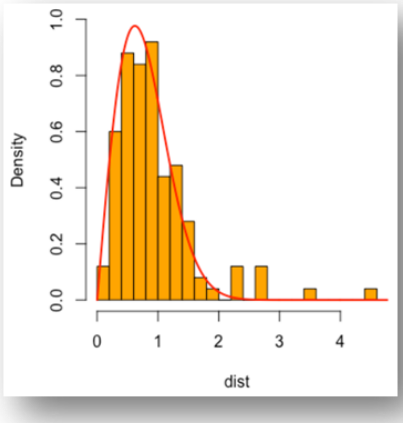

Figure 3.8. Rayleigh fit distribution for SeITE01 intracellular data.

Table 3.5. SeITE01 intracellular metabolites p-values.

METABOLITE	p-value
Glutathione	$1.2x10^{-11}$
N-acetyl-N-cysteine	$5.5x10^{-8}$
4-hydroxybenzoate	$5.7x10^{-5}$
Indole-3-pyruvic acid	$8.3x10^{-5}$
4-coumarate	$1.5x10^{-4}$
Trans-4-hydroxyproline	$7.2x10^{-4}$

Unfortunately, in the case of the combination of Bayesian Inference with the T^2 statistics it was not possible to calculate the relative p-values as it involved the use of a variable "moderation" factor, whose value also involved different p-values. Thus, for this approach it was decided to evaluate the metabolites occupying the first 13 positions (first 10%) of the ranking list obtained after the T^2 statistics, as listed in Table 3.6.

Table 3.6. SeITE01 ordered list of intracellular metabolites identified by Bayesian Inference-T^2 statistics.

BAYESIAN INFERENCE-T^2 STATISTICS: METABOLITE ORDER	
1) Glutathione	8) Adenosine 2', 3'-cyclic monophosphate
2) N-acetyl-L-cysteine	9) L-aspartate
3) L-alanine	10) Pyrrol-2-carboxylate
4) 2-acetamido-2-deoxy-β-D-glucosylamine	11) Homogentisate
5) Trans-4-hydroxyproline	12) L-methionine
6) Indole-3-acetic acid	13) 2''-deoxyguanosine
7) L-proline	

Hence, Scheme 3.8 gives a Venn diagram of the results for both the statistical approaches and the overlap of the individual evaluations applied for the intracellular datasets.

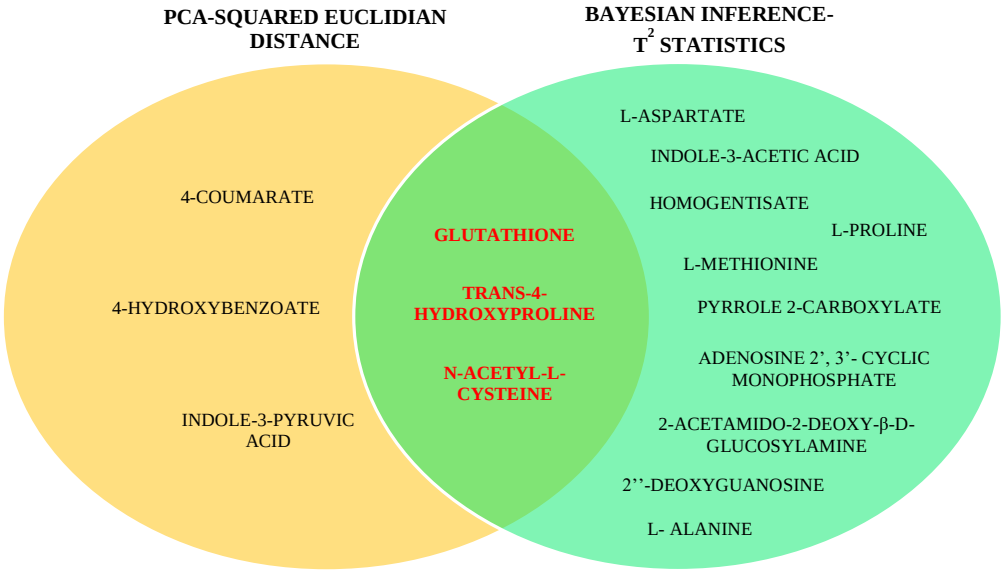

Scheme 3.8. SeITE01 statistical elaboration of intracellular data between the two approaches.

From this dual approach, three common metabolites are highlighted: Glutathione (GSH), Trans-4-hydroxyproline (Hyp), and N-acetyl-L-cysteine (NAC).

The PCA-Squared Euclidean Distance approach identifies the 4-hydroxybenzoate, 4-coumarate and indole-3-pyruvic acid (IPyA), while the Bayesian Inference-T^2 statistics, for example, includes the L-proline (Pro), indole-3-acetic acid (IAA), L-aspartate (Asp), or pyrrole 2-carboxylate.

By reconstructing the heat map considering these most important organic compounds to the statistical difference (Figure 3.9), it is possible to obtain a less complicated situation than that of the raw data, and identify any key temporal trend(s) of the metabolites.

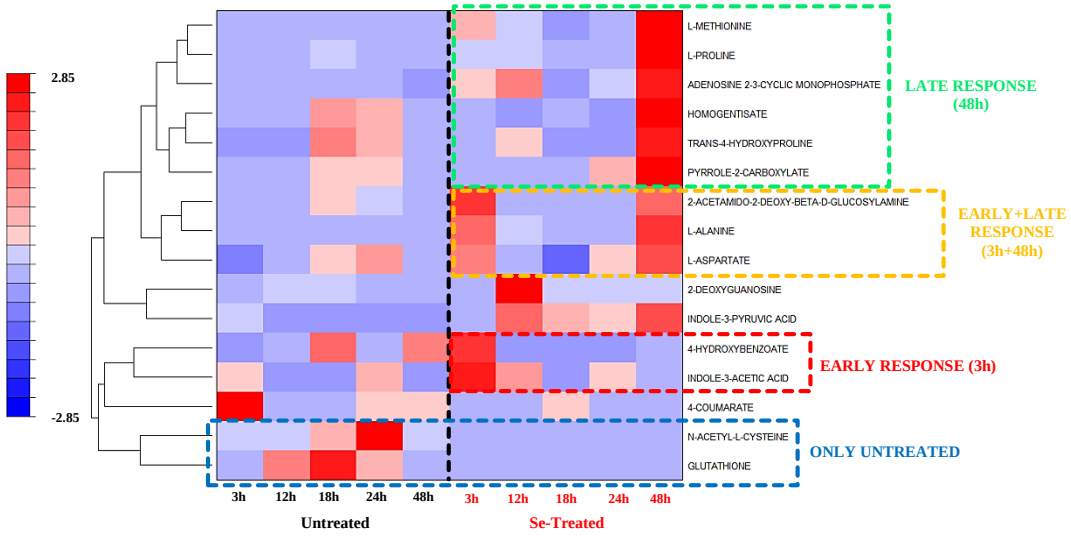

Figure 3.9. SeITE01 clustered heat map of the most relevant intracellular metabolites.

In the case of the Se-treated samples, it is interesting to highlight the presence of three metabolic responses:

- Early response (3 h), surrounded with a red dotted rectangle;
- Late response (48 h), indicated by a green dotted rectangle;
- Combination of an early and a late response (3 h + 48 h), recognized with an orange dotted rectangle.

The presence of different temporal responses is very fascinating. Various hypotheses can be advanced connected to both the different growth phase of the cell, the stage of the biogenic SeNPs synthesis, and the release of these nanostructures in the spent medium. Moreover, the hypothesis of a possible toxicity exerted by Bio-SeNPs on the stationary cells could be advanced. This observation could explain the clear cellular decline experienced by the exposed cells after 48 h of incubation with Na_2SeO_3. However, to prove this supposition further investigations and experiments are necessary.

On the contrary, in the case of the untreated samples it is not possible to identify families of metabolites that show the same temporal trend. However, there are two important metabolites, underlined with a light blue dotted rectangle and belonging to the intersection of common compounds, whose concentrations are absent in the case of the exposed one: GSH and NAC.

These compounds are ubiquitous low-molecular-weight (LMW) thiols, and they have crucial functions in maintaining an intracellular reducing environment and in preventing oxidative stress and cellular damage.

Nevertheless, GSH is mainly ubiquitous in the Eukarya and it is found in most Gram-negative prokaryotes. Instead of GSH, many Gram-positive species produce other structurally different LMW thiols, which metabolic functions are similar to GSH. Bacillithiol (BSH) represents an example of this novel class of biothiols. It is widely distributed among low-G + C Gram-positive bacteria (*Firmicutes*) and sporadically present in more distantly related microorganisms. These comprehend bacilli (e.g., *Bacillus subtilis*, *B. cereus*, *B. anthracis*, *B. pumilis*, *B. megaterium*), some staphylococci (e.g., *Staphylococcus aureus*, *S. saprophyticus*) and streptococci (e.g., *Streptococcus agalactiae*) [69, 70, 218-220].

The emerging and predominant function of BSH as principal thiol redox buffer was discovered in 2009, and since then new hypotheses have been advanced concerning its involvement in metal detoxification and in bacterial redox reactions for the reduction of damaging oxyanions [70, 220].

However, the metabolic detection of GSH but not of the BSH must not be considered as a total lack of this bacillithiol form in the intracellular environment of SeITE01. This could be attributed to the absence of the relative RT and m/z of BSH in the pre-defined list of metabolites used for the compound's identification in Maven software. The recognition of NAC, the acetylated form of the amino acid L-cysteine (Cys), is then closely connected to GSH. This compound is, in fact, the precursor of GSH and BSH [221] and it plays a pivotal role as a potent antioxidant, anti-inflammatory, free radical scavenger, and a store for the bio regeneration of GSH.

The chemical structures of these relevant solutes and the bar plots describing the trend of GSH and NAC in the untreated and Se-treated samples are reported in Figure 3.10, respectively.

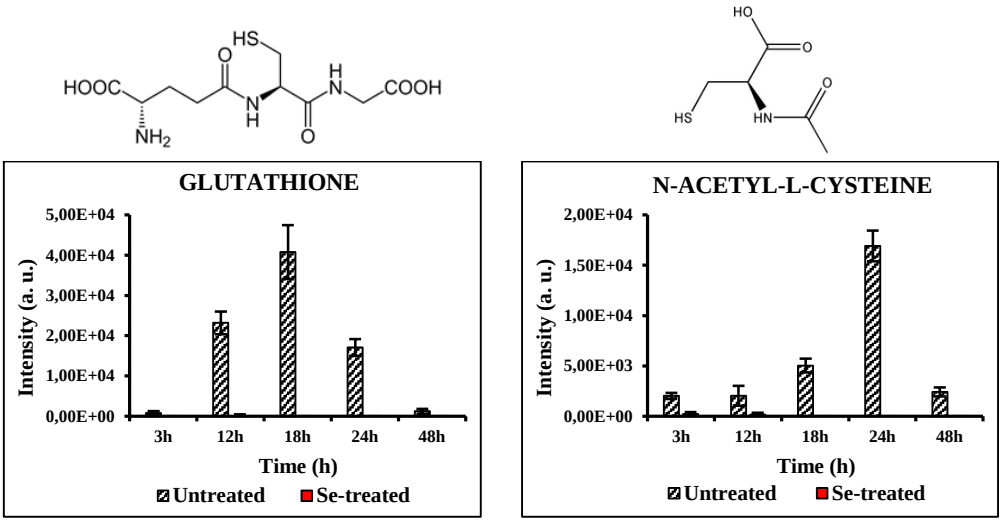

Figure 3.10. Chemical structures and bar plots of intracellular GSH and NAC.

In SeITE01 cultured in NB medium, the intracellular GSH concentration increases during the exponential phase and then decreases rapidly recovering the late stationary phase. On the contrary, the NAC level is maintained at a relatively low level for almost all the growth stage, but then increases when cells reach the stationary phase. This opposite NAC concentration trend compared to that of GSH especially in the last phases of bacterial growth may be linked to the cellular attempt to regenerate the cytosolic pool of GSH.

Moreover, these variations agree with those proposed by Sharma et al. in the study of BSH as principal redox element in cultures of *B. subtilis* [219], and they are further evidence of the active implication of these SH in the physiological homeostasis of SeITE01. Instead, when the cultures are treated with SeO_3^{2-}, a total depletion is observed of both these molecules. Their complete absence emphasizes their primary importance and central involvement during the reduction reactions of the toxic oxyanion likely through a Painter reaction leading to the reduction of SeO_3^{2-} and oxidation of biothiol. They also serve as substrate or a reductive supply for the biochemical reactions, and act as antioxidants by donating electrons to reactive radicals preventing deadly cellular damages, which are increased under SeO_3^{2-} attack.

Together with GSH and NAC, another main metabolite that resides in the intersection originated by the two statistics is Hyp.

Kim and collaborators demonstrated that this organic compound is an important solute accumulated within the cells of *Halobacillus halophilus* in response to osmotic stress under high NaCl conditions. Moreover, they reported that a variety of halophilic and halotolerant microorganisms, including *H. halophilus*, *Acinetobacter baylyi*, and *Bacillus subtilis*, can use different solutes to cope with high salinity, such as glutamate (Glu), glutamine (Gln), glycine betaine, trehalose, mannitol and proline (Pro) [222].

It is interesting to note that the observations exposed by these researchers can be connected to the results obtained with the present metabolomics experiment.

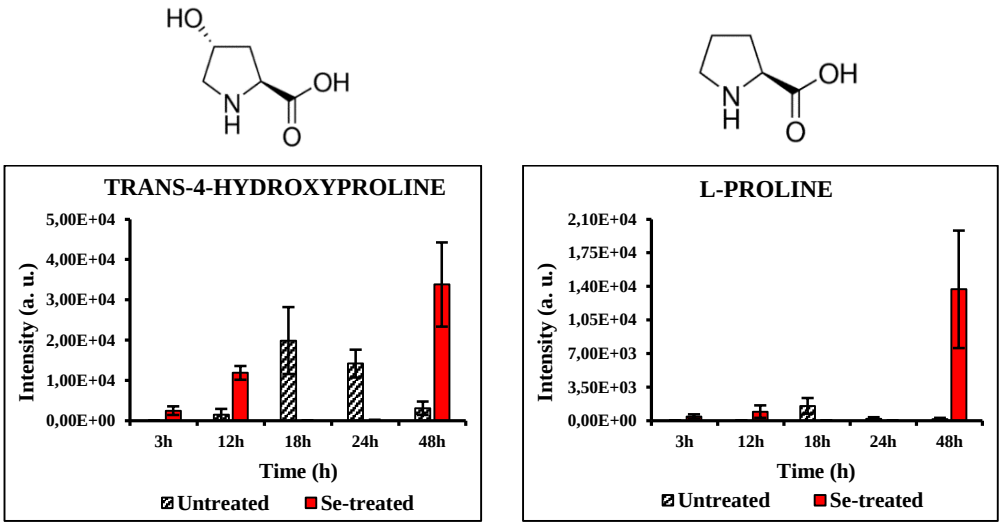

Figure 3.11. Chemical structures and bar plot of intracellular Hyp and Pro.

Figure 3.11 shows the similarity of Hyp and Pro in both their chemical structures and concentration tendencies, although the intensity of Pro is lower than that of Hyp and not clearly visible with this graphical representation.

In the case of the cells grown in absence of Na_2SeO_3, both trends seem to recall that of GSH with an evident increase in concentrations during the exponential phases and a subsequent decrease in the stationary phases. Conversely, it is interesting to observe that the Se-treated cells start immediately to accumulate these solutes concurrently with SeO_3^{2-} uptake and processing, with a significant increase in intensities observed upon reaching the stationary phases. Their intracellular bio-store corresponding to the first phases of acquisition and processing of the oxyanion could actually place these metabolites in the

cytosolic pool involved in the balancing of the cellular osmotic pressure. Besides, the considerable intensity reached at 48 h could have an interesting connection with the release of Bio-SeNPs in the exhausted medium. This intracellular accumulation could result as a further protective action against the toxicity of the nanostructures triggered by the cells leading to a hypothesis that SeNPs production leads to an osmotic pressure response.

The presence of L-aspartate (Asp) (Figure 3.12) in the list of metabolites identified by the Bayesian Inference-T^2 statistics approach can reinforce the present hypothesis.

The amino acid Asp plays multiple and diversified roles within the cell.

Zaprasis and co-workers observed that in *B. subtilis* this solute, together with Glu, functions as a key link between the amino acid biosynthesis and central carbon metabolism. They investigated the physiological processes through which this species can gain osmotic stress protection exploiting the uptake and metabolic conversion of different amino acids. In that project, Asp together with Glu, Gln, and Asn are employed to refill the cellular pool of Glu, the metabolic precursor of Pro production [223].

A study presented by Zhao et al., showed that mutant cells subjected to Asp limitation under nutrient rich conditions exhaust the peptidoglycan precursor meso-2,6-diaminopimelate (mDAP), with the consequence of the inhibition of peptidoglycan synthesis, leading to up-regulation of the cell envelope stress response and cellular lysis [224].

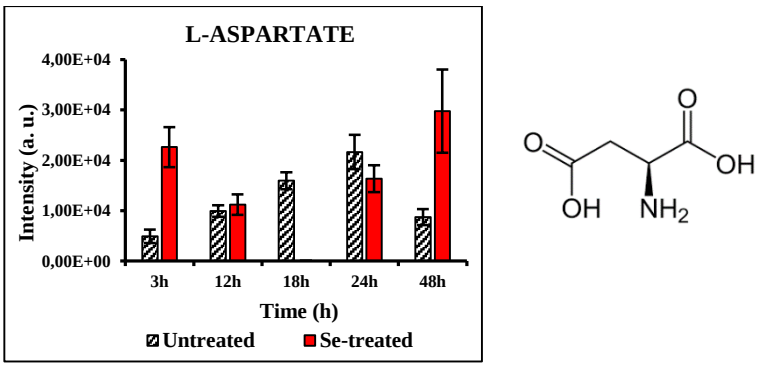

Figure 3.12. Chemical structure and bar plot of Asp.

The analysis of the untreated cultures trend reminds considerably that of the NAC molecule previously described as a storage for GSH biosynthesis and refilling. The Se-treated bacterial suspensions do not present a linear rise in concentration with the time, but rather an increasing synthesis during the first hours of growth and during the cellular decline. As previously anticipated, the increasing level of this metabolite concomitant with SeO_3^{2-} uptake, reduction and Bio-SeNPs release focuses on the fact that it could be involved in the activation of different pathways, for both the regeneration of the Pro pools and the correct morphological development and stability of the cell wall.

A similar function could also be performed by another metabolite, the 4-hydroxybenzoate (4-HB) (Figure 3.13), which is a precursor of ubiquinone (coenzyme Q; Q) when synthesized from the shikimate pathway via chorismate.

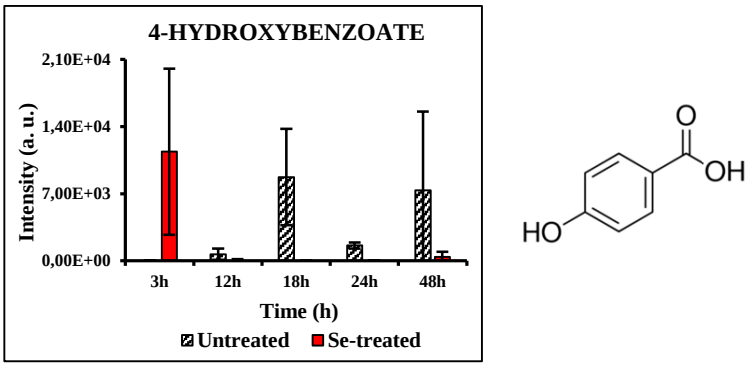

Figure 3.13. Chemical structure and bar plot of 4-HB

Important biological functions are associated with the class of ubiquinones and terpenoides: they are, for example, involved in gene regulation and expression, and they operate as oxygen radical's scavengers and redox mediators during the respiration [225].

In this investigation, the 4-HB could be playing the role of an antioxidant molecule and ROS scavenger. Its immediate accumulation within the Se-treated samples at the earliest stages of cell growth could suggest a role in helping to deal with the oxidative stress exerted by the SeO_3^{2-} for both 4-HB and Q.

Sévin and Sauer in April 2014 have demonstrated that the intracellular accumulation of Q in *E. coli* can also improve osmotic-stress tolerance through the modification of the composition of the internal membranes [226].

Accordingly, SeITE01 cells could cope with the osmotic stress caused by SeO_3^{2-} by adapting its intracellular osmolality with the accumulation of 4-HB in the lipid bilayers. The structural modification of its membranes can increase the hydrophobic thickness, with the resulting enhancement of cell wall's mechanical stability.

The detection of the precursor and not of Q could be explained by the fact that the ddH_2O-MetOH extraction used was not optimal to capture lipid such as Q. Unfortunately, this represents a major limitation of the metabolomics approach that depending on the extraction method and LC-MS technique only subsets of metabolites are detected.

Regardless, based on these considerations, the data here advance the hypothesis that 4-HB, Hyp and Pro molecules in *Bacillus mycoides* SeITE01 also provide protective and balancing actions. The theme of these molecules is osmo protection that suggests a previously unsuspected toxicity mechanism of SeO_3^{2-} and Bio-SeNPs, that of osmotic disruption. In fact, 4-HB could promote an immediate cellular response directly linked to the presence of SeO_3^{2-} in the growth NB medium, and therefore cover a role of "first defense" dealing first with radical scavenging as well as enhancing also the stability of the cytoplasmic membranes. Hyp and Pro, instead, can act as a "second defense line" and activate a late response against the presence of Bio-SeNPs that have accumulated in the medium after 48h of incubation time with Na_2SeO_3, conferring cellular osmo stress resistance in addiction to antioxidant properties. Finally, indole-3-acetic acid (IAA) is a further entity whose presence may improve the defense against impairments caused by adverse conditions and physiological alterations. IAA is a ubiquitous molecule able to actuate genetic and protein changes in both prokaryotic and eukaryotic organisms leading to different stress conditions. This phytohormone with an auxin activity is mainly synthesized from tryptophan (Trp) via indole acetamide (IAM) or indole-3-pyruvic acid (IPyA) pathways, and it is involved in the production of phenylacetic acid (PAA) [227, 228]. IAA belongs to the family of indoles that are often synthesized by both Gram-positive and Gram-negative microorganisms. Biological functions of this class of molecules are multiple, as

reported by Han and co-workers [229]. In *E. coli*, for example, indole is involved in drug resistance, plasmid stability, biofilm formation and virulence control. Moreover, it can regulate phenotypes of other species that cannot produce this molecule, such as increasing drug resistance in *Salmonella enterica* and attenuating virulence in *Pseudomonas aeruginosa*. Despite the growing importance of these molecules, several debates are still open aimed at defining their roles in cell signalling, bacterial physiology and response coordination [230-232].

Although IAA and IPyA have been listed separately, both the statistics underscore the significant relevance of these two metabolites which are enhanced during Se-cell interactions (Figure 3.14).

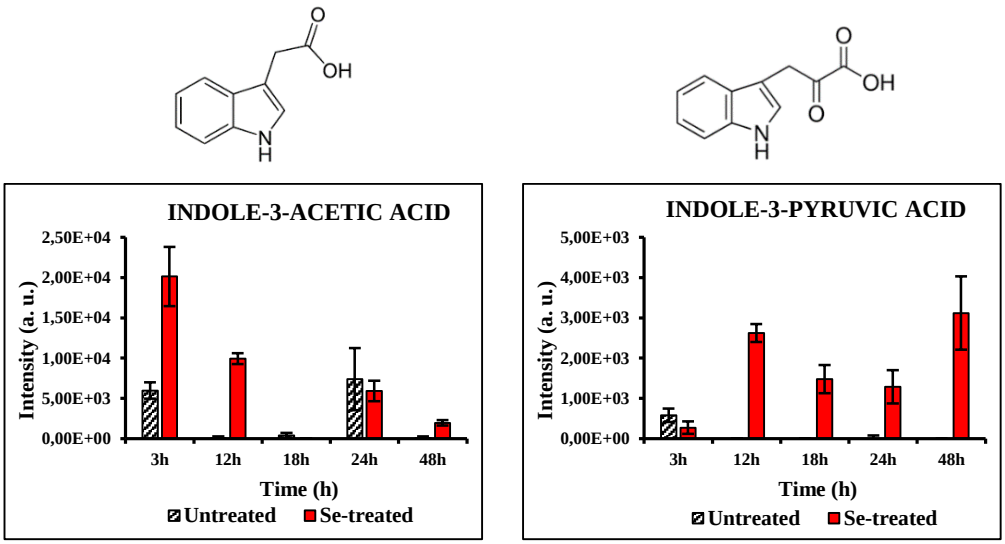

Figure 3.14. Chemical structure and bar plots of IAA and IPyA.

Under optimal growth conditions, the untreated cells do not seem to accumulate large amounts of these compounds. However, during SeO_3^{2-} exposure their intensities increase considerably, albeit with opposite temporal trends. Such behavior has also been observed and described in the previously discussed compounds, and would seem to be typical of the relationship between the synthesized molecule and its precursor. Therefore, in presence of the Se-stress these metabolites may activate different strategies to control the cellular adaptation process. This could result in the intracellular accumulation of protective compounds that screen vital macromolecules from irreversible

damage, or by the activation of intracellular and extracellular signals to regulate the cellular behavior. This is congruent with that observed and proposed by Bianco et al. in the case of *E. coli* cells, where IAA can trigger an increased tolerance to several stress conditions (heat and cold shock, UV-irradiation, osmotic and acid shock and oxidative stress) and different toxic compounds (antibiotics, detergents and dyes) [227]. These properties suggest that IAA and its precursor IPyA can report a level of alert against external adverse conditions and enhance protection by coordinately enhancing different cellular defence systems.

The intracellular metabolites so far presented and characterized seem to be the most statistically significant when cells are grown in presence of Na_2SeO_3 and also the most involved against the harmful effect of SeO_3^{2-} and/or Bio-SeNPs. Scheme 3.9 gives a graphical summary of the biochemical pathways mostly influenced by the presence of the toxic oxyanion.

The KEGG database (www.genome.jp/kegg/mapper.html) was used to annotate all the compounds, whose behavior was modified by the presence of SeO_3^{2-}, to their metabolic pathways, in order to calculate the functional enrichment of metabolic systems providing the SeO_3^{2-} stress fingerprinting for the bacterial strain SeITE01.

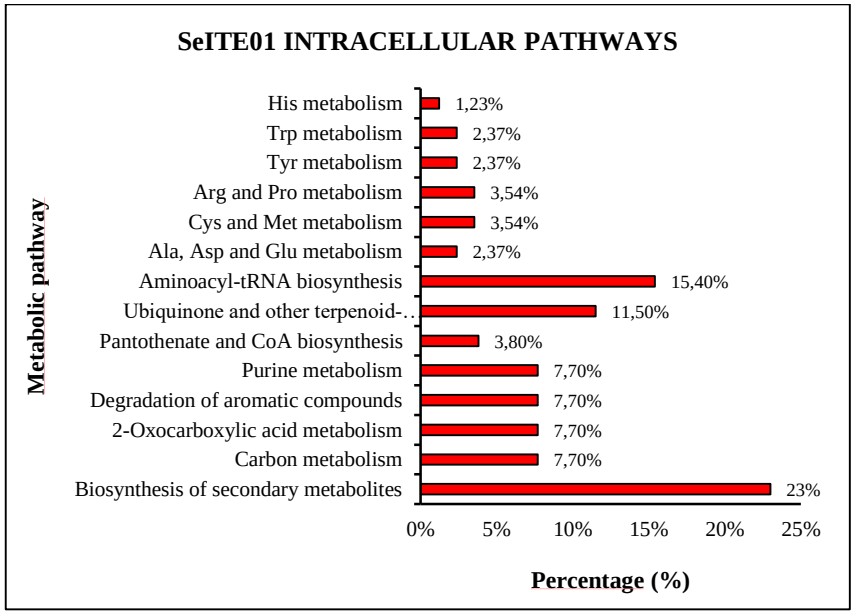

Scheme 3.9. SeITE01 intracellular pathways most influenced by the presence of Na_2SeO_3.

The pathways to which the metabolites mostly flow are represented by the biosynthesis of secondary metabolites (23%), followed by the biosynthesis of amino acids (15.4%), Aminoacyl-tRNA biosynthesis (15.4%), and ubiquinone and other terpenoid-quinone metabolism (11.5%).

Secondary metabolites, as described above, are organic compounds that are not directly involved in the normal growth of the organism, but they often play an important role in stationary phase stasis and defence. The amino acids Cys and Met metabolism (3.54%) and Arg and Pro metabolism (3.54%) are the most active at intracellular level. Aminoacyl-tRNAs, together with the conjugated enzyme synthetases, are fundamental for the correct biosynthesis of the amino acids. Finally, ubiquinones, terpenoids and other structures belonging to this biochemical family can operate as oxygen radicals scavengers and redox mediators during the respiration.

Therefore, the functional enrichments analysis supports the developing hypothesis that the intracellular metabolic and biochemical responses induced by SeO_3^{2-} in *Bacillus mycoides* SeITE01 are mainly aimed at activating osmotic protective processes and counteract the possible formation of oxidizing radicals which, if combined, would lead to cell damage and subsequent death.

Extracellular data elaboration

PCA investigations on extracellular metabolites were conducted using the same settings described above for the intracellular ones. As previously, the temporal information can be compressed to the first two components PC1 and PC2, thanks to the cumulative variance equal to 95% for the untreated samples and the 89% for the Se-treated ones (Tables 3.7 and 3.8).

Table 3.7. SeITE01 extracellular PCs percentage of variances of the untreated samples.

PRINCIPAL COMPONENT (PC)	UNTREATED SAMPLES % OF VARIANCE	UNTREATED CUMULATIVE % OF VARIANCE
PC1	80.31	80.31
PC2	15.09	95.4
PC3	3.58	98.98
PC4	0.85	99.83
PC5	0.17	100.00

Table 3.8. SeITE01 extracellular PCs percentage of variances of the Se-treated samples.

PRINCIPAL COMPONENT (PC)	Se-TREATED SAMPLES % OF VARIANCE	Se-TREATED CUMULATIVE % OF VARIANCE
PC1	72.09	72.09
PC2	16.69	88.78
PC3	6.48	95.26
PC4	3.76	99.02
PC5	0.98	100.00

The resulting biplots are reported in the Figure 3.15, where the untreated samples are plotted on the left and the Se-treated on the right.

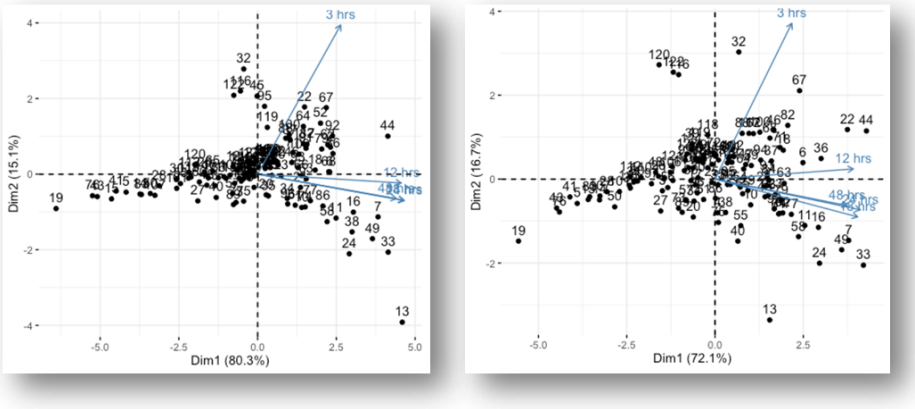

Figure 3.15. SeITE01 extracellular PCA biplots of the untreated (left) and Se-treated (right) metabolites.

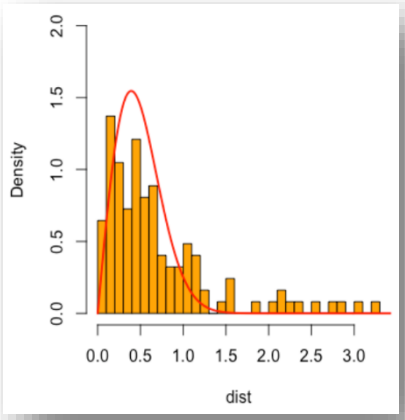

Figure 3.16. Rayleigh fit distribution for SeITE01 extracellular data.

The calculation of Euclidean distances once again confirmed a Rayleigh type distribution of the data (Figure 3.16) and allowed the calculation of the relative p-values ($<10^{-4}$), as listed in Table 3.9 for the statistically relevant metabolites.

Tables 3.9. SeITE01 extracellular metabolites p-values.

METABOLITE	p-value	METABOLITE	p-value
L-histidine	$5.5x10^{-16}$	Adipic acid	$3.46x10^{-7}$
Succinate	$2.99x10^{-14}$	N-α-acetyl-L-Lysine	$6.2x10^{-7}$
L-methionine	$2.47x10^{-12}$	N-acetyl-DL-methionine	$1.3x10^{-5}$
4-acetamidobutanoate	$9.3x10^{-12}$	Anthranilate	$4.4x10^{-4}$
Adenosine 2', 3'-cyclic monophosphate	$1.4x10^{-9}$	N-acetyl-L-phenylalanine	$4.99x10^{-4}$
4-methyl-2-oxopentanoic acid	$2.03x10^{-8}$	Indole-3-pyruvic acid	$5.5x10^{-4}$
L-phenylalanine	$8.3x10^{-8}$	L-tryptophan	$8.8x10^{-4}$
3-hydroxyphenylacetate	$2.8x10^{-7}$		

The metabolites occupying the top 10% positions of the ranking list provided by Bayesian Inference - T^2 statistics (13 metabolites) are reported in Table 3.10.

Table 3.10. SeITE01 ordered list of extracellular metabolites identified by Bayesian Inference-T^2 statistics.

BAYESIAN INFERENCE-T^2 STATISTICS: METABOLITE ORDER	
1) L-histidine	8) N-acetyl-L-phenylalanine
2) 4-methyl-2-oxo-pentanoic acid	9) Indole-3-pyruvic acid
3) 4-acetamidobutanoate	10) L-methionine
4) N-α-acetyl-L-lysine	11) L-phenylalanine
5) Adenine	12) Trans-4-hydroxyproline
6) Fumarate	13) Adenosine 2', 3'-cyclic monophosphate
7) α-hydroxyisobutyric acid	

Scheme 3.10 illustrates the summary representation of the results obtained with the two statistic tools.

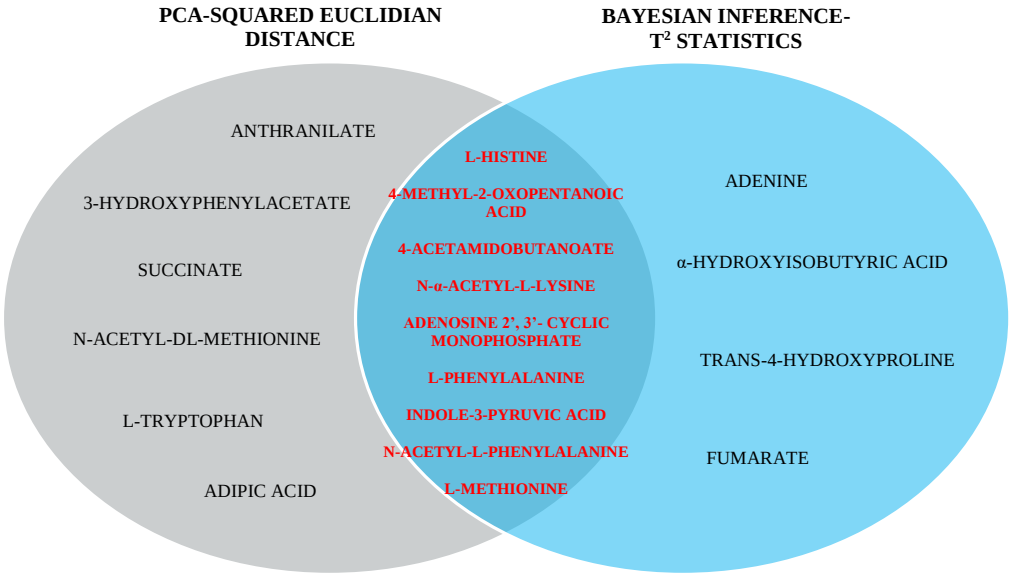

Scheme 3.10. SeITE01 statistical elaboration of extracellular data between the two approaches.

For the secreted metabolites, there are far common compounds present in the intersection of the Venn diagram, including L-methionine, N-acetyl-L-phenylalanine, 4-acetamidobutanoate and indole-3-pyruvic acid.

As before, a preliminary inspection of the data can be obtained from the remodeling of the heat map built with the 19 metabolites showing significant changes (Figure 3.17).

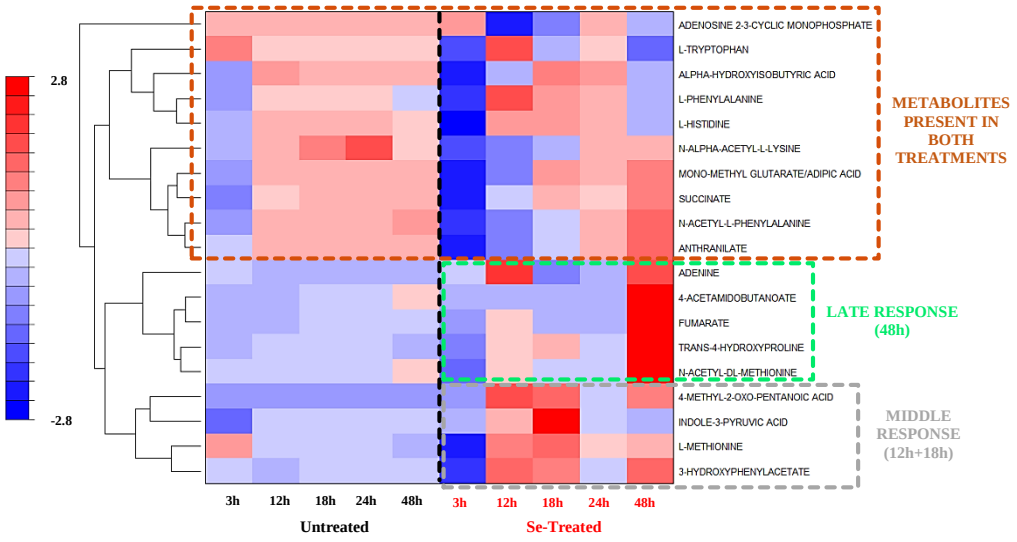

Figure 3.17. SeITE01 clustered heat map of the most relevant extracellular metabolites.

From this heat map's clustering, the list of metabolites may be divided into two distinct groups. The first belongs to the lower part of the map, in which the metabolites are totally "turned off" and consumed/absent in the spent NB; the second, instead, involves the metabolites found in the upper position of the heat map (brown dotted rectangle), where they are totally "turned on" and secreted in the medium for almost all the time course. This particular trend is perfectly in line with the growth curve shown in Figure 3.5B. Once the end of the exponential phase is reached at around 12 h and the stationary phase has begun at 18 h until 48 h, the cells seem to experience the same metabolic trend with no Se-exposure. The metabolites listed in the same brown rectangle but referring to the Se-Treated ones, on the other hand, show a more dynamic attitude that reflects the different cellular phases experienced by the cells exposed to Na_2SeO_3. However, a common behavior between the untreated and the Se-treated metabolites is observed at 24 h, when the stationary phase is reached also by the Se-treated cells.

Although the extracellular trend is not so defined as it was in the case of the intracellular samples, one can observe two main responses:

- Middle response (12 h + 18 h), indicated with a grey dotted rectangle;
- Late response (48 h), underlined by a light green dotted rectangle.

Before starting the discussion of the data, a clarification on the method adopted for their possible interpretation must be noted. When examining the extracellular metabolites, it must be kept in mind that they are the result of extrusion processes carried out by cells due to different physiological responses and activities. This may be caused by the total consumption of carbon or nitrogen sources, by the production of waste/noxious metabolites, or by the fact that some pathways may be switched off/on from the presence/absence of other products. This situation, in comparison with the intracellular counterpart, reflects a greater complexity and added difficulty in assigning a correct relationship between the metabolites and SeO_3^{2-} or Bio-SeNPs. For this reason, the main purposes of the following discussion will be the presentation of metabolites, the roles fulfilled in the cells, and the identification of possible

connections with other metabolites or interconnections between multiple metabolic pathways.

The metabolite of most significance is L-histidine (His), an essential amino acid synthesized *de novo* in microorganisms. This organic compound performs multiple functions within the cell: can be converted to intermediates of the tricarboxylic acid (TCA) cycle; along with other amino acids such as Pro and Arg, it can take part in deamination processes; and it can directly influence Trp biosynthesis by stimulating anthranilate synthetase activity. Overall, its complete catabolism can supply with carbon and nitrogen source additional biosynthetic pathways.

Together with His a few other metabolites are present in the list identified with high statistical significance. This includes Tryptophan, anthranilate, a precursor of Trp in the shikimate pathway via chorismate, and IPyA, also an intermediate in the biosynthesis of IAA from Trp, and already encountered during the treatment of intracellular metabolites (Figure 3.18).

A relationship between His and Trp biosynthesis has been observed in a number of different organisms, and has been also studied in *B. subtilis* [233]. In that research, the authors described the intriguing His-Trp relation as an example of "metabolic interlock" between the pathways of the two amino acids. This phenomenon of contemporary regulatory interaction derived from the presence of common reaction intermediate (PP-ribose-P) and the striking similarity of some enzymes in both the His and Trp pathway. This is consistent with the speculation that at some point in the evolution, the enzymes of the two pathways may have had a common genetic origin. Moreover, it was found that the His markers within the aromatic cluster on the *B. subtilis* chromosome are adjacent to the Trp loci, and this observation could reinforce the close link between the two molecules.

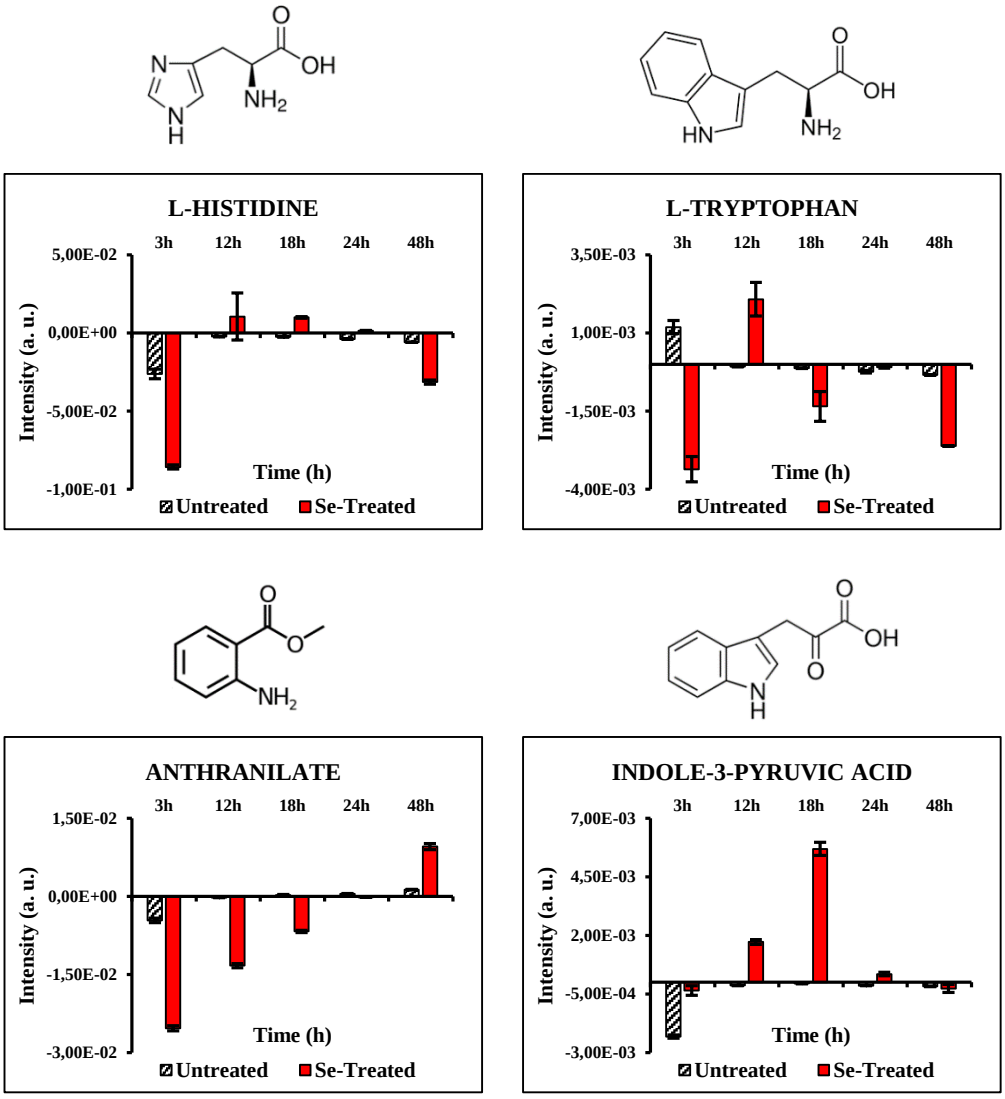

Figure 3.18. Chemical structures and bar plots of His, Trp, anthranilate and IPyA.

In the case of the biochemical compounds involved in Trp pathway, the simultaneous presence in the NB medium is observed of both anthranilate and IPyA. As previously mentioned, they occupy two antithetical positions, as the first acts as a precursor for the synthesis of the amino acid, while the second is the result of Trp catabolism. However, their presence could be related to the adaptation of the bacterium to the surrounding environment thanks to the regulation of the pathway's activity in order to respond to different conditions or a need for certain molecules or substrates. Besides, a possible connection could also be made with the complex nature of the medium chosen for the experiments. Although the analysis was carried out on "cleaned up" and

subtracted data, the rich composition of NB could influence the simultaneous presence of different solutes belonging to the same metabolic pathway, and their use and processing during the bacterial growth could explain their presence in the exhausted culture broth.

The previous explanations could be adopted to explain also the concomitant presence of amino acids with their acetylated forms. In SeITE01, this happens for both methionine (Met) and phenylalanine (Phe), as reported in Figure 3.19. The first plays a critical role in the metabolism and health of many species, as it acts as the substrate for the bio-production of other amino acids (e.g., Cys and taurine), or important antioxidant molecules (e.g., GSH). In microorganisms, its biosynthesis belongs to the aspartate family, along with threonine (Thr) and lysine (Lys) (via diaminopimelate).

The second, instead, is an essential α-amino acid and it can be biologically converted into L-tyrosine (Tyr).

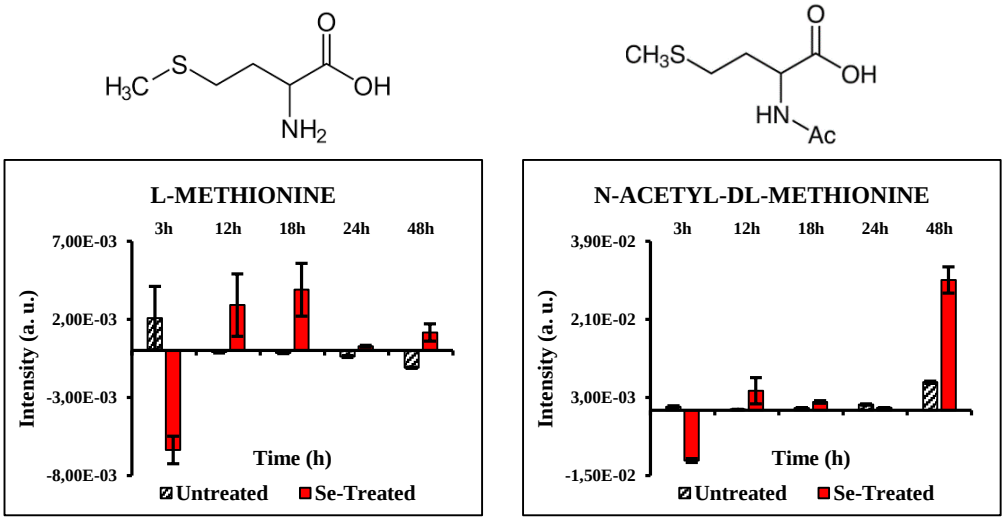

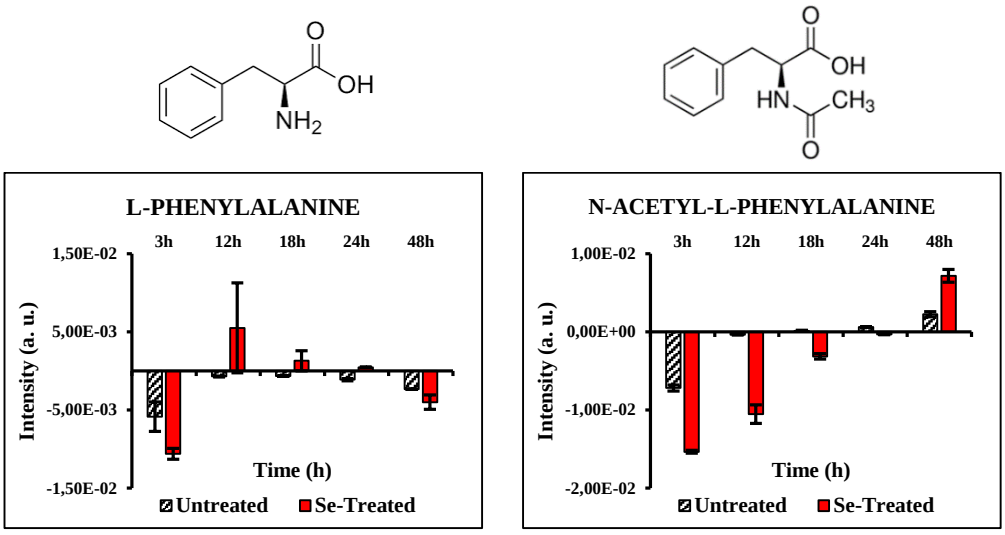

Figure 3.19. Chemical structures and bar plots of Met, N-acetyl-DL-methionine, Phe, and N-acetyl-L-phenylalanine.

In literature, it is difficult to find articles aimed at understanding and explaining acetylation of amino acids. Great attention has always been given to the study of protein acetylation, as this covalent modification has important implications not only in numerous DNA regulation processes, such as gene expression, replication, repair and recombination, but can affect protein enzymatic activities and DNA transactions, and modulate diverse biological processes, including RNA metabolism, chemotaxis, and cell shape [234]. Moreover, acetylation occurs on proteins involved in many central metabolic processes (e.g., synthesis of acetyl-CoA, glycolysis, gluconeogenesis, the TCA cycle, amino acid biosynthesis, and fatty acid metabolism), and it might regulate metabolic flux, directing carbon destinations according to cellular needs. Finally, protein N-acetylation farther adds complexity to the essential twenty encoded amino acids and extends the range of distinct protein isoforms and the number of possible molecular structures [235].

The detection and identification of these metabolites is however, an important information and a starting point for future studies, as it suggests their involvement in cellular metabolism, especially when the bacteria are exposed to SeO_3^{2-} stress. It could be hypothesized that the presence of these free

acetylated amino acids may be the product of breakdown of acetylated residues in proteins or the intermediates forms in the synthesis of other amino acids.
The extracellular detection of 2', 3'-cyclic adenosine monophosphate (2', 3'-cAMP), a positional isomer of the second messenger 3', 5'-cAMP, is very intriguing and can provide various reflections (Figure 3.20).

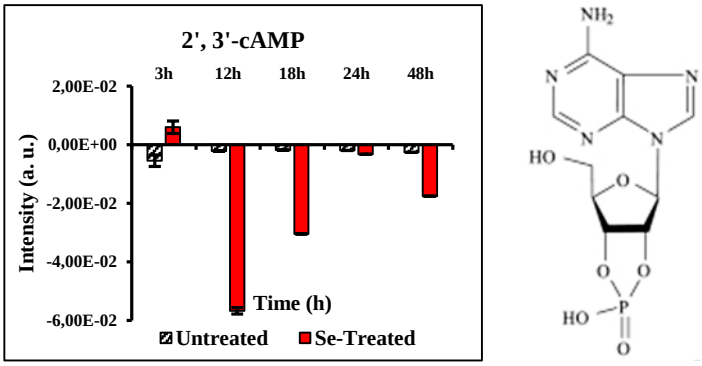

Figure 3.20. Chemical structure and bar plot of 2', 3'-cAMP.

Several studies conducted on animal samples since 2009 [236, 237] have demonstrated that 2', 3'-cAMP can own an extracellular physiological role as a protective molecule against cellular apoptosis and necrosis. This action takes place by removing its intracellular accumulation and by converting it into 2'-AMP and 3'-AMP and hence to adenosine (A). In this regard, it is likely that some 2', 3'-cAMP can be metabolized in the intracellular counterpart for the production of 2-AMP and 3-AMP, before efflux can occur. At this point, the uses of these two molecules may be different: they can be transported extracellularly and metabolized to adenosine, or they can be immediately converted intracellularly to adenosine and used for different biochemical processes. Although this information mainly derives from experiments carried out on eukaryotic cells, the detection of this metabolite in SeITE01 could open the way to new target experiments in order to confirm also in the prokaryotic cells the presence of similar pathways. Therefore, the presence of 2', 3'-cAMP in the Se-treated medium could be associated once again with a protective action against the toxicity of the oxyanion SeO_3^{2-}, urging the cells to trigger further biochemical processes for the supply of energy or bases for the genetic material.

Finally, another metabolite identified by the statistics and related to 2', 3'-cAMP is adenine (Ade) (Figure 3.21). This molecule is one of the two-purine nucleobases used in forming nucleotides of the nucleic acids. In DNA, in fact, this molecule binds to thymine (T), while in RNA, which is used for protein synthesis, it binds to uracil (U).

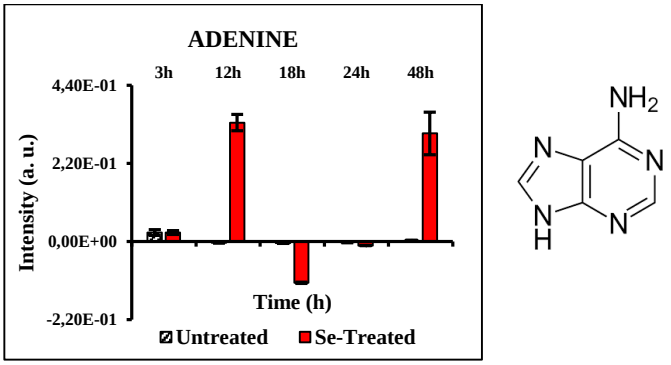

Figure 3.21. Chemical structure and bar plot of Ade.

When attached to ribose this molecule can form adenosine (A), whose cellular role has already been mentioned during the discussion of the 2', 3'-cAMP.

Adenine, therefore, could act as a nitrogen and carbon source and in chemical energy supply, but could also be the end product of RNA, 2', 3'-cAMP, or AMP degradation.

On the other hand, a correct and full interpretation based on these results is very difficult, although a first and interesting description of the metabolic foot printing of this strain has been drawn.

As in the case of intracellular metabolites, even with the extracellular ones it is possible to define the main metabolic pathways activated after the Na_2SeO_3 exposition, as shown in Scheme 3.11.

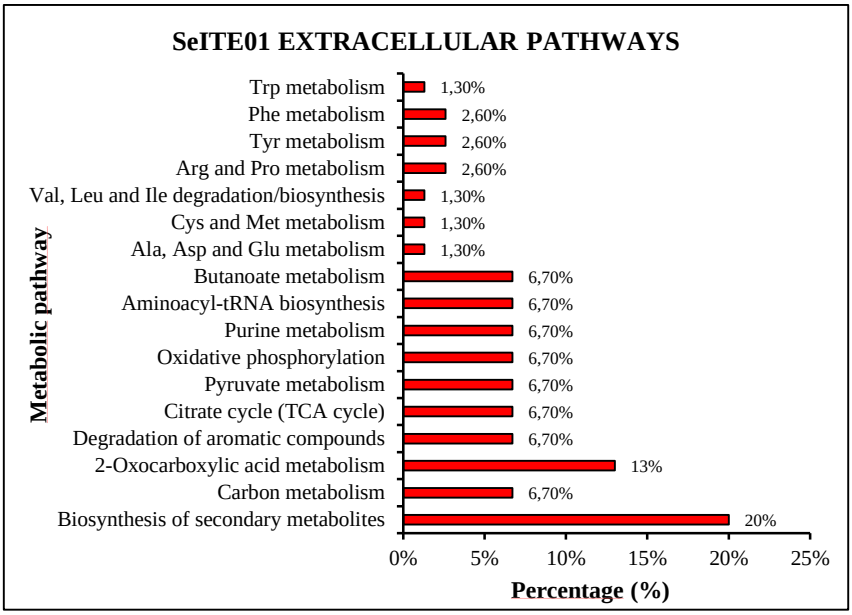

Scheme 3.11. SeITE01 extracellular metabolic pathways most influenced by the presence of Na_2SeO_3.

Biosynthesis of secondary metabolites (20%) and amino acids (13%) represent as with intracellular metabolites the most active responses. However, unlike the previous case, the compounds connected to the ubiquinone and other terpenoid-quinone biosynthesis completely disappear, while another biochemical pathway seems to be activated, the 2-Oxocarboxylic acid metabolism (13%). They represent a group of chemically closely related compounds, and their biochemical transformation and involvement into the Krebs cycle and the glycolysis gives them a relevant role in the cellular metabolism.

Also in the case of the metabolic foot printing there is the mobilization of several biochemical paths destined to the activation of protective processes.

In this case, common pathways destined to supply carbon, nitrogen and energy, necessary for cell turnover and to cope with the presence of stress factors seem to participate.

3.4.3 TEM imaging

In the present thesis the temporal and physiological evolution of the bacterial cells of SeITE01 have been investigated by TEM microscopy. The images of both treatments according to the previously established time course were acquired using the Hitachi H-7650 microscope (120 kV), and are illustrated in Figures 3.22 and 3.24.

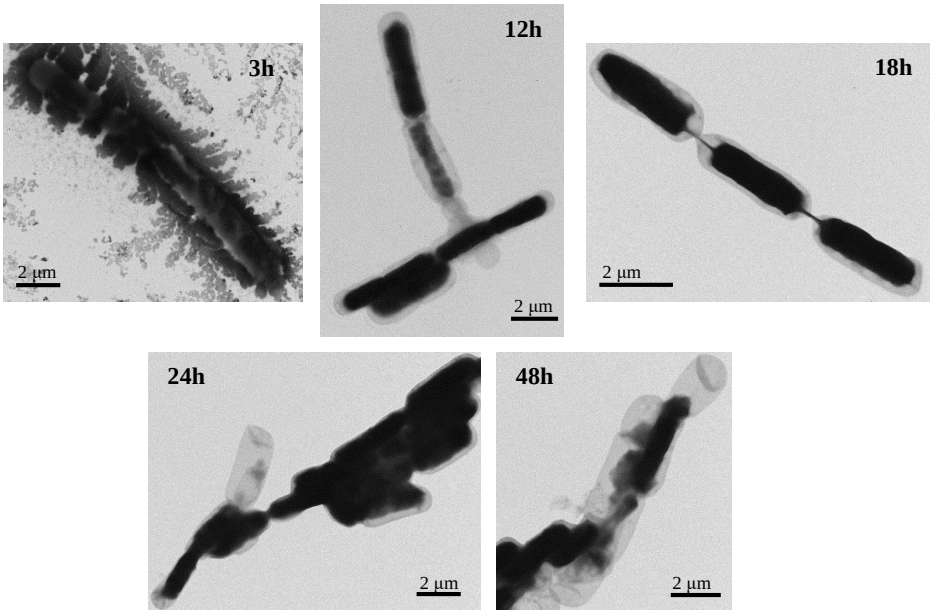

Figure 3.22. TEM time course of SeITE01 untreated cells.

During the time course of SeITE01 untreated cells, a normal cellular development can be observed. The cells already after 3 h of growth exhibit a rod-shaped morphology, typical of this species, although the image collected at this time is not well defined. A possible explanation could derive from the steps necessary for the preparation of this sample, which at 3 h has just started the exponential phase. The centrifugation, the dilution to reach the optimal number of cells to be observed under the microscope ($4x10^4$ cells), and the air drying of the grid for 24 h could have damaged or stressed the cells with the consequent release of organic material that is secreted by the cells and seems to surround them. The images collected at 12 h and 18 h of growth in NB rich medium, whose times represent the end of the exponential phase and the beginning of the stationary phase, describe the cells during their cellular and reproductive

activity (12 h) and as individual entities (18 h). In these images, as in the following ones, it is possible to distinguish the electron-dense cells from further non electron-dense structures thanks to the density they obtain. A dark grey-black color is associated with the cells, while the grey-whitish color is correlated with other structures such as the cell walls or bacterial ghosts. These ghosts already appear at 12 h following the rapid cell turnover (Figure 3.23 A, black arrows), but then increase in number at both 24 h and 48 h as a sign of the cellular decline and arrest of bacterial growth (red arrows), as showed in Figure 3.23 B.

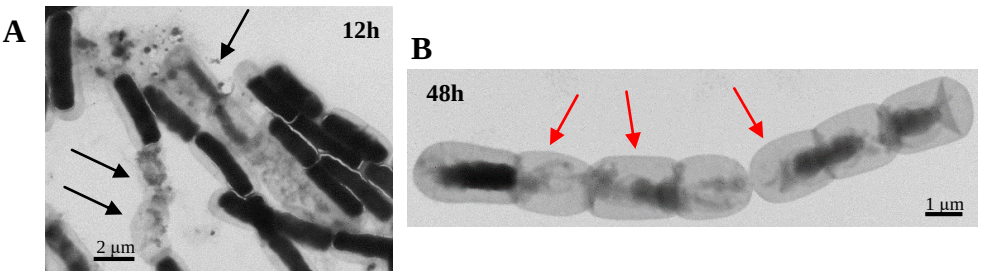

Figure 3.23. SeITE01 bacterial ghosts of untreated cells after 12 h (A) and 48 h (B).

After 24 h and 48 h, the cells begin to lose the integrity of their cell wall structures with the final consequent formation of numerous cellular aggregates. The time course of SeITE01 Se-treated cells grown in presence of Na_2SeO_3 is, instead, described in Figure 3.24.

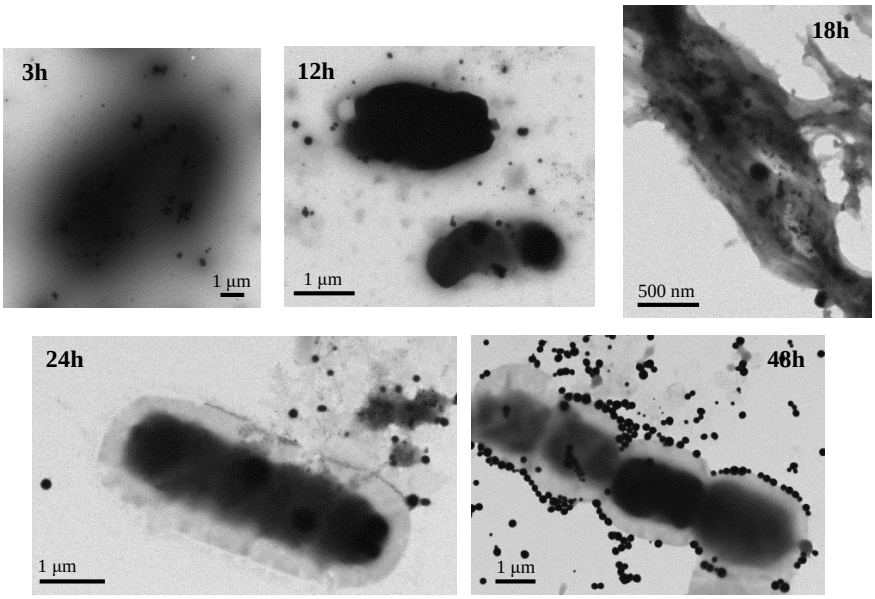

Figure 3.24. TEM time course of SeITE01 Se-treated cells with Na_2SeO_3.

The addition of Na_2SeO_3 to the bacterial media causes a significant malformation of SeITE01 cells especially in the early stages of their growth (3 h and 12 h). In the 3 h and 12 h images, it is possible to observe how the toxic effect and the stress exerted by SeO_3^{2-} on the cells lead to their slowing down and inability to correctly develop their rod-shape morphology. In fact, the interpretation of the metabolites showed a possible osmotic action exerted by SeO_3^{2-} on the cells and in particular on the cellular membranes. Furthermore, the activation of significant protection mechanisms against the ROS formation could lead to think of a toxic action of these molecules on lipid fluidity.

Both electron and non-electron dense materials are also present near to the cells, especially in the image describing the 12 h (end of the lag phase). However, it is not possible with only this image to say precisely whether they are Se nanoparticles, bacterial cells, spores or organic material produce by the bacteria. On the other hand, these structures are not visible in the untreated sample collected at the same time point, thus their appearance must be connected to the action and presence of the oxyanion.

In the images related to the cells after 24 h and 48 h of exposure, it is possible to observe a certain morphological similarity with the untreated cultures, even if in the latter there are no electron-dense black or dark grey spots, which correspond to the biogenic SeNPs deriving from the bacterial Se(IV) reductive process.

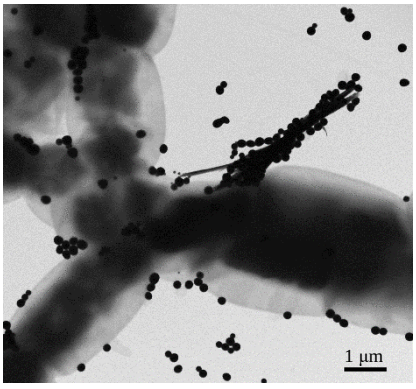

Figure 3.25. Aggregation of SeNPs and formation of SeNRs after 48 h of incubation.

Finally, with the achievement of the 48 h, the number of secreted Se nanostructures in the growth medium seems to increase considerably, and a modification of their morphology from spherical (Bio-SeNPs) to 1-dimension growth of rods (Bio-SeNRs) through a potential aggregation processes seems to occur, as shown in Figure 3.25.

PART II: *Stenotrophomonas maltophilia* SeITE02

3.4.4 Bacterial growth and biotic SeO_3^{2-} removal efficiency

The physiological and behavioral study on *Stenotrophomonas maltophilia* SeITE02 followed the same experimental approach adopted for *Bacillus mycoides* SeITE01.

Figure 3.26 A, B, C describes SeITE02 cell replication in flasks untreated and Se-treated with 0.5 mM Na_2SeO_3, the relative growth curves and the bio-conversion of Se(IV) into Se^0.

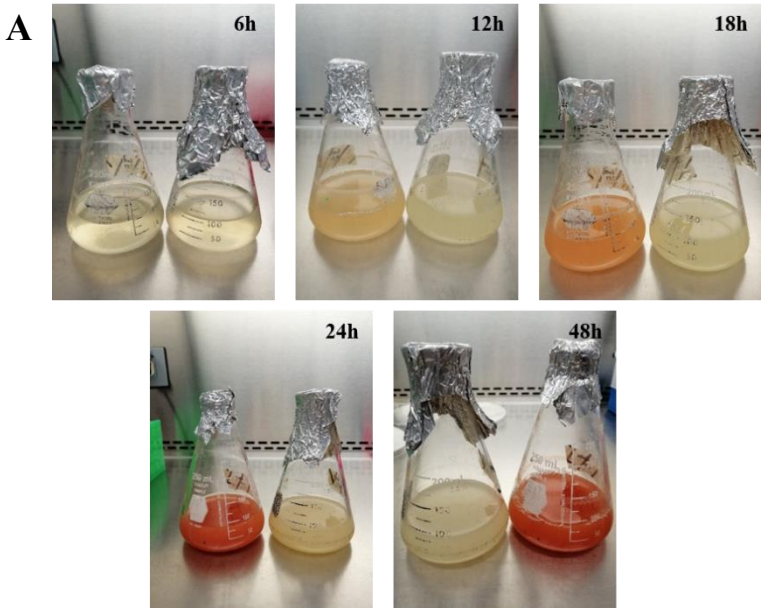

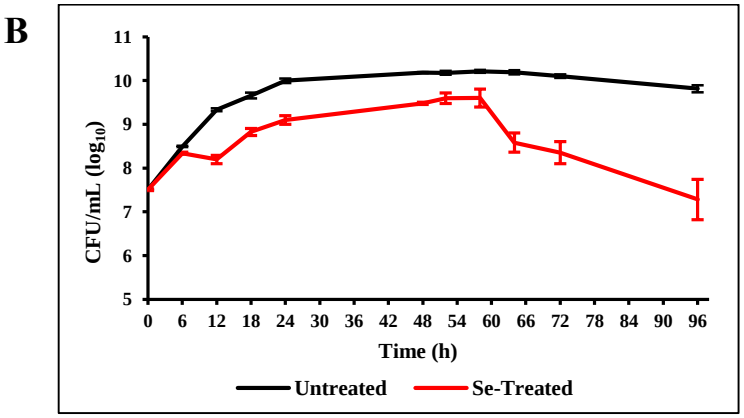

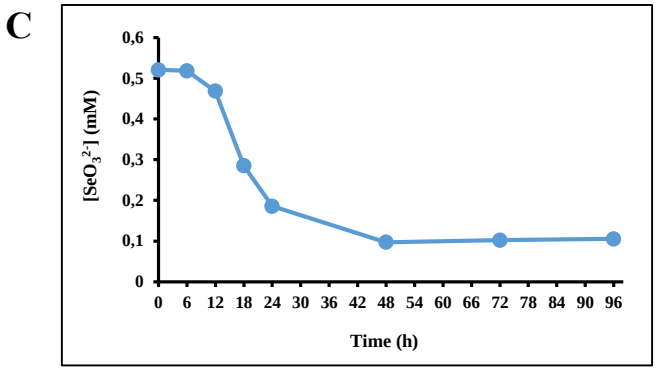

Figure 3.26. (A) Time course of SeITE02 grown in the untreated and Se-treated flasks, (B) the relative growth curves, and (C) SeO_3^{2-} depletion.

As in the case of SeITE01, also SeITE02 cell replication is negatively affected by the addition of SeO_3^{2-} in the growth media. However, the final cells yield seems to be less affected by the presence of the oxyanion compared with the Gram-positive bacterium (1 unit Log lower against ~ 2 unit Log).

With 0.5 mM Se(IV) in the culture media, a marked stalling of bacterial cell replication was registered between 6 h and 12 h. Afterwards, a partial recovery took place, with microbial growth reaching the trend similar to those observed in the untreated cells. Nevertheless, after 58 h of incubation, the culture dies off at a fairly constant rate.

Previous studies conducted in our laboratory in Verona had highlighted this similar trend, using and testing different concentrations of Na_2SeO_3 [80, 101, 102]. Besides, the curve related to SeO_3^{2-} depletion seems to confirm the data previously collected [80, 101, 102], as in the present study it is almost totally removed from the media within 48 hours of bacterial growth, as shown in Figure 3.26 C.

3.4.5 Metabolomics investigation

Metabolomics experiments were designed following the same settings adopted previously. For this bacterial strain, the time course was constructed considering the following growth phases: beginning (6 h) and end (12 h) of the lag phase, the achievement of the exponential phase (24 h) and, at the end, the attainment of the stationary phase (48 h).

In addition, the interpretation and discussion of the individual compounds will follow the same approach selected for SeITE01, introducing first the metabolites identified in the intracellular samples and then those highlighted in the extracellular ones. The only exception is reserved for the representation of the raw data shown in Figure 3.27, where both the heat maps generated from the intracellular (A) and extracellular (B) metabolites are illustrated together.

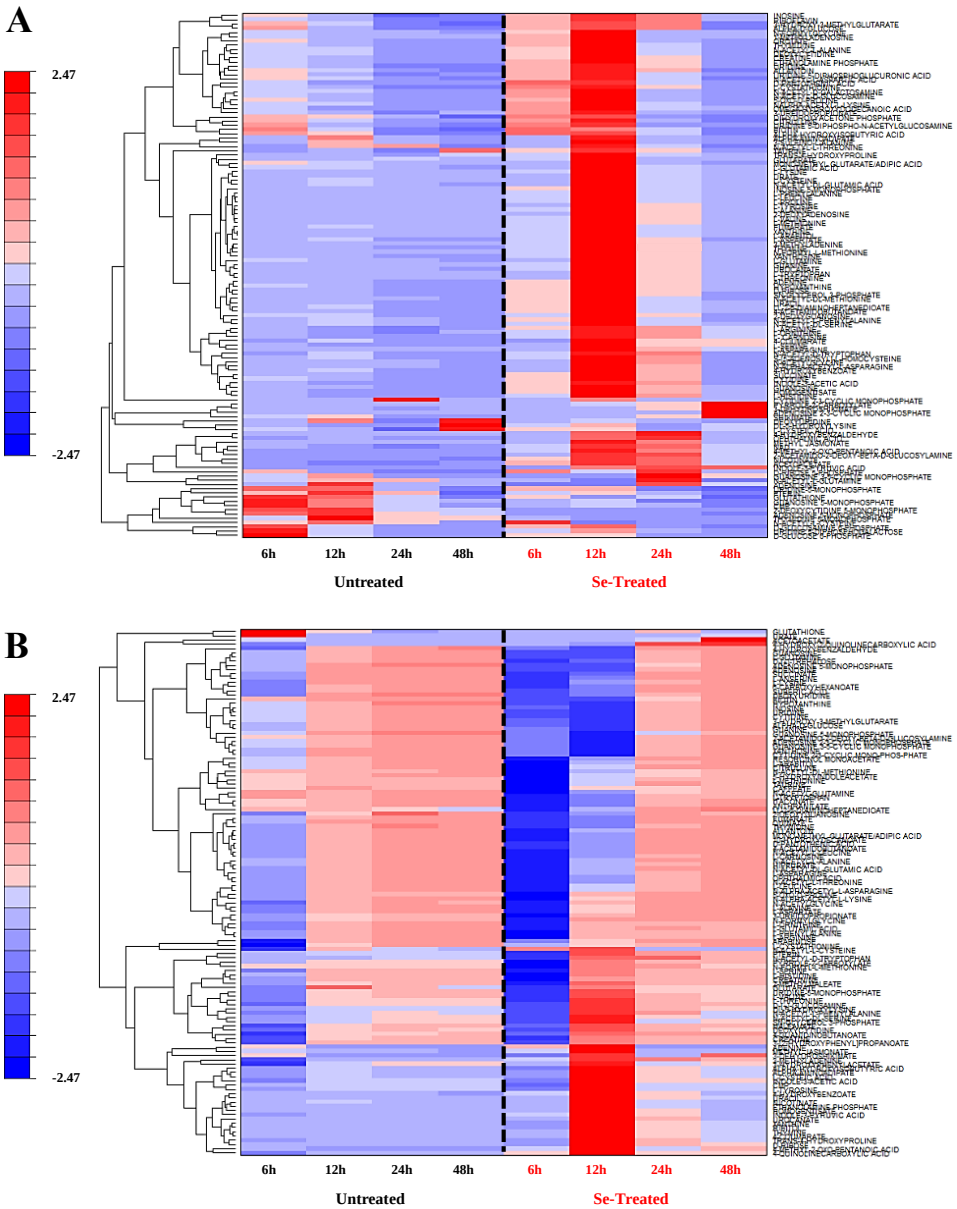

Figure 3.27. SeITE02 clustered heat maps of intracellular (A) and extracellular (B) compounds recognized after the metabolomics run. Rows represent the metabolites, columns the specific time points.

From a first general analysis of all the 125 compounds detected for the intracellular data and 124 for the extracellular one, it is possible to observe a relatively homogeneous distribution of their concentration levels during almost all the time course. For the cells grown in the untreated NB media, only some intracellular compounds seem to hint at a transformation during the exponential stage and in the stationary phase. Instead, the situation experienced by the Se-treated cells appears to be slightly more "animated". In this case, it is possible to notice a remarkable and almost general modification around 12 h, the time point where the cells register a negative decrease in their replication. Thus, the recognition of active metabolites and/or their possible interconnection with different metabolic pathways can bring to light several reflections that may explain this notable cellular deflection and characteristic behavior of SeITE02 cells when exposed to Na_2SeO_3.

Intracellular data elaboration

The first step is the statistical processing of the datasets. Since the metabolomics analysis on SeITE02 was carried out on a time course consisting of four time points, the PCs on which to conduct the PCA analysis are in a final number equal to four. Then, the calculation of the PCs shows that it is possible to compress the temporal information to the first two PCs (PC1 and PC2). Very high values of the cumulative percentage of variance have been achieved, reaching the 94.6% in the case of the untreated samples and the 95.7% in the Se-treated ones. The respective PCs values and relative biplots are reported in Tables 3.11 and 3.12 and in Figure 3.28, respectively.

Table 3.11. SeITE02 intracellular PCs percentage of variances of the untreated samples.

PRINCIPAL COMPONENT (PC)	UNTREATED SAMPLES % OF VARIANCE	UNTREATED CUMULATIVE % OF VARIANCE
PC1	86.11	86.11
PC2	8.49	94.6
PC3	3.53	98.13
PC4	1.87	100.00

Table 3.12. SeITE02 intracellular PCs percentage of variances of Se-treated samples.

PRINCIPAL COMPONENT (PC)	Se-TREATED SAMPLES % OF VARIANCE	Se-TREATED CUMULATIVE % OF VARIANCE
PC1	89.19	89.19
PC2	6.5	95.69
PC3	2.61	98.3
PC4	1.7	100.00

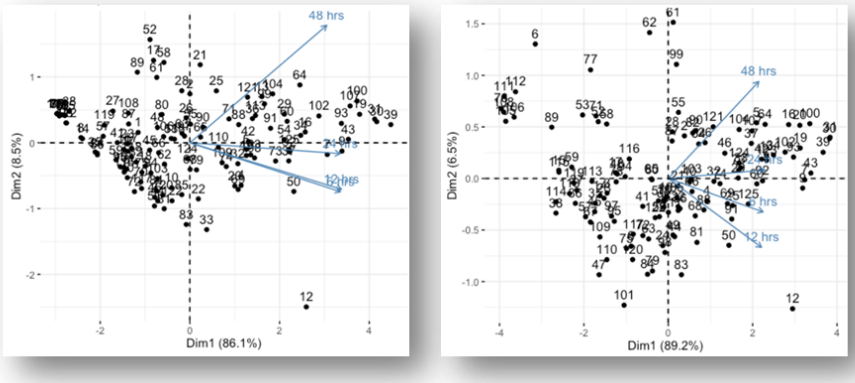

Figure 3.28. SeITE02 PCA biplots of intracellular untreated (left) and Se-treated (right) metabolites.

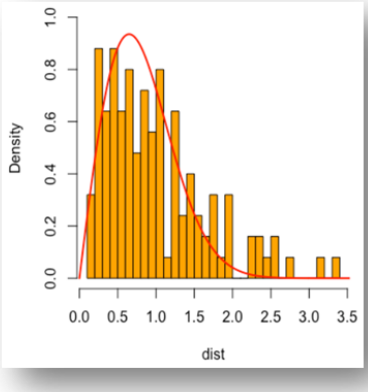

Figure 3.29. Rayleigh fit distribution for SeITE02 intracellular data.

Table 3.13. SeITE02 intracellular metabolites p-values.

METABOLITE	p-value
Adenosine 5'-monophosphate	$2.4x10^{-6}$
2''-deoxycytidine 5''-monophosphate	$1.04x10^{-5}$
2''-deoxyadenosine	$1.5x10^{-4}$
N-acetyl-glutamine	$3.3x10^{-4}$
Thymidine 5''-monophosphate	$4.8x10^{-4}$
4-methyl-2-oxopentanoic acid	$9.6x10^{-4}$

The calculation of the Euclidean distances confirms again a Rayleigh type distribution of SeITE02 intracellular data (Figure 3.29) and allowed the estimation of the relative p-values ($<10^{-4}$), as listed in Table 3.13.
In Table 3.14, instead, are registered the top 10% metabolites indicated by the statistical approach Bayesian Inference-T^2 statistics.

Table 3.14. SeITE01 ordered list of extracellular metabolites identified by Bayesian Inference-T^2 statistics.

BAYESIAN INFERENCE-T^2 STATISTIC: METABOLITE ORDER	
1) 2''-deoxyadenosine	8) L-tryptophan
2) Glutarate	9) Guanine
3) 2-acetamido-2-deoxy-β-d-glucosylamine	10) 4-methyl-2-oxopentanoic acid
4) N- acetyl-glutamine	11) Homogentisate
5) Adenosine 5''-monophospate	12) L-histidine
6) L-carnosine	13) Indole-3-acetic acid
7) L-proline	

The graphical representation of the union of the statistically significant metabolites obtained from the two approaches is illustrated in Scheme 3.12.

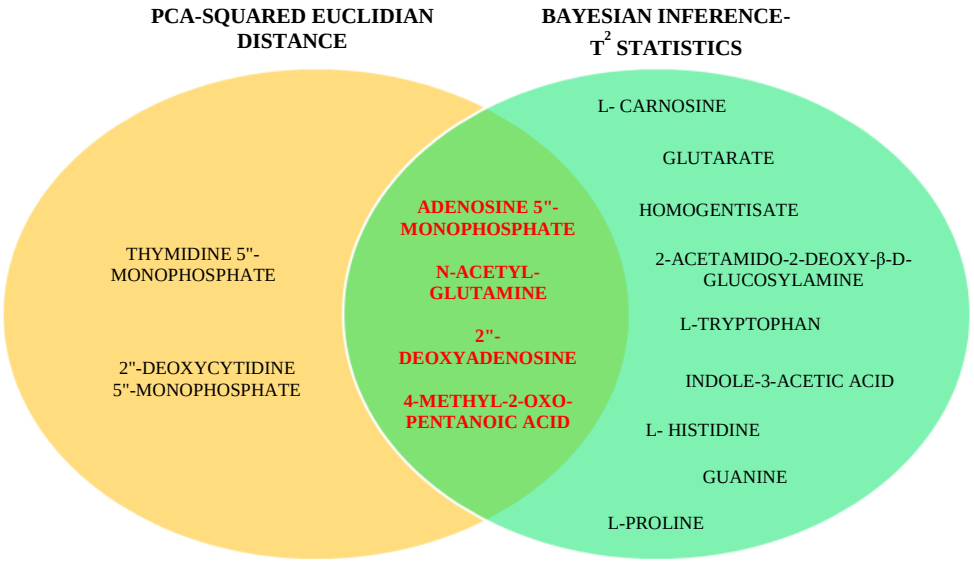

Scheme 3.12. SeITE02 statistical elaboration of intracellular data between the two approaches.

In the case of intracellular data, the two statistics have identified the presence of four common metabolites: Adenosine 5”-monophosphate (AMP), N-acetyl-glutamine, 2”-deoxyadenosine (dA), and 4-methyl-2-oxo-pentanoic acid.

The PCA-Squared Euclidean Distance lists other two compounds, thymidine 5”-monophosphate (TMP) and 2”-deoxycytidine 5”-monophosphate (dCTMP), while in the Bayesian Inference-T^2 statistics the metabolites scheduled are, for example, glutarate, guanine (G) or L-carnosine. However, the separated classification of these molecules based on the statistical tool used does not bind them to a total “isolation”. As has been seen in SeITE01 interpretation, they can communicate through the same metabolic pathways or common biochemical intermediates, reinforcing the importance and strength of the statistical choice adopted for the analysis of these complex datasets.

The use of the heat map (Figure 3.30) with the most significant compounds (n = 15) highlights the peculiar evolution of SeITE02 response during the time course.

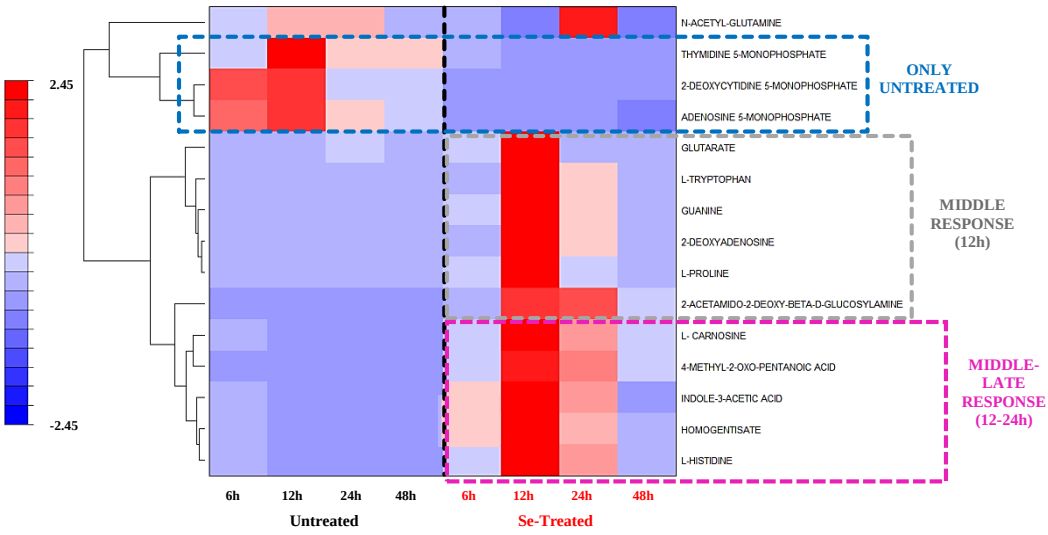

Figure 3.30. SeITE02 clustered heat map of the most relevant intracellular metabolites.

In the case of this Gram-negative strain, Na_2SeO_3 exposition mainly accentuates two cellular responses:

- Middle response (12 h), indicated by a grey dotted rectangle;
- Middle-late response (12 h - 24 h), revealed by a purple dotted rectangle.

The heat map describes the total absence of a biochemical response related to the late cellular phases, and in particular, connected to the release and presence of Bio-SeNPs in the medium. The different organic composition of the external capping could therefore have different effects on bacterial cells, making them less toxic and dangerous. This statement is also supported by the observation that the most metabolomics changes are observed only during the lag phase, and in particular at the end of this period around the 12 h.

Data discussion once again starts from one of the metabolites present in the intersection of the Venn diagram, the N-acetyl-glutamine. This is the acetylated form of glutamine (Gln), a central and versatile metabolite in bacterial physiology.

Different metabolic functions can be attributed to this compound. Firstly, it is one of the 20 standard amino acids involved in protein production and it is the primary product of ammonium assimilation. Secondly, it acts as nitrogen and carbon donor in various biosynthesis reactions and it can play an important role as a signaling molecule monitoring the intracellular and extracellular nitrogen level and state of the cells. Finally, it is used not only to supply ammonium for Glu and Cys synthesis (Pro and GSH precursors) for the production of the proteinogenic amino acid Trp, but it is also employed for the generation of new nucleotides, nucleosides and their derivatives [238, 240].

Thus, this important amino acid is strongly connected with many metabolites listed in Scheme 3.12, and both its chemical structure and temporal trend are presented in Figure 3.31.

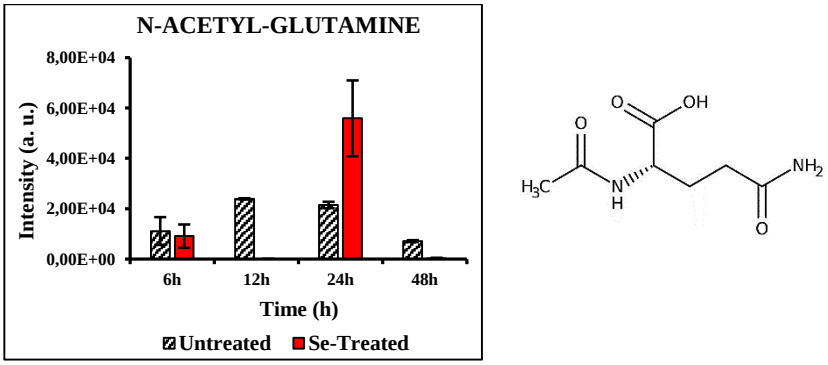

Figure 3.31. Chemical structure and bar plot of N-acetyl-glutamine.

In listing all the meaningful roles performed by Gln, it was anticipated that it serves as an important nitrogen resource for the synthesis of proteins, amino acids and nitrogenous bases. It is well known, then, that the biosynthetic pathways of the amino acids are connected to each other by the presence of common precursors and intermediaries. In the case of N-acetyl-glutamine it is possible to advance the hypothesis that the cells, when exposed to Na_2SeO_3, can use its catabolism to supply nitrogen for the biosynthetic pathway of the amino acids His, Pro and Trp. This can be confirmed by the comparison of the respective Se-treated trends, as shown in Figure 3.32.

In the case of the precursor (N-acetyl-glutamine), its maximum accumulation within the exposed cells occurs only during the exponential phase, although there is a first low accumulation during the beginning of the lag phase. Cells grown in the untreated conditions, instead, present a mostly linear trend with an accumulation and a low consumption of this metabolite throughout their life cycle. Conversely, the three products (His, Pro and Trp) seem to demonstrate opposite behaviors (Figure 3.32) being key to the 12h time point even where SeO_3^{2-} consumption starts in haste.

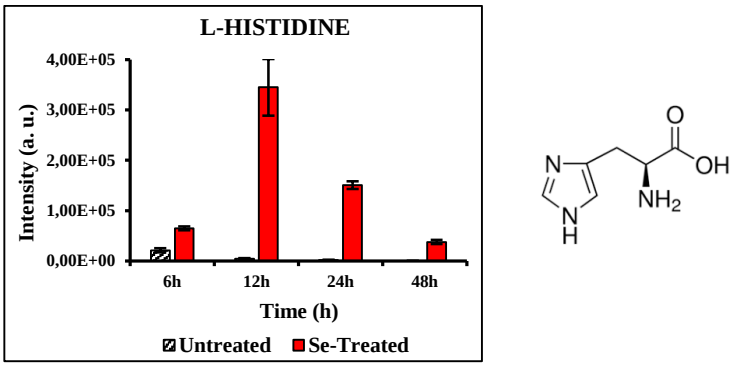

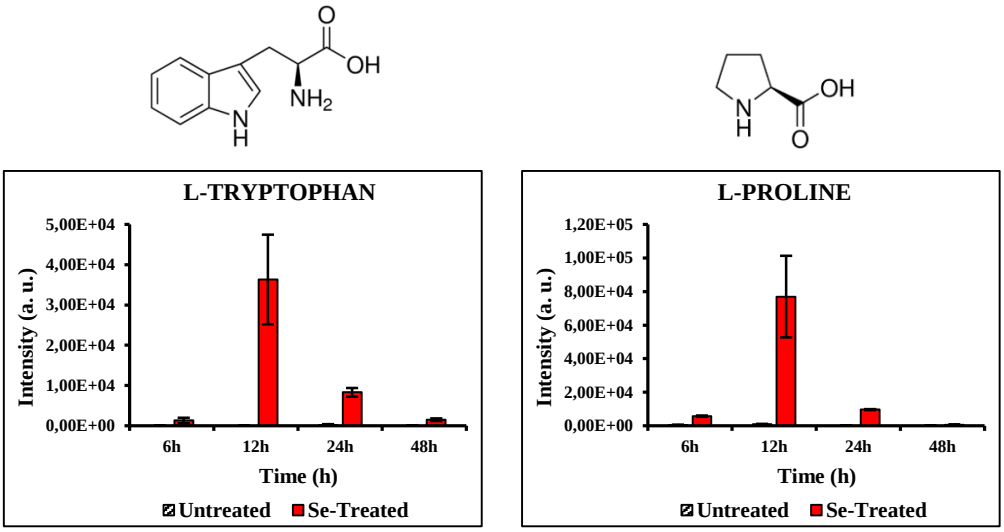

Figure 3.32. Chemical structure and bar plots of His, Pro and Trp.

If compared, the trends of the three organic solutes are absolutely mirrored and record the maximum intensity on reaching the end of the lag phase at 12 h. Their accumulation at this particular point of the time course can take on different meanings: they can operate as precursors for new amino acids and proteins in order to cope with cellular recovery, and/or they can act as a defense for the new biosynthesized Se nanostructures in order to avoid their immediate damages as this is also when SeO_3^{2-} action begins.

The total absence of these three metabolites in the untreated samples reinforces the hypothesis of their immediate intervention during the cellular renewal and proliferation only when the cells are subject to a state of stress and not when they grow in optimal conditions. Even if the description of the functions performed by these metabolites has already been presented in the previous sections of the chapter, it is possible to briefly summarize their salient features. His performs multiple roles within the cells interacting with TCA cycle and the synthesis of numerous other amino acids; Pro can act as osmoprotectant; and numerous studies conducted on eukaryotes shown that Trp can affect various physiological processes and may contribute to activate anti-inflammatory and anti-oxidative responses.

The same relation that associates the N-acetyl-glutamine with these three amino acids can also be traced between this particular precursor and the other two

nitrogenous products: the deoxyribonucleoside 2''-deoxyadenosine (dA) and the nucleobase guanine (G) (Figure 3.33).

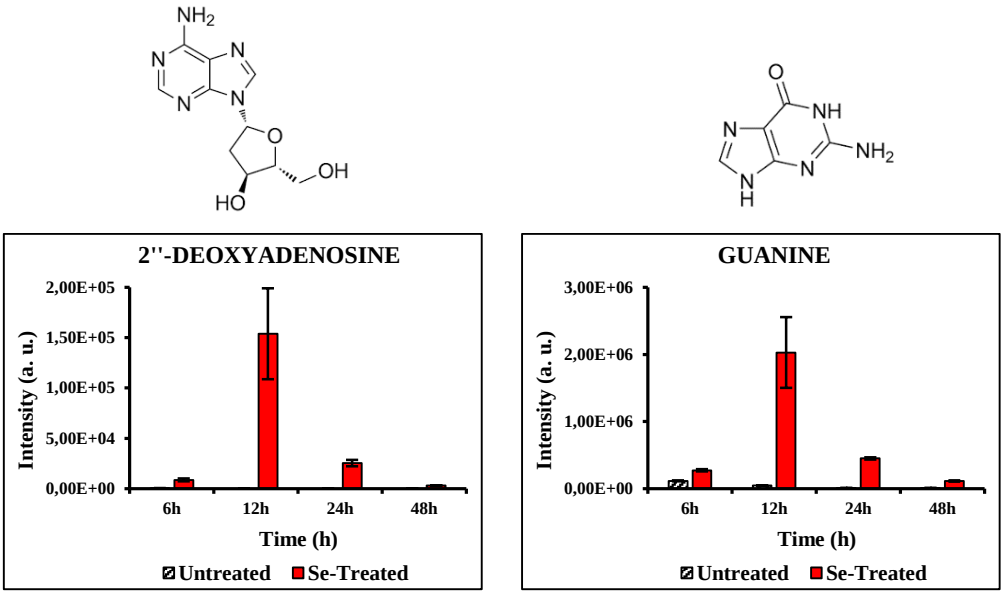

Figure 3.33. Chemical structure and bar plots of dA and G.

Since they are purine bases and their importance in the cellular homeostasis does not require clarification, different possible explanations for their remarkable accumulation within the Se-treated cell at the end of the lag phase could be proposed. Firstly, they can stabilize the bacterial DNA structure following the toxic interaction with the oxyanions during the first phases of growth to avoid drastic changes in the helical conformation and the onset of mutations and fatal injuries. Secondly, their substantial presence could constitute an intracellular pool of nucleosides necessary for the synthesis of new genetic material or for its immediate repair. In addition, the cells could accumulate these considerable amounts of molecules to protect them from possible oxidation processes. Several studies have in fact reported the genotoxicity of the modified purines, which cause oxidative damage to DNA and generate final lesions and mutations [240-242]. In particular, it has been observed that the guanine bases are the preferred DNA targets and hot spots for the introduction of "hole" constituted by different radical cations. These reactions occur primarily at guanines because they are the nucleobases with the

lowest oxidation potential (E_{ox}). In comparison, the pyrimidines are much more difficult to oxidize, and probably also for this reason the cells must not accumulate large quantities of these bases when they are exposed in stressful situations. This statement, in fact, allows introducing and discussing two other relevant metabolites: TMP and dCMP.

As reported by the heat map illustrated in Figure 3.30 and confirmed by the relative bar plots shown in Figure 3.34, these compounds are mainly expressed in the untreated samples.

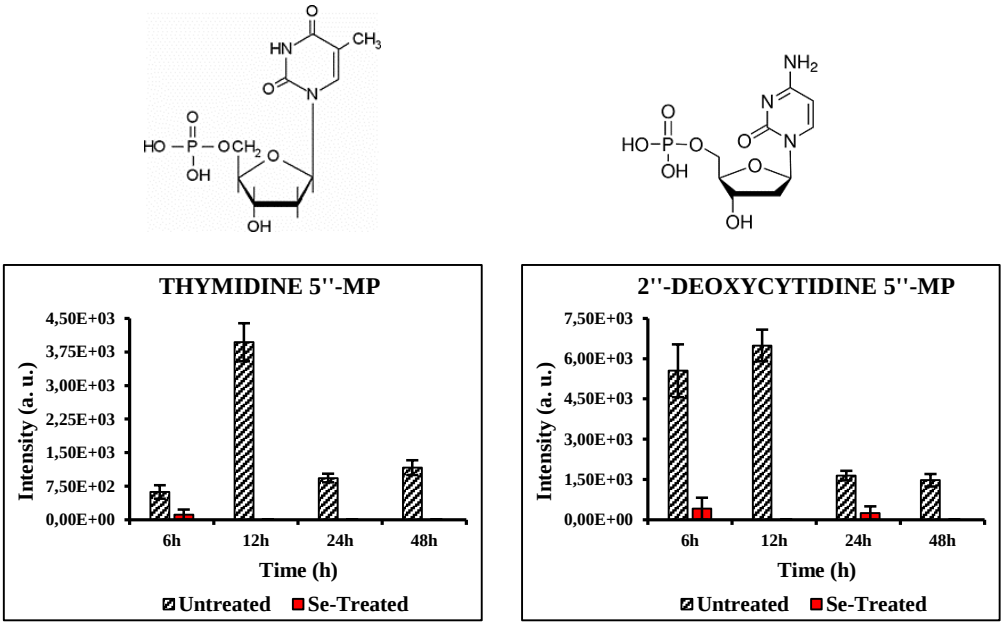

Figure 3.34. Chemical structure and bar plots of TMP and dCMP.

The consumption of both TMP and dCMP by the Se-treated cells during the entire time course can indicate an active participation of these metabolites in the possible DNA synthesis and repair. As in the previous situation, this promotes the cellular proliferation and recovery after the negative stage of replication occurred in the lag phase. In unchallenged growth conditions, instead, there is a remarkable accumulation of these molecules, increasing their level of intensity between 6 h and 12 h, when the cells are in the active exponential phase.

The marked presence of these nucleotides, however, could also suggest their possible use as phosphate and sugar bio-stores, which can be spent and chemically modified by the cells for energy production.

The intracellular molecule AMP (Figure 3.35), which is a component in the synthesis of RNA, is the result of ATP turnover producing pyrophosphate and thus has important function in many cellular processes, could also play this role.

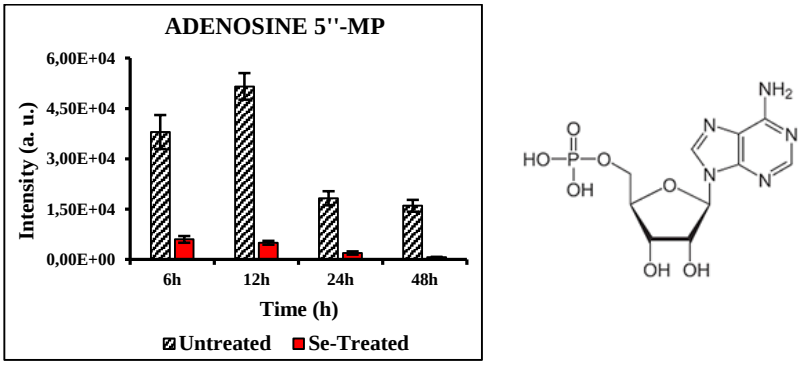

Figure 3.35. Chemical structure and bar plot of AMP.

Its metabolic trend recalls that of the previous metabolites and in particular that of the dCMP. This reinforces the hypothesis of a general activation of various nitrogenous bases involved in the repair and synthesis of new genetic material. Furthermore, being interconverted to ADP and/or ATP, this metabolite could supply energy to the cells to favor the cellular recovery of Se stress.

Finally, the metabolite families identified in SeITE02 thanks to the use of the KEGG platform underline a considerable importance of both the biosynthesis of secondary metabolites (17.40%), Aminoacyl-tRNA biosynthesis (17%), and amino acids (22%). Nevertheless, in this Gram-negative strain a new class seems to be particularly active when exposed to SeO_3^{2-}: the purine metabolism (13%).

Scheme 3.13 shows the most relevant metabolic pathways enriched in the presence of Na_2SeO_3 and reports the percentages related to the organic compounds that flow into a given biochemical path.

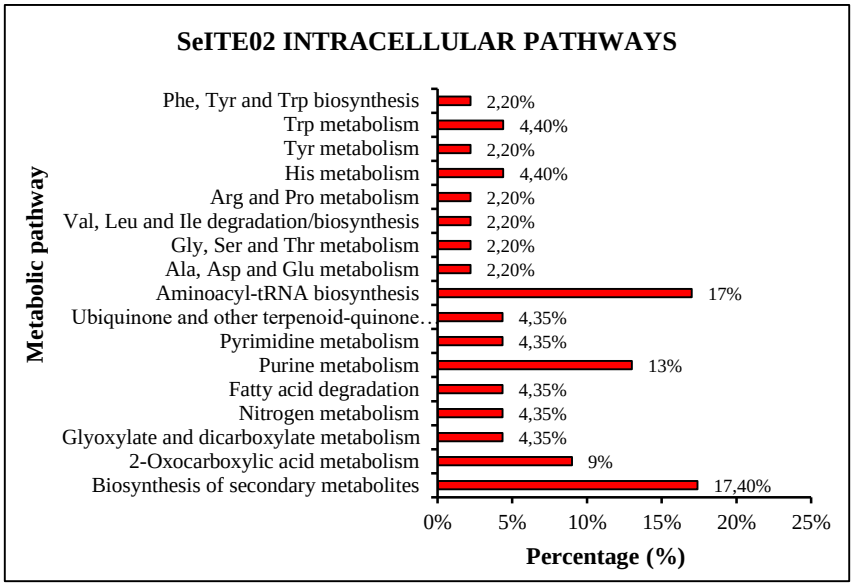

Scheme 3.13. SeITE02 intracellular metabolic pathways most influenced by the presence of Na_2SeO_3.

Accordingly, it is possible to conclude the treatment of the intracellular metabolites mostly expressed by the bacterium *Stenotrophomonas maltophilia* SeITE02 with the observation that the nature of the detected metabolites is mainly related to the metabolism of ammonium and biosynthesis of amino acids and nucleic acids.

The intracellular accumulation of these metabolites in response to the SeO_3^{2-} stress factor may be linked to the fact that the cells try to protect/repair their own DNA and promote cellular proliferations, inducing only secondarily biochemical pathways related to the production of specific defense and protective molecules.

Extracellular data elaboration

PCA analysis of the extracellular untreated and Se-treated datasets allows the compression of the temporal information to the first two main components PC1 and PC2.

As in the case of the intracellular samples, the data have almost reached a cumulative percentage of the variance close to 100%, arriving at 95.02% and 91.05% for the untreated and the Se-treated samples, respectively.

Tables 3.15 and 3.16 report the variance percentage's values of each PC, while Figure 3.36 shows the resulting biplots of the untreated (left) and Se-treated (right) samples.

Table 3.15. SeITE02 extracellular PCs percentage of variances of the untreated samples.

PRINCIPAL COMPONENT (PC)	UNTREATED SAMPLES % OF VARIANCE	UNTREATED CUMULATIVE % OF VARIANCE
PC1	82.45	82.45
PC2	12.57	95.02
PC3	3.39	98.41
PC4	1.59	100.00

Table 3.16. SeITE02 extracellular PCs percentage of variances of the Se-treated samples.

PRINCIPAL COMPONENT (PC)	Se-TREATED SAMPLES % OF VARIANCE	Se-TREATED CUMULATIVE % OF VARIANCE
PC1	77.81	77.81
PC2	13.24	91.05
PC3	7.31	98.36
PC4	1.64	100.00

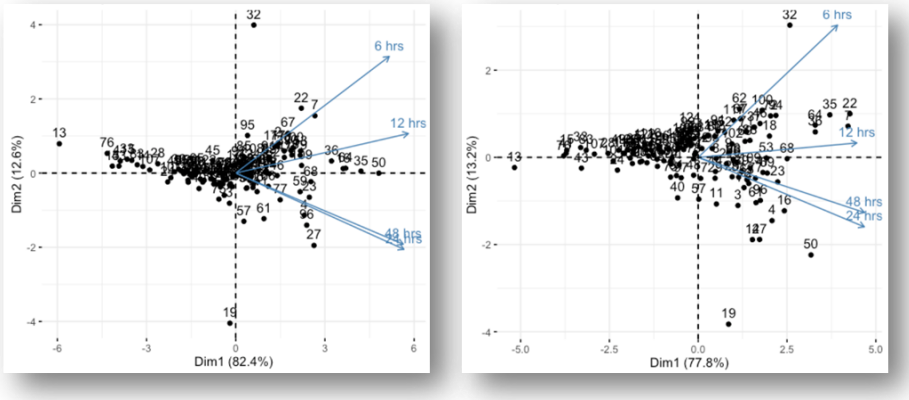

Figure 3.36. SeITE02 extracellular PCA biplots of the untreated (left) and Se-treated (right) metabolites.

Figure 3.37, moreover, describes and confirms a Rayleigh type distribution of SeITE02 extracellular data obtained after the calculation of the Squared Euclidean Distance.

The estimation of the relative p-values ($<10^{-4}$) is then reported in Tables 3.17.

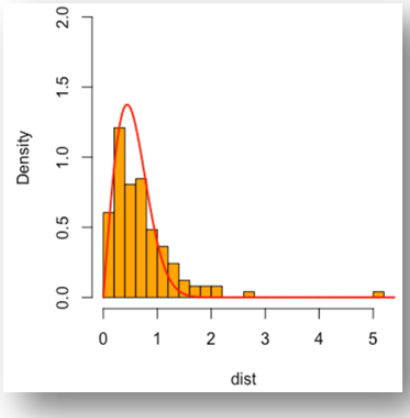

Figure 3.37. Rayleigh fit distribution for SeITE02 extracellular data.

Table 3.17. SeITE02 extracellular metabolites p-values.

METABOLITE	p-value
L-threonine	$2.3x10^{-9}$
Xanthine	$2.6x10^{-9}$
4-methyl-2-oxopentanoic acid	$4.2x10^{-6}$
Adenine	$4.4x10^{-6}$
Indole-3-pyruvic acid	$5.1x10^{-5}$
L-serine	$2.1x10^{-4}$
Nicotinate	$2.5x10^{-4}$
Uracil	$3.4x10^{-4}$

In Table 3.18, instead, are listed the top 10% metabolites (first 13 organic compounds) indicated by the statistical approach Bayesian Inference-T^2 statistics.

Table 3.18. SeITE02 ordered list of extracellular metabolites identified by Bayesian Inference-T^2 statistics.

BAYESIAN INFERENCE-T^2 STATISTICS: METABOLITE ORDER	
1) 4-methyl-2-oxopentanoic acid	8) N-acetyl-DL-methionine
2) Adenine	9) Arabinose
3) L-threonine	10) D-[+]-glucosamine
4) Uracil	11) L-glutamine
5) Xanthine	12) D-ribose
6) N-acetylglycine	13) 4-hydroxybenzaldehyde
7) Acetoacetate	

The Venn diagram shown in Scheme 3.14 represents the final and overall result of the two distinct statistical elaborations.

The metabolites present in the intersection and shared between the two approaches are the following: the purine bases adenine (Ade) and xanthine, the pyrimidine base uracil (U), the amino acid L-threonine (Thr), and the 2-oxo monocarboxylic acid 4-methyl-2-oxo-pentanoic acid.

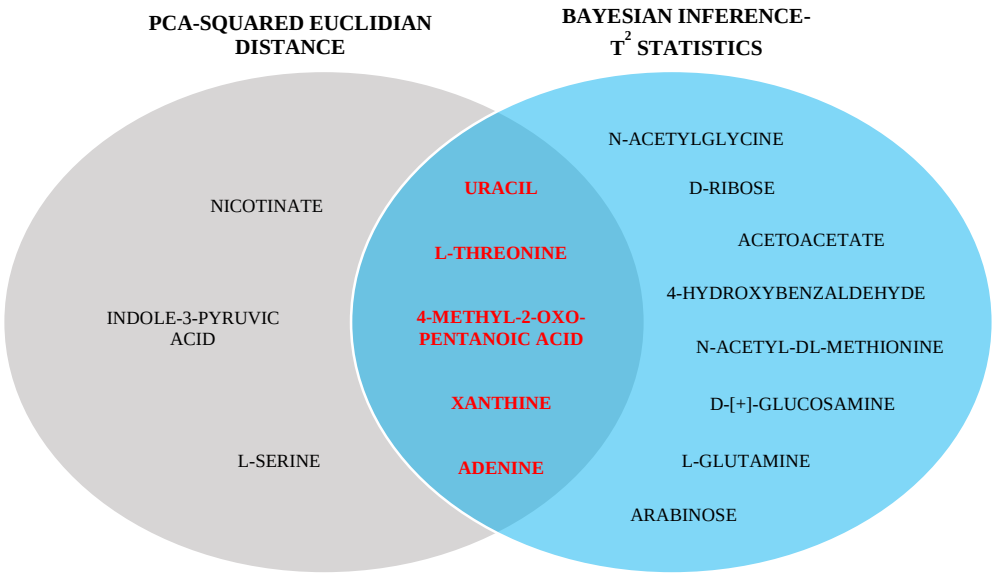

Scheme 3.14. SeITE02 statistical elaboration of extracellular data between the two approaches.

The graphical representation of the statistically significant metabolites (n = 16) for the identification of possible temporal responses and common trends is once again reported as a clustered heat map, as shown in Figure 3.38.

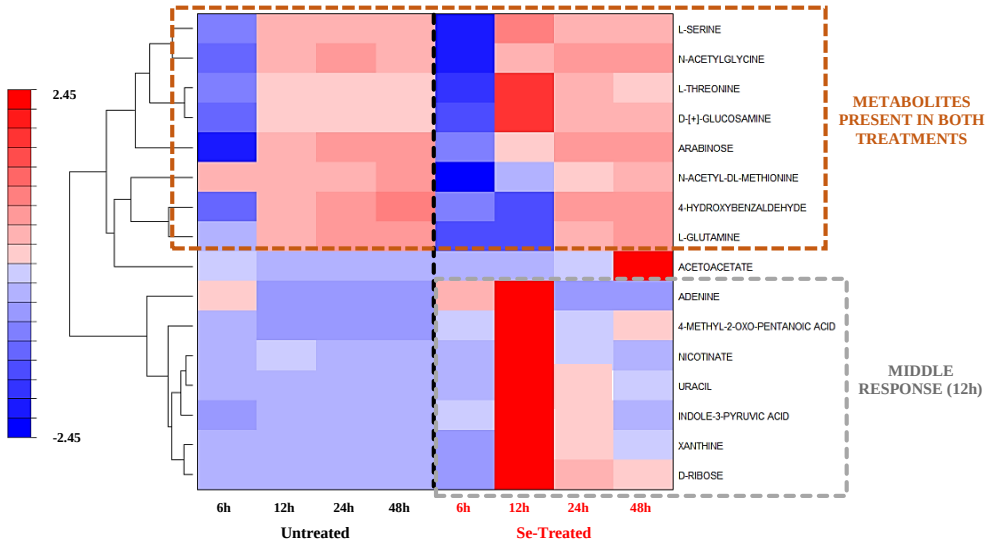

Figure 3.38. SeITE02 clustered heat map of the most relevant extracellular metabolites.

Its observation strongly reminds the heat map describing the metabolites extruded from the bacterial strain SeITE01 (Figure 3.17). In particular, clear similarities are observable in the case of the untreated metabolites and in those Se-treated grouped together in the dotted brown rectangle of Figure 3.38.

In both strains, in fact, the untreated compounds are evidently divided in two distinct classes. The first includes the solutes occupying the lower part of the graph that do not appear to be extruded from the cells or they are secreted in undetectable quantities. In the second, instead, are present the metabolites secreted by the cells starting at around 12 h (upper part of the heat map), whose trend and intensity seem then to remain unchanged until 48 h. This similar attitude is noticed also in the case of the Se-treated samples listed in the upper part of the map, whose behavior once the 24 h is reached, perfectly follows that of the samples grown in the absence of Na_2SeO_3.

Conversely, the metabolites activated by the presence of SeO_3^{2-} and underlined with a dotted grey rectangle seem to follow the trend of the intracellular

metabolites (Figure 3.30), with a notable increase in intensity at the end of the lag phase (12 h).

Therefore, considering the information deriving both from the brief presentation of the common metabolites and the analysis of the heat map, it is possible to discuss a few points toward a theme.

As described above, three of the five metabolites present at the intersection of the Venn diagram are nucleobases. This places a strong connection between the metabolites accumulated in the intracellular compartment and those instead extruded from the bacterial cells. In fact, Ade, U and xanthine may be the end-products of different chemical and degradation processing on the AMP, TMP and G molecules, respectively. The relative chemical structures and the temporal responses of these solutes are presented in Figure 3.39.

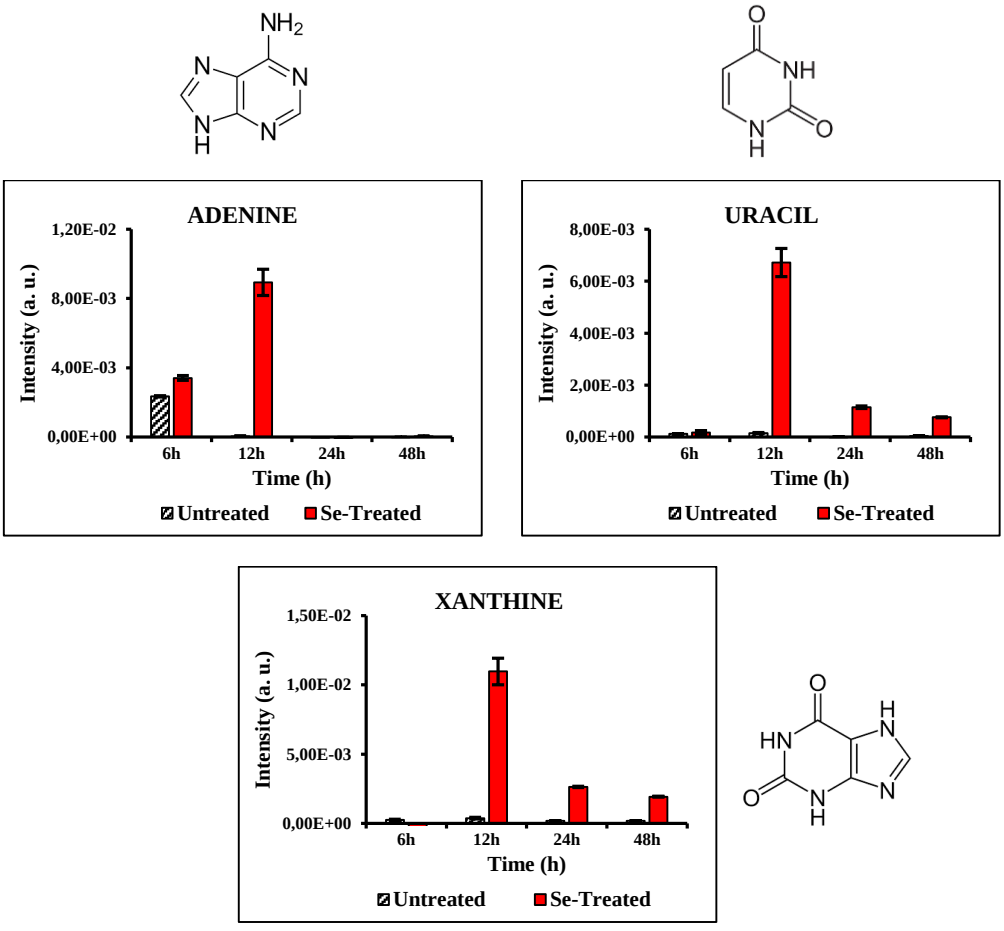

Figure 3.39. Chemical structures and bar plots of Ade, U and xanthine.

The intracellular nucleotides and nucleoside encountered in the previous section may have undergone hydrolysis, demethylation, deamination and phosphoribosyl transferase reactions that result in the formation of the respective nucleosides and free phosphates. The latter can be recycled by surrounding cells and reused for nucleotides re-synthesis or other biochemical reactions. The nucleotides, instead, can undergo further chemical modifications with the concomitant loss of the sugars and the final conversion to the pure bases. These modifications, in fact, could explain the extracellular presence of the purine and pyrimidine bases in the spent growth medium, even if their presence should not only be considered only as a waste. Their extrusion in the media could also be connected to the formation of an extracellular pool of bases to which the cell can draw in further situations of stress. Moreover, the degradation of these molecules can also produce numerous substrates, such as carbon dioxide or ammonia for the biochemical synthesis of new solutes.

However, the nucleobases degradation is not the only process implemented by SeITE02 to respond to the cellular recovery when exposed to SeO_3^{2-} stress. To satisfy the biochemical needs for the bacterial growth, two other compounds deriving from the catabolism of relevant amino acids are presented: the IPyA and the nicotinate (Figure 3.40).

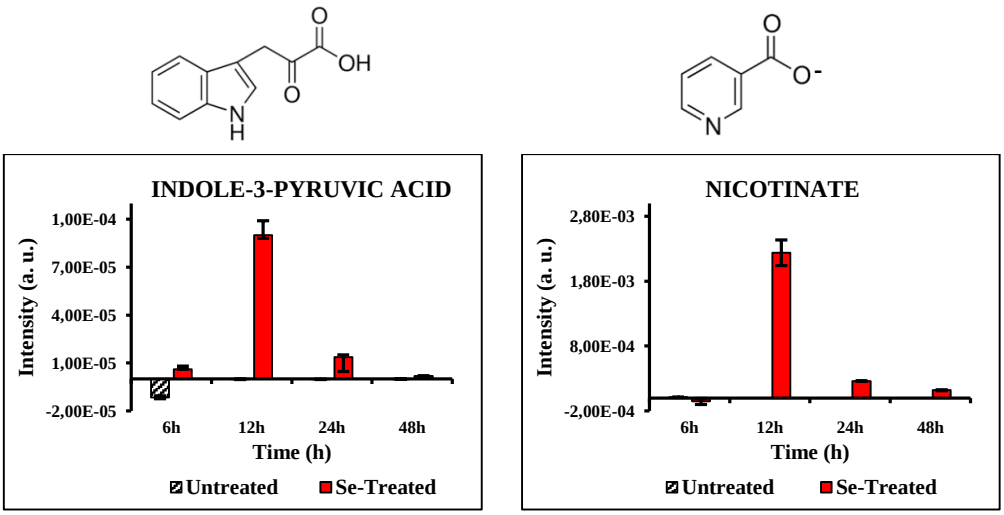

Figure 3.40. Chemical structures and bar plots of IPyA and nicotinate.

IPyA is a frequently observed molecule in both the intracellular and extracellular treatment of the metabolomics data of both SeITE01 and SeITE02. As mentioned several times, it is the result of the catabolic pathway of the amino acid Trp, whose roles within the cells have already been elucidated.

Nicotinate, instead, is a pyridinemonocarboxylate and the conjugate base of nicotinic acid (NA), a form of vitamin B3 and the precursor for the pyridine cofactors NAD and NADP. This molecule can derive from the oxidation of the amino acids Asp or from the catabolism of Trp via kynurenine and quinolinic acids.

It is well known that NA and its derivatives are important growth factors and they play a fundamental role in bacterial metabolism. Molecules that derive from this compound are, for example, Coenzyme I and II (di- and tri-phosphopyridine nucleotide), which are the most important hydrogen carriers within the living cells. Moreover, the nicotinamide adenine dinucleotides (NAD, NADH, NADP, and NADPH) are essential cofactors in all living systems and function as hydrogen acceptors (NAD, NADP) and donors (NADH, NADPH) in biochemical redox reactions [243].

Although there are no prokaryotic studies, several investigations conducted on eukaryotic cells have shown an active role of NA in genomic stability, DNA repair, ATP production and PARP-1 (poly-ADP-ribose polymerase-1) activation, which is a nuclear enzyme that detects DNA damage, binds to DNA single or double strand breaks, and then use NAD^+ to form nicotinamide and ADP-ribose [244, 245].

Thus, this molecule could actively participate in the repair of genetic material, activating a series of cascade reactions for the production of specific enzymes and cofactors. Furthermore, it can act as carbon, nitrogen, and energy source.

Scheme 3.15 overviews all the pathways most influenced by SeO_3^{2-}.

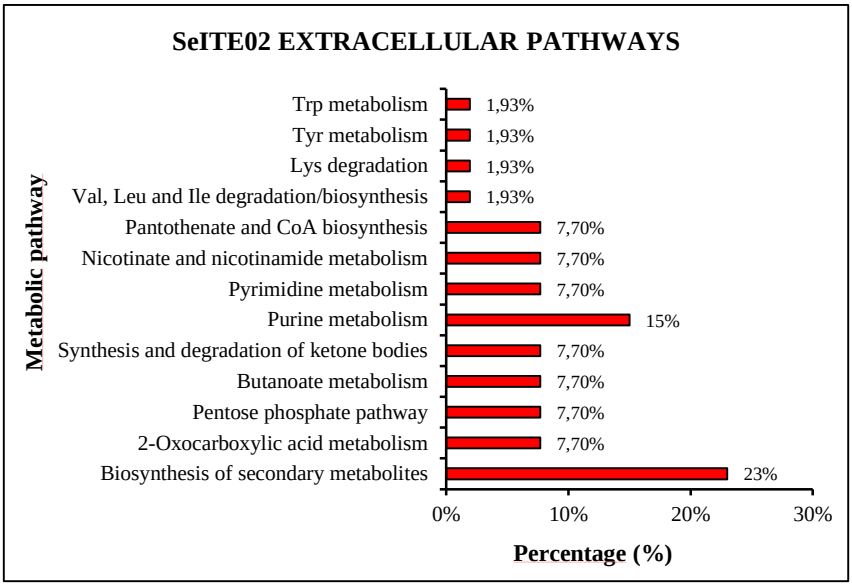

Scheme 3.15. SeITE02 extracellular metabolic pathways most influenced by the presence of Na_2SeO_3.

In the case of the secreted metabolites, there is an enhancement of both the biosynthesis of secondary metabolites (23%) and purine metabolism (15%), but a clear decrease of the biosynthesis of amino acids (7.70%), and the total disappearance of the Aminoacyl-tRNA biosynthesis.

The extracellular presence of numerous nucleosides could explain the presence of intracellular nucleotides synthesized to cope with the cellular arrest that occurs late in the lag phase and before the SeO_3^{2-} begins to be rapidly consumed.

3.4.6 TEM imaging

The acquisition of the TEM images for the investigation of SeITE02 behavior and morphology was carried out on the same time points considered for the metabolomic study (6, 12, 24 and 48 h).

The cells grown in absence of stress caused by the toxic action of the oxyanion SeO_3^{2-} are illustrated in Figure 3.41.

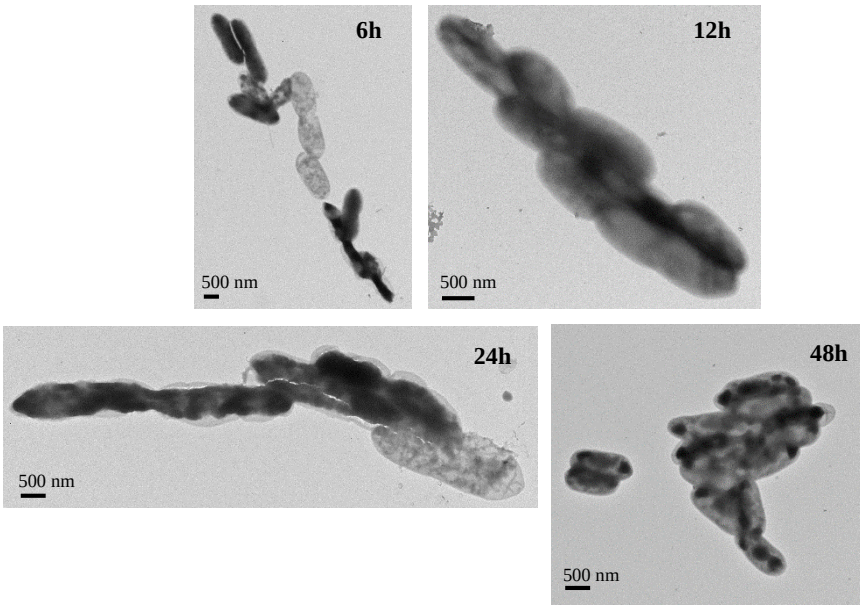

Figure 3.41. TEM time course of SeITE02 untreated cells.

In these conditions, the cells grow and develop optimally. The image shown in Figure 3.42 is an enlargement of a cellular agglomerate formed after 6 h of growth time, and from its analysis different observations can be deduced.

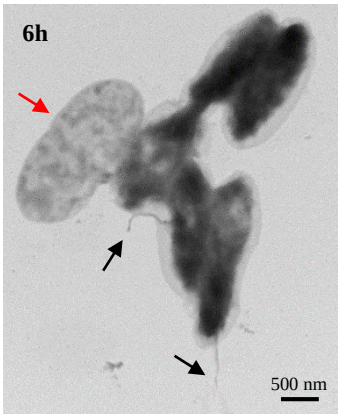

Figure 3.42. SeITE02 TEM image after 6 h of growth time.

Black arrows highlight the protrusion from the cell surfaces of polar flagellum-like filaments necessary for the cellular movement and important for surface adherence. Even a ghost cell appears in the same image (red arrow). The presence of these dying cells are due to the rapid cellular turnover that occurs during the exponential phase.

Only after 24 h of growth, the cells begin to lose the integrity of the membranes and the cell walls, and the number of ghosts begins to increase significantly, an event that marks the entry of cells into the stationary phase.
The images collected from the samples exposed to Na_2SeO_3 describe, instead, a different cellular attitude and morphological response (Figure 3.43).

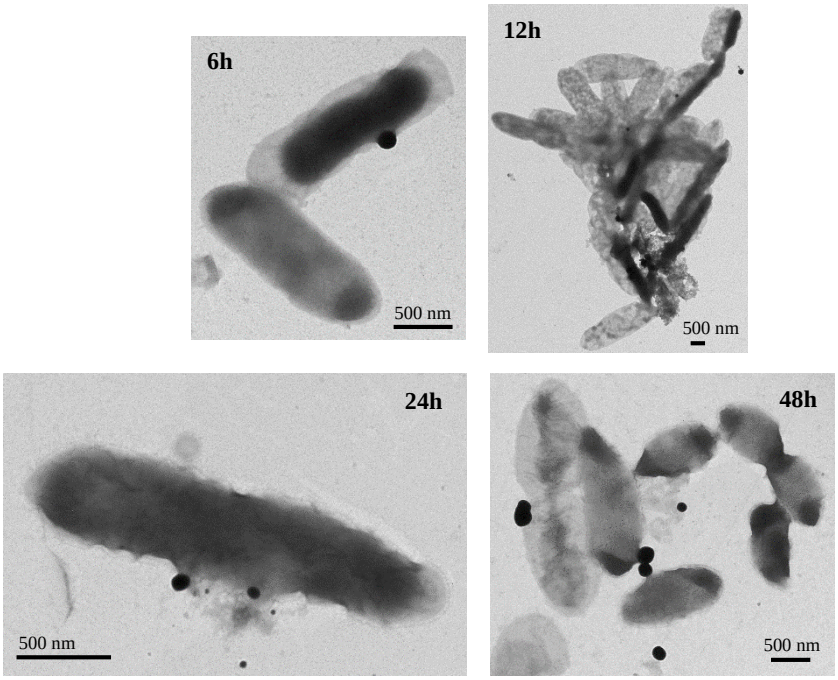

Figure 3.43. TEM time course of SeITE02 Se-treated cells with Na_2SeO_3.

A marked change is observed in the image describing the 12 h Se-treated cells after 12 h of exposition with SeO_3^{2-}. If compared with the untreated one, it is possible to observe an increased presence of ghost cells, a behavior that confirms the SeITE02 cellular arrest that occurs in this particular phase.
The electron-dense biogenic nanostructures (black-dark spots) bio-synthesized by this strain begin to be extruded from the cells and released into the culture medium starting at 24 h, and their number seems to increase when the cells reach the 48 h of exposure time.

3.5 CONCLUSIONS

In the present study, untargeted metabolomics was adopted for a comprehensive analysis of the diachronic metabolic fingerprinting and foot printing of the Gram-positive bacterium *Bacillus mycoides* SeITE01 and the Gram-negative bacterium *Stenotrophomonas maltophilia* SeITE02 in response to the stress from SeO_3^{2-}-oxyanion.

Our experimental set allowed the collection of both the intracellular and extracellular samples, while the two different statistical approaches gave confidence to the choice of metabolites on which interpretation had been focused within both the datasets.

Nevertheless, as the analyses were carried out on solely one Gram-negative bacterium and one Gram-positive bacterium, conclusions can not be drawn at this step that describe general attitudes and trends in bacteria as a whole since it is unlikely that all strains can behave identically. In fact, the obtained results evidenced two different attitudes and responses in the two microorganisms tested.

B. mycoides SeITE01 seems to face the toxic effect of SeO_3^{2-} by activating different defense pathways, especially in both the first and last phases of the time course (3 h and 48 h). These mechanisms consist in the intracellular accumulation of osmo-protective solutes and antioxidants, as well as the activation of ROS scavengers and substances that mechanically stabilize the cytoplasmic membranes. Furthermore, the presence in the medium of numerous secreted amino acids and second messenger molecules can supply the cells with important carbon and nitrogen sources through their catabolism.

These evidences strengthen the hypothesis of a deleterious effect that the bio-synthesized SeNPs exert toward *B. mycoides* SeITE01, as there is a marked metabolic response testified by the release of Bio-SeNPs into the growth medium at approximately 48 h.

The images acquired by TEM allowed the observation of SeITE01 cell aspect and dynamic alterations deriving from the exposure to SeO_3^{2-}. The comparison between untreated and Se-treated cells underlined a difficulty for the cells to deal with the first stages of growth when exposed to the oxyanion (also

evidenced by the growth curve), while an evident cell wall degeneration was observed.

A different response was noted in the case of *S. maltophilia* SeITE02. In this bacterium, SeO_3^{2-} exposure causes a significant accumulation of amino acids and nitrogenous bases intended for both the synthesis and repair of DNA, as well as involved in the activation of biochemical pathways linked to the cellular defense only at a later time. Most of the compounds released from the cells fall into this class of metabolites. Their excretion is related to the degradation of intracellular biopolymers and the discard of waste compounds no longer necessary for the cell under Bio-SeNPs production.

In the case of SeITE02, TEM images did not underline an evident morphological difference between Se-treated and untreated cells. The only exception is represented by an increase of cells ghost at the end of the lag phase, after 12 h cultivation.

The completely new adoption of the time course for metabolomics investigation with these bacterial strains makes it easier and more accurate to interpret metabolites primarily involved in the response against SeO_3^{2-} when compared to endpoint analysis most often applied. That allowed highlighting essential events of both bacterial growth and SeO_3^{2-} consumption.

The results achieved with the study carried out for the elaboration of the present PhD thesis broaden the vision on this topic paving the way to a better understanding of the complex metabolic response of bacterial cells to SeO_3^{2-} associated stress. Thanks to these new insights, drawing up of new protocols for future targeted metabolomics experiments will be possible, thus allowing for more detailed investigations on the toxic effects of this oxyanion towards bacterial cells as well as a tuned control on the formation of biogenic SeNPs.

CHAPTER IV:

FINAL CONCLUSIONS

In the present thesis, several different approaches were used including spectroscopic, metabolomics and imaging techniques to study the biotransformation process of SeO_3^{2-} and the effect of this oxyanion on the bacterial cultures of the Gram-positive bacterial isolate *Bacillus mycoides* SeITE01 and the Gram-negative bacterial strain *Stenotrophomonas maltophilia* SeITE02. The results have shown that:

- **FTIR spectroscopic analyses of intact cells under optimum growth conditions revealed similar trends for both strains, with the presence of all classes of biochemical macromolecules**. During the entire time course, untreated bacterial cultures of SeITE01 and SeITE02 maintained the same bio-molecular composition and spectroscopic trend. Carbohydrates, lipids, proteins and nucleic acids were identified as the main constituents of the complex biochemical structure of these cells.
- **The Gram-positive strain SeITE01 showed more variability in composition and response to SeO_3^{2-}, with the activation of metabolic pathways for cells defense.** A marked variation in the FTIR spectral composition of lipids and carbohydrates was observed in the Se-treated cultures of SeITE01 starting at 48 h. Metabolomics analysis of the intracellular metabolites performed at the same time point underlined a significant accumulation of molecules with osmo-protective and antioxidant properties, as well as the activation of ROS scavengers and solutes for cell membrane stabilization. At this incubation time, numerous Bio-SeNPs released into the medium and their direct contact with the cells possibly led to toxicity effects with the consequent impairment of stability and functionality of both bacterial walls and membranes. Although the two techniques present different sensitivities and detections limits, both have coincided in detecting cell's response to the stress due to the SeNPs biologically synthesized.

- **SeO_3^{2-} exposure did not alter organic composition, the spectral profile and dynamics of metabolites in cells of the Gram-negative strain SeITE02.** FTIR spectra recorded for samples of Se-treated cultures of this bacterial isolate did not evidence changes in composition and trend of functional groups compared to what was observed in samples of untreated cultures. Moreover, metabolomics investigation revealed that metabolites accumulating as a consequence of SeO_3^{2-} stress were those mainly involved in maintaining the pivotal vital functions, such as the synthesis and repair of the genetic material. Only secondarily, related biochemical pathways were found altered in the course of their accumulation.
- **TEM images confirmed two different behaviors between SeITE01 and SeITE02.** The images acquired by TEM allowed observing a morphological alterations and a marked malformation on the cell wall of SeITE01 cells that had experienced SeO_3^{2-} exposure during the first stages of growth. On the other hand, the addition of the toxic oxyanions to the bacterial cultures of SeITE02 did not reveal a significant modification or alteration of cell structures.

Furthermore, the characterization of the selenium nanostructures bio-synthesized by the strains SeITE01 and SeITE02 was also investigated.
Steps and specific observations of this part of the study were as follows:

- **Collection and analysis of SeNPs bio-synthesized intracellularly and extracellularly by SeITE01 and SEITE02 after 24 h and 48 h of incubation in presence of SeO_3^{2-}.** The use of two extraction methods allowed investigating separately the intracellular and extracellular SeNPs bio-produced by the two strains. Processing of cell pellets resulted in the recovery of Bio-SeNPs from the inside of the bacterial cells, whilst Bio-SeNPs released into the culture medium were collected by vacuum filtration.
- **Bio-SeNPs by SeITE01 revealed different molecular composition of the organic capping layer depending on their localization and how long they were exposed to SeO_3^{2-}.** FTIR spectra of intracellularly deposited Bio-

SeNPs at 24 h showed a high presence of lipids and carbohydrates and a tendency of secondary protein structures to assume a disordered conformation. At 48 h, an increase in proteins and a decrease in lipids was recorded, indicating a better stabilization and balance between the protein and the lipid components. On the other hand, in the case of the extracellular Bio-SeNPs, marked differences were not registered and quite similar spectra were acquired for both the samples collected at 24 h and 48 h. Proteins, lipids and carbohydrates resulted as the main classes found associated with the capping layer of extracellularly deposited Bio-SeNPs.

- **Bio-SeNPs from SeITE02 evidenced a constant composition of their external coatings.** Interpretation of all FTIR spectra concerning the Bio-SeNPs from SeITE02 allowed to assume quite a similar trend with respect to both the extraction method and the exposure timing. Bands attributable to lipids and carbohydrates were recorded, but mostly signals from proteins and nucleic acids were registered.
- **Bio-SeNPs extracted from the both bacterial strains SeITE01 and SeITE02 revealed different stability and average size.** Analyses by means of DLS and TEM demonstrated greater stability of Bio-SeNPs from SeITE02 and a greater uniformity in size. In particular, an average dimension of 314 ± 2.2 nm and 306 ± 4.2 nm was registered respectively for the intracellular Bio-SeNPs extracted after 24 h and 48 h, while 163 ± 1.8 nm and 165 ± 2 nm were ascertained for the extracellular ones. Bio-SeNPs from SeITE01, instead, showed lower stability, possible presence of aggregates with an average size between 637 ± 34 nm and 393 ± 9.8 nm for the intracellular Bio-SeNPs at 24 h and 48 h, and 148 ± 0.9 nm and 147 ± 0.4 nm for the extracellular ones. Moreover, a change in their coating's composition is observed starting from 48 h of incubation with Na_2SeO_3.

A summary consideration can be drawn in the end of this PhD thesis.

Since the analyses done were performed on two strains inadequately representing - as single references - the whole Gram-negative bacteria, on one

side, and all Gram-positive bacteria, on the other, it is not possible therefore to advance conclusions that can describe general shared attitudes of the members of both bacterial typology. Nevertheless, the results obtained with the multiple instrumental approaches seem to tendentially indicate two distinct dynamics as a response to the exposure to SeO_3^{2-} followed by Bio-SeNPs synthesis in the bacterial strains considered in this study.

A significant contribution of this research to the knowledge in the field of bacterial biogenesis of SeNPs is that the data collected shed light on novel aspects of nanoparticle synthesis at different growth stages of both strains SeITE01 and SeITE02.

ACKNOWLEDGEMENTS

I would like to acknowledge all the people that constitute the soul of the Environmental Microbiology research group of University of Verona. In particular, my supervisor, Prof. Giovanni Vallini, for giving me the opportunity to work in this research group on this exciting topic, Prof. Silvia Lampis for her helpful advices, encouragement and guidance, especially in the experimental part, and all my colleagues Marco, Chiara, Elena, Alessandro, Alessandra and Viviana for their support and friendship during my PhD study period.

Special thanks goes to Prof. Raymond J. Turner from University of Calgary (AB, Canada), not only for giving me the opportunity to work in his research group, for his support and his important help with writing my thesis, but also for his friendship and his attention in making me feel at home during the research period in Canada. I thank Damon, Elina, Natalie and Nadia of the Microbial Biochemistry Laboratory of University of Calgary for the wonderful moments spent in the laboratory and for their support and friendship during the nine months in Calgary. I also thank Ryan of Lewis Research Group for his constant encouragement and help in dealing with metabolomics experiments and Prof. Ian Lewis for allowing me to work with this technique.

Besides, I would like to thank Prof. Francesca Monti for teaching me the FTIR spectroscopy technique and for her confidence in letting me handle the instrument by myself, and Prof. Roberto Chignola for his fundamental help in statistical analysis.

Finally, I would like to thank my family and friends for their constant support and for having always accepted and supported all the choices I made during this three exciting yet difficult years of my studies.

BIBLIOGRAPHIC REFERENCES

[1] Trofast J (2011). Chemistry International, 16-19 www.degruyter.com
[2] Weeks ME (1932). The discovery of the elements. VI. Tellurium and selenium. Journal of Chemical Education 9, 474.
[3] Garousi F (2015). The toxicity of different selenium forms and compounds-Review. Acta Agraria Debreceniensis, 33-38
[4] Zannoni D, Borsetti F, Harrison JJ, and Turner RJ (2008). The bacterial response to the chalcogen metalloids Se and Te. Advances in Microbial Physiology 53, 1-72.
[5] Dou L, Chang WH, Gao J, Chen CC, You J, and Yang Y (2012). A Selenium-Substituted Low-Bandgap Polymer with Versatile Photovoltaic Applications. Advanced Materials, 1-7.
[6] Saha U, Fayiga A, Hancock D, and Sonon L (2016). Selenium in Animal Nutrition: Deficiencies in Soils and Forages, Requirements, Supplementation and Toxicity. International Journal of Applied Agricultural Sciences, 6, 112-125.
[7] Susarla S, Tsafack T, Owuor PS, Puthirath AB, Hachtel JA, Babu G, Apte A, Jawdat BI, Hilario MS, Lerma A, Calderon HA, Robles Hernandez FC, Tam DW, Li T, Lupini AR, Idrobo JC, Lou J, Wei B, Dai P, Tiwary CS, and Ajayan PM (2019). High-K dielectric sulfur-selenium alloys. Science Advances, 5, 1-8.
[8] Tapiero H, Townsend DM, and Tew KD (2003). The antioxidant role of selenium and seleno-compounds. Biomedicine & Pharmacotherapy, 57, 134-144.
[9] Fleming J, Ghose A, and Harrison PR (2001). Molecular mechanisms of cancer prevention by selenium compounds. Nutrition and Cancer, 40, 42-49.
[10] Tan HW, Mo HY, Lau ATY, and Xu YM (2019). Selenium Species: Current Status and Potentials in Cancer Prevention and Therapy. International Journal of Molecular Science, 20, 75, 1-26.
[11] Lau ATY, Tan HW, and Xu YM (2017). Epigenetic effects of dietary trace elements. Current Pharmacology Reports, 3, 232-241.
[12] Schomburg L (2017). Dietary Selenium and Human Health. Nutrients, 9, 22, 1-7.
[13] Lopes G, Ávila FW, and Guimarães Guilherme LR (2017). Selenium behavior in the soil environment and its implication for human health. Ciência e Agrotecnologia, 41, 6, 605-615.
[14] El-Ramady, H. R. Éva Domokos-Szabolcsy, Neama A. Abdalla, Tarek A. Alshaal, Tarek A. Shalaby, Attila Sztrik, Józef Prokisch, Miklós Fári (2014). Selenium and nano-selenium in agroecosystems. Environmental Chemistry Letters, 12, 495-510.
[15] Lenz M, and Lens PNL (2009). The essential toxin: the changing perception of selenium in environmental sciences. Science of the Total Environment, 407, 3620-3633.

[16] Nancharaiah YV, and Lens PNL (2015). Ecology and Biotechnology of Selenium-Respiring Bacteria. Microbiology and Molecular Biology Reviews, 79, 61-80.
[17] Shrift A (1964). A selenium cycle in nature. Nature, 201:1304-1305.
[18] Staicu LC, Oremland RS, Tobe R, and Mihara H (2017). Chapter 6. Bacteria Versus Selenium: A View from the Inside Out. Springer International Publishing, E.A.H. Pilon-Smits et al. (eds.), Selenium in plants, Plant Ecophysiology 11.
[19] Eswayah AS, Smith TJ, and Gardiner PHE (2016). Microbial Transformations of Selenium Species of Relevance to Bioremediation. Applied and Environmental Microbiology, 82, 16, 4848-4859.
[20] Staicu LC, and Barton LL (2017). Bacterial Metabolism of Selenium-For Survival or Profit. Bioremediation of Selenium Contaminated Wastewater, Springer, 1-31.
[21] Macy JM, Michel TA, and Kirsch DG (1989). Selenate reduction by *Pseudomonas* species: a new mode of anaerobic respiration. FEMS Microbiology Letters, 61, 195-198.
[22] Oremland RS, Hollibaugh JT, Maest AS, Presser TS, Miller LG, and Culbertson CW (1989). Selenate reduction to elemental selenium by anaerobic bacteria in sediments and culture: biogeochemical significance of a novel sulfate-independent respiration. Applied and Environmental Microbiology, 55, 2333-2343.
[23] Oremland RS, Switzer Blum J, Culberston CW, Visscher PT, Miller LG, Dowdle P, and Strohmaier FE (1994). Isolation, growth and metabolism of an obligately anaerobic, selenate-respiring bacterium, strain SES-3. Applied and Environmental Microbiology, 60, 3011-3019.
[24] Fujita M, Ike M, Nishimoto S, Takahashi K, and Kashiwa M (1997). Isolation and characterization of a novel selenate-reducing bacterium, *Bacillus sp* SF-1. Journal of Fermentation and Bioengineering, 83, 517-522.
[25] Knight VK, and Blakemore RP (1998). Reduction of diverse electron acceptors by *Aeromonas hydrophila*. Archives of Microbiology, 169, 239-248.
[26] Switzer Blum J, Bindi AB, Buzzelli J, Stolz JF, and Oremland RS (1998). *Bacillus arsenoselenatis* sp. nov., and *Bacillus selenitireducens* sp. nov.; two haloalkaliphiles from Mono Lake, California, which respire oxyanions of selenium and arsenic. Archives of Microbiology, 171, 19-30.
[27] Switzer Blum J, Stolz JF, Ohren A, and Oremland RS (2001). *Selenihalanaerobacter shriftii* gen. nov. sp. nov., a halophilic anaerobe from Dead Sea sediments that respires selenate. Archives of Microbiology, 175, 208-219.
[28] Macy JM, Rech S, Auling G, Dorsch M, Stackebrandt E, and Sly LI (1993). *Thauera selenatis* gen. nov., sp. nov., a member of the beta subclass of proteobacteria with a novel type of anaerobic respiration. International Journal of Systematic Bacteriology, 43, 135-142.
[29] Losi ME, and Frankenberger WT (1997). Reduction of selenium oxyanions by *Enterobacter cloacae* SLD1a-1: isolation and growth of the bacterium and its

expulsion of selenium nanoparticles. Applied Environmental Microbiology, 63, 3079-3084.
[30] Stolz JF, Oremland RS (1999). Bacterial respiration of arsenic and selenate. FEMS Microbiology Reviews, 23, 615-627.
[31] Oremland RS, Herbel MJ, Blum JS, Langley S, Beveridge TJ, Ajayan PM, Sutto T, Ellis AV, and Curran S (2004). Structural and spectral features of selenium nanospheres produced by Se-respiring bacteria. Applied Environmental Microbiology, 70, 52-60.
[32] Labunskyy VM, Hatfield DL, and Gladyshev VN (2014). Selenoproteins: molecular pathways and physiological roles. Physiological Reviews, 94, 739-777.
[33] Chhabria S, and Desai K (2016). Selenium Nanoparticles and Their Applications. Encyclopedia of Nanoscience and Nanotechnology 20, 1-32.
[34] Medina Cruz D, Mi G, and Webster TJ (2018). Synthesis and characterization of biogenic selenium nanoparticles with antimicrobial properties made by *Staphylococcus aureus*, methicillin-resistant *Staphylococcus aureus* (MRSA), *Escherichia coli*, and *Pseudomonas aeruginosa*. Journal of Biomedical Materials Research Part A.
[35] Sofer Z, Bartunek V, Junkovà J, Ulbrich P, Babunek M, and Kuchar M (2016). Synthesis of spherical amorphous selenium nano and microparticles with tunable sizes. Micro & Nano Letters, 11, 91-93.
[36] Qin B, Bai Y, Zhou Y, Liu J, Xie X, and Zheng W (2009). Structure and characterization of TeO_2 nanoparticles prepared in acid medium. Materials Letters, 63, 1949-1951.
[37] Li Y, Pan J, Jiang K, Zhou Y, Huang J, Ye J, and Bai Y (2013). Preparation of elemental tellurium nanoparticles-Sucrose sol and its antioxidant activity in vitro. The Journal of Wuhan University of Technology-Material Science Ed 28, 1048-1052.
[38] Thanh NTK, and Green LAW (2010). Functionalization of nanoparticles for biomedical applications. Nanotoday, 5, 213-230.
[39] Song JM, Lin YZ, Zhan YJ, Tian YC, Liu G, and Yu SH (2008). Superlong high-quality tellurium nanotubes: synthesis, characterization, and optical property. Crystal Growth & Design, 8, 1902-1908.
[40] Li J, Zhang J, and Qian Y (2008). Surfactant-assisted synthesis of bundle-like nanostructures with well-aligned Te nanorods. Solid State Sciences, 10, 1549-1555.
[41] Hong W, Wang J, and Wang E (2014). Facile synthesis of PdAgTe nanowires with superior electrocatalytic activity. Journal of Power Sources, 272, 940-945.
[42] B. Gates, B. Mayers, B. Cattle, and Y. Xia (2002). Synthesis and Characterization of Uniform Nanowires of Trigonal Selenium. Advanced Functional Materials, 12, 219-227.
[43] Smith TW, and Cheatham RA (1980). Functional Polymers in the Generation of Colloidal Dispersions of Amorphous Selenium. Macromolecules 13, 5, 1203-1207.

[44] Zhang J, Wang X, and Xu TT (2008). Elemental Selenium at Nano Size (Nano-Se) as a Potential Chemopreventive Agent with Reduced Risk of Selenium Toxicity: Comparison with Se-Methylselenocysteine in Mice. Toxicological Sciences, 101, 1, 22-31.
[45] Prokisch J, and Zommara MA (2010). Process for producing elemental selenium nanospheres. Patent US 20100189634 A1.
[46] Shakibaie M, Forootanfar H, Golkari Y, Mohammadi-Khorsanda T, and Shakibaie MR (2015). Anti-biofilm activity of biogenic selenium nanoparticles and selenium dioxide against clinical isolates of *Staphylococcus aureus*, *Pseudomonas aeruginosa*, and *Proteus mirabilis*. Journal of Trace Elements in Medicine and Biology 29, 235-241.
[47] Srivastava N, and Mukhopadhyay M (2015). Green synthesis and structural characterization of selenium nanoparticles and assessment of their antimicrobial property. Bioprocess and Biosystems Engineering 38, 1723-1730.
[48] Chudobova D, Cihalova K, Dostalova S, Ruttkay-Nedecky B, Rodrigo MAM, Tmejova K, Kopel P, Nejdl, L, Kudr J, Gumulec J, Krizkova S, Kynicky J, Kizek R, and Adam V (2014). Comparison of the effects of silver phosphate and selenium nanoparticles on *Staphylococcus aureus* growth reveals potential for selenium particles to prevent infection. FEMS Microbiology Letters, 351, 195-201.
[49] Zonaro E, Lampis S, Turner RJ, Qazi SJS, and Vallini G (2015). Biogenic selenium and tellurium nanoparticles synthesized by environmental microbial isolates efficaciously inhibit bacterial planktonic cultures and biofilms. Frontiers in Microbiology 6, 584.
[50] Cremonini E, Zonaro E, Donini M, Lampis S, Boaretti M, Dusi S, Melotti P, Lleo MM, and Vallini G (2016). Biogenic selenium nanoparticles: characterization, antimicrobial activity and effects on human dendritic cells and fibroblasts. Microbial Biotechnology 9, 758-771.
[51] Piacenza E, Presentato A, Zonaro E, Lemire JA, Demeter M, Vallini G, Turner RJ, and Lampis S (2017). Antimicrobial activity of biogenically produced spherical Se-nanomaterials embedded in organic material against *Pseudomonas aeruginosa* and *Staphylococcus aureus* strains on hydroxyapatite-coated surfaces. Microbial Biotechnology 10, 804-818.
[52] Gerrard T, Telford J, Williams H (1974). Detection of selenium deposits in *Escherichia coli* by electron microscopy. Journal of Bacteriology, 119, 1057-1060.
[53] Tugarova AV, and Kamnev AA (2017). Proteins in microbial synthesis of selenium nanoparticles. Talanta, 174, 539-547.
[54] Aguilar-Barajas E, Díaz-Pérez C, Ramírez-Díaz MI, Riveros-Rosas H, and Cervantes C (2011). Bacterial transport of sulfate, molybdate, and related oxyanions. Biometals, 24, 4, 687–707.
[55] Rosen BP, and Liu Z (2009). Transport pathways for arsenic and selenium: a minireview. Environment International, 35, 3, 512-515.

[56] Sarret G, Avoscan L, Carrière M, Collins R, Geoffroy N, Carrot F, Covés J, and Gouget B (2005). Chemical forms of selenium in the metal-resistant bacterium *Ralstonia metallidurans* CH34 exposed to selenite and selenite. Applied and Environmental Microbiology, 71, 5, 2331-2337.
[57] Schröder I, Rech S, Krafft T, and Macy JM (1997). Purification and Characterization of the Selenate Reductase from *Thauera selenatis*. The Journal of Biological Chemistry, 272, 38, 23765-23768.
[58] Butler CS, Debieux CM, Dridge EJ, Splatt P, and Wright M (2012). Biomineralization of selenium by the selenate-respiring bacterium *Thauera selenatis*. Biochemical Society Transactions, 40, 1239-1243.
[59] Rabenstein DL, and Tan KS (1988). ^{77}Se NMR studies of bis(alkylthio)selenides of biological thiols. Magnetic Resonance in Chemistry, 26, 1079-1085.
[60] Debieux CM, Dridge EJ, Mueller CM, Splatt P, Paszkiewicz K, Knight I, Florance H, Love J, Titball RW, Lewis RJ, Richardson DJ, and Butler CS (2011). A bacterial process for selenium nanosphere assembly. Proceedings of the National Academy of Science USA, 108, 13480-13485.
[61] Losi ME, and Frankenberger WT (1997). Reduction of selenium oxyanions by *Enterobacter cloacae* SLD1a-1: isolation and growth of the bacterium and its expulsion of selenium nanoparticles. Applied and Environmental Microbiology, 63, 3079-3084.
[62] Ridley H, Watts CA, Richardson DJ, and Butler CS (2006). Resolution of distinct membrane-bound enzymes from *Enterobacter cloacae* SLD1a-1 that are responsible for selective reduction of nitrate and selenate oxyanions. Applied and Environmental Microbiology, 72, 5173-5180.
[63] Fujita M, Ike M, Nishimoto S, Takahashi K, and Kashiwa M (1997). Isolation and characterization of a novel selenate-reducing bacterium, *Bacillus* sp SF-1. Journal of Fermentation and Bioengineering, 83, 517-522.
[64] Yamamura S, Yamashita M, Fujimoto N, Kuroda M, Kashiwa M, Sei K, Fujita M, and Ike M (2007). *Bacillus selenatarsenatis* sp. nov., a selenateand arsenate-reducing bacterium isolated from the effluent drain of a glass-manufacturing plant. International Journal of Systematic and Evolutionary Microbiology, 57, 1060-1064.
[65] Painter EP (1941). The chemistry and toxicity of selenium compounds with special reference to the selenium problem. Chemical Reviews, 28:179 -213.
[66] Ganther HE (1971). Reduction of the selenotrisulfide derivative of glutathione to a persulfide analog by glutathione reductase. Biochemistry 10, 4089-4098.
[67] Yamada A, Miyashita M, Inoue K, and Matsunaga T (1997). Extracellular reduction of selenite by a novel marine photosynthetic bacterium. Applied and Environmental Microbiology, 48, 367-372.
[68] Turner RJ, Weiner JH, and Taylor DE (1998). Selenium metabolism in *Escherichia coli*. Biometals, 11, 223-237.

[69] Kessi J, and Hanselmann KW (2004). Similarities between the abiotic reduction of selenite with glutathione and the dissimilatory reaction mediated by *Rhodospirillum rubrum* and *Escherichia coli*. Journal of Biological Chemistry, 279, 50662-50669.
[70] Lampis S, Zonaro E, Bertolini C, Bernardi P, Butler CS, and Vallini G (2014). Delayed formation of zero-valent selenium nanoparticles by *Bacillus mycoides* SeITE01 as a consequence of selenite reduction under aerobic conditions. Microbial Cell Factories, 13, 35, 1-14.
[71] Björnstedt M, Kumar S, and Holmgren A (1992). Selenodiglutathione is a highly efficient oxidant of reduced thioredoxin and a substrate for mammalian thioredoxin reductase. Journal of Biological Chemistry, 267, 8030-8034.
[72] Hockin SL, and Gadd GM (2003). Linked redox precipitation of sulfur and selenium under anaerobic conditions by sulfate-reducing bacterial biofilms. Applied and Environmental Microbiology, 69, 7063-7072.
[73] Pettine M, Gennan F, Campanella L, Casentini B, and Marani D (2012). The reduction of selenium(IV) by hydrogen sulfide in aqueous solutions. Geochimica et Cosmochimica Acta, 83:37-47.
[74] Zawadzka AM, Crawford RL, and Paszczynski AJ (2006). Pyridine-2,6-bis(thiocarboxylic acid) produced by *Pseudomonas stutzeri* KC reduces and precipitates selenium and tellurium oxyanions. Applied and Environmental Microbiology, 72, 3119-3129.
[75] Basaglia M, Toffanin A, Baldan E, Bottegal M, Shapleigh JP, and Casella S (2007). Selenite-reducing capacity of the copper-containing nitrite reductase of *Rhizobium sullae*. FEMS Microbiology Letters, 269, 124-130.
[76] Harrison G, Curie C, and Laishley EJ (1984). Purification and characterization of an inducible dissimilatory type sulphite reductase from *Clostridium pasteurianum*. Archives of Microbiology, 138, 72-78.
[77] DeMoll-Decker H, and Macy JM (1993). The periplasmic nitrite reductase of *Thauera selenatis* may catalyze the reduction of selenite to elemental selenium. Archives of Microbiology, 160, 241-247.
[78] Li DB, Cheng YY, Wu C, Li WW, Li N, Yang ZC, Tong ZH, and Yu HQ (2014). Selenite reduction by *Shewanella oneidensis* MR-1 is mediated by fumarate reductase in periplasm. Scientific Reports, 4, 3755.
[79] Kessi J, Ramuz M, Wehrli E, Spycher M, and Bachofen R (1999). Reduction of selenite and detoxification of elemental selenium by the phototrophic bacterium *Rhodospirillum rubrum*. Applied and Environmental Microbiology, 65, 4734 - 4740.
[80] Lampis S, Zonaro E, Bertolini C, Cecconi D, Monti F, Micaroni M, Turner RJ, Butler CS, and Vallini G (2017). Selenite biotransformation and detoxification by *Stenotrophomonas maltophilia* SeITE02: novel clues on the route to bacterial biogenesis of selenium nanoparticles. Journal of Hazardous Materials, 324 (Part A), 3-14.

[81] Tomei FA, Barton LL, Lemanski CL, Zocco TG, Fink NH, and Sillerud LO (1995). Transformation of selenate and selenite to elemental selenium by *Desulfovibrio desulfuricans*. Journal of Industrial Microbiology & Biotechnology, 14, 329-336.
[82] Ostwald W (1896). Lehrbuch Der Allgemeinen Chemie. W. Engelmann: Vol. 2.
[83] Jain R, Seder-Colomina M, Jordan N, Dessi P, Cosmidis J, van Hullebusch ED, Weiss S, Farges F, and Lens PN (2015). Entrapped elemental selenium nanoparticles affect physicochemical properties of selenium fed activated sludge. Journal of Hazardous Materials, 295, 193-200.
[84] Lenz M, Kolvenbach B, Gygax B, Moes S, and Corvini PFX (2011). Shedding Light on Selenium Biomineralization: Proteine Associated with Bionanominerals. Applied and Environmental Microbiology, 77, 13, 4676-4680.
[85] Dobias EI, Suvorova R, and Bernier-Latmani (2011). Role of proteins in controlling selenium nanoparticle size. Nanotechnology 22, 19, 1-9.
[86] Jain R, Jordan N, Weiss S, Foerstendorf H, Heim K, Kacker R, Hübner R, Kramer H, van Hullebusch ED, Farges F, and Lens PNL (2015). Extracellular Polymeric Substances Govern the Surface Charge of Biogenic Elemental Selenium Nanoparticles. Environmental Science & Technology, 49, 1713-1720.
[87] Gonzalez-Gil G, Lens PNL, and Saikaly PE (2016). Selenite Reduction by Anaerobic Microbial Aggregates: Microbial Community Structure, and Proteins Associated to the Produced Selenium Spheres. Frontiers in Microbiology, 7, 571, 1-14.
[88] Bulgarini A, Cecconi D, Lampis S, and Vallini G (2016). Proteomic Study of the Outer Layer of Biogenic Selenium Nanoparticles. Proceedings of the World Congress on Recent Advances in Nanotechnology (RAN'16) Prague, Czech Republic - April 1-2, 2016. Paper No. ICNNFC 114.
[89] Piacenza E, Bulgarini A, Lampis S, Vallini G, and Turner RJ (2017). Biogenic SeNPs from *Bacillus mycoides* SelTE01 and *Stenotrophomonas maltophilia* SelTE02: Characterization with reference to their associated organic coating. AIP Conference Proceedings, Vol. 1873, N°1, p. 020005.
[90] Winkel LHE, Johnson CA, Lenz M, Grundl T, Leupin OX, Amini M, and Charlet L (2012). Environmental selenium research: from microscopic processes to global understanding. Environmental Science & Technology, 46, 571-579.
[91] Stark WJ (2011). Nanoparticles in Biological Systems. Angewandte Chemie International Edition 50, 1242-1258.
[92] Jain R, Dominic D, Jordan N, Rene ER, Weiss S, van Hullebusch ED, Hübner R, and Lens PNL (2016). Preferential adsorption of Cu in a multi-metal mixture onto biogenic elemental selenium nanoparticles. Chemical Engineering Journal 284, 917-925.
[93] Prateeksh Singh BR, Shoe M, Sharma S, Naqvi AH, Gupt VK, and Singh BN (2017). Scaffold of Selenium Nanovectors and Honey Phytochemicals for

Inhibition of *Pseudomonas aeruginosa* Quorum Sensing and Biofilm Formation. Frontiers in Cellular and Infection Microbiology, 7, 93.
[94] Vallini G, Gregorio SD, and Lampis S (2005). Rhizosphere induced selenium precipitation for possible applications in phytoremediation of Se polluted effluents. Zeitschrift für Naturforschung C, 60, 349-356.
[95] Di Franco C, Beccari E, Santini T, Pisaneschi G, and Tecce G (2002). Colony shape as a genetic trait in the pattern-forming *Bacillus mycoides*. BMC Microbiology, 13, 2, 33.
[96] Kloepper JW, Ryu C-M, and Zhang S (2004). Induced systemic resistance and promotion of plant growth by *Bacillus spp*. Phytopathology, 94, 1259-1266.
[97] Kumar P, Patel SK, Lee JK, and Kalia VC (2013). Extending the limits of *Bacillus* for novel biotechnological applications. Biotechnology Advances.
[98] Garbisu C, Carlson D, Adamkiewicz M, Yee BC, Wong JH, Resto E, Leighton T, and Buchanan BB (1999). Morphological and biochemical responses of *Bacillus subtilis* to selenite stress. Biofactors, 10, 311-319.
[99] Baesman SM, Stolz JF, Kulp TR, and Oremland RS (2009). Enrichment and isolation of *Bacillus beveridgei* sp. nov., a facultative anaerobic haloalkaliphile from Mono Lake, California, that respires oxyanions of tellurium, selenium, and arsenic. Extremophiles, 13, 695-705.
[100] Mishra RR, Prajapati S, Das J, Dangar TK, Das N, and Thatoi H (2011). Reduction of selenite to red elemental selenium by moderately halotolerant *Bacillus megaterium* strains isolated from Bhitarkanika mangrove soil and characterization of reduced product. Chemosphere, 84, 1231-1237.
[101] Di Gregorio S, Lampis S, and Vallini G (2005). Selenite precipitation by a rhizospheric strain of *Stenotrophomonas sp.* isolated from the root system of *Astragalus bisulcatus*: a biotechnological perspective. Environmental International 31, 233-241.
[102] Antonioli P, Lampis S, Chesini I, Vallini G, Rinalducci S, Zolla L, and Righetti PG (2007). *Stenotrophomonas maltophilia* SeITE02, a new bacterial strain suitable for bioremediation of selenite contaminated environmental matrices. Applied and Environmental Microbiology, 73, 6854-6863.
[103] Lambert B, and Joos H (1989). Fundamental aspects of rhizobacterial plant growth promotion research. Trends in Biotechnology, 7, 215-219.
[104] Berg G, Marten P, and Ballin G (1996). *Stenotrophomonas maltophilia* in the rhizosphere of oilseed-rape occurrence, characterization and interaction with phytopathogenic fungi. Microbiological Research, 151, 19-27.
[105] Berg G, Roskot N, and Smalla K (1999). Genotypic and phenotypic relationships between clinical and environmental isolates of *Stenotrophomonas maltophilia*. Journal of Clinical Microbiology, 37, 3594-3600.
[106] Dungan RS, Yates SR, and Frankenberger WT Jr. (2003). Transformations of selenate and selenite by *Stenotrophomonas maltophilia* isolated from a seleniferous agricultural drainage pond sediment. Environmental Microbiology, 5, 287-295.

[107] Brian CS (2011). Fundamentals of Fourier Transform Infrared Spectroscopy. Second Edition, CRC Press Taylor & Francis Group.
[108] Pavia DL, Lampman GM, Kriz GA, and Vyvyan JR (2014). Introduction to Spectroscopy. Fifth Edition (www.books.google.com).
[109] Naumann D (2000). Infrared Spectroscopy in Microbiology. Encyclopedia of Analytical Chemistry. R.A. Meyers (Ed.) John Wiley & Sons Ltd, Chichester, 102-131.
[110] Davis R, and Mauer LJ (2010). Fourier transform infrared (FT-IR) spectroscopy: A rapid tool for detection and analysis of foodborne pathogenic bacteria. Current Research, Technology and Education Topics in Applied Microbiology and Microbial Biotechnology. A. Méndez-Vilas (Ed.).
[111] Stuart B (2004). Infrared Spectroscopy: Fundamentals and Applications. John Wiley & Sons, Ltd., Analytical Techniques in the Science. ISBNs: 0-470-85427-8.
[112] Perkins WD (1986). Fourier Transform-Infrared Spectroscopy. Part I. Instrumentation. Journal of Chemical Education, 63, A5-A10.
[113] Perkins WD (1987). Fourier Transform-Infrared Spectroscopy. Part II. Advantages of FT-IR. Journal of Chemical Education, 64, A269-A271.
[114] Clark D (2002). The Analysis of Pharmaceutical Substances and Formulated Products by Vibrational Spectroscopy. Handbook of Vibrational Spectroscopy, Vol. 5, Chalmers JM and Griffiths PR (Eds), Wiley, Chichester, UK, 3574-3589.
[115] Bunaciu AA, Aboul-Enein HY, and Fleschin S (2010). Application of Fourier Transform Infrared Spectrophotometry in Pharmaceutical Drugs Analysis. Applied Spectroscopy Reviews, 45, 206-219.
[116] Li-Chen ECY, Ismail AA, Sedman, J, and van de Voort FR (2002). Vibrational Spectroscopy of Food and Food Products. Handbook of Vibrational Spectroscopy, Vol. 5, Chalmers JM and Griffiths PR (Eds), Wiley, Chichester, UK, 3629-3662.
[117] Bartick EG (2002). Applications of Vibrational Spectroscopy in Criminal Forensic Analysis. Handbook of Vibrational Spectroscopy, Vol. 4, Chalmers JM and Griffiths PR (Eds), Wiley, Chichester, UK, 2993-3004.
[118] Rodriguez-Saona LE, and Allendorf ME (2011). Use of FTIR for Rapid Authentication and Detection of Adulteration of Food. Annual Review of Food Science and Technology, 2, 467-483.
[119] Williams P (2002). Near-infrared Spectroscopy of Cereals. Handbook of Vibrational Spectroscopy, Vol. 5, Chalmers JM and Griffiths PR (Eds), Wiley, Chichester, UK, 3693-3719.
[120] Leclerc DF, and Trung TP (2002). Vibrational Spectroscopy in the Pulp and Paper Industry. Handbook of Vibrational Spectroscopy, Vol. 4, Chalmers JM and Griffiths PR (Eds), Wiley, Chichester, UK, 2952-2976.
[121] Carr C (2002). Vibrational Spectroscopy in the Paint Industry. Handbook of Vibrational Spectroscopy, Vol. 4, Chalmers JM, and Griffiths PR (Eds), Wiley, Chichester, UK, 2935-2951.

[122] Griffith DWT (2002). FTIR Measurements of Atmospheric Trace Gases and their Fluxes. Handbook of Vibrational Spectroscopy, Vol. 4, Chalmers JM and Griffith PR (Eds), Wiley, Chichester, UK, 2823-2841.
[123] Simonescu CM (2012). Application of FTIR Spectroscopy in Environmental Studies. Advanced Aspects of Spectroscopy, Chapter 2, 49-84.
[124] Shaw RA, and Mantsch HH (2000). Infrared Spectroscopy in Clinical and Diagnostic Analysis. Encyclopedia of Analytical Chemistry, Vol. 1, Meyers RA (Ed.), Wiley, Chichester, UK, 83-102.
[125] Stuart BH (2000). Infrared Spectroscopy of Biological Applications. Encyclopedia of Analytical Chemistry Vol. 1, Meyers RA (Ed.), Wiley, Chichester, UK, 529-559.
[126] Jackson M, and Mantsch HH (2002). Pathology by Infrared and Raman Spectroscopy. Handbook of Vibrational Spectroscopy, Vol. 5, Chalmers JM and Griffiths PR (Eds), Wiley, Chichester, UK, 3227-3245.
[127] Mascarenhas M, Dighton J, and Arbuckle GA (2000). Characterization of Plant Carbohydrates and Changes in Leaf Carbohydrate Chemistry Due to Chemical and Enzymatic Degradation Measured by Microscopic ATR FT-IR Spectroscopy. Applied Spectroscopy, 54, 681-686.
[128] Jiang W, Saxena A, Song B, Ward BB, Beveridge TJ, and Myneni SCB (2004). Elucidation of Functional Groups on Gram-Positive and Gram-Negative Bacterial Surfaces Using Infrared Spectroscopy. Langmuir 20, 11433-11442.
[129] Schmitt J, and Flemming HC (1998). FTlR-spectroscopy in microbial and material analysis. International Biodeterioration & Biodegradation 4l, l-11.
[130] Faghihzadeh F, Anaya NM, Schifman LA, and Oyanedel-Craver V (2016). Fourier transform infrared spectroscopy to assess molecular-level changes in microorganisms exposed to nanoparticles. Nanotechnology for Environmental Engineering, 1, 1-16.
[131] Zarei H, and Malekfar R (2014). Characterization of CIGS thin films fabricated from nanoparticles under selenization process. Advanced Materials Research, 829, 357-361.
[132] Zhang Y, Wang J, and Zhang L (2010). Creation of Highly Stable Selenium Nanoparticles Capped with Hyperbranched Polysaccharide in Water. Langmuir, 26, 17617-17623.
[133] Chen W, Li Y, LinYue SY, Jiang Q, and Xia W (2015). Synthesis and antioxidant properties of chitosan and carboxymethyl chitosan-stabilized selenium nanoparticles. Carbohydrate Polymers, 132, 574-581.
[134] Ramamurthy CH, Sampath KS, Arunkumar P, Suresh Kumar M, Sujatha V, Premkumar K, and Thirunavukkarasu C (2013). Green synthesis and characterization of selenium nanoparticles and its augmented cytotoxicity with doxorubicin on cancer cells. Bioprocess and Biosystems Engineering 36, 1131-1139.

[135] Zhang B (2019). Preparation of Nanoparticles by Green Synthesis and a Study on their Antibacterial and Anticancer Properties. www.search.proquest.com, 1-107.
[136] Anu K, Singaravelu G, Murugan K, and Benelli G (2017). Green-Synthesis of Selenium Nanoparticles Using Garlic Cloves (*Allium sativum*): Biophysical Characterization and Cytotoxicity on Vero Cells. Journal of Cluster Science, 28, 551-563.
[137] Chandramohan S, Sundar K, and Muthukumaran A (2018). Monodispersed spherical shaped selenium nanoparticles (SeNPs) synthesized by *Bacillus subtilis* and its toxicity evaluation in zebrafish embryos. Material Research Express, IOP Publishing Ltd.
[138] Sonkusre P, Nanduri R, Gupta P, and Cameotra SS (2014). Improved Extraction of Intracellular Biogenic Selenium Nanoparticles and their Specificity for Cancer Chemoprevention. Journal of Nanomedicine and Nanotechnology, 5, 1-9.
[139] Radhika Rajasree SR, and Gayathri S (2015). Extracellular Biosynthesis of Selenium Nanoparticles using some species of *Lactobacillus*. Indian Journal of Geo-Marine Sciences, 43, 776-775.
[140] Zonaro E, Piacenza E, Presentato A, Monti F, Dell'Anna R, Lampis S, and Vallini G (2017). *Ochrobactrum* sp. MPV1 from a dump of roasted pyrites can be exploited as bacterial catalyst for the biogenesis of selenium and tellurium nanoparticles. Microbial Cell Factories, 16, 1-17.
[141] Kamnev AA, Ristić M, Antonyuk LP, Chernyshev AV, and Ignatov VV (1997). Fourier transform infrared spectroscopic study of intact cells of the nitrogen-fixing bacterium *Azospirillum brasilense*. Journal of molecular structure, 408/409, 201-205.
[142] Kamnev AA, Mamchenkova PV, Dyatlova YA, and Tugarova AV (2017). FTIR spectroscopic studies of selenite reduction by cells of the rhizobacterium *Azospirillum brasilense* Sp7 and the formation of selenium nanoparticles. Journal of Molecular Structure, 1140, 106-112.
[143] Tugarova AV, Mamchenkova PV, Dyatlova YA, and Kamnev AA (2018). FTIR and Raman spectroscopic studies of selenium nanoparticles synthesised by the bacterium *Azospirillum thiophilum*. Spectrochimica Acta Part A: Molecular and Biomolecular Spectroscopy 192, 458-463.
[144] Zhang W, Chen Z, Liu H, Zhang L, Gao P, and Li D (2011). Biosynthesis and structural characteristics of selenium nanoparticles by *Pseudomonas alcaliphila*. Colloids and Surfaces B: Biointerfaces, 88, 196-201.
[145] Kora AJ, and Rastogi L (2016). Biomimetic synthesis of selenium nanoparticles by *Pseudomonas aeruginosa* ATCC 27853: An approach for conversion of selenite. Journal of Environmental Management, 181, 231-236.
[146] Wadhwani SA, Gorain M, Banerjee P, Shedbalkar UU, Singh R, Kundu GC, and Chopade BA (2017). Green synthesis of selenium nanoparticles using

Acinetobacter sp. SW30: optimization, characterization and its anticancer activity in breast cancer cells. International Journal of Nanomedicine, 12, 6841-6855.
[147] Kora AJ, and Rastogi L (2017). Bacteriogenic synthesis of selenium nanoparticles by *Escherichia coli* ATCC 35218 and its structural characterisation. IET nanobiotechnology, 11, 179-184.
[148] Rehman I, Movasaghi Z, and Rehman S (2012). Vibrational spectroscopy for tissue analysis. CRC Press, 1-356.
[149] Filipa Z, Herrmanna S, and Kubat J (2004). FT-IR spectroscopic characteristics of differently cultivated *Bacillus subtilis*. Microbiological Research 159, 257-262.
[150] Hajipour MJ, Fromm KM, Ashkarran AA, Jimenez de Aberasturi D, Ruiz de Larramendi I, Rojo T, Serpooshan V, Parak WJ, and Mahmoudi M (2012). Antibacterial properties of nanoparticles. Trends in Biotechnology, 1-13.
[151] Heys KA, Riding MJ, Strong RJ, Shore RF, M. Pereira G, Jones KC, Semple KT, and Martin FL (2014). Mid-infrared spectroscopic assessment of nanotoxicity in Gram-negative vs. Gram-positive bacteria. Analyst, 1-30.
[152] Riding MJ, Martin FL, Trevisan J, Llabjani V, Patel II, Jones KC, and Semple KT (2012). Concentration-dependent effects of carbon nanoparticles in gram-negative bacteria determined by infrared spectroscopy with multivariate analysis. Environmental Pollution, 163, 226-234.
[153] Wani MY, Hashim MA, Nabi F, and Malik MA (2011). Nanotoxicity: Dimensional and Morphological Concerns. Advances in Physical Chemistry, 1-15.
[154] Klaine SJ, Alvarez PJJ, Batley GE, Fernandes TF, Handy RD, Lyon DY, Mahendra S, Mclaughlin MJ, and Lead JR (2008). Nanomaterials in the Environment: Behavior, Fate, Bioavailability, and Effects. Environmental Toxicology and Chemistry, 27, 1825-1851.
[155] Lead JR, Batley GE, Alvarez PJJ, Croteau MN, Handy RD, McLaughlin MJ, Judy JD, and Schirmer K (2018). Nanomaterials in the environment: behavior, fate, bioavailability, and effects-an updated review. Environmental Toxicology and Chemistry, 37, 2029-2063.
[156] Self W, Pierce R, and Stadtman TC (2004). Cloning and heterologous expression of a *Methanococcus vannielii* gene encoding a selenium-binding protein. IUBMB Life, 56, 501-507.
[157] Dynamic Light Scattering. Common Terms Defined (2011). Malvern Instruments Limited. http://www.biophysics.bioc.cam.ac.uk
[158] Romero-Pérez A, García-García E, Zavaleta-Mancera A, Ramírez-Bribiesca JE, Revilla-Vázquez A, Hernández-Calva LM, López-Arellano R, and Cruz-Monterrosa RG (2010). Designing and evaluation of sodium selenite nanoparticles in vitro to improve selenium absorption in ruminants. Veterinary Research Communications 34, 71-79.
[159] Villas-Bôas SG, Roessner U, Hansen MAE, Smedsgaard J, Nielsen J (2007). Metabolome analysis: an introduction. Wiley, Hoboken.

[160] Navid A (2012). Microbial Systems Biology: Methods and Protocols. Methods in Molecular Biology, Springer, Vol. 881.
[161] Boccard J, Veuthey JL, and Rudaz S (2010). Knowledge discovery in metabolomics: An overview of MS data handling. Journal of Separation Science, 33, 290-304.
[162] Warwick BD, and Ellis DI (2005). Metabolomics: current analytical platforms and methodologies. Trends in Analytical Chemistry, 24, 285-294.
[163] Griffin JL (2004). Metabolic profiles to define the genome: can we hear the phenotypes? Philosophical Transactions of the Royal Society B: Biological Science, 359, 857-871.
[164] Bender DA (2005). Perspective. The promise of metabolomics. Journal of the Science of Food and Agriculture, 85, 7-9.
[165] Gygi SP, Rochon Y, Franza BR, and Aebersold R (1999). Gene expression: Correlation between protein and mRNA abundance in yeast. Molecular and Cellular Biology, 19, 1720-1730.
[166] Sumner LW, Mendes P, and Dixon RA (2003). Plant metabolomics: Large-scale phytochemistry in the functional genomics era. Phytochemistry, 62, 817-836.
[167] Fiehn O (2002). Metabolomics-the link between genotypes and phenotypes. Plant Molecular Biology 48, 155-171.
[168] Villas-Boâs SG, Mas S, Åkesson M, Smedsgaard J, and Nielsen J (2004). Mass Spectrometry and Metabolome Analysis. Mass Spectrometry Reviews, 24, 613-646.
[169] Barh D, and Azevedo V (2017). Omics Technologies and Bio-engineering: Towards Improving Quality of Life. Emerging Field, Animals and Medical Biotechnologies, Vol. 1. Academic Press, Elsevier Inc.
[170] Goodacre R, Vaidyanathan S, Dunn WB, Harrigan GG, and Kell DB (2004). Metabolomics by numbers: acquiring and understanding global metabolite data. Trends in Biotechnology, 22, 245-252.
[171] Der Greef J, and Smilde AK (2005). Symbiosis of chemometrics and metabolomics: past, present, and future. Journal of Chemometrics, 19, 376-386.
[172] Gates SC, and Sweeley CC (1978). Quantitative Metabolic Profiling Based on Gas Chromatography. Clinical Chemistry, 24/10, 1663-1673.
[173] Young DS (1970). High-pressure column chromatography of carbohydrates in the clinical laboratory. American Journal of Clinical Pathology, 53, 803.
[174] Williams GZ, Young DS, Stein MR, and Cotlove E (1970). Biological and analytic components of variation in long-term studies of serum constituents in normal subjects. I. Objectives, subject selection, laboratory procedures and estimation of analytic deviation. Clinical Chemistry, 16, 1016.
[175] Burtis CA, Goldstein G, and Scott CD (1970). Fractionation of human urine by gel chromatography. Clinical Chemistry, 16, 201.
[176] Horning EC, and Horning MG (1971). Human metabolic profiles obtained by GC and GC/MS. Journal of Chromatographic Science, 9, 129.
[177] Horning EC, and Horning MG (1971). Metabolic profiles: Gas-phase methods for analysis of metabolites. Clinical Chemistry, 17, 802.
[178] Oliver SG, Winson MK, Kell DB, and Baganz F (1998). Systematic functional analysis of the yeast genome. Trends in Biotechnology, 16, 373-378.

[179] Kell DB, Brown M, Davey HM, Dunn WB, Spasic I, and Oliver SG (2005). Metabolic foot printing and systems biology: the medium is the message. Nature Reviews Microbiology, 3, 557-565.
[180] Smith CA, I'Maille G, Want EJ, Qin C, Trauger SA, Brandon TR, Custodio DE, Abagyan R, and Siuzdak G (2005). METLIN: a metabolite mass spectral database. Therapeutic Drug Monitoring, 27, 6: 747-51.
[181] Wishart DS, Tzur D, Knox C, et al. (2007). HMDB: the Human Metabolome Database. Nucleic Acids Research, 35, D521-526.
[182] Guo AC, Jewison T, Wilson M, Liu Y, Knox C, Djoumbou Y, Lo P, Mandal R, Krishnamurthy R, and Wishart DS (2012). ECMDB: The *E. coli* Metabolome Database. Nucleic Acids Research, 41, D625-30.
[183] Udayakumar M, Chandar DP, Arun N, Mathangi J, Hemavathi K, and Seenivasagam R (2011). PMDB: Plant Metabolome Database-A Metabolomic Approach. Medicinal Chemistry Research, 21, 47-52.
[184] Pinu FR, and Villas-Boâs SG (2017). Extracellular Microbial Metabolomics: The State of the Art. Metabolites, 7, 43.
[185] Dettmer K, and Hammock BD (2004). Metabolomics-A New Exciting Field within the "omics" Sciences. Environmental Health Perspectives, 112, A396-A397.
[186] Dettmer K, Aronov PA, and Hammock BD (2007). Mass Spectrometry-Based Metabolomics. Mass Spectrometry Reviews, 26, 51-78.
[187] Zhang A, Sun H, Wang P, Han Y, and Wang X (2012). Modern analytical techniques in metabolomics analysis. Analyst, 137, 293-300.
[188] Theodoridis GA, Gika HG, Want EJ, and Wilson ID (2012). Liquid chromatography–mass spectrometry based global metabolite profiling: A review. Analytica Chimica Acta, 711, 7-16.
[189] Kamphorst JJ, and Lewis IA (2017). Editorial overview: Recent innovations in the metabolomics revolution. Current Opinion in Biotechnology, 43, iv-vii.
[190] Markley JL, Brüschweiler R, Edison AS, Eghbalnia HR, Powers R, Raftery D, and Wishart DS (2017). The future of NMR-based metabolomics. Current Opinion in Biotechnology, 43, 34-40.
[191] Haggarty J, and Burgess KEV (2017). Recent advances in liquid and gas chromatography methodology for extending coverage of the metabolome. Current Opinion in Biotechnology, 43, 77-85.
[192] Tranchida PQ, Franchina FA, Dugo P, and Mondello L (2016). Comprehensive two-dimensional gas chromatography-mass spectrometry: Recent evolution and current trends. Mass Spectrometry Reviews, 35, 524-534.
[193] Pirok BWJ, Gargano AFG, and Schoenmakers PJ (2018). Optimizing separations in online comprehensive two-dimensional liquid chromatography. Journal of Separation Science, 41, 68-98.
[194] Kamal S, and Sharad W (2018). Step-up in liquid chromatography from HPLC to UPLC: A comparative and comprehensive review. The Pharma Innovation Journal, 7, 342-347.
[195] Zhang W, Hankemeier T, and Ramautar R (2017). Next-generation capillary electrophoresis-mass spectrometry approaches in metabolomics. Current Opinion in Biotechnology, 43, 1-7.
[196] Booth SC, Workentine ML, Weljie AM, and Turner RJ (2011). Metabolomics and its application to studying metal toxicity. Metallomics, 11, 1-11.

[197] García-Sevillano MA, García-Barrera T, and Gómez-Ariza JL (2015). Environmental metabolomics: Biological markers for metal toxicity. Electrophoresis, 36, 2348-2365.
[198] Dubey S, Shri M, Gupta A, Rani V, and Chakrabarty B (2018). Toxicity and detoxification of heavy metals during plant growth and metabolism. Environmental Chemistry Letters, 16, 1169-1192.
[199] Sun X, Zhang J, Zhang H, Ni Y, Zhang Q, Chen J, and Guan Y (2010). The responses of *Arabidopsis thaliana* to cadmium exposure explored via metabolite profiling. Chemosphere, 78, 840-845.
[200] Sarry JE, Kuhn L, Ducruix C, Lafaye A, Junot C, Hugouvieux V, Jourdain A, Bastien O, Fievet JB, Vailhen D, Amekraz B, Moulin C, Ezan E, Garin J, and Bourguignon J (2006). The early responses of *Arabidopsis thaliana* cells to cadmium exposure explored by protein and metabolite profiling analyses. Proteomics, 6, 2180-2198.
[201] Pidatala VR, Li K, Sarkar D, Wusirika R, and Datta R (2018). Comparative metabolic profiling of vetiver (*Chrysopogon zizanioides*) and maize (*Zea mays*) under lead stress. Chemosphere 193, 903-911.
[202] Gao Y, Lu Y, Huang S, Gao L, Liang X, Wu Y, Wang J, Huang Q, Tang L, Wang G, Yang F, Hu S, Chen Z, Wang P, Jiang Q, Huang R, Xu Y, Yang X, and Ong CN (2014). Identifying Early Urinary Metabolic Changes with Long-Term Environmental Exposure to Cadmium by Mass-Spectrometry-Based Metabolomics. Environmental Science and Technology, 48, 11, 6409-6418.
[203] Dudka I, Kossowska B, Senhadri H, Latajka R, Hajek J, Andrzejak R, Antonowicz-Juchniewicz J, and Gancarz R (2014). Metabonomic analysis of serum of workers occupationally exposed to arsenic, cadmium and lead for biomarker research: A preliminary study. Environment International, 68, 71-81.
[204] Gieger C, Geistlinger L, Altmaier E, Hrabe´ de Angelis M, Kronenberg F, Meitinger T, Mewes HW, Wichmann HE, Weinberger KM, Adamski J, Illig T, and Suhre K (2008). Genetics Meets Metabolomics: A Genome-Wide Association Study of Metabolite Profiles in Human Serum. PLoS Genetics, 4, 11, 1-12.
[205] Zhai Q, Xiao Y, Narbad A, and Chen W (2018). Comparative metabolomic analysis reveals global cadmium stress response of *Lactobacillus plantarum* strains. Metallomics, 10, 1065-1077.
[206] Booth SC, Workentine ML, Wen J, Shaykhutdinov R, Vogel HJ, Ceri H, Turner RJ, and Weljie AM (2011). Differences in Metabolism between the Biofilm and Planktonic Response to Metal Stress. Journal of Proteome Research, 10, 7, 3190-3199.
[207] Lemire J, Kumar P, Mailloux R, Cossar K, and Appanna VD (2008). Metabolic adaptation and oxaloacetate homeostasis in *P. fluorescens* exposed to aluminum toxicity. Journal of Basic Microbiology, 48, 252-259.
[208] Beriault R, Hamel R, Chenier D, Mailloux R, Joly H, and Appanna V (2006). The overexpression of NADPH-producing enzymes counters the oxidative stress evoked by gallium, an iron mimetic. BioMetals, 20, 165-176.
[209] Tremaroli V, Workentine ML, Weljie AM, Vogel HJ, Ceri H, Viti C, Tatti E, Zhang P, Hynes AP, Turner RJ, and Zannoni D (2009). Metabolomic Investigation of the Bacterial Response to a Metal Challenge. Applied and Environmental Microbiology, 75, 719-728.

[210] Lu W, Su X, Klein MS, Lewis IA, Fiehn O, and Rabinowitz JD (2017). Metabolite Measurement: Pitfalls to Avoid and Practices to Follow. Annual Review of Biochemistry, 86, 277-304.
[211] Melamud E, Vastag L and Rabinowitz JD (2010). Metabolomic Analysis and Visualization Engine for LC-MS Data. Analytical Chemistry, 82, 9818-9826.
[212] Tai YC, and Speed TP (2006). A multivariate empirical Bayes statistic for replicated microarray time course data. Annals of Statistics, 34, 2387-2412.
[213] Jansen JJ. Hoefsloot HCJ, van der Greef J, Timmerman ME, and Smilde AK (2005). Multilevel component analysis of time-resolved metabolic fingerprinting data. Analytical Chimica Acta, 530, 173-183.
[214] Dai D, Gao Y, Chen J, Huang Y, Zhang Z, and Xu F (2016). Time-resolved metabolomics analysis of individual differences during the early stage of lipopolysaccharide-treated rats. Scientific Reports, 6, 1-12.
[215] Zar JH (2010). Biostatistical Analysis. Fifth Edition. Prentice-Hall, Upper Saddle River, NJ, Chapter 13.
[216] Bartlett MS (1947). The Use of Transformations. Biometrics, Vol. 3, 39-52. JSTOR www.jstor.org/stable/3001536.
[217] Wang T, Yang L, Zhang B, Liu J (2010). Extracellular biosynthesis and transformation of selenium nanoparticles and application in H_2O_2 biosensor. Colloid Surface B, 80, 94-102.
[218] Helmann JD (2011). Bacillithiol, a New Player in Bacterial Redox Homeostasis. Antioxidants & Redox Signaling, 15, 123-133.
[219] Sharma SV, Arbach M, Roberts AA, Macdonald CJ, Groom M, and Hamilton CJ (2013). Biophysical Features of Bacillithiol, the Glutathione Surrogate of *Bacillus subtilis* and other Firmicutes. ChemBioChem, 14, 2160-2168.
[220] Fang Z, and Dos Santos PC (2015). Protective role of bacillithiol in superoxide stress and Fe-S metabolism in *Bacillus subtilis*. MicrobiologyOpen, 4, 616-631.
[221] He YY, and Hader DP (2002). UV-B-induced formation of reactive oxygen species and oxidative damage of the cyanobacterium *Anabaena sp.*: protective effects of ascorbic acid and N-acetyl-L-cysteine. Journal of Photochemistry and Photobiology, 115-124.
[222] Kim KH, Jia B, and Jeon CO (2017). Identification of Trans-4-Hydroxy-L-Proline as a Compatible Solute and Its Biosynthesis and Molecular Characterization in *Halobacillus halophilus*. Frontiers in Macrobiology, 1-11.
[223] Zaprasis A, Bleisteiner M, Kerres A, Hoffmann T, and Bremera E (2015). Uptake of Amino Acids and Their Metabolic Conversion into the Compatible Solute Proline Confers Osmoprotection to *Bacillus subtilis*. Applied and Environmental Microbiology, 81, 250-259.
[224] Zhao H, Roistacher DM, and Helmann JD (2018). Aspartate deficiency limits peptidoglycan synthesis and sensitizes cells to antibiotics targeting cell wall synthesis in *Bacillus subtilis*. Molecular Microbiology, 109, 826-844.
[225] Søballe B, and Poole RK (1999). Microbial ubiquinones: Multiple roles in respiration, gene regulation and oxidative stress management. Microbiology, 145, 1817-1830.
[226] Sévin DC, and Sauer U (2014). Ubiquinone accumulation improves osmotic-stress tolerance in *Escherichia coli*. Nature Chemical Biology, 10, 266-274.

[227] Bianco C, Imperlini E, Calogero R, Senatore B, Amoresano A, Carpentieri A, Pucci P, and Defez R (2006). Indole-3-acetic acid improves *Escherichia coli*'s defences to stress. Archives of Microbiology, 1-10
[228] Somers E, Ptacek D, Gysegom P, Srinivasan M, and Vanderleyden J (2005). *Azospirillum brasilense* Produces the Auxin-Like Phenylacetic Acid by Using the Key Enzyme for Indole-3-Acetic Acid Biosynthesis. Applied and Environmental Microbiology, 71, 1803-1810.
[229] Han TH, Lee JH, Cho MH, Wood TK, and Lee J (2011). Environmental Factors Affecting Indole Production in *Escherichia coli*. Research in Microbiology, 162, 108-116.
[230] Kim J, and Park W (2015). Indole: a signaling molecule or a mere metabolic byproduct that alters bacterial physiology at a high concentration? Journal of Microbiology, 53, 421-428.
[231] Lee JH, and Lee J (2010). Indole as an intercellular signal in microbial communities. FEMS Microbiology Reviews, 34, 426-444.
[232] Martino PD, Fursy R, Bret L, Sundararaju B, and Phillips RS (2003). Indole can act as an extracellular signal to regulate biofilm formation of *Escherichia coli* and other indole-producing bacteria. Canadian Journal of Microbiology, 49, 443-449.
[233] Kane JI, and Jensen RA (1970). Metabolic Interlock. The influence of histidine on tryptophan biosynthesis in *Bacillus subtilis*. The Journal of Biological Chemistry, 245, 2384-2390.
[234] Carabetta VJ, and Cristea IM (2017). Regulation, Function, and Detection of Protein Acetylation in Bacteria. Journal of Bacteriology, 199, 1-15.
[235] Hu LI, Lima BP, and Wolfe AJ (2010). Bacterial Protein Acetylation: the Dawning of a New Age. Molecular Microbiology, 77, 15-21.
[236] Jackson EK, Ren J, and Mi Z (2009). Extracellular 2', 3'-cAMP Is a Source of Adenosine. The Journal of Biological Chemistry, 284, 33097-33106.
[237] Jackson EK (2015). Discovery and Roles of 2', 3'-cAMP in Biological Systems. Springer International Publishing Switzerland, R. Seifert (ed.), Non-canonical Cyclic Nucleotides, Handbook of Experimental Pharmacology, 238.
[238] Forchhammer K (2007). Glutamine signaling in bacteria. Frontiers in Bioscience, 12, 358-370.
[239] Boer VM, Crutchfield CA, Bradley PH, Botstein D, and Rabinowitz JD (2010). Growth-limiting Intracellular Metabolites in Yeast Growing under Diverse Nutrient Limitations. Molecular Biology of the Cell, 21, 198-211.
[240] Pratviel G, and Meunier B (2006). Guanine Oxidation: One- and Two-Electron Reactions. Chemistry - A European Journal, 12, 6018-6030.
[241] Sugden KD, Campo CK, and Martin BD (2001). Direct Oxidation of Guanine and 7, 8-Dihydro-8-oxoguanine in DNA by a High-Valent Chromium Complex: A Possible Mechanism for Chromate Genotoxicity. Chemical Research in Toxicology, 14, 1315-1322.
[242] Ghosh A, Joy A, Schuster BG, Doukib T, and Cadet J (2008). Selective one-electron oxidation of duplex DNA oligomers: reaction at thymines. Organic and Biomolecular Chemistry, 6, 916-928.
[243] Begley TP, Kinsland C, Mehl RA, Osterman A, and Dorrestein P (2001). The biosynthesis of nicotinamide adenine dinucleotides in bacteria. Vitamins & Hormones, 61, 103-119.

[244] Surjana D, Halliday GM, and Damian DL (2010). Role of Nicotinamide in DNA Damage, Mutagenesis, and DNA Repair. Journal of Nucleic Acids, 1-14.
[245] Crowley CL, Payne CM, Bernstein H, Bernstein C, and Roe D (2000). The NAD^+ precursors, nicotinic acid and nicotinamide protect cells against apoptosis induced by a multiple stress inducer, deoxycholate. Cell Death and Differentiation, 7, 314-326.